Magnetic Wreaths, Cycles, and Buoyant Loops in Convective Dynamos

by

Nicholas J. Nelson

B.S., Brigham Young University, 2007

M.S., University of Colorado, 2010

A thesis submitted to the

Faculty of the Graduate School of the

University of Colorado in partial fulfillment

of the requirements for the degree of

Doctor of Philosophy

Department of Astrophysical & Planetary Sciences

2013

This thesis entitled:
Magnetic Wreaths, Cycles, and Buoyant Loops in Convective Dynamos
written by Nicholas J. Nelson
has been approved for the Department of Astrophysical & Planetary Sciences

Juri Toomre

John Bally

Keith Julien

Mark Miesch

Mark Rast

Michael Shull

Date

The final copy of this thesis has been examined by the signatories, and we find that both the content and the form meet acceptable presentation standards of scholarly work in the above mentioned discipline.

Nelson, Nicholas J. (Ph.D., Astrophysical & Planetary Sciences)

Magnetic Wreaths, Cycles, and Buoyant Loops in Convective Dynamos

Thesis directed by Prof. Juri Toomre

Solar-like stars exhibit a rich variety of magnetic activity, which is driven by dynamo action in the stellar interior. In the Sun, strong dynamo action creates global-scale magnetic fields which undergo cyclic reversals as well as smaller-scale dipolar active regions which have global-scale organization. Dynamo action is a highly nonlinear process which is enabled by the interplay of turbulent convection, rotation, and stratification. Seeking to explore the convective origins of magnetism in sun-like stars, we have used 3D MHD simulations with the Anelastic Spherical Harmonic (ASH) code to model elements of these dynamos. Previous simulations have demonstrated that large-scale "wreaths" of toroidal magnetic field can be achieved in the convection zone without a tachocline of shear at its base, as was thought to be necessary, and that these wreaths can yield reversals in global magnetic polarity.

We find that cyclic reversals of global magnetic polarity in wreath-building dynamos can be achieved by increasing the level of turbulence in solar-like simulations. By decreasing the effective diffusion we demonstrate that large-scale magnetic wreaths can persist in simulations where explicit diffusion has been decreased to levels at which it no longer plays a significant role in the key dynamical balances required to achieve wreath-building dynamo action. Magnetic reversals are attained when resistive diffusion of the poloidal magnetic fields becomes too small to prevent turbulent magnetic induction from generating opposite polarity poloidal fields.

In order to attain even less diffusive simulations, we explore more a dynamic Smagorinsky model. Using the dynamic Smagorinsky model, we achieve a dynamo simulation capable of building buoyant magnetic loops which rise coherently through our simulated domain. These loops ascend via a combination of magnetic buoyancy and advection by convective

giant cells. These buoyant loops originate within sections of the magnetic wreaths in which turbulent flows amplify the fields to much higher values than is possible through laminar processes. We measure statistical trends in the polarity, twist, and tilt of these loops. Loops are shown to preferentially arise in longitudinal patches somewhat reminiscent of active longitudes in the Sun, although broader in extent. We show that the strength of the axisymmetric toroidal field is not a good predictor of the production rate for buoyant loops or the amount of magnetic flux in the loops that are produced.

Finally, we explore the effects of a new upper boundary condition on ASH simulations. Previous simulations have employed an impenetrable upper boundary condition, which imposed an unphysical viscous boundary layer in the upper layers of the convection zone. We have implemented and tested an alternative boundary condition which imposes small-scale convective plumes on the upper boundary, mimicking the small-scale convective motions from the near-surface layers. We find that for suitable choices of plume parameters we can largely remove the viscous boundary layer and significantly decrease the convective velocities at mid-convection zone, thus increasing the level of rotational constraint and helping the simulations to achieve more solar-like behavior.

Dedication

To my adviser, Juri Toomre, for his infectious enthusiasm for stars. To my parents, Neil and Laurie Nelson, for preparing me to follow this path. To my endlessly supportive wife, Rachel Nelson, who reminds me that sub-grid scale representations of turbulence are not the most important things in life. To God, for whom I have quite a few questions about dynamo action and magnetic buoyancy in stars.

Acknowledgements

In February 2007 I met Juri Toomre for the first time and his singular enthusiasm for his research convinced me to come to the University of Colorado. I have never regretted that decision. Over the past six years, Juri has become a trusted mentor and a valued friend. Mark Miesch has been my "adviser in the trenches", so to speak, who has guided me through all sorts of nuanced and detailed physical, mathematical, and computational arguments. Sacha Brun has been my adviser from afar, providing insight and support with his regular visits to Boulder. In many ways advising me has been a group collaboration between Juri, Mark, and Sacha. I would not be where I am today without their combined efforts.

I learned much of my craft from the graduate students who came before me, especially Ben Brown, Geoff Vassil, Nicholas Featherstone, and Kyle Augustson, and from the senior researchers in our group Brad Hindman and Regner Trumpadarch. Special thanks are due to Ben Brown, François Hibbert and Christopher Chronopoulos, who endured sharing an office with me, and thus engaging in many hours of conversations related to various detours and roadblocks over the years. It takes a lot of patience to act interested in my ramblings for extended periods of time, something they all did very well. I thank them for putting up with me.

Finally, I would be remiss if I did not acknowledge Gwen Dickinson for keeping our research group alive and functional. I never had enough time to chat with Gwen as much as I would have liked. One of my greatest achievements in graduate school has been staying off her "problem child" list.

Contents

Tables

Figures

Chapter 1

Solar and Stellar Magnetic Activity

1.1 Magnetism in Sun-like Stars

Stellar variability due to magnetic activity is one of the most enduring topics of astronomical research. Scientific observations of sunspots began with Galileo's regular descriptions and drawings of sunspots over 400 years ago (see Drake, 1957). Shortly after the turn of the 20th Century, Hale (1908) showed that sunspots contain strong, coherent magnetic fields. We now know that sunspots appear as dark patches on the Sun's surface due to the inhibition of convective heat transport by strong, organized magnetic fields. Solar magnetism is of course not limited to sunspots. The Sun's magnetic fields exist on a wide range of scales from the magnetized solar wind which fills the heliosphere to the smallest resolvable scales on the photosphere. Magnetic processes in these widely disparate regimes drive much of the temporal variability of the Sun's surface and extended atmosphere.

Figure 1.1 illustrates the magnetic nature of sunspots. In visible light they appear as small, dark patches with temperatures typically lower than the surrounding solar surface by about 1000K. These lower temperatures are the result of strong magnetic fields inhibiting the convective mixing present over the solar surface, which constantly replenishes the energy lost to radiation. Thus material in sunspots is initially of the same temperature and brightness as the rest of the solar surface, however radiative losses quickly lead to a strong deficit in temperature in the spot. The dark spots shown here in modern space-based observations from the Solar Dynamics Observatory are the most easily observed consequences of solar

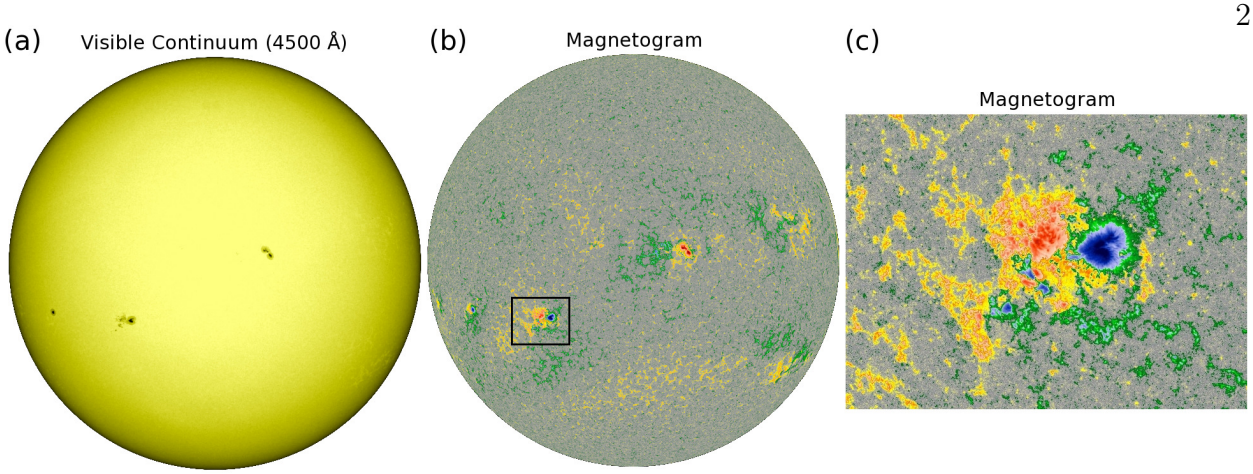

Figure 1.1: Sample views of magnetic features on the solar surface taken by the Solar Dynamics Observatory (SDO) on October 25, 2012. (a) Sunspots are visible as dark spots in the visible continuum centered at 4500Å using the Atmospheric Imaging Array (AIA). Here three major sunspot groups can be seen, two in the southern hemisphere and one in the north. (b) Companion magnetogram from the Heliospheric and Magnetic Imager (HMI) where color gives line-of-sight magnetic field strength (blue negative, red positive, peak field strengths are about 10 kG). Here the strongest fields are clearly concentrated in the sunspot groups, though considerable magnetic fields are also visible in plage regions surrounding sunspot groups and the magnetic network which extends over most of the solar surface. (c) Zoom-in view of the region around one sunspot pair indicated in (b), showing the complex nature of the fields which emerge through the solar surface.

magnetism (see reviews Borrero & Ichimoto, 2011; Rempel & Schlichenmaier, 2011).

When narrow-band imaging is used to detect Zeeman splitting, line-of-sight magnetic field can be measured and the magnetic nature of these spots becomes easily apparent. The magnetogram in Figure 1.1(b) reveals the strong magnetic fields which make up the sunspot pairs (see zoomed-in region in Figure 1.1(c)), but also makes visible the rich topology of the magnetic network. Sunspots typically have field strengths on the order of 10 kG and areas on the order of 100 Mm^2. Also visible are regions of weaker, less coherent magnetic field known as plage which surround active regions with magnetic field strengths on the order of 1 kG (Guglielmino et al., 2012). At even smaller scales and field strengths is the magnetic network, which roughly traces the boundaries of supergranules with typical field strengths on the order of 100 G (Rieutord & Rincon, 2010). On granular scales high resolution observations reveal

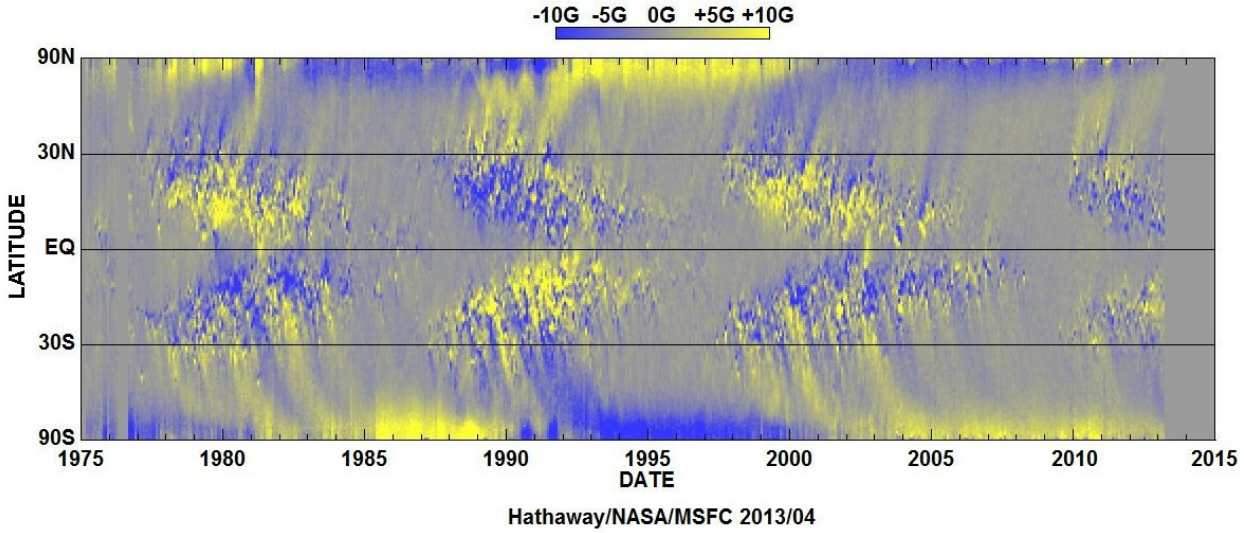

Figure 1.2: Azimuthally-averaged magnetic fields on the sun as a function of latitude at time from 1975 to 2013 (color gives polarity). Clear indications of spatial and temporal organization can be seen in the equatorward propagation of active latitudes, the 11-year cycles of magnetic activity, and the 22-year cycles of magnetic polarity. Courtesy David Hathaway, NASA-Marshall. For more information see Hathaway (2010).

magnetic bipoles as small as 100 km in size which emerge at a rate of roughly four per minute per granule (Danilovic et al., 2010). It is likely that magnetic fields continue at even smaller scales, however there are currently no telescopes capable of resolving such small scales (see review Mackay & Yeates, 2012).

Both sunspots and the magnetic network are most easily observed at the surface. However they continue up into the solar atmosphere and down into the solar interior. In the solar atmosphere, magnetism can be monitored using UV and X-ray observations (Mackay & Yeates, 2012). In the interior it becomes extremely difficult to detect magnetic fields directly, however considerable effort has been made to map the flows and thermal fields around sunspots using helioseismology (Hindman et al., 2009; Borrero & Ichimoto, 2011). Understanding these flows and thermal structures provides clues as to the topology and magnitude of sub-surface fields.

While sunspots are relatively localized structures whose individual lifetimes, ampli-

tudes, and locations of appearance are at least somewhat random, collectively these spots exhibit global-scale organization both spatially and temporally. Figure 1.2 shows one version of the famous solar butterfly diagram. Sunspots undergo magnetic activity cycle of roughly 11 years in duration. At the start of each cycle sunspots appear at mid-latitudes. Each sunspot group persists for anywhere from a few weeks to a few months. Over the course of each cycle new spots appear on average at progressively lower latitudes until they reach the equator. New spots then begin appearing at mid-latitudes and the cycle begins again. Upon further inspection, it becomes clear that additional global-scale organization exists in the form of preferential polarities on the poleward and equatorward sides of each active band in each hemisphere. For example, in the previous activity cycle from roughly 1997 to 2008 (cycle 23), sunspot pairs preferentially appeared with the negative polarity spot slightly poleward from the positive polarity spot in the northern hemisphere. In the current cycle this preference has reversed. Thus the 11-year activity cycle is really part of the longer 22 year magnetic polarity cycle (see review Hathaway, 2010).

Indian, Chinese, Korean, and possibly Native American sources have recorded naked eye observations of sunspots since at least 165 BC (Whittmann & Xu, 1987). Telescopic sunspot observations began with Galileo in 1611 (Sakurai, 1980). The 11-year activity cycle appears in the observational record from at least 1611 until 1645, and then again after 1715 to the present. Since 1715 there have been 24 11-year activity cycles. From about 1645 to 1715, the sunspot cycle apparently ceased in what is known as the Maunder Minimum (Hathaway, 2010). Longer-term records through surrogate methods indicate that this pattern of regular 11-year activity cycles with occasional interruptions by Grand Minima, such as the Maunder Minimum, have been occurring for at least the last 10,000 years (Usoskin, 2008). Usoskin et al. (2007) calculate that since 9,500 BC the Sun has spent roughly one-sixth of its existence in Grand Minima.

The Sun is not alone in its ability to generate magnetic spots and cycles of magnetic activity. Solar-type stars generate magnetism almost without exception, particularly at ro-

tation rates greater than that of the current Sun (see review Reiners, 2012). Proxies for stellar magnetism such as Calcium H and K emission and X-ray flux have long indicated that many sun-like stars are magnetically active (Hall, 2008). More recent developments in high-precision photometry and spectropolarimetry are providing new and independent measurements of stellar magnetism (Donati & Landstreet, 2009). These advances in observational techniques are, for the first time, permitting us to understand the Sun in context rather than as a single example of stellar dynamo action.

As observations of solar and stellar magnetism improve, there is a need for corresponding advances in theoretical models of convective dynamo action. In this thesis we will explore how 3D computational models inspired by solar and stellar observations can help us understand the physical mechanisms which drive dynamo action in sun-like stars.

1.1.1 Ingredients for Solar Dynamo Action

The interior of a sun-like star may be divided into three distinct regions. The centermost portion of the solar interior is the nuclear-burning core, which takes up roughly 25%, or about 173 Mm (1.73×10^8 m), of the solar interior by radius. Moving outward, the next region is the radiative zone which extends up to 71% of the solar radius or 490 Mm. In this layer energy is transported by the slow outward diffusion of photons. In the radiative zone the stratification is stable to overturning motions. The outermost of the three regions is the convective zone which begins at 71% of the solar interior by radius (a depth of 200 Mm) and extends to the solar surface. In this region the plasma becomes too opaque for photons to transport the solar luminosity outward and thus energy must be transported by fluid motions. This convective transport continues up to the solar photosphere where the plasma becomes largely transparent to visible light, allowing photons to stream freely and efficiently carry the solar luminosity again. This interior structure has been confirmed by helioseismic measurements (Christensen-Dalsgaard, 2002). Using continuous observations of

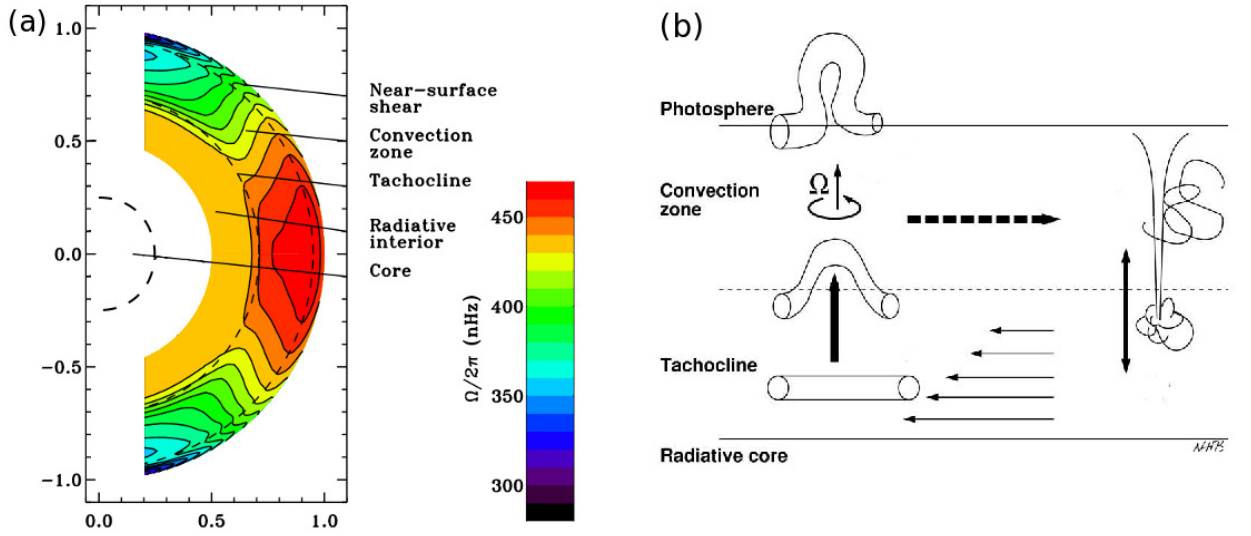

Figure 1.3: (a) The solar differential rotation profile (in angular velocity Ω) as revealed by helioseismology using 12 years of data from the Michelson-Doppler Imager (MDI) instrument on the Solar and Heliospheric Observatory (SOHO). Areas left white represent regions where reliable measurements are not currently possible. Adapted from Howe (2009). (b) Schematic overview of the generally favored model for large-scale solar dynamo action. Small-scale fields are generated by turbulent convection and pumped down into the lower convection zone and tachocline. There they are organized into large-scale toroidal structures by differential rotation. Once they become sufficiently strong and coherent, the large-scale toroidal structures can rise via magnetic buoyancy effects. Some loops are destroyed by turbulent convection while others emerge through the photosphere to become sunspots. Image courtesy Nic Brummell, UC-Santa Cruz.

resonant acoustic modes, remarkably precise measurements can be made of the Sun's average radial structure. Coupling these measurements with 1D structure models has produced solar models which match profiles derived from helioseismic measurements and constraints from solar neutrino observations to within a few percent (Christensen-Dalsgaard et al., 1996).

In the convection zone three general classes of flows are believed to play important roles in the dynamo mechanism (see review Miesch, 2005). First is the Sun's differential rotation as measured by the angular velocity Ω as a function of radius and latitude. While it has long been known that the solar surface displays faster rotation at the equator than at high latitudes, global helioseismology has yielded detailed measurements of the solar differential

rotation as shown in Figure 1.3(a). The magnitude of the shear is quite striking with a contrast of roughly 30% between equator and pole. The radiative interior rotates as a solid body (Howe, 2009). The boundary between the radiative and convective regions is home to the tachocline, which is marked by a sharp transition to differential rotation with a fast equator and slow poles. How such sharp gradients are maintained is a subject of considerable interest as the timescale for the spread of differential rotation into the radiative zone is much shorter than the age of the Sun (e.g., Spiegel & Zahn, 1992; Rudiger & Kitchatinov, 1997; Gough & McIntyre, 1998; Strugarek et al., 2011). However a definitive answer to this question remains elusive. In the bulk of the convective zone the surfaces of constant rotation are roughly conical (tilted about 25° from the rotation axis), particularly at mid-latitudes. Finally the outer 5% by radius (35 Mm) of the Sun forms a near-surface shear layer where the radial gradient of rotation rate becomes negative (see review Miesch & Toomre, 2009). The total rotational velocity peaks at about 2 km s^{-1}. Subtracting the bulk rotation rate of the Sun gives differential rotation velocities on the order of 100 m s^{-1}.

The second class of flow is the meridional circulation. Direct observations of the solar surface show a roughly 10 m s^{-1} poleward flow in each hemisphere (Hathaway, 1996). Helioseismic measurements demonstrate that this flow continues through at least the near-surface shear layer (e.g., Haber et al., 2002; Ulrich, 2010). Below this layer, however, reliable measurements of the meridional circulation become extremely challenging. The deep meridional flow plays a key role in many flux transport dynamo models which rely on a single circulation cell to transport magnetic flux to high latitudes and then down to the base of the convection zone (Charbonneau, 2010). Recently, Hathaway (2012) has reported measurements of equatorward meridional flow at depths of about 50 Mm. The structure of the meridional flow as a function of depth and latitude in the bulk of the solar convection zone remains a subject of active debate (e.g., Sivaraman et al., 2010; Dikpati, 2011).

The third class of flows involves the highly turbulent convective motions responsible for carrying the solar luminosity. These convective motions are inherently three-dimensional,

highly variable, and chaotic in time. To add difficulty, the turbulence is neither homogeneous nor isotropic since rotation, stratification, and magnetism play important roles on a wide range of spatial and temporal scales. The dominant scale of convection changes at different depths in the solar interior. At the surface convection is dominated by granulation of the order of 1 Mm in size with typical velocities on the order of 5 km s^{-1} (Nordlund et al., 2009). In the near-surface layers supergranulation on scales on the order of 20 Mm becomes the preferred convective scale with typical velocities of 300 m s^{-1} (Rieutord & Rincon, 2010). In the deep interior it is believed that flows on still larger scales exist. Termed giant cells, these convective structures are realized in theoretical and numerical treatments of solar convection, where they have typical length scales between 100 and 200 Mm (see review Miesch, 2005). Local helioseismology has provided detailed descriptions of the near-surface layers of the solar interior (see review Gizon & Birch, 2005). Detection of the granular and supergranular convective motions has been achieved, however the deep giant cell convection remains elusive (Miesch & Toomre, 2009), though their amplitude can be constrained from theoretical arguments to be at least 30 m s^{-1} (Miesch et al., 2012).

Given the Sun's differential rotation, meridional circulation, and turbulent convection, schematic models of the solar dynamo can be constructed (see review Charbonneau, 2010). The details vary but many nonlinear dynamo models follow the general outline shown in Figure 1.3(b). Turbulent motions generate small-scale, incoherent fields that pervade the bulk of the convection zone. The convective upflows and downflows are continuously providing shearing motions which can amplify small-scale magnetic fields to magnetic energy densities in roughly equipartition with the kinetic energy of the convection itself. In the solar convection zone that suggests disorganized fields on the order of a kilogauss should be common in the deep interior. Some of these small-scale fields are pumped downward into regions of strong shear at the base of the convection zone and the tachocline. Figure 1.3(a) reveals that strong latitudinal and radial gradients in rotation rate can be found in and above the tachocline. The differential rotation tends to comb the small-scale fields into coherent

large-scale magnetic structures which are predominantly longitudinal, as radial or latitudinal fields will tend to be sheared into longitudinal fields by the differential rotation. Portions of these toroidal structures eventually become sufficiently strong and coherent that their magnetic pressure begins to replace the gas pressure required to keep them in equilibrium with their surroundings. This leads to the gas density dropping in regions of very strong field, which makes them buoyant. Magnetic buoyancy will tend to make regions of strong field rise through the convection zone. Once these regions of strong field have entered the convective layer there are also convective upflows which can assist in the flux emergence process. Some of the loops will be disrupted by unfavorable interactions with the turbulent convective flows, while others will successfully reach the photosphere where they emerge as sunspot pairs.

1.2 Guidance and Challenges from Observations

With this general schematic in hand, we can now examine what is known observationally about dynamo action in sun-like stars. Solar observations can provide exquisitely detailed data about a single star. Stellar observations are far more limited for any given star, though the large numbers of stars studied by a wide range of techniques is helping unlock additional understanding of dynamo processes and their dependence on parameters like rotation rate and stellar type. Observations of stellar magnetism can be neatly divided into two groups: our nearby star which has been and continues to be studied in unmatched detail, and all other stars for which observations are far more difficult but the potential targets are far more numerous.

1.2.1 The Magnetism of Our Local Star

Proxies for solar magnetic activity can reliably measure solar magnetic activity much farther into the past than recorded observations of sunspots. Perhaps the best proxy for solar activity involves measuring cosmogenic radionuclides such as ^{10}Be and ^{14}C in ice cores, tree rings, and marine sediments. These radioactive isotopes are primarily generated by spallation when high-energy cosmic rays strike the upper atmosphere. Stronger and more variable heliospheric magnetic fields increase the probability that high energy cosmic rays will be deflected out of the heliosephere or scattered to lower energies. Both mechanisms reduce the total energy flux of cosmic rays hitting the Earth's upper atmosphere (Potgieter, 2013). This drives a strong inverse correlation between solar magnetic activity and the generation of cosmogenic radionuclides. The concentration of these isotopes provides reliable estimates of the Sun's magnetic activity for the last 12,000 years (see review Usoskin, 2008). As useful as such long-term data are, they are highly limited both in their coarse temporal resolution and due to their nature as an integrated quantity over essentially the entire heliosphere.

Since the advent of telescopic observations of sunspots in 1611, data have been available as to the size and position of sunspot groups on the solar surface. Tracking these features permitted the first measurements of the solar activity cycle as well as the bulk rotation rate and surface differential rotation (see review Hathaway, 2010). These data have allowed some of the important large-scale signatures of the solar dynamo to be observed. These include the equatorward migrations of active latitudes resulting in the "butterfly diagram" of Figure 1.2; Hale's polarity law describing the hemispheric preference as to the eastward and westward polarities of sunspot pairs in each activity cycle; and Joy's law for the average latitudinal tilt of sunspot pairs. These patterns were first deduced by Hale et al. (1919) and have been confirmed many times since (e.g., Babcock & Babcock, 1955; Wang & Sheeley, 1989). Most recently Stenflo & Kosovichev (2012) have used 16 years of space-based observations with the Michelson Doppler Imager (MDI) on SOHO to catalogue these patterns in 160,079 pairs of

bipolar magnetic spots, revealing some previous unknown features of these laws. These data demonstrate the continuation of Joy's law to magnetic bipoles much smaller than sunspots, and show that roughly 5% of sunspot pairs violate Hale's polarity law.

Helioseismic observations have been used extensively to study the near-surface structure of sunspots (see review Rempel & Schlichenmaier, 2011). One recent development of particular interest is the detection of subsurface active regions prior to their emergence through the photosphere by Ilonidis et al. (2011). Detailed studies of the statistical properties of pre-emergence active regions are providing some clues as to the physical source of these detections (Leka et al., 2013; Birch et al., 2013). As these observations improve they may provide important observational guidance for the process of flux emergence, which is currently only constrained observationally by surface measurements and near-surface helioseismic constraints on flows and thermal structures (Gizon & Birch, 2005).

Advances in spectropolarimetry have permitted measurements of full vector magnetic fields. These vector magnetograms have revealed a hemispheric helicity law. Helicity represents the degree of twist in magnetic field lines and plays a key role in many theoretical models of dynamo action and flux emergence. Sunspot pairs show statistical preferences for the handedness of their twist in each hemisphere with left-handed twist preferred in the northern hemisphere and right-handed twist preferred in the south (Pevtsov et al., 1995). This preference has been confirmed to be constant over the past three magnetic activity cycles (Pevtsov et al., 2008).

1.2.2 The Challenge and Promise of Observing Stellar Magnetism

The Sun is not alone in its magnetic variability. Solar-type stars generate magnetism almost without exception, particularly at rotation rates greater than that of the current Sun. Young, rapidly rotating suns appear to have much stronger magnetic fields at their surfaces than our Sun (Hall, 2008). Observations reveal a clear correlation between rotation

and magnetic activity, as inferred from proxies such as coronal X-ray and chromospheric EUV emission (Saar & Brandenburg, 1999; Pizzolato et al., 2003; Wright et al., 2011). These measurements, however, are generally only available at a single epoch and thus cannot comment on the variability of stellar magnetic activity due to cycles. There have been a number of attempts to monitor the magnetic activity cycles of other stars using solar-calibrated proxies for magnetic activity such as the Calcium H and K lines which are strongly sensitive to magnetic activity in the Sun (e.g., Baliunas et al., 1995; Hempelmann et al., 1996; Oláh et al., 2009; Metcalfe et al., 2013). These programs require long, sustained periods of consistent observations, and are therefore rare. To date, the largest such project is the Mount Wilson HK survey, which measured chromospheric Ca lines as a proxy for magnetic activity for 111 solar-like stars over a 25-year period ending in 1991. In that study almost half of the stars showed cyclic behavior, including 21 with regular periods between 7 and 25 years (Baliunas et al., 1995). Recently long-term X-ray observations have provided the first evidence for a companion coronal activity cycle to a previously measured chromospheric activity cycle on a young solar-like star (Sanz-Forcada et al., 2013). The existence of sun-like stars both with and without clear cycles of magnetic activity suggest that there may be families of dynamo models that lie very close together in parameter space but exhibit markedly different degrees of temporal variability in their large-scale magnetic features.

All of the methods described above are disk-integrated measures of proxies for stellar magnetism. Ongoing developments in new observational techniques are permitting observations of the magnetic topology of magnetism on other stars (Donati & Landstreet, 2009). Perhaps of equal importance, data are becoming available on stellar bulk and differential rotation, which play a critical role in stellar dynamo mechanisms (Aerts et al., 2010). Spot-tracking from Kepler photometry is beginning to permit measurements of the numbers, latitudes, and migration rate of starspots (Meibom et al., 2011; Llama et al., 2012). Zeeman-Doppler imaging (ZDI) combines spectropolarimetry with Doppler shifts due to stellar rotation to create surface maps of stellar magnetism (Petit et al., 2008; Gaulme et al., 2010;

Morgenthaler et al., 2012). This ZDI technique is yielding estimates of the size, frequency, and magnetic flux of starspots and the topology and spatial variability of photospheric magnetic fields. The development of large optical interferometers such as the CHARA array are allowing resolved imaging of main-sequence stars. To date this capability has primarily been used in conjunction with spectral and asteroseismic observations to constrain stellar parameters such as radius, mass, and age with errors on the order of 1% (Huber et al., 2012; White et al., 2013). The forthcoming optical interferometer at the Magdalena Ridge Observatory should achieve angular resolution of a few milliarcseconds, allowing it to image solar-like stars out to distances of about 10 parsecs (Buscher et al., 2013).

1.3 Theoretical Frameworks for Convective Dynamos

Cyclic dynamos are fundamentally three-dimensional, nonlinear, and chaotic. No single 3D numerical model has yet been able to capture all of the physical mechanisms required to reproduce solar dynamo action (see review by Charbonneau, 2010). This has led dynamo theorists to explore reduced treatments. Much of the groundwork for modern dynamo theory has been laid in analytic mean-field models (e.g., Parker, 1955; Moffatt, 1978; Krause & Raedler, 1980). The generation of toroidal field as differential rotation acts on a poloidal field, for example, can be well described using these models. The so-called Ω-effect relies on shear from differential rotation in the convection zone or the tachocline at its base to stretch poloidal field into bands of toroidal field. The regeneration of poloidal field or the generation of opposite polarity poloidal field is parameterized in mean-field theory through the α-effect which is intended to represents small-scale turbulent correlations between the velocity and magnetic field.

Mean-field models attempt to reduce the dynamo problem to a 2D formulation. As Cowling (1933) famously showed, the magnetic induction equation does not permit a 2D dynamo solution. The root of this prohibition is that the axisymmetric induction equation

for poloidal magnetic field does not contain a source term. Mean-field models circumvent this problem by approximating the effects of 3D turbulent induction using a Taylor expansion of the 2D axisymmetric fields. Taking this expansion to first order yields two possible source terms for the poloidal magnetic field. By far the most favored of these parameters is a rank-two symmetric tensor α_{ij} which seeks to represent turbulent correlations between small-scale velocities and magnetic fields (Krause & Raedler, 1980). Current mean-field models favor non-local generation of poloidal field by the unresolved rise and twist of toroidal field (Babcock, 1961; Leighton, 1964). The Babcock-Leighton mechanism has been employed in a variety of mean-field models which can be used to obtain cyclic dynamo solutions which can reproduce the 22-year magnetic cycle, the sunspot butterfly diagram, and Hale's polarity law (e.g., Dikpati & Gilman, 2006; Choudhuri et al., 2007). These models are not particularly reliable when predicting the amplitude of future solar cycles such as the current cycle 24, but are the only dynamo models to date which can offer any predictive capability (see reviews Hathaway, 2009; Petrovay, 2010).

To confront the complex nature of solar-like dynamo action, 3D numerical models have been developed to explore aspects of various dynamo processes. As no single numerical model can include or resolve all relevant physical processes, modelers are forced to choose between global and local models. Global models capture the largest-scales of interest and the correct global geometry, but must approximate the effects of unresolved small-scale dynamics. Local models can offer much higher resolution over a small volume, which removes much of the dependence on the unresolved scales, but these simulations cannot then model the large scales of solar magnetism which are generally of the most interest.

Local simulations have been effectively used to model magnetic flux emergence. Flux emergence models track the rise of buoyant magnetic structures that have been inserted into stratified domains and then allowed to rise. One class of models uses the thin flux-tube approximation where there is no back-reaction of the magnetic structures on the fluid via the Lorentz force (e.g., Caligari et al., 1995; Moreno-Insertis & Emonet, 1996; Fan &

Fisher, 1996; Weber et al., 2011, 2012). Thin flux-tube models have the advantage that they are far less computationally demanding than MHD models and so a much broader range of parameter space can be explored. MHD models, while computationally expensive, more faithfully represent the dynamics of rising magnetic structures. By inserting a magnetic structure into the base of the simulated convective layer, these models can track the buoyant rise of these structures and assess processes which may disrupt or weaken them as they rise (e.g., Fan & Abbett, 2003; Fan, 2008; Jouve & Brun, 2009). A third type of flux emergence model uses a forced shear layer to generate magnetic structures which then become buoyant, thereby assuring that the magnetic structure can be generated through dynamo action (e.g., Cline et al., 2003; Vasil & Brummell, 2009). In a variation on this method, Guerrero & Käpylä (2011) have shown that dynamo action in a domain with convection and a forced shear layer can produce strong dynamo action and yield buoyant magnetic structures. Finally, near-surface models which include radiative transfer have succeeded in reproducing many essential features of sunspots by introducing bundles of magnetic field into their high-resolution simulations as a time-dependent lower boundary condition (Rempel et al., 2009; Cheung et al., 2010). These "sunspot in a box" simulations are of sufficient quality that it can be difficult to distinguish synthetic observations of the model from real observations of sunspots.

Pioneering work into global dynamo models by Gilman (1983) and Glatzmaier (1985) produced the first 3D MHD simulations of cyclic dynamo action in a rotating spherical shell. Major efforts have been made towards building convective dynamo models capable of addressing the generation of large-scale magnetic fields. In these models correct global geometry plays a key role. Here we will highlight three major codes which are being used to address convective dynamo action in stratified, rotating, spherical shells, namely the Pencil, EULAG-MHD, and ASH codes. Figure 1.4 shows samples of convective patterns from each of these codes. While the general pattern of rotationally-aligned convection near the equator and more isotropic convection at mid- to high-latitudes occurs in all three simulations, the

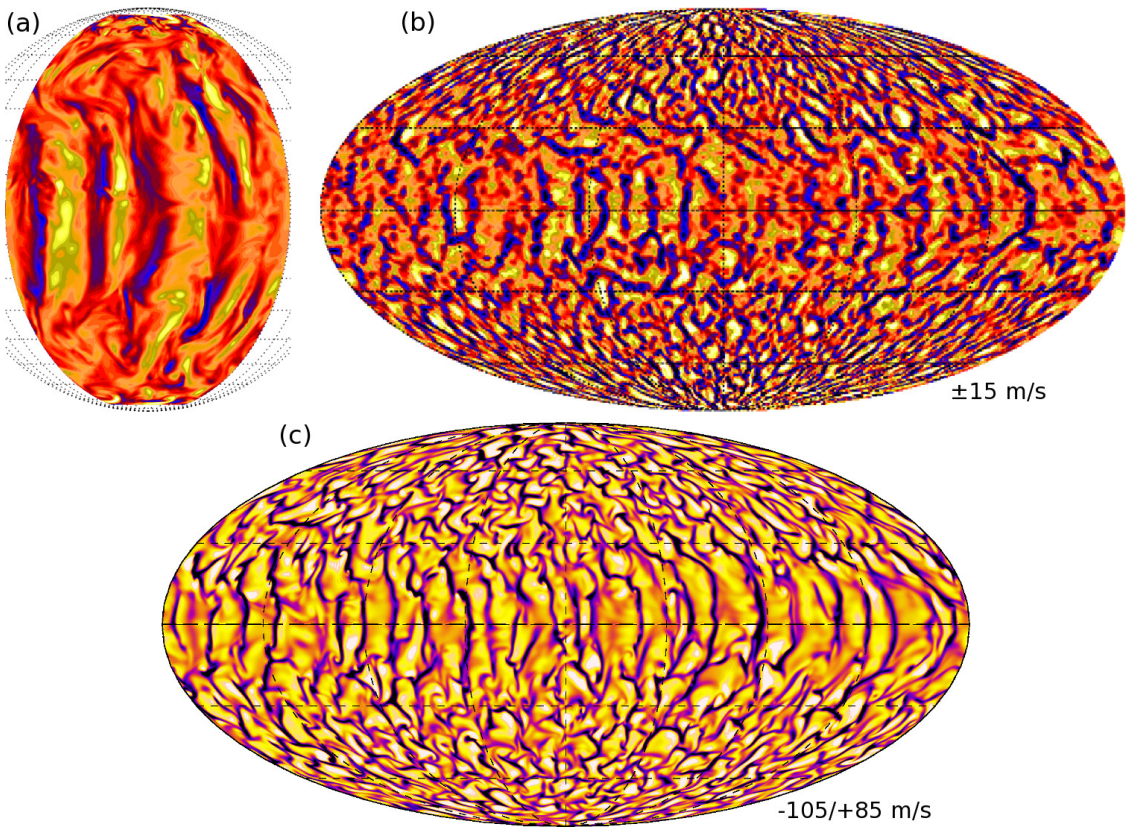

Figure 1.4: Radial velocity patterns in three convective dynamo simulations from (a) Warnecke et al. (2012) using the Pencil code, (b) Ghizaru et al. (2010) using EULAG-MHD, and (c) Nelson et al. (2013a) using ASH. Shown are (a) an orthographic projection for case A5 at $0.89R_\odot$ (scale not given in original), (b) a Mollweide projection at $0.945R_\odot$ (scale indicated), and (c) a Mollweide projection for case D3b at $0.95R_\odot$ (scale indicated). For all images dark tones indicate downflows while light tones indicate upflows. All three simulations shown produce cyclic dynamo action.

details of the flows realized are quite different due to a myriad of factors including the computational method, the numerical resolution of the simulation, the choices of diffusion models, the background stratification, the convective driving, and many more. Here we will not attempt to catalogue all possible sources of these variations, but rather will attempt to give a brief description of each code in order to give some idea about the major differences in these three numerical tools. We will return to the ASH code in greater detail in Chapter 2.

The Pencil code uses a high-order finite difference scheme to solve the compressible

MHD equations in 3D. Numerical cost limits the Pencil code's ability to reach high latitudes, thus the polar regions are generally excluded from the simulation domain. Using the Pencil code to simulate spherical wedges, Käpylä et al. (2011) explored the generation and maintenance of strong, solar-like differential rotation. When magnetic fields are added, these models achieved cyclic dynamo action with reversals of global magnetic polarity (Käpylä et al., 2012b). Warnecke et al. (2012) further explored the ability of these models to resolve the rise and emergence of magnetic flux structures.

The EULAG-MHD code has been used to simulate solar-like dynamo action. Numerically EULAG-MHD uses an implicit large-eddy simulation (ILES) framework in which there is no explicit physical diffusion and numerical operators are chosen to be as stable as possible, leading to significant numerical diffusion. It is also capable of simulating entire spherical surfaces and thus does not require the poles to be excluded from the simulated domain. Using EULAG-MHD, Ghizaru et al. (2010) have shown large-scale organization of the toroidal field as well as magnetic activity cycles in a solar-like simulation. Regular reversals of global magnetic polarity with a roughly 60 year period for a complete cycle were achieved. Racine et al. (2011) has interpreted these results in terms of mean-field dynamo theory, while Simard et al. (2013) have used the resulting mean-field dynamo parameters such as the α-tensor to generate companion mean-field models which display similar cyclic behavior.

The third code is the Anelastic Spherical Harmonic (ASH) code. All of the simulations presented here use the ASH code. ASH is a large-eddy simulation (LES) code which requires an explicit sub-grid scale (SGS) model to parameterize the effects of unresolved scales on the resolved dynamics. The use of pseudospectral methods allows ASH to treat dynamics over full spherical shells (Clune et al., 1999). Specifically, ASH uses spherical harmonic transforms in the longitudinal and latitudinal directions, and can either use a projection onto Chebyshev polynomials or a finite difference scheme in the radial direction. Miesch et al. (2006, 2008) have explored the interplay of rotation, stratification, and moderately

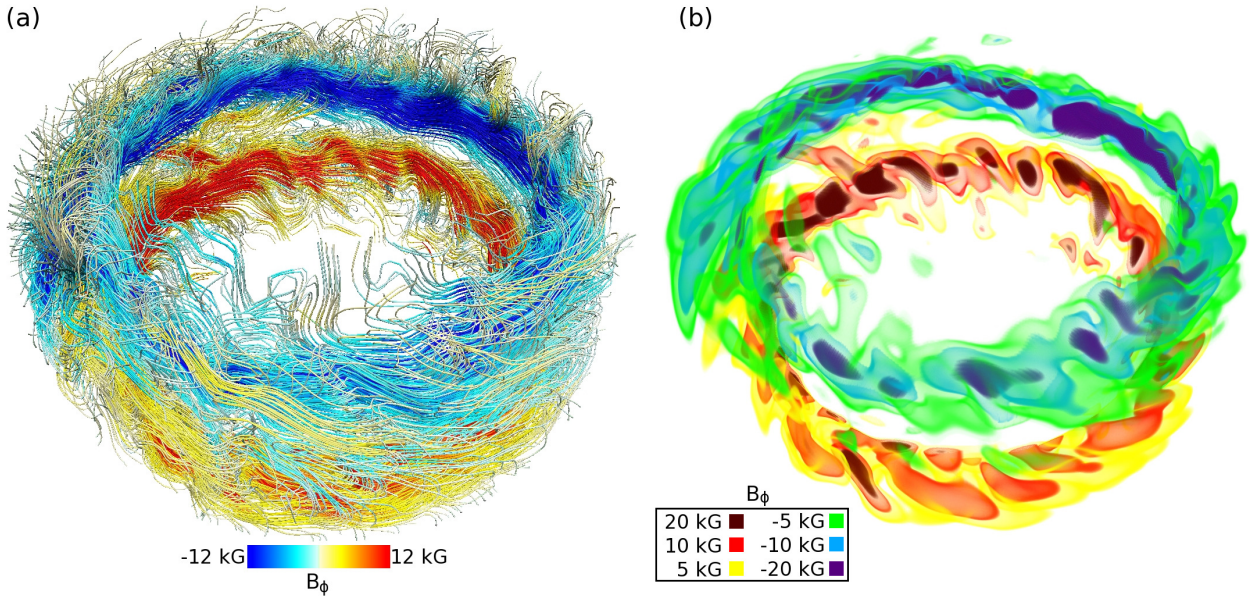

Figure 1.5: Magnetic wreaths from a convective dynamo simulation of a young Sun rotating at three times the solar rate (case D3) shown in two 3D volume renderings taken at the same instant. (a) Magnetic fields lines colored by longitudinal magnetic field B_ϕ which highlight the strong connectivity between the two wreaths and between each wreath and the rest of the domain. (b) Isosurfaces of B_ϕ at 20 kG (brown), 10 kG (red), 5 kG (yellow), -5 kG (green), -10 kG (blue), and -20 kG (purple) between $\pm 30°$ of latitude which highlight the non-axisymmetric components of the of the wreaths which are strongly modulated by convective flows. Perspective is looking from approximately 45° N through the center of the star. These magnetic wreaths are able to persist in the bulk of the convection zone for as long as the simulation was run (here 61.6 years). Case D3 is discussed in detail in Brown et al. (2010).

turbulent convection to produce strong differential rotation in a hydrodynamic setting. When magnetism is admitted the resulting dynamo produces reversals of global polarity but is dominated by non-axisymmetric fields with little global organization (Brun et al., 2004). By adding an overshooting region of strong shear which mimics the solar tachocline, global-scale organization of the toroidal field was achieved but without reversals in global magnetic polarity over about 30 simulated years (Browning et al., 2006). Miesch & Brown (2012) have explored 3D convective dynamo action with a Babock-Leighton term in order to include flux transport by means of a parameterization of magnetic buoyancy.

ASH has also been used to simulate the dynamics within the deep convective envelopes of young stars rotating faster than our current Sun. Brown et al. (2008) began with hydrodynamic simulations involving a range of rotation rates up to ten times the solar rotation rate ($10\Omega_\odot$), finding that strong differential rotation is realized, and that the columnar convection at low latitudes can exhibit significant modulation in amplitude with longitude, even appearing as nearly isolated active nests. Brown et al. (2010) examined dynamo action achieved in a MHD simulation carried out at $3\Omega_\odot$, finding that the convection can build ordered global-scale magnetic fields that appear as two wreaths of strong toroidal field positioned above and below the equator. These striking structures shown in Figure 1.5 can persist for long intervals despite being embedded within a turbulent convective layer. These wreaths strongly interact with the convective flows, causing strong non-axisymmetric components which can be seen in both Figures 1.5(a) and 1.5(b). However the convection does not destroy the wreaths. It also does not fully pin them to the base of the simulation, as might be expected from arguments about magnetic pumping, nor does it quickly eject the magnetic fields out the top of the domain, as might be expected from considerations of magnetic buoyancy in convective layers (Thompson & Weiss, 2009).

Turning to dynamo action proceeding at a faster rotation rate of $5\Omega_\odot$, Brown et al. (2011) showed that self-consistently generated magnetic wreaths at low latitudes can undergo reversals in global magnetic polarity and even quasi-cycles of magnetic activity. The complex steps involved in the magnetic field reversals are accompanied by variations in the differential rotation, including bands of relatively fast and slow fluid propagating toward the poles. In these models, ASH simulations have made contact with some of the key features believed to be present in the solar dynamo, specifically the strong toroidal structures which can yield reversals of global magnetic polarity. The work of Brown et al. (2010, 2011) provides much of the inspiration for this thesis, which seeks to understand how these wreaths behave in more turbulent environments and how magnetic reversals are achieved.

1.4 Thesis Overview: Wreaths, Cycles, and Buoyant Loops in 3D Dynamo Models

Encouraged by the results of previous 3D ASH simulations, we have conducted a new series of related simulations with ASH designed to explore three fundamental science questions:

(1) How might sun-like stars build large-scale magnetic fields?

(2) How can those fields undergo cycles of magnetic activity and reversals in global magnetic polarity?

(3) How can magnetic structures rise from their generation sites toward the stellar surface?

In order to address these questions, we will begin with a discussion of the ASH code which has enabled simulations of convective dynamo action. Chapter 2 will discuss the numerical implementation of ASH code and how our simulations with ASH compare to other simulations of solar-like convective dynamo action. The implementation and validation of a new sub-grid scale (SGS) model in ASH will be covered in Chapter 3. Our initial discovery of buoyant magnetic loops in a convective dynamo simulation will be presented in Chapter 4. These buoyant magnetic loops are enabled by the use of a dynamic Smagorsinsky SGS model which greatly reduces the effects of diffusion in our simulations.

In Chapter 5 the effects of reduced explicit diffusion on magnetic wreaths are investigated. Here we show that strong magnetic wreaths can be maintained as simulations are made more turbulent and that the fundamental balances which are required to maintain wreath-building dynamo action can persist as explicit diffusion is reduced. Next we will explore the cyclic magnetic activity which occurs in our more turbulent models in Chapter 6. Special attention will be focused on the nature of the magnetic reversals achieved. We then investigate in Chapter 7 the most turbulent dynamo simulation yet achieved with the ASH

code, which generates large numbers of buoyant magnetic loops. Chapter 8 discusses the collective properties of the generation of buoyant loops over a magnetic activity cycle. These loops mimic some observed properties of solar active regions, specifically Hale's polarity law, Joy's law for latitudinal tilts, and the hemispheric helicity rule.

As ASH is not capable of resolving the small-scales of motion which dominate dynamics near the photosphere, all previous ASH simulations have used an impenetrable upper boundary condition placed around 0.97 or $0.98R_{\odot}$. Chapter 9 investigates a new boundary condition which allows plumes modeled on those achieved in local near-surface simulations to pass through the upper boundary and into the computational domain. Finally, we will conclude in Chapter 10 with a discussion of the over-arching themes of this work and the potential for continued advances.

Chapter 2

Modeling Convection and Dynamo Action with ASH

We seek to investigate large-scale convective dynamo action in stellar interiors like those of our Sun. To do this we need a numerical tool which can include physical processes such as spherical geometry, rotation, turbulent convection, and magnetic induction on scales comparable to the size of the solar convection zone. Spherical geometry is required to capture the convective motions driven in a spherical shell between the base of the solar convection zone at approximately $0.72R_\odot$ and the photosphere. As differential rotation plays a key role in essentially all theoretical models for large-scale dynamo action, our numerical model must be capable of generating bulk zonal flows, preferably due to redistribution of angular momentum by the resolved convective flows. Dynamo action is defined as the self-sustaining generation of magnetic fields without an influx of magnetic energy through either the lower or upper boundary. Beyond simply permitting dynamo action, if one wishes to study possible mechanism for the generation of magnetic loops the numerical tools must allow sufficiently fine resolution and avoid diffusing these magnetic structures on short time scales.

The final and perhaps most challenging element needed is the ability to achieve turbulent flows. The level turbulence as measured by the Reynolds number in our simulations is many orders of magnitude smaller than the level of turbulence in real stars. As computing resources continue their exponential growth convective dynamo models have shown a remarkable ability to keep pace. Gilman (1983) published the first convective dynamo simulation which reported on models with 16 radial, 36 latitudinal, and 72 longitudinal grid points with

roughly 8000 time steps. The largest computational simulation reported in this thesis (case D3b) uses 145 radial, 512 latitudinal, and 1024 longitudinal grid points over 9.8 million time steps (see Nelson et al., 2013b). Thus over 20 years the size of convective dynamo models has increased by a factor of 2^{21}. By comparison, Intel Corporation's state-of-the-art commercial chip increased in performance by a factor of $2^{14.6}$ between 1983 and 2013 (Hellemans, 2013). The largest reason for the improvement of convective dynamo models is that the number of time steps which can be computed has increase by a factor of 10^3 while the spatial resolution has only increased by factors of roughly 10 in each direction. This is in part a product of the increased availability of large competitively available supercomputing resources funded by agencies such as the National Science Foundation and NASA.

With the continued growth of computing power, one can speculate on when computational resources might permit a global simulation resolve the Kolmogorov scale, which has been estimated based on atomic values to be on the order of 10 to 100 m (Braginskii, 1965). If Moore's law continues to hold and convective dynamo models continues to mimic its growth, the answer is roughly 200 years. It is likely, however, that most if not all of the global-scale behaviors are not dynamically linked to scales over a million times smaller. Thus we proceed with these models, hopeful that by resolving the largest scales of motion and achieving the most turbulent states possible with current computational resources, we may be able to capture some or perhaps all of the physical mechanisms which are essential to realize large-scale dynamo action as it occurs in sun-like stars.

To conduct these simulations we use the equations of magnetohydrodynamics (MHD). Specifically for the solar interior where the flows are orders of magnitude slower than the sound speed, we use the anelastic approximation for subsonic convective flows developed by Gough (1969) and further formulated for stellar convection by Latour et al. (1976). Our computational tool for solving these equations is the anelastic spherical harmonic (ASH) code. The hydrodynamic portion of ASH is described in detail in Clune et al. (1999), while the inclusion of magnetism is covered in Brun et al. (2004). ASH solves the 3D anelastic

MHD equations in rotating spherical shells. ASH uses 1D stellar structure models to provide the background stratification or reference state. The 3D equations of mass conservation, momentum conservation, energy conservation, and magnetic induction are solved using a pseudo-spectral or mixed pseudo-spectral and finite difference method for spatial derivatives. Time evolution is computed using a semi-implicit Crank-Nichelson scheme for linear terms and an Adams-Bashforth explicit scheme for nonlinear terms.

What follows is not intended to provide a complete overview of the ASH code but rather a description of its key elements. Particular attention will be paid to the components which are of particular importance to this thesis. Specifically, we will provide an overview of the anelastic MHD equations and how ASH solves them, while providing increased focus on the sub-grid scale models used in ASH which are crucial for our discussion of buoyant magnetic loops in Chapters 4, 7, and 8, as well as ASH's boundary conditions which will inform our discussion of plume boundary conditions in Chapter 9.

2.1 The Anelastic MHD Equations

The anelastic MHD equations are an approximate version of the fully compressible MHD equations which have been specifically designed for regions such as stellar convective layers. The anelastic approximation allows for strong density stratification without requiring the computational model to track sound waves which can propagate at tens of kilometers per second in the deep interior while convective motions are orders of magnitude slower. Thus the anelastic approximation permits much larger time steps than fully compressible codes. The anelastic formulation also formally decomposes the thermal state into a background with small perturbations around it. In this way we can avoid the very long timescale for changing the mean thermal stratification. ASH is thus able to avoid both the very short time scales of sound propagation and the very long time scales of stellar evolution in order to focus on the time scales of convective overturning and dynamo action. In the Sun these

are on the order of weeks to tens of years. For comparison the sound-crossing time in the Sun is about two hours and the thermal relaxation time scale for the solar convective layer (or its Kelvin-Helmholtz time) is about 10^5 years.

The anelastic approximation splits all variables into a spherically-symmetric reference state and 3D fluctuations about that reference state. The reference state is generally held constant, but can be updated by periodically removing the mean value at each radial level from the fluctuations and adding it to the reference state. The reference state for thermodynamic variables such as density $\bar{\rho}$, temperature $\bar{T}$, entropy $\bar{S}$, and pressure $\bar{P}$ are assigned using the results of 1D stellar structure models (where over-bars denote the reference state), while it is assumed that the reference state for velocity and magnetic field is zero. Fluctuations about the reference state are denoted as ρ, T, S, P, $\vec{u}$, and $\vec{B}$, where $\vec{u}$ and $\vec{B}$ are respectively the velocity and magnetic field. The decomposition into reference and fluctuating components are written as

$$\rho_{\rm tot}(r,\theta,\phi,t) = \bar{\rho}(r) + \rho(r,\theta,\phi,t) \tag{2.1}$$

$$P_{\rm tot}(r,\theta,\phi,t) = \bar{P}(r) + P(r,\theta,\phi,t) \tag{2.2}$$

$$T_{\rm tot}(r,\theta,\phi,t) = \bar{T}(r) + T(r,\theta,\phi,t) \tag{2.3}$$

$$S_{\rm tot}(r,\theta,\phi,t) = \bar{S}(r) + S(r,\theta,\phi,t) \tag{2.4}$$

$$\vec{u}_{\rm tot}(r,\theta,\phi,t) = \vec{u}(r,\theta,\phi,t) \tag{2.5}$$

$$\vec{B}_{\rm tot}(r,\theta,\phi,t) = \vec{B}(r,\theta,\phi,t). \tag{2.6}$$

The anelastic MHD equations consist of two equations of constraint, seven evolution equations, and an equation of state for both the reference state and the thermodynamic fluctuations. The constraint equations are the anelastic conservation of mass equation and the solenoidal constraint on the magnetic field, given by

$$\nabla \cdot (\bar{\rho}\vec{u}) = 0 \tag{2.7}$$

$$\nabla \cdot \vec{B} = 0. \tag{2.8}$$

The evolution equations express conservation of momentum and energy as well as the magnetic induction equation. They are solved in a reference frame which is rotating at angular velocity Ω_0. This gives two vector equations and one scalar equation written as

$$\bar{\rho}\frac{\partial \vec{u}}{\partial t} = -\bar{\rho}\left(\vec{u}\cdot\nabla\right)\vec{u} - 2\bar{\rho}\Omega_0 \times \vec{u} - \nabla P + \rho\vec{g} - \nabla\cdot\underline{\mathcal{D}} - \frac{1}{4\pi}\left(\nabla\times\vec{B}\right)\times\vec{B} \tag{2.9}$$

$$\begin{aligned}\bar{\rho}\bar{T}\frac{\partial S}{\partial t} =& -\bar{\rho}\bar{T}\vec{u}\cdot\nabla\left(S+\bar{S}\right) + \nabla\cdot\left[\kappa_r\bar{\rho}C_P\nabla\bar{T} + \kappa\bar{\rho}\bar{T}\nabla\left(S+\bar{S}\right)\right] \\ &+ \frac{\eta}{4\pi}\left(\nabla\times\vec{B}\right)^2 + 2\bar{\rho}\nu\left[e_{ij}e_{ij} - \frac{1}{3}\left(\nabla\cdot\vec{u}\right)^2\right]\end{aligned} \tag{2.10}$$

$$\frac{\partial \vec{B}}{\partial t} = \nabla\times\left(\vec{v}\times\vec{B}\right) - \nabla\times\left(\eta\nabla\times\vec{B}\right), \tag{2.11}$$

where $\vec{g}$ is gravitational acceleration, $\underline{\mathcal{D}}$ is the viscous stress tensor, e_{ij} is the strain-rate tensor, and C_P is the specific heat at constant pressure. Diffusion coefficients for momentum, entropy, radiative diffusion, and magnetic fields are given by ν, κ, κ_r, and η, respectively.

ASH follows the large-eddy simulation (LES) paradigm where those scales of motion which are smaller than the computational resolution are represented by a sub-grid scale (SGS) model. The viscous diffusion tensor is dependent upon the SGS model chosen, but for Newtonian diffusion it can be written as

$$\underline{\mathcal{D}} = \mathbf{D}_{ij} = -2\bar{\rho}\nu\left[e_{ij} - \frac{1}{3}\left(\nabla\cdot\vec{u}\right)\delta_{ij}\right]. \tag{2.12}$$

We will reserve further discussion of SGS models in ASH for Chapter 3.

The equation of state used in ASH is that of a perfect gas. For the reference state that is written

$$\bar{P} = \mathcal{R}\bar{\rho}\bar{T}, \tag{2.13}$$

where $\mathcal{R}$ is the gas constant. For our ideal gas it is $\mathcal{R} = 2C_P/5$. The equation of state for the fluctuations is linearized in the anelastic approximation, which leads to

$$\frac{\rho}{\bar{\rho}} = \frac{P}{\bar{P}} - \frac{T}{\bar{T}} = \frac{P}{\gamma\bar{P}} - \frac{S}{C_P}. \tag{2.14}$$

The linearized equation of state prevents ASH from investigating domains where perturbations become significant compared to mean values.

2.2 Numerical Methods

ASH incorporates the equations of constraint on the mass flux and the magnetic field by solving for streamfunctions. Toroidal streamfunctions Z and A describe, respectively, streamlines and magnetic field lines which close on a spherical surface, while the poloidal streamfunctions W and C describe streamlines and magnetic fields which do not. Formally the decomposition is given by

$$\bar{\rho}\vec{u} = \nabla \times (Z\hat{r}) + \nabla \times [\nabla \times (W\hat{r})] \tag{2.15}$$

$$\vec{B} = \nabla \times (A\hat{r}) + \nabla \times [\nabla \times (C\hat{r})]\,. \tag{2.16}$$

Thus the evolution variables used in ASH are the mass flux streamfunctions W and Z, the specific entropy S, the pressure P, and the magnetic streamfunctions C and A. Equations 2.9, 2.10 and 2.11 lead to evolution equations for W, Z, S, C, and A. The resulting equation for P is not an evolution equation but rather is elliptic and must be satisfied at each instant over the entire domain. Physically, this indicates that information about pressure perturbations in the anelastic approximation is instantly propagated everywhere.

As suggested by its name, ASH uses spherical harmonic transforms to compute derivatives in the latitudinal and longitudinal directions. Spherical harmonics are formally the angular portion of solutions to Laplace's equation on a sphere, and as such are the natural basis functions when working in spherical coordinates. Figure 2.1 shows 3D renderings of three representative spherical harmonic functions. Following convention, we write these functions as $Y_m^\ell(\theta, \phi)$, where m is the azimuthal wavenumber in units of the circumference and ℓ represents the latitudinal order of the function. Spherical harmonics are the product of sine and cosine functions of ϕ and associated Legendre polynomials of $\cos\theta$. Thus

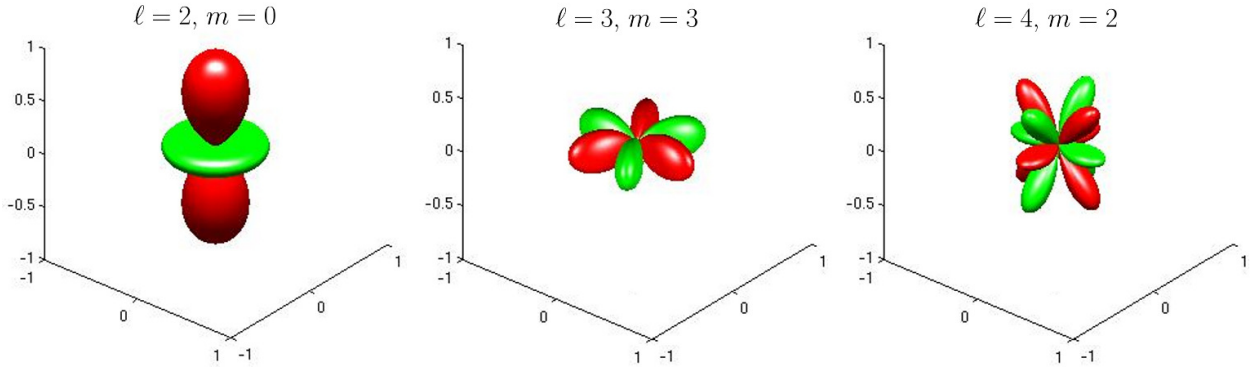

Figure 2.1: 3D volume rendering of the real parts of three selected spherical harmonic functions. Here the radial position gives the amplitude of the function for each value of θ and ϕ. Note that the number of nodes in longitude is given by m and the number of nodes in latitude in given by $\ell - m$.

ASH accomplishes the spherical harmonic transform with a combination of a Fast Fourier Transform (FFT) and a Legendre transform. Unfortunately there does not yet exist a robust fast Legendre transform, so that aspect of our numerical algorithm scales as the maximum spherical harmonic degree $\ell_{\max}$ squared, whereas the FFT scales as $2\ell_{\max} \ln(2\ell_{\max})$.

These equations are solved using one of two numerical methods for the radial spatial derivatives. The first uses Chebyshev polynomials in the radial direction. This version of ASH was developed in the late 1990's. The use of spherical harmonics allows for uniform resolution over the spherical surface, provides spectral accuracy, and removes the coordinate singularity at the poles. The use of Chebyshev polynomials in the radial direction also has many positive properties. Chebyshev polynomials place large numbers of grid-points in the boundary layers at the top and bottom of the layer where convective boundary layers require high resolution. This version of ASH also achieves spectral convergence properties in the spatial derivatives, although the overall accuracy of the scheme is limited by the time-stepping used. When using Chebyshev polynomials ASH also employs a Chebyshev colocation scheme in radius, which reduces the Chebyshev transform to a discrete cosine transform, which scales as $N_r \ln N_r$, where N_r is the number of radial grid points. This

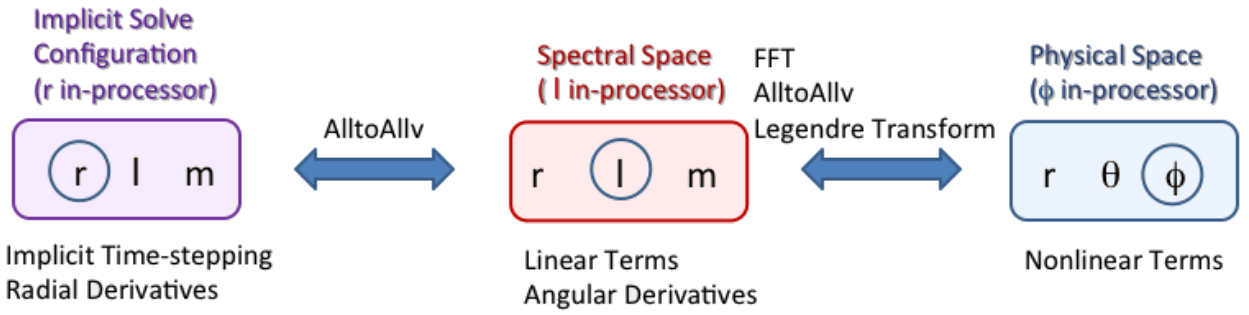

Figure 2.2: Schematic overview of the numerical method used to solve the anelastic MHD equations in ASH. Three data configurations are represented, as well as the steps needed to move between each. (Courtesy Nicholas Featherstone, University of Colorado).

colocation scheme concentrates resolution near the boundaries of the domain which can have negative implications for the size of the time step if significant radial flows exist in those regions.

The second version of ASH uses a hybrid pseudo-spectral/finite difference scheme for spatial derivatives. It retains the use of spherical harmonics in the θ and ϕ directions but uses a variable-order centered finite difference scheme in the radial direction. All simulations here use a 5th order scheme. This permits the use of arbitrary grids in the radial direction. It also reduces the computational cost of the radial derivative scheme, which scales as N_r. This decrease in cost is accompanied by a decrease in accuracy. The Chebyshev transform is spectrally accurate while the finite difference scheme is not. This version of ASH is often referred to as ASH-FD. Both versions have been incorporated into a single ASH framework, allowing direct comparison between the different radial derivative schemes.

ASH is designed to efficiently operate on modern massively parallel supercomputers. Thus special attention has been paid to the parallelization of its numerical scheme. The existence of an elliptic equation for the pressure field requires at least one global communication at each time-step. In ASH, we chose a numerical technique which incorporates global communication as required by the elliptic pressure equation and also allows other desirable

features such as spectrally accurate derivatives and semi-implicit time stepping of linear terms. This is accomplished through a highly efficient series of data transposes. Figure 2.2 gives a visual representation of the numerical method employed by ASH. Radial derivatives and implicit time-stepping occurs in our 'Implicit Solve Configuration' with spherical harmonic modes distributed and all radial points at a given ℓ and m in processor. A global transpose (achieved using the Message Passing Interface (MPI) command 'AlltoAllv') moves data to our 'Spectral Space Configuration' so that radial and m grid points are distributed and ℓ in processor. In this configuration linear terms are computed and angular derivatives are taken. Through a FFT, another global transpose, and a Legendre transform data is moved to physical space with radial and latitudinal grid points distributed and longitudinal grid points in processor. This is our 'Physical Space Configuration'. In physical space the nonlinear terms can be calculated and then transformed and transposed back to the Spectral Space Configuration where the next time-step can begin.

When simulating physical systems with ranges of physical and temporal scales beyond the capacity of computational resources, modeling the behavior of the largest scales requires some approximation to be made about the behavior of scales below some cutoff so that the numerical requirements match the computational resources. ASH follows the philosophy of a Large-Eddy Simulation (LES). The LES paradigm relies on sub-grid scale (SGS) models to represent the effects of unresolved scales. Explicit SGS models can range from substituting so-called turbulent diffusivities for the much smaller atomic diffusivities to much more complex schemes which attempt to model the turbulent cascade of energy from large to smaller scales and use physical arguments such as scale-invariance or self-similarity to extrapolate the behavior of unresolved scales based on resolved ones. ASH is an explicit LES code, as are the Pencil (Brandenburg, 2003) and MagIC (Gastine et al., 2012) codes which have been used extensively for convective dynamo simulations.

Alternatively, implicit SGS models have gained wide-spread popularity in a number of settings. Outside of the field of convective dynamos, Wachtor et al. (2013) have used

the radiative combustion code RAGE to simulate inertial confinement fusion and Patnaik et al. (2012) have used the atmospheric chemical mixing code FAST3D-CT to simulate the transport of pollution in cities. Both RAGE and FAST3D-CT follow the ILES philosophy which uses highly stable spatial and temporal derivative schemes in the place of explicit diffusion terms. These derivative operators include significant numerical diffusion, but only when needed for numerical stability. ILES models can generally achieve much lower levels of diffusion than explicit LES codes. However, they have the disadvantage that their diffusion is motivated purely by numerical considerations rather than physical ones, and that they generally cannot measure their diffusion as it is not explicitly computed. Implicit LES codes which have been used to model stellar dynamo action include EULAG-MHD (Prusa et al., 2008). A number of convective dynamo codes have been designed using implicit LES numerical methods and can also include explicit SGS models, making them either implicit or hybrid implicit/explict LES codes. These hybrid codes including MuRAM (Cheung et al., 2010), FSAM (Fan et al., 2013), and Stagger (Beeck et al., 2012).

2.3 Boundary Conditions

As with any system of partial differential equations, the solutions to the anelastic MHD equations depends strongly on the choice of boundary conditions. In the solar convection zone the inner and outer boundaries are at the radiative interior and in the solar atmosphere. While it is possible to simulate a radiative interior (e.g., Browning et al., 2006; Brun et al., 2011), the simulations presented here chose to omit that region. Whereas simulations which include a tachocline are extremely interesting, they are also extremely challenging, both conceptually and computationally. In the past several years there has been significant work done to address the long-standing question of the maintenance of the tachocline using 3D simulations (Strugarek et al., 2011; Brun et al., 2011). There has also been significant work to address the validity of the anelastic approximation in stably stratified layers (Brown et al.,

2012; Vasil et al., 2013). The effects of a convective over-shooting region with strong shear on convective dynamo simulations in ASH is an active area of research that is beyond the scope of this thesis. We will discuss the possibilities for future research in this direction in Chapter 10.

The upper boundary in ASH is perhaps even more challenging than the lower boundary. Sun-like stars go through extremely large changes in their stratification near their surfaces. Radiative transport and non-ideal thermodynamic processes such as ionization play important roles. The preferred scales of convection drop dramatically until at the surface the granulation is on the order of 1 Mm or at spherical harmonic degree of about $\ell_{\max} \approx 4500$. The largest ASH simulations to date achieve a maximum spherical harmonic degree of $\ell_{\max} = 1360$. ASH does not have the resolution or the physics needed to simulate surface convection. Thus we must place an upper boundary somewhere in the interior of the Sun.

2.3.1 Thermal Boundary Conditions

The convective driving of our simulations is the result of the transport of thermal energy through our spherical shell. Heat is input at the base of the domain through a radiative diffusion term which is taken from a 1D stellar model. This acts as a source term which carries the entire luminosity at the bottom of the domain and decreases to essentially zero over the bottom 15% of the domain. Likewise we must transport heat out of the top of the domain. We generally chose to do this through a diffusive flux, although in Chapter 9 we will discuss an alternative method which uses an imposed pattern of plumes to transport the energy flux through the upper boundary via convection.

For our entropy equation we can set one of two boundary conditions. Either we can set the value of S or the value of $\partial S/\partial r$. As we are simulating a convective layer, we generally chose to set $\partial S/\partial r = 0$ at the lower boundary. By doing so we define the bottom of our

domain as the base of the convection zone. For the upper boundary we have groups of simulations which use either condition. Earlier cases were generally run with $\partial S/\partial r$ set such that the diffusive flux out of the domain was exactly one solar luminosity. Our more recent cases have set S on the upper boundary, thereby allowing the convection to build a boundary layer self-consistently in order to achieve the same goal. The first method is computationally cheaper as the thermal equilibration time is quite short, however the second removes a potentially troubling issue where the total entropy of the domain is unconstrained when both the upper and lower boundary conditions are of the second type. As the lower boundary is designed to represent the base of the convection zone where $\partial S/\partial r = 0$ by definition, we find it conceptually preferable to set the gradient of S to zero at the base of the domain and the value of S at the top of the domain.

Coupled with the choice of entropy boundary conditions is our choice of the thermal diffusivity κ. As was mentioned, a radiative flux is responsible for carrying the energy flux at the lower boundary in both our simulations and real stars. There is no such radiative flux at the top of our computational domain. In stars the flux would be carried by convection all the way to the photosphere, though with impenetrable boundary conditions placed below the photosphere this is not possible. Thus we employ diffusion on the spherically symmetric entropy profile to carry the required luminosity. This means that our choice of the thermal diffusion coefficient κ plays an important role in specifying the thermal state of our upper boundary.

We have several parameters with which to specify κ, but generally the parameter which has the greatest impact on the upper boundary layer is our specification of the thermal diffusion on the spherically-symmetric entropy, or κ_{00}. We can either strongly taper κ_{00} so that it is large at the upper boundary and small though the rest of the domain, or set $\kappa_{00} = \kappa$ so that thermal diffusion acts uniformly on all modes. In this work, all simulations which employed a $\partial S/\partial r$ boundary condition at the upper boundary also used a strongly tapered profile for κ_{00}, while all those which set S at the boundaries set $\kappa_{00} = \kappa$.

2.3.2 Momentum Boundary Conditions

Previous ASH simulations have employed an impenetrable upper boundary condition such that the radial velocity

$$v_r = 0. \tag{2.17}$$

In Chapter 9 we will present a new boundary condition which allows specified flows to cross through the upper boundary and thus leave or enter the computational domain.

On both the upper and lower boundaries, ASH simulations are generally run with stress-free boundary conditions. These can be written as

$$\frac{\partial}{\partial r}\left(\frac{v_\theta}{r}\right) = \frac{\partial}{\partial r}\left(\frac{v_\phi}{r}\right) = 0. \tag{2.18}$$

The combination of impenetrable and stress-free boundary conditions prevents any hydrodynamic torques on the domain from the boundaries, thus conserving angular momentum to the numerical accuracy of our simulations. As many of our simulations can continue for millions of time-steps, the total angular momentum of the system can and in practice does change as a random walk away from the initial values. In order to more precisely conserve angular momentum over long time evolutions, we can also employ what we term angular momentum cleaning. This takes advantage of our streamfunction formalism as follows.

The total angular momentum in our computational domain about the axis of rotation can be written as

$$\mathcal{L}_z = \int_{r_i}^{r_o}\int_0^{\pi}\int_0^{2\pi} (\vec{r}\times\vec{u})\cdot\hat{z}\, r^2\sin\theta\, dr\, d\theta\, d\phi = \int_{r_i}^{r_o}\int_0^{\pi}\int_0^{2\pi} \bar{\rho}u_\phi r^3\sin^2\theta\, dr\, d\theta\, d\phi, \tag{2.19}$$

where $\vec{r}$ is the radial vector from the origin and $\hat{z}$ is the unit vector along the axis of rotation. Note that we have not considered the rotation rate of the frame, so initially $\mathcal{L}_z = 0$. Using the streamfunction formalism

$$\bar{\rho}u_\phi = \frac{1}{r\sin\theta}\frac{\partial^2 W}{\partial r\partial\phi} - \frac{1}{r}\frac{\partial Z}{\partial\theta}. \tag{2.20}$$

Carrying out the ϕ integral removes the W term which contains a ϕ derivative, leaving

$$\mathcal{L}_z = -2\pi \int_{r_i}^{r_o} \int_0^{\pi} \frac{\partial \langle Z \rangle}{\partial \theta} r^2 \sin^2\theta \, dr \, d\theta, \tag{2.21}$$

where $\partial\langle Z\rangle$ is the longitudinally-averaged portion of Z. Thus we can already see that $\mathcal{L}_z$ only depends on the spherical harmonic components of Z with $m = 0$. Thus $\langle Z \rangle = \sum_{\ell=0}^{\infty} \tilde{Z}_\ell^0 Y_\ell^0$ Now let us consider the latitudinal integral such that

$$\mathcal{L}_z = -2\pi \int_{r_i}^{r_o} \mathcal{T} r^2 \, dr, \tag{2.22}$$

where

$$\mathcal{T} = \int_0^{\pi} \frac{\partial \left(\sum_{\ell=0}^{\infty} \tilde{Z}_\ell^0 Y_\ell^0 \right)}{\partial \theta} \sin^2\theta \, d\theta. \tag{2.23}$$

If we now take the derivative through the sum and use a derivative identity for spherical harmonics (Dennery & Krzywicki, 1996), we find that

$$\frac{\partial Y_\ell^0}{\partial \theta} = C Y_\ell^0, \tag{2.24}$$

where C is simply a constant which depends on the normalization used. Thus we can write

$$\mathcal{T} = C \sum_{\ell=0}^{\infty} \left(\tilde{Z}_\ell^0 \int_0^{\pi} Y_\ell^0 \sin\theta \sin\theta \, d\theta \right). \tag{2.25}$$

Recognizing the integral to be an inner product between two spherical harmonics,

$$\mathcal{T} = D \sum_{\ell=0}^{\infty} \left(\tilde{Z}_\ell^0 \delta_{\ell 1} \right) = D \tilde{Z}_1^0, \tag{2.26}$$

where again D is merely a constant dependent upon the normalization chosen.

Returning to Equation 2.22, we can now write the total angular momentum about the axis of rotation as

$$\mathcal{L}_z = -2\pi D \int_{r_i}^{r_o} \tilde{Z}_1^0 r^2 \, dr. \tag{2.27}$$

We can therefore assure that angular momentum is conserved by keeping

$$\int_{r_i}^{r_o} \tilde{Z}_1^0 r^2 \, dr = 0 \tag{2.28}$$

at each time step. It can be shown that the other two components of total angular momentum can similarly be expressed as radial integrals of $\tilde{Z}_1^1$ and $\tilde{Z}_1^{-1}$. By choosing the boundary values of these three components of Z such that Equation 2.28 is satisfied, we can enforce conservation of angular momentum to machine precision at each time step.

2.3.3 Magnetic Boundary Conditions

While there are clear physical arguments for our standard hydrodynamic boundary conditions, the choices of magnetic boundary conditions are somewhat more varied. In ASH we have three choices, which are as follows.

- The boundary is a perfect conductor, such that the electric field $\vec{E}$ is

$$E_\theta = E_\phi = 0. \tag{2.29}$$

  Combined with the impenetrable condition described above, this leads to a condition on $\vec{B}$ given by

$$B_r = \frac{\partial B_\theta}{\partial r} + \frac{B_\theta}{r} = \frac{\partial B_\phi}{\partial r} + \frac{B_\phi}{r} = 0 \tag{2.30}$$

- The boundary matches to an external potential field with

$$\vec{B} = \nabla\Phi \tag{2.31}$$

  which means that

$$\nabla^2\Phi = 0. \tag{2.32}$$

- The magnetic field is required to be purely radial at the boundaries, such as would happen at the boundary to a highly permeable external medium. This is expressed at $\vec{B} = B_r\hat{r}$.

For all of the magnetic simulations presented here we have chosen to employ a perfect conductor on the inner boundary and a potential field on the outer boundary. Brown (2009)

contains additional discussion of the rationale for various magnetic boundary conditions and their impact on dynamo simulations.

2.4 Overview of Simulations

Using ASH we have conducted three major sets of numerical experiments to explore questions related to convective dynamo action in ASH. The first set of simulations, containing cases Na, Nb, and S, were designed to test the dynamic Smagorisnky SGS model in ASH and compare it to the enhanced eddy viscosity model. This comparison will be discussed primarily in Chapter 3. They were run in 2009 on the Sun Constellation Linux Cluster named Ranger at the Texas Advanced Computing Center.

The second set of simulations are convective dynamo models designed to probe physical mechanisms which may be present in solar-like dynamos. Case D3 was originally begun by Benjamin Brown and was discussed in detail in Brown et al. (2010). Cases D3-pm1 and D3-pm2 were also run primarily by Bejamin Brown as part of his thesis work at the University of Colorado. Working with Benjamin, I ran cases D3a, D3b, and S3 in order to explore the effects of decreased diffusion on the dynamo-generated magnetic wreaths attained in case D3. Cases D3a and D3b were run from 2007 through 2010 on a number of systems including the IBM Blue Gene Cluster at the San Diego Supercomputing Center, the Ranger system, and the Cray XT5 system Kraken at the National Institute for Computational Sciences. These models will be discussed in detail in Chapters 4 through 8.

Table 2.1: Computational parameters for ASH simulations. Shown are the number of radial, latitudinal, and longitudinal grid points. The SGS model employed for viscous, thermal, and magnetic diffusion (if applicable) is shown as either the enhanced eddy (EE) model or the dynamic Smagorisnky (DS) model. Thermal diffusion on the spherically-symmetric entropy profile is either equal to thermal diffusion on all other modes or strongly tapered near the upper boundary. The number of time-steps taken is given by N_t. Cases are either magnetic or purely hydrodynamic. Boundary conditions are either closed (C) or imposed plumes (P) (see Chapter 9). All simulations here use stress-free (SF) boundaries. For closed boundaries one can also select if they impose values of the entropy (S) or the entropy gradient (DS). Magnetic boundary conditions are either perfect conductors (PC) or match to an external potential field (PF). The method of taking radial derivatives $\partial/\partial r$ is either using a projection onto Chebyshev polynomials (Cheby) or finite differences (FD).

Computational Parameters for ASH Simulations

Case	N_r, N_θ, N_ϕ	SGS Model	$\kappa_{00} = \kappa$?	N_t	Magnetic?	Lower B. C.'s	Upper B. C.'s	$\partial/\partial r$
Na	192, 512, 1024	EE	No	1.2×10^6	No	C, SF, DS	C, SF, DS	Cheby
Nb	257, 1024, 2048	EE	No	4.3×10^5	No	C, SF, DS	C, SF, DS	Cheby
S	192, 512, 1024	DS	No	7.5×10^5	No	C, SF, DS	C, SF, DS	Cheby
D3	97, 256, 512	EE	No	5.8×10^6	Yes	C, SF, DS, PC	C, SF, DS, PF	Cheby
D3-pm1	145, 256, 512	EE	No	5.7×10^6	Yes	C, SF, DS, PC	C, SF, DS, PF	Cheby
D3-pm2	145, 512, 1024	EE	No	4.8×10^6	Yes	C, SF, DS, PC	C, SF, DS, PF	Cheby
D3a	97, 256, 512	EE	No	1.2×10^7	Yes	C, SF, DS, PC	C, SF, DS, PF	Cheby
D3b	145, 512, 1024	EE	No	9.8×10^6	Yes	C, SF, DS, PC	C, SF, DS, PF	Cheby
S3	145, 512, 1024	DS	No	3.4×10^6	Yes	C, SF, DS, PC	C, SF, DS, PF	Cheby
Ia	300, 512, 256	EE	Yes	6.5×10^5	No	C, SF, DS	C, SF, S	FD
Ib	500, 1024, 512	EE	Yes	9.3×10^5	No	C, SF, DS	C, SF, S	FD
Ic	500, 1024, 512	EE	Yes	8.6×10^5	No	C, SF, DS	C, SF, S	FD
P	500, 1024, 512	EE	Yes	2.7×10^5	No	C, SF, DS	P	FD

Table 2.2: Dimensional parameters for the ASH simulations. Shown are the location of the inner R_i and outer R_o radial boundaries in units of the solar radius $R_\odot = 6.95 \times 10^{10}$ cm, the fractional density contrast over the domain ρ_i/ρ_o, the RMS velocity $v_{\rm RMS}$ in m s^{-1} and RMS magnetic field strength $B_{\rm RMS}$ in kG at mid-convection zone, the bulk rotation rate Ω_0 in units of the mean solar rotation rate $\Omega_\odot = 2.7 \times 10^{-6}$ s^{-1} (thus the period $P_\odot = 2\pi/\Omega_\odot = 26.9$ days), the viscous ν, thermal κ, and magnetic η diffusion coefficients in units of cm^2 s^{-1}, the mean time step Δt in seconds, and the total evolution time T_E in days for each simulation. For cases S and S3 using the dynamic Smagorinsky SGS model, the values quoted are based on the time-averaged rms viscosity, conductivity, and resistivity at mid-depth, noting that these diffusion coefficients have near hundred-fold spatial variations.

Dimensional Parameters and Diagnostics for ASH Simulations

Case	$R_i/R_\odot$	$R_o/R_\odot$	ρ_i/ρ_o	$v_{\rm RMS}$	$B_{\rm RMS}$	$\Omega_0/\Omega_\odot$	ν	κ	η	$\bar{\Delta t}$	T_E
Units	–	–	–	m s^{-1}	kG	–	cm s^{-2}	cm s^{-2}	cm s^{-2}	s	days
Na	0.719	0.967	24.3	54.4	–	3.0	5.15×10^{11}	2.06×10^{11}	–	340	4820
Nb	0.719	0.967	24.3	57.2	–	3.0	3.43×10^{11}	1.37×10^{11}	–	142	1120
S	0.719	0.967	24.3	55.2	–	3.0	1.49×10^{10}	5.98×10^{10}	–	319	2760
D3	0.719	0.967	24.3	51.6	3.24	3.0	1.44×10^{12}	5.77×10^{12}	2.89×10^{12}	337	22500
D3-pm1	0.719	0.967	24.3	50.1	5.20	3.0	1.44×10^{12}	5.77×10^{12}	1.44×10^{12}	104	6860
D3-pm2	0.719	0.967	24.3	50.5	9.39	3.0	1.44×10^{12}	5.77×10^{12}	7.22×10^{11}	89.9	4980
D3a	0.719	0.967	24.3	53.8	6.13	3.0	9.40×10^{11}	3.76×10^{12}	1.88×10^{12}	175	24500
D3b	0.719	0.967	24.3	55.9	5.79	3.0	5.67×10^{11}	2.27×10^{12}	1.13×10^{12}	54.5	6180
S3	0.719	0.967	24.3	56.4	5.31	3.0	2.18×10^{10}	8.71×10^{10}	4.35×10^{10}	40.0	1520
Ia	0.719	0.983	149	41.8	–	1.0	2.41×10^{12}	9.64×10^{12}	–	998	7510
Ib	0.719	0.983	149	70.9	–	1.0	1.20×10^{12}	4.81×10^{12}	–	628	6800
Ic	0.719	0.983	149	74.5	–	1.0	6.02×10^{11}	2.41×10^{12}	–	280	1960
P	0.719	0.983	149	101	–	1.0	6.02×10^{11}	2.41×10^{12}	–	171	830

Table 2.3: Dimensionless parameters for the ASH simulations. Evaluated at mid-depth are the rms Reynolds number $\mathrm{Re} = v_{\mathrm{rms}}L/\nu$ and fluctuating Reynolds number $\mathrm{Re}' = v'_{\mathrm{rms}}L/\nu$, the Rayleigh number $\mathrm{Ra} = (-\partial\rho/\partial S)(\mathrm{d}\bar{S}/\mathrm{d}r)gL^4/\rho\nu\kappa$, the Taylor number $\mathrm{Ta} = 4\Omega_0^2L^4/\nu^2$, the Rossby number $\mathrm{Ro} = \omega/2\Omega_0$, and the convective Rossby number $\mathrm{Roc} = (\mathrm{Ra}/\mathrm{Ta}\,\mathrm{Pr})^{1/2}$, and the Prandtl number $\mathrm{Pr} = \nu/\kappa$. For MHD simulations the magnetic Reynolds number $\mathrm{Rm} = v_{\mathrm{rms}}L/\eta$ and fluctuating magnetic Reynolds number $\mathrm{Rm}' = v'_{\mathrm{rms}}L/\eta$, and magnetic Prandtl number $\mathrm{Pm} = \nu/\eta$ are also given. Here the fluctuating velocity v' has the axisymmetric component removed: $v' = v - \langle v\rangle$, with angle brackets denoting an average in longitude. For cases S and S3 using the dynamic Smagorinsky SGS model, the values quoted are based on the time-averaged rms values of Re, Re′, Ra, Ta, Rm and Rm′ at mid-depth, noting that these parameters depend on diffusion coefficients which have near hundred-fold spatial variations (see Table 2.2).

Dimensionless Parameters for ASH Simulations

Case	Re	Re′	Ra	Ta	Ro	Roc	Pr	Rm	Rm′	Pm
Na	1080	337	2.13×10^6	8.03×10^7	0.725	0.307	0.25	–	–	–
Nb	1650	517	4.02×10^6	1.81×10^8	0.859	0.287	0.25	–	–	–
S	9210	2870	2.76×10^8	1.28×10^{11}	0.735	0.0293	0.25	–	–	–
D3	173	104	3.28×10^5	1.22×10^7	0.374	0.315	0.25	86	52	0.5
D3-pm1	149	102	2.98×10^5	1.22×10^7	0.372	0.300	0.25	149	102	1.0
D3-pm2	145	101	3.08×10^5	1.22×10^7	0.370	0.306	0.25	291	202	2.0
D3a	244	154	5.84×10^5	2.41×10^7	0.447	0.295	0.25	122	77	0.5
D3b	343	273	1.11×10^6	6.08×10^7	0.566	0.257	0.25	171	136	0.5
S3	8050	5750	7.68×10^8	4.46×10^{10}	0.581	0.262	0.25	4030	2880	0.5
Ia	94	52	6.20×10^4	5.66×10^5	1.34	0.462	0.25	–	–	–
Ib	215	177	1.50×10^5	2.27×10^6	1.88	0.515	0.25	–	–	–
Ic	458	418	4.97×10^5	9.07×10^6	2.09	0.568	0.25	–	–	–
P	328	253	1.60×10^5	2.27×10^6	2.07	0.532	0.25	–	–	

The final set of simulations are four hydrodynamic models designed to explore the effects of an alternate upper boundary condition in ASH which is designed to more faithfully represent the dynamics present in the upper portion of the solar interior. This plume boundary condition is a novel addition to the ASH code which is described in Chapter 9. Cases Ia, Ib, and Ic use the standard impenetrable upper boundary condition, but extend to $0.983R_\odot$ to include as much of the convective layer as possible. Case Ia has moderately high values of ν and κ and has a solar-like differential rotation profile. It is modeled after case AB2 from Brun & Toomre (2002). Both diffusion coefficients are reduced by a factor of two in case Ib, which has a weak solar-like differential rotation profile. Case Ic has diffusivities that are again reduced by a factor of two and produces an anti-solar differential rotation profile. Case P uses our plume upper boundary condition with ν and κ equal to those of case Ib and retains a strong solar-like differential rotation profile. These simulations were run on the Dell PowerEdge Cluster named Stampede at the Texas Advanced Computing Center and the SGI ICE Cluster named Pleiades at NASA's Ames Research Center.

Tables 2.1, 2.2, and 2.3 present, respectively, the computational, dimensional, and dimensionless parameters for all the ASH simulations which will be referenced in this thesis. Though many of these parameters will be restated later in our analysis of the various simulations, this presentation is intended to provide an easy and comprehensive reference to the reader as well as an overview.

2.4.1 Comparison with Other Dynamo Simulations

As was previously discussed, there are several other codes which are used to conduct similar simulations to those that we discuss here. It is generally quite challenging to make direct comparisons between results from ASH simulations and those using other codes. Many other codes use implicit LES formulations, which generally means that they do not have access to parameters related to viscous, thermal, or magnetic diffusion. Additionally no two

Table 2.4: Dimensional parameters from selected simulations conducted with the Pencil code. These values are adapted from the non-dimensional parameters given in Käpylä et al. (2011), Warnecke et al. (2012), and Käpylä et al. (2013) (abbreviated K11, W12, and K13). Dimensional parameters include the RMS velocity in units of m/s, the viscosity in units of $cm^2\ s^{-1}$, the magnetic diffusivity in units of $cm^2\ s^{-1}$, the rotation rate, and the luminosity, both in solar units.

Dimensional Parameters for Selected Pencil Code Simulations

Reference	Run	$v_{\rm RMS}$ (m s^{-1})	ν (cm s^{-2})	κ (cm s^{-2})	$\Omega_0/\Omega_\odot$	$L/L_\odot$
K11	A0	10100	8.78×10^{13}	–	0.0	2.9×10^{6}
K11	A1	9610	8.87×10^{13}	–	1.1	2.9×10^{6}
K11	A2	9610	8.87×10^{13}	–	2.1	2.9×10^{6}
K11	A3	9610	8.63×10^{13}	–	4.3	2.9×10^{6}
K11	A4	12700	8.77×10^{13}	–	10.6	2.9×10^{6}
K11	A5	9610	8.87×10^{13}	–	21.9	2.9×10^{6}
K11	A6	7870	8.71×10^{13}	–	42.5	2.9×10^{6}
K11	B0	8740	5.37×10^{13}	–	0.0	2.9×10^{6}
K11	B1	8740	5.09×10^{13}	–	10.4	2.9×10^{6}
K11	B2	7870	5.22×10^{13}	–	21.4	2.9×10^{6}
K11	B3	6990	5.28×10^{13}	–	43.0	2.9×10^{6}
K11	C1	3500	9.67×10^{13}	–	23.5	1.56×10^{6}
K11	D1	5240	1.93×10^{13}	–	23.6	6.46×10^{5}
K11	D2	5240	1.96×10^{13}	–	35.8	6.46×10^{5}
W12	A5	3150	3.17×10^{14}	3.17×10^{13}	19.6	1.81×10^{7}
W12	A5a	4590	1.52×10^{13}	1.52×10^{13}	18.3	1.81×10^{7}
W12	Ar1	1750	1.53×10^{13}	1.53×10^{13}	77.6	1.81×10^{7}
K13	A1	404	5.21×10^{13}	5.21×10^{13}	3.6	7.92×10^{5}
K13	A2	373	5.21×10^{13}	5.21×10^{13}	3.3	7.92×10^{5}
K13	B1	584	8.83×10^{13}	8.83×10^{13}	5.2	7.92×10^{5}
K13	B2	531	8.83×10^{13}	8.83×10^{13}	4.7	7.92×10^{5}
K13	C1	929	8.83×10^{13}	8.83×10^{13}	8.2	7.92×10^{5}
K13	C2	823	8.83×10^{13}	8.83×10^{13}	7.3	7.92×10^{5}
K13	D1	473	1.42×10^{14}	4.73×10^{13}	4.2	1.31×10^{5}
K13	D2	572	7.59×10^{13}	3.80×10^{13}	5.1	1.31×10^{5}
K13	E3	929	8.82×10^{13}	8.82×10^{13}	8.2	7.92×10^{5}
K13	E4	897	1.06×10^{14}	1.06×10^{14}	8.0	7.92×10^{5}

codes solve exactly the same numerical evolution equations. One notable example can be found when comparing the energy equations solved by ASH and EULAG-MHD. EULAG-

MHD includes a thermal drag term which keeps the thermal state from moving away from the specified background stratification (Prusa et al., 2008; Ghizaru et al., 2010). This term is small compared to other terms in the EULAG-MHD energy equations. However upon careful examination this term plays a crucial role in allowing EULAG-MHD simulations at the solar rotation rate to retain a solar-like differential rotation (fast equator, slower poles) and achieve cycles of magnetic activity, whereas ASH simulations at the solar rotation rate which are sufficiently turbulent to achieve magnetic cycles have anti-solar differential rotation profiles. This is one example of the variations between codes that make direct comparison difficult.

In contrast, Jones et al. (2011) conducted a detailed comparison of ASH with several codes designed for planetary dynamo simulations. Included in this analysis was the MaGIC code, which has also been used in low-mass stellar models (Gastine et al., 2012). They found that when carefully formulated, benchmark problems can be used to test differences in numerical methods and computational implementation. Unfortunately, similar work has not been done to compare ASH, EULAG-MHD, and the Pencil code, in part because these three codes emily fundamentally different computational approaches.

We have undertaken to compare ASH results with those from the Pencil code, specifically the simulations presented by Käpylä et al. (2011), Warnecke et al. (2012), and Käpylä et al. (2013). The Pencil code is especially favorable for comparing with ASH as both codes generally use explicit diffusion which is only a function of depth. The Pencil code is non-dimensional while ASH uses dimensional units. Thus to compare the two codes we have computed dimensional units for the Pencil code simulations with the help of Jörn Warnecke, which are given in Table 2.4. Simulations using the Pencil code have achieved convective dynamo simulations with strong solar-like differential rotation, the ejection of magnetic structures generated by dynamo action, and equatorward propagation of magnetic features. It is thus very useful to understand the similarities and differences between those simulations and others using ASH.

Dimensional parameters from ASH simulations are given in Table 2.2 and similar parameters for the Pencil code simulations are shown in Table 2.4. Upon comparison it becomes immediately clear that although some parameters such as the diffusion coefficients are very similar, the luminosities and RMS velocities are much larger in Pencil code models than the values in our ASH simulations. The Pencil code simulations also explore a much broader range of rotation rates than the ASH simulations shown here. The widest range of rotation rates explored for solar-like stars in ASH was done by Brown et al. (2008) who considered rotation rates between one and ten times the solar value. The ability to achieve qualitatively similar physical mechanism in such widely disparate regions of parameter space may indicate that some aspects of convective dynamo action are robust over a broad range of physical settings. It may equally inspire caution as one might interpret these results to mean that one can find regions of parameter space which produce qualitatively similar results for very different physical reasons. We will discuss the possibility for further comparisons between the results of ASH, Pencil, and EULAG-MHD models in Chapter 10.

Chapter 3

Enhanced Subgrid-Scale Models for Stellar Convection

As discussed in Chapter 2, the ASH code follows an explicit LES framework in which the largest scales of the solar interior are simulated and the effects of scales below our numerical resolution must be parameterized using a SGS model. In this chapter we will present two SGS models, which we term the Enhanced Eddy and Dynamic Smagorinsky models. The Enhanced Eddy (EE) model has been used in ASH extensively (e.g., Brun & Toomre, 2002; Brun et al., 2004; Miesch et al., 2006; Brown et al., 2010; Brun et al., 2011), while the Dynamic Smagorinsky (DS) model was only recently implemented in the ASH code. This chapter outlines an analysis designed to asses the validity and effectiveness of the DS model. Sections of this chapter follow the text of my Master's Thesis, submitted to the University of Colorado in 2009, but with significant revisions and additions. I was the sole author of that thesis. The DS SGS model was originally implemented in ASH by Mark Miesch. I performed significant changes to this implementation to make it numerically stable. I conducted and analyzed all of the simulations presented here.

3.1 The Large-Eddy Simulation Framework

We seek to use computational tools to explore the nature of large-scale solar and stellar convective and dynamo processes. Turbulence likely plays a key role in both the convection and the generation of magnetic fields. It links the scales of interest with scales that are

below the resolution limits of current numerical simulations. In this work we seek to use subgrid-scale (SGS) models which parameterize the effects of this turbulent cascade in order to improve our global models of solar and stellar convection.

Convection in the solar interior is a highly nonlinear process that involves a wide range of scales in both length and time. As an example, the solar convection zone spans roughly 200 Mm in radius while the length scale for diffusion of momentum, or Kolmogorov scale, may be on the order of meters – a separation in scales of a factor of 10^8. A brute-force approach that attempted to resolve all scales of motion in the solar convection zone would require far more powerful computers than are envisioned in the foreseeable future. The problem is made tractable by the use of SGS models which parameterize the effects of small-scale motions. Simulations can then capture large-scale features at reasonable computational costs. The use of SGS models has allowed remarkable advances towards creating large-scale models consistent with solar and stellar observations, such as simulating solar differential rotation (Brun & Toomre, 2002; Miesch et al., 2006) or cycles of magnetic activity and reversals of magnetic polarity (Brown et al., 2011). By improviFng our SGS treatment, we hope to achieve even more realistic solar and stellar models.

In all ASH cases, finite computational resources prohibit the use of molecular values for the diffusion of momentum, heat, and magnetic fields. This requires a SGS scheme which replaces molecular viscosity, thermal conductivity, and magnetic resistivity with turbulent values designed to represent unresolved small-scale mixing. Previous ASH simulations have used an Enhanced Eddy (EE) SGS model that uses a diffusion term of the same form as that used in the Navier-Stokes equation, but which has a kinematic viscosity that is many orders of magnitude larger than molecular values. Additionally, this viscosity is scaled by the background density (in this work $\nu \propto \bar{\rho}^{-1/2}$), and thus is constant on horizontal surfaces. This EE viscosity model is computationally convenient and retains the same mathematical form as a direct numerical simulation (DNS) of the solar interior. It has produced important insights into convection, differential rotation, and dynamo action in the sun and other stars.

However this SGS prescription becomes prohibitively expensive for very large Reynolds numbers where the simulation cost scales roughly as Re^4. This scaling assumes that doubling the Reynolds number requires doubling the number of grid points in each dimension and suffering a corresponding halving of the time step due to CFL constraints. More complex SGS models hopefully represent small-scale effects more faithfully, allowing less diffusively influenced dynamics to be achieved without increasing resolution, thus reducing computational cost. In this chapter, we will explore the effects of an additional SGS turbulence parameterization, the Dynamic Smagorinsky model (hereafter the DS model) developed by Germano et al. (1991), and compare it with simulations using the EE diffusion model.

3.2 SGS Models

In the LES framework the resolved scales are formally expressed as a convolution of the true velocity and thermodynamic fields with some filter function which removes the unresolved scales. In practical terms this filter is usually the discrete grid on which the numerical equations are solved. We consider the resolved velocity field $\hat{u}_i$ to be the true velocity field u_i convolved with a grid-scale filter G, which we write as a hat for convenience. We can write the evolution equation for $\vec{u}$ as

$$\frac{\partial \hat{\vec{u}}}{\partial t} = -\left(\hat{\vec{u}} \cdot \nabla\right) \hat{\vec{u}} - \nabla \cdot \left(\widehat{u_i u_j} - \hat{u}_i \hat{u}_j\right) + ... \tag{3.1}$$

where we have omitted the additional terms which include the effects of density stratification, viscosity, gravity, and magnetism for brevity. The full set of terms can be found in Equation 2.9. Clearly, the evolution of the resolved velocity field depends on not only the resolved scales but on correlations in the unresolved scales as well. To close the equation we must write

$$\widehat{u_i u_j} - \hat{u}_i \hat{u}_j \approx \underline{\mathcal{T}}, \tag{3.2}$$

where $\underline{\mathcal{T}}$ is the unresolved stress tensor. This approximation becomes exact if one can a find the correct form of the stress tensor on the grid scale, which is not possible in most, if not all, physical systems. In computational settings $\underline{\mathcal{T}}$ must be calculable. Thus the components of $\underline{\mathcal{T}}$ can be constants or functions of position, the background thermal state, or the resolved 3D thermal and velocity fields. Choosing to make $\underline{\mathcal{T}}$ a function of the evolutionary variables introduces additional nonlinearities into the mathematical system, which may or may not be undesirable for a given numerical scheme. This term is given by the divergence of a second-rank tensor, which is the same form as the viscous diffusion term in the momentum equation. If small-scale motions are purely dissipative, it then makes sense for the SGS model to take the general form of a diffusive operator and set $\underline{\mathcal{T}} = \underline{\mathcal{D}}$. This is of course a significant assumption and there are likely non-dissipative effects from small-scale turbulence, but the leading effect is likely to be diffusive in nature.

Previous ASH simulations using the EE viscosity model have used a stress tensor of the form

$$\underline{\mathcal{D}} = \mathcal{N}_{ij} = -2\bar{\rho}\nu_{\mathrm{EE}}\left[e_{ij} - \frac{1}{3}\left(\nabla \cdot \vec{u}\right)\delta_{ij}\right], \tag{3.3}$$

where $\underline{\mathcal{D}}$ is the viscous stress tensor found in Equation 2.12 and ν_{EE} is a function of radius only (for a derivation see Kundu & Cohen, 2004). Since molecular values of ν and κ are beyond current computational capabilities, much larger values must be used for computational stability. In practice, values of ν and κ are chosen to be as small as possible for a given level of resolution. In this work those coefficients are on the order of a few times 10^{12} cm^2 s^{-1} (see Table 2.2).

The EE viscosity model has several drawbacks. First, the Sun operates at very large Reynolds numbers, possibly as high as 10^{14}. With the EE diffusion model the computational cost of a simulation scales roughly as Re^4. This makes continued progress towards the Reynolds number of the solar convection zone slow at best. Additionally many of the smallest scales in models using the EE SGS scheme are dominated by diffusive effects rather than truly

resolving convective dynamics, causing a simulation's effective resolution to be less than the total computational resolution. In other words, one must pay for scales that one knows are not reproducing physical behavior. More advanced SGS treatments can provide much lower levels of diffusion at lower computational cost. The DS model uses the scale-invariance of the inertial range in a turbulent cascade to encode effects from unresolved scales. It attempts to limit diffusion on resolved scales, increasing the effective resolution of the simulation.

A second motivation for more advanced SGS treatments is that the viscosity in the EE model is required to be large across the entire domain. If the eddy viscosity represents small scale mixing one might imagine that it should be lower in regions with small gradients in flows or thermal fields. The EE viscosity model uses a uniform viscosity across horizontal surfaces that is set to be as small as computationally allowed. The viscosity is allowed to vary with radius, but the radial contrast is generally quite small (here $\nu_{\rm top}/\nu_{\rm bot} \approx 5$) and is input into the model as a parameter. Thus the viscosity over the entire domain is set by the minimum viscosity allowable at any grid point. While some small number of grid points demand high viscosities for computational stability, the majority of the domain could run at much lower values of ν. The EE model sets the viscosity for the entire domain based on its worst handful of grid points. The DS model allows for lower levels of viscosity in regions that computationally permit lower viscosities in a self-consistent fashion.

There exist a number of SGS models beyond the DS model referenced here. Some of the most used SGS models that will not be covered here are similarity models (Bardina et al., 1980) and the Lagrangian-averaged Navier Stokes (LANS) alpha model (Hecht et al., 2008). We hope to extend our analysis to include these models at a later date. For a review of various SGS models, see Meneveau & Katz (2000).

Additionally a number of numerical diffusion models which are not designed to model sub-grid scale behavior but rather are numerical techniques to reduce diffusion or limit it to a very small range of scales exist. These models include hyperviscosity (e.g., Stein & Nordlund, 2006; Trampedach & Stein, 2011) and slope-limited diffusion models (e.g., Cheung

et al., 2010; Augustson et al., 2011). These numerical diffusion models proceed essentially along the same philosophical direction as Implicit LES codes. Though we will not explore them here, we do anticipate doing so in the near future.

3.3 The Dynamic Smagorinsky Model

The EE viscosity model uses a stress tensor (see Equation 3.3) of the form expected in a DNS simulation. In a true DNS, molecular values of the diffusion coefficients would be functions of the thermodynamic state and thus would essentially be functions of radius with very small variations due to perturbations of the thermodynamic state caused by convection. However the effective diffusion due to the scales of motion not resolved by our simulations should be orders of magnitude greater than mixing due to atomic diffusion. If the eddy viscosity represents unresolved small-scale mixing, one might expect it to depend on the characteristics of the resolved flow. The Smagorinksy model defines a stress tensor $\mathcal{S}_{ij}$ of the same form as $\mathcal{D}_{ij}$ except replacing $\nu(r)$ with a spatially varying $\nu_s(r, \theta, \phi, t)$, resulting in

$$\underline{\mathcal{D}} = \mathcal{S}_{ij} = -2\bar{\rho}\nu_s \left[\mathbf{e}_{ij} - \frac{1}{3} \left(\nabla \cdot \vec{u} \right) \delta_{ij} \right]. \tag{3.4}$$

In the original model put forward by Smagorinsky (1963), $\nu_s = C_s \Delta^2 \sqrt{\mathbf{e}_{ij}\mathbf{e}_{ij}}$, where Δ is the local grid spacing and C_s is a constant of order unity that depends on the geometry, Reynolds number, boundary conditions, and other simulation parameters. For anisotropic grids like those used in ASH simulations, Δ is defined as the geometric mean of the grid spacings in each direction $\Delta = (\Delta_r \Delta_\theta \Delta_\phi)^{1/3}$. By defining ν_s as a function of the local shear, a strong nonlinearity is introduced in what was previously a linear term. For an extensive discussion of this model refer to Pope (2000). In this work, we also use a dynamic thermal diffusivity κ_s that is defined, using an eddy Prandtl number Pr_e, to be $\kappa_s = \nu_s / \mathrm{Pr}_e$. As in the cases using the EE model, $\mathrm{Pr}_e = 1/4$ and is constant over the computational domain.

3.3.1 The Dynamic Procedure

A major limitation to the usefulness of the Smagorinsky model is the constant C_s which must be hand-tuned for each simulation. Using scale-invariance arguments Germano et al. (1991) have formulated a dynamic procedure to calculate C_s from resolved components of the flow. The dynamic procedure is not a SGS model but rather a way to use the resolved flow and an assumption of scale-invariance to set any undetermined coefficients in a given SGS model.

The resolved flow fields are spectrally filtered at some test filter scale $\beta\Delta$. Traditionally and in this work $\beta = 2$, which is assumed to be in the inertial range of the turbulent spectra. Only high resolution ASH simulations with a maximum spherical harmonic degree of 340 or higher were able to assure that $\beta\Delta$ ($\ell_\beta = \ell_{\max}/\beta \gtrsim 170$) was suitably within an inertial range. Lower resolution simulations produced essentially noise-dominated values of C_s and were computationally unstable. This requirement for high spatial resolution indicates that this dynamic procedure would have been unfeasible as little as a decade ago.

We define the stress tensor at the grid-scale Δ as

$$\hat{\mathbf{S}}_{ij} = \widehat{u_i u_j} - \hat{u}_i \hat{u}_j \tag{3.5}$$

with hats denoting the grid-scale filtering. If we have this term exactly then our closure approximation is no longer an approximation. It encodes the difference between the unresolved velocity correlations (which we do not simulate) filtered on the grid scale, and the resolved velocity correlations. The stress tensor at the test filter scale $\beta\Delta$ is defined as

$$\tilde{\hat{\mathbf{S}}}_{ij} = \widetilde{\widehat{u_i u_j}} - \tilde{\hat{u}}_i \tilde{\hat{u}}_j \tag{3.6}$$

with tildes denoting test-scale filtering. This encodes the difference between the stresses at the test scale the true correlations filtered on the test scale. Finally, the resolved stresses can be written as

$$\mathcal{R}_{ij} = \widetilde{\hat{u}_i \hat{u}_j} - \tilde{\hat{u}}_i \tilde{\hat{u}}_j. \tag{3.7}$$

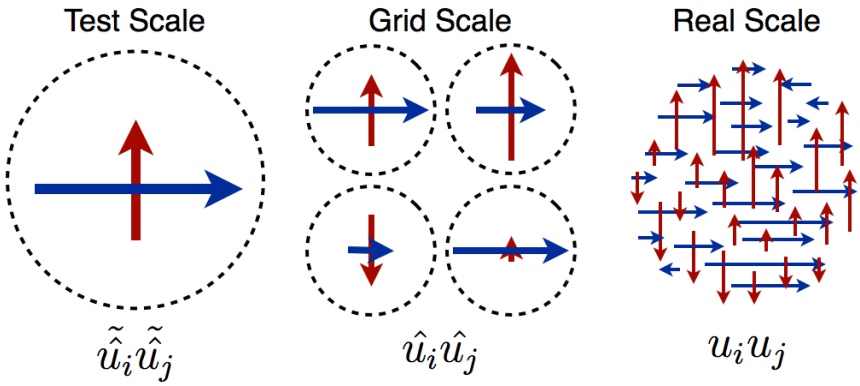

Figure 3.1: Schematic diagram of correlations between two components of a fictitious velocity field on the test scale $\beta\Delta$, the grid scale Δ, and the true scale set by atomic dissipation in the physical system. Circles represent discrete cells in a numerical simulation while the velocity field in the physical system is continuous.

The resolved stresses are simply the difference between the correlations in the test scale velocities and the correlations in the grid scale velocities filtered at the test scale. Note that $\mathcal{R}_{ij}$ can be computed directly from the resolved flows while $\hat{\mathbf{S}}_{ij}$ and $\tilde{\hat{\mathbf{S}}}_{ij}$ require an SGS model, such as the Smagorinsky model, to represent the unresolved correlations.

Figure 3.1 illustrates a sample velocity field on the three scales of interest – the test scale $\beta\Delta$, the grid scale Δ, and the true scale of the physical system, which is of course not a single scale but a range of scales which is limited only by atomic diffusion. In a numerical code we must compute filtered values of the field at discrete grid points, which are represented by the circles, which each contain values for two vector components. The nonlinearity of the correlation procedure means that it does not commute with the filtering procedure, hence taking the correlations at the grid scale and filtering them is not equal to filtering the velocity fields and then taking the correlations.

By assuming scale-invariance in the inertial range of the turbulent spectra, one can state that

$$\mathcal{R}_{ij} = \tilde{\hat{\mathbf{S}}}_{ij} - \hat{\mathbf{S}}_{ij}. \tag{3.8}$$

This simple statement hides a profound assumption about the nature of turbulence. We

are using the resolved stresses which encode the difference between the test and grid scales to determine the difference between the true correlations in the velocity field filtered at the test and grid scales with the correlations in the filtered velocity field at the test and grid scales. Essentially, this is demanding that the behavior between the test and grid scales be replicated when comparing the differences between the test and true scales with the grid and true scales. Thus Equation 3.8 is stating that the behavior between the test and grid scales is representative of the behavior all the way down to the scales of atomic dissipation. This constitutes the dynamic procedure. Other SGS models with undetermined coefficients can also be put through this dynamic procedure by invoking scale-invariance.

3.3.2 Implementation of the DS Model in ASH

Now that we have defined the dynamic procedure, we must apply it to the Smagorinsky SGS model. This constitutes an additional assumption, namely that unresolved correlations on both the test scale and grid scale can be represented by the same parameterization. This again requires that the test scale be well beyond any of the convectively-driven scales in the simulation. Applying the Smagorinsky model and contracting with $\hat{\mathbf{e}}_{ij}$ to obtain a scalar equation results in

$$\mathcal{R}_{ij}\hat{\mathbf{e}}_{ij} = -2C_s\left(\beta^2\Delta^2\left|\hat{\bar{\mathbf{e}}}_{ij}\right|\hat{\bar{\mathbf{e}}}_{ij}\hat{\mathbf{e}}_{ij} - \Delta^2\left|\hat{\mathbf{e}}_{ij}\right|\hat{\mathbf{e}}_{ij}\hat{\mathbf{e}}_{ij}\right). \tag{3.9}$$

Solving for C_s gives

$$C_s = -\frac{\mathcal{R}_{ij}\hat{\mathbf{e}}_{ij}}{2\left(\beta^2\Delta^2\left|\hat{\bar{\mathbf{e}}}_{ij}\right|\hat{\bar{\mathbf{e}}}_{ij}\hat{\mathbf{e}}_{ij} - \Delta^2\left|\hat{\mathbf{e}}_{ij}\right|\hat{\mathbf{e}}_{ij}\hat{\mathbf{e}}_{ij}\right)}. \tag{3.10}$$

To prevent the denominator from becoming zero it is generally averaged in some way. In this work a spectral filter is applied that removes high wavenumber components in both the numerator and denominator. Additionally a nearest-neighbor averaging is applied to C_s in physical space to prevent grid-scale ringing in the C_s field. Note that the strain-rate tensor and therefore ν_s are not subject to these averaging and smoothing procedures. Equations 3.4, 3.7, and 3.10 constitute the DS model.

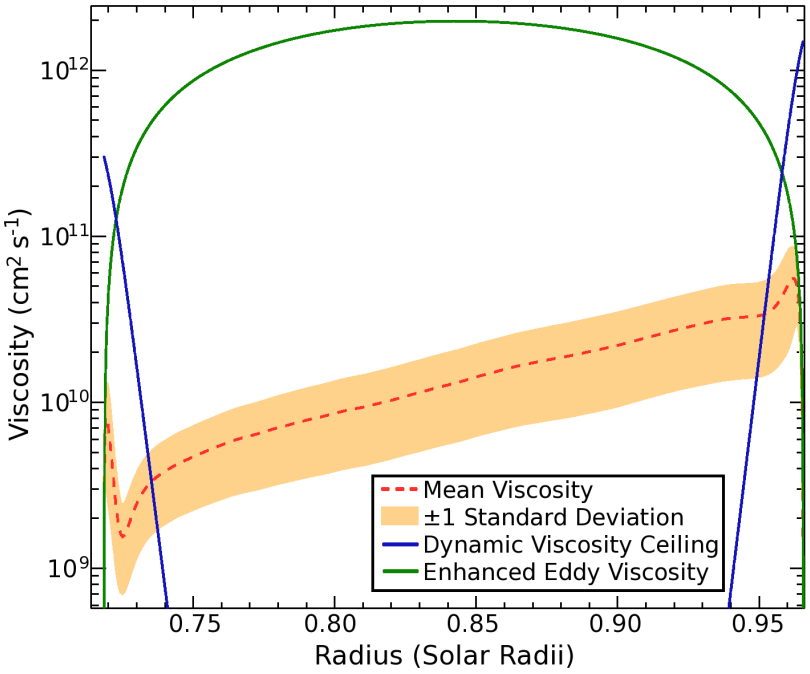

Figure 3.2: Radial profile of ν_S in case S. Kinematic viscosities in case S showing the horizontal and temporal mean value of ν_s as a function of radius (dashed red line) with $\pm 1\sigma$ variations shown in the orange shaded region, along with the EE viscosity (solid blue line) at the top and bottom of the domain for stability, and the viscosity ceiling (solid green line) to prevent large viscosities near the top and bottom of the domain from limiting the time step. The dynamic procedure attempts to produce the required viscosity at the boundaries, but is not successful in stabilizing the simulation without additional EE viscosity.

One of the known problems with the DS model is its inability to mimic behaviors near boundaries. As a turbulent flow nears a wall it becomes laminar in the viscous boundary layer and anisotropic due to the introduction of a strongly preferred direction perpendicular to the wall. Both of these violate the assumption of scale-invariance, which occurs in isotropic turbulence, upon which the dynamic procedure is predicated. In our implementation of the DS model we also find that viscous boundary layers are not correctly formed at the top and bottom of the domain. This results in convective plumes hitting the upper and lower boundaries at high speeds, causing excessive ringing. To resolve these problems, we include a smoothly-varying EE viscosity that is significant over a distance of 0.02 $R_\odot$ at the bottom boundary and 0.01 $R_\odot$ near the top of the simulation.

In the DS model the nonlinear nature of the diffusion term requires an explicit time stepping scheme which imposes an upper limit on the size of our time-step. In order to control the time-step, an artificial ceiling is placed on the DS viscosity. In case S, on average, the ceiling is applied to 700 out of 76 million grid points at each time step. The functional form of the ceiling is given by

$$\nu_{\max} = t_{\max} \Delta_{\min}^2, \tag{3.11}$$

where $\Delta_{\min}$ is the smallest local grid-spacing in any direction and $t_{\max}$ is the desired size time step. In case S $t_{\max}$ is set to 400 seconds.

Both the near-boundary EE diffusion buffers and the DS viscosity ceiling effects are illustrated in Figure 3.2, which also clearly shows that the DS viscosity is dominant throughout the bulk of convection zone. Future simulations could add a stable radiative zone at the bottom of the simulation, which would remove the need for the EE viscosity buffer and possibly the DS viscosity ceiling at the bottom of the domain.

In astrophysics, the non-dynamic version of the Smagorinsky model has been used in low-resolution ($N_r = 32$, $\ell_{\max} = 31$) simulations of stratified, rotating solar convection (Glatzmaier, 1985), similar to those proposed here, and more recently in simulations of the geodynamo at low to moderate resolution (Buffett, 2003). In both cases, however, the dynamic procedure would likely have failed. The DS model has been used in simulations of turbulence in the interstellar medium (Chernyshov et al., 2008) and in convective excitation of solar p-modes (Jacoutot et al., 2008).

Figures 3.3(a) shows the values for ν_s over a spherical shell at 0.84 $R_\odot$ at a single instant in time. The largest values of ν_s are concentrated at the edges of downflow lanes where strong horizontal gradients of vertical velocity are present. Figure 3.3(b) shows the time-averaged probability distribution function of the DS viscosity. Probability distribution functions (PDF) are denoted $F_C(a)$, where a is the desired variable and C represents the simulation. All PDFs in this work are given as the amount of surface area covered on average

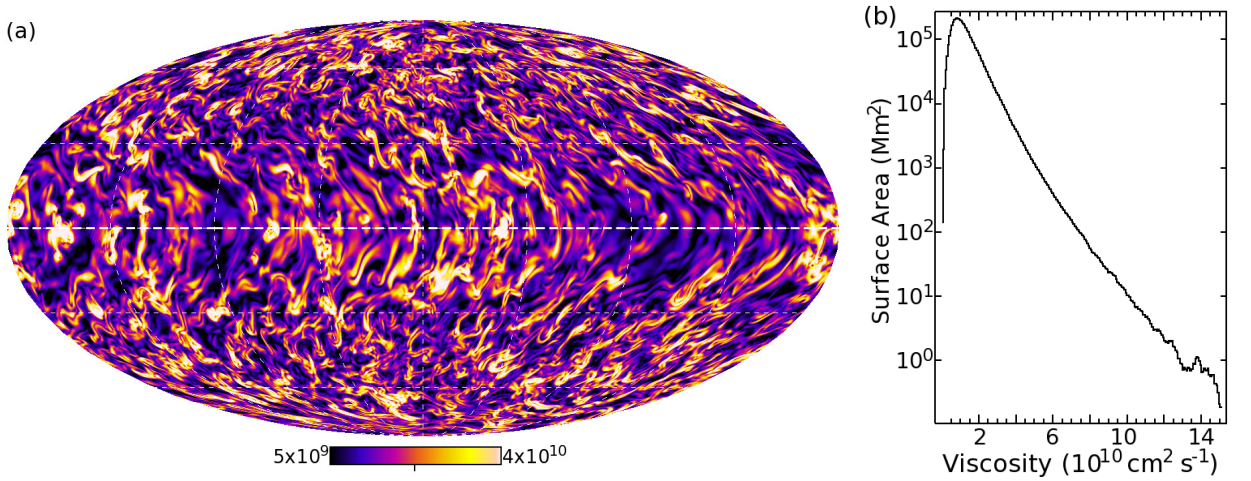

(a) ν_S (b) $F_S(\nu_S)$

Figure 3.3: (a) Kinematic viscosities from the DS SGS model ν_s at 0.84 $R_\odot$ in Mollweide projection. Values are in units of cm^2 s^{-1}. Colors are on a logarithmic scale, showing small values in dark tones and large values in light tones. High-viscosity regions tend to occur on the edges of downflows while upflows tend to have very little diffusion. (b) Probability distribution function of kinematic viscosities $F_S(\nu_s)$ from case S averaged over roughly 1000 days. The distribution peaks at about 8.2×10^9 cm^2 s^{-1} and then follows a roughly exponential decay towards higher values. Peak values of ν_S at mid-convection zone are about 1.5×10^{11} cm^2 s^{-1}. For comparison Case Nb has a value of 3.4×10^{11} cm^2 s^{-1} at the same depth.

by the chosen field over a small range of values of the field at mid-convection zone. Surface area is computed rather than number of pixels to account for the non-uniform grid spacing over spherical surfaces. As expected the bulk of the domain has relatively low viscosity with the peak of the distribution at 8.26×10^9 cm^2 s^{-1} and then follows a roughly exponential decay to a maximum value of about 1.5×10^{11} cm^2 s^{-1}.

3.3.3 Non-dimensional Parameters with the DS Model

The strong spatial and temporal variations in the coefficients of viscosity, thermal conductivity, and magnetic resistivity make it difficult to construct meaningful non-dimensional parameters involving diffusive processes for comparison with simulations using other SGS models. In Table 2.3 we used the RMS values for ν_S, κ_S, and η_S which were averaged over

long times, however other possible methods of estimating parameters exist.

Let us take the Reynolds number as an example. In case S we report a value for the Reynolds number of 9210 when calculated as

$$\mathrm{Re} = \frac{\sqrt{\overline{(v^2)}}L}{\sqrt{\overline{(\nu_S^2)}}}, \tag{3.12}$$

where the overbars denote averages over a spherical shell, which here are taken at mid-convection zone, and L is the depth of the convection zone. This includes the differential rotation; thus we also define a fluctuation or convection Reynolds number with the axisymmetric flows removed, given by

$$\mathrm{Re}' = \frac{\sqrt{\overline{(v - \langle v \rangle)^2}}L}{\sqrt{\overline{(\nu_S^2)}}}, \tag{3.13}$$

where brackets denote the longitudinal average. For case S this yields a value of 2870. When compared with case Nb, which has $\mathrm{Re} = 1650$ and $\mathrm{Re}' = 517$, and, as we will show, exhibits comparable or even greater levels of turbulence by other metrics, the values for case S seem inflated.

Alternatively, we can construct another Reynolds number, which we will term the mean local Reynolds number or $\mathrm{Re_m}$, by

$$\mathrm{Re_m} = L\overline{\left(\frac{|v - \langle v \rangle|}{\nu_S}\right)}. \tag{3.14}$$

For case S the mean local Reynolds number is 8530, which still seems to over-estimate the level of turbulence achieved in the simulation. This is caused by correlations between high velocities and low levels of diffusion. Those areas with strongest shear (and hence strongest diffusion) tend to be the downflow lanes where the velocities are highest. In case S regions with $v - \langle v \rangle > 100$ m s^{-1} have an average local Reynolds number of 11600, while regions with $v - \langle v \rangle < 100$ m s^{-1} have an average value of 6450.

Finally, we can estimate the Reynolds number by using a scale-analysis on the DS

viscosity itself. We can approximate ν_S using scale arguments as

$$\nu_s = C_s \Delta^2 \sqrt{\mathbf{e}_{ij}\mathbf{e}_{ij}} \approx C_s \Delta v, \tag{3.15}$$

thus yielding a Smagorinsky Reynolds number $\mathrm{Re_S}$ as

$$\mathrm{Re_S} = \frac{L}{C_s \Delta}. \tag{3.16}$$

The Smagorinsky Reynolds number can be thought of as simply the range of scales in the simulation scaled by the dynamic parameter, which for case S yields a value of 2040.

We have shown four possible methods for computing a Reynolds number for case S which yield values differing by as much as a factor of four. Clearly a range of possible values for any non-dimensional parameter involving diffusion coefficients become viable when using the DS SGS model. This discussion is not aimed to provide a definitive conclusion as to which method for computing these parameters is best but rather to illustrate the difficulty in interpreting these parameters, whichever method is chosen.

3.4 Simulation Parameters

We have conducted three simulations that compare the two SGS models. Various properties of these three simulations are listed in Table 3.1 (see also Tables 2.1, 2.2, and 2.3). Two cases labeled Na and Nb use the EE diffusion SGS model and case S uses the DS model. Cases Na and S have a maximum spherical harmonic degree of 341 while case Nb has a maximum spherical harmonic degree of 682. In the EE diffusion cases the values of ν were chose to be as small as permissible at the given levels of resolution. Although they are not DNS, cases Na and Nb will be used as benchmarks to assess the performance of case S.

All three simulations are conducted at a rotation rate of three times the solar value. Previous studies with ASH have shown that for high levels of turbulence and rotation rates less that the solar rate, the simulations produce an anti-solar differential rotation profile

Table 3.1: Shown are the number of radial, latitudinal, and longitudinal grid points. The SGS model employed for viscous and thermal diffusion is shown as either the enhanced eddy (EE) model or the dynamic Smagorisnky (DS) model. The total evolution time T_E for each simulation is given in days. The viscosity ν in units of cm^2 s^{-1} is shown at mid-convection zone. For case S the RMS value is used. The fluctuating Reynolds number $\mathrm{Re}' = v'_{\mathrm{rms}} L/\nu$ gives some indication of the relative level of turbulence in each model. Again the RMS value for ν_S was used for case S.

Selected Parameters for Cases Na, Nb, and S

Case	N_r, N_θ, N_ϕ	SGS Model	T_E (days)	ν (cm s^{-2})	Re$'$
Na	192, 512, 1024	EE	4820	5.15×10^{11}	337
Nb	257, 1024, 2048	EE	1120	3.43×10^{11}	517
S	192, 512, 1024	DS	2760	1.49×10^{10}	2870

(Brown, 2009). This transition is caused by inertial forces becoming dominant compared to Coriolis forces, removing the rotational influence which drives the equatorward transport of angular momentum needed to maintain solar-like differential rotation. By using a more rapid rotation rate, differential rotation retains some aspects of a solar differential rotation profile, including a fast equator and slow mid-latitudes. Thus while these simulations may be at a dimensional rotation rate faster than that of the current Sun, their non-dimensional Rossby number is on the order of 0.5. Without direct measurements of convective giant cell velocities the exact value of the solar Rossby number is somewhat uncertain, but can be constrained from observations of differential rotation and meridional circulation to be no more than about 0.5 (Miesch et al., 2012).

All cases are qualitatively similar to case G3 in Brown et al. (2008), from which case Na originated. Case G3 was evolved for approximately 4000 days when case Na was spawned from it. Case Na was then run for roughly 3000 days to a statistically steady state in terms of its volume-averaged energy densities and angular momentum transport. Cases Nb and S were then created using case Na as initial conditions. Case S was evolved to a statistically steady state, while case Nb was run for as long as available resources would allow.

SGS models are designed to more faithfully represent turbulent processes at lower resolution, thus reducing the computational expense. In our discussion of the various SGS models, it is also important to keep in mind the computational cost associated with each model. Table 3.1 shows the total time over which each case was evolved. Cases Na and S were able to be run as long as desired to achieve a statistically steady state. For case Na additional evolution was computed in order to provide very long time averages for computation of spectra and probability distribution functions. Case Nb is more than an order of magnitude more expensive than case Na and therefore has not been evolved as long as the other cases.

In addition to considering the effectiveness of the DS SGS model, we must also consider the additional computational resources required to compute the Smagorinsky viscosity. The DS model is roughly four times more expensive than case Na while case Nb is roughly twelve times more expensive than case Na. This means that to be worthwhile case S needs to only show a third as much improvement in the desired aspect of a simulation over case Na as case Nb shows over case Na. While it is difficult to define quantitative metrics for this improvement, one might be interested in a simulation very low levels of explicit diffusion. We will show that case S displays more than a order of magnitude less viscous force per unit volume than case Na or case Nb without any obvious pathologies in other aspects of the simulation (e.g., differential rotation, convective transport, etc.). As the objectives of simulations using the DS SGS model will vary, we do not attempt to compute a single metric for simulation quality. Rather we will describe several possible methods for comparing aspects of cases Na, Nb, and S. Hopefully this will permit the reader to assess the usefulness of the DS SGS model for their specific numerical experiment.

3.5 Direct Comparisons of SGS Models

There are two important ways to compare and evaluate SGS models. One can either examine the form of the diffusive terms added to the equations in each model or use statis-

tical measures to compare solutions evolved with each SGS treatment. We will call these direct and statistical comparisons. Meneveau & Katz (2000) refer these two classes of tests, respectively, as a priori and a posteriori comparisons. Evolved comparisons involve examining simulations using various SGS models, as we have done with cases Na, Nb, and S, where the solution has experienced feedback from the SGS model and settled into a statistically steady state. The ultimate objective of any SGS treatment is to reproduce the results of observations, so it may be argued that evolved comparisons are all that matter. As these are highly nonlinear systems, altering the diffusive processes will also alter the flow patterns, energy transport mechanisms, angular momentum transport, and potentially any number of other features of our simulations. By comparing the statistically steady states into which each case evolves, we can assess how the effects of a SGS model propagate through the simulation.

In contrast to evolved comparisons, direct comparisons involve directly examining the changes to the viscous term in the momentum equation. They can provide valuable insight into the physical processes that are changed by a SGS model. In implementing a SGS model one is modifying the underlying physics of diffusion of momentum and entropy in sometimes non-intuitive ways. Once the system has begun to feedback upon itself, it becomes extremely difficult to track the origin of changes in behavior. Thus it is useful to perform direct comparisons because they isolate the immediate changes to the diffusive terms in our equations in a way that permits detailed comparisons to be made between the two SGS treatments.

In this work, we will directly compare the diffusion term in the radial component of the momentum equation, which is given by

$$\left(\nabla \cdot \underline{\mathcal{D}}\right)_r = \frac{1}{r^2}\frac{\partial}{\partial r}\left(r^2 \mathcal{D}_{rr}\right) + \frac{1}{r\sin\theta}\frac{\partial}{\partial \theta}\left(\sin\theta \mathcal{D}_{\theta r}\right) + \frac{1}{r\sin\theta}\frac{\partial \mathcal{D}_{\phi r}}{\partial \phi} - \frac{\mathcal{D}_{\theta\theta} + \mathcal{D}_{\phi\phi}}{r}, \tag{3.17}$$

where the rr, θr, ϕr, $\theta\theta$, and $\phi\phi$ components of the stress tensor for both the EE and DS

models are, respectively,

$$\mathcal{D}_{rr} = -2\bar{\rho}\nu \left[\frac{\partial u_r}{\partial r} + \frac{u_r}{3} \frac{\partial \ln \bar{\rho}}{\partial r} \right] \tag{3.18}$$

$$\mathcal{D}_{\theta r} = -\bar{\rho}\nu \left[\frac{1}{r} \frac{\partial u_r}{\partial \theta} + \frac{\partial u_\theta}{\partial r} - \frac{u_\theta}{r} \right] \tag{3.19}$$

$$\mathcal{D}_{\phi r} = -\bar{\rho}\nu \left[\frac{1}{r \sin\theta} \frac{\partial u_r}{\partial \phi} + \frac{\partial u_\phi}{\partial r} - \frac{u_\phi}{r} \right] \tag{3.20}$$

$$\mathcal{D}_{\theta\theta} = -2\bar{\rho}\nu \left[\frac{1}{r} \frac{\partial u_\theta}{\partial \theta} + \frac{u_r}{r} + \frac{u_r}{3} \frac{\partial \ln \bar{\rho}}{\partial r} \right] \tag{3.21}$$

$$\mathcal{D}_{\phi\phi} = -2\bar{\rho}\nu \left[\frac{1}{r \sin\theta} \frac{\partial u_\phi}{\partial \phi} + \frac{u_r}{r} + \frac{\cot\theta u_\theta}{r} + \frac{u_r}{3} \frac{\partial \ln \bar{\rho}}{\partial r} \right]. \tag{3.22}$$

The difference between the EE and DS models comes purely from the definition of ν, which in the EE model only varies with radius, whereas in the DS model it is a strongly varying function of all three dimensions and time.

We chose to examine the radial viscous force in order to gain some intuition into the modified physics of the DS model. We could have just as easily looked at the viscous force in another direction, but the radial component is particularly important as it impacts the process of acceleration of the convective plumes and their entrainment of the surrounding fluid. Entrainment is essential to compressible convective transport, making it an appropriate diagnostic. To do this we have run three simulations matching the parameters of cases Na, Nb, and S but starting all three simulations from identical initial conditions taken from case Na in an evolved state. Since the starting point for each simulation was taken from case Na, we would expect no ringing in the diffusion term for case Na due to the transition (or lack thereof). If the radial viscous force in case S shows large deviations from the morphology seen for cases Na or Nb, we may reasonably conclude that it is not appropriately capturing the diffusive dynamics around convective plumes.

When the form of the equations being solved changes abruptly, some Gibbs ringing is expected from the transition, which is essentially a small temporal discontinuity. Each case was evolved for exactly five time steps of exactly 100 seconds each to allow most of the Gibbs ringing from the transition to dissipate but not enough time for any significant evolution of

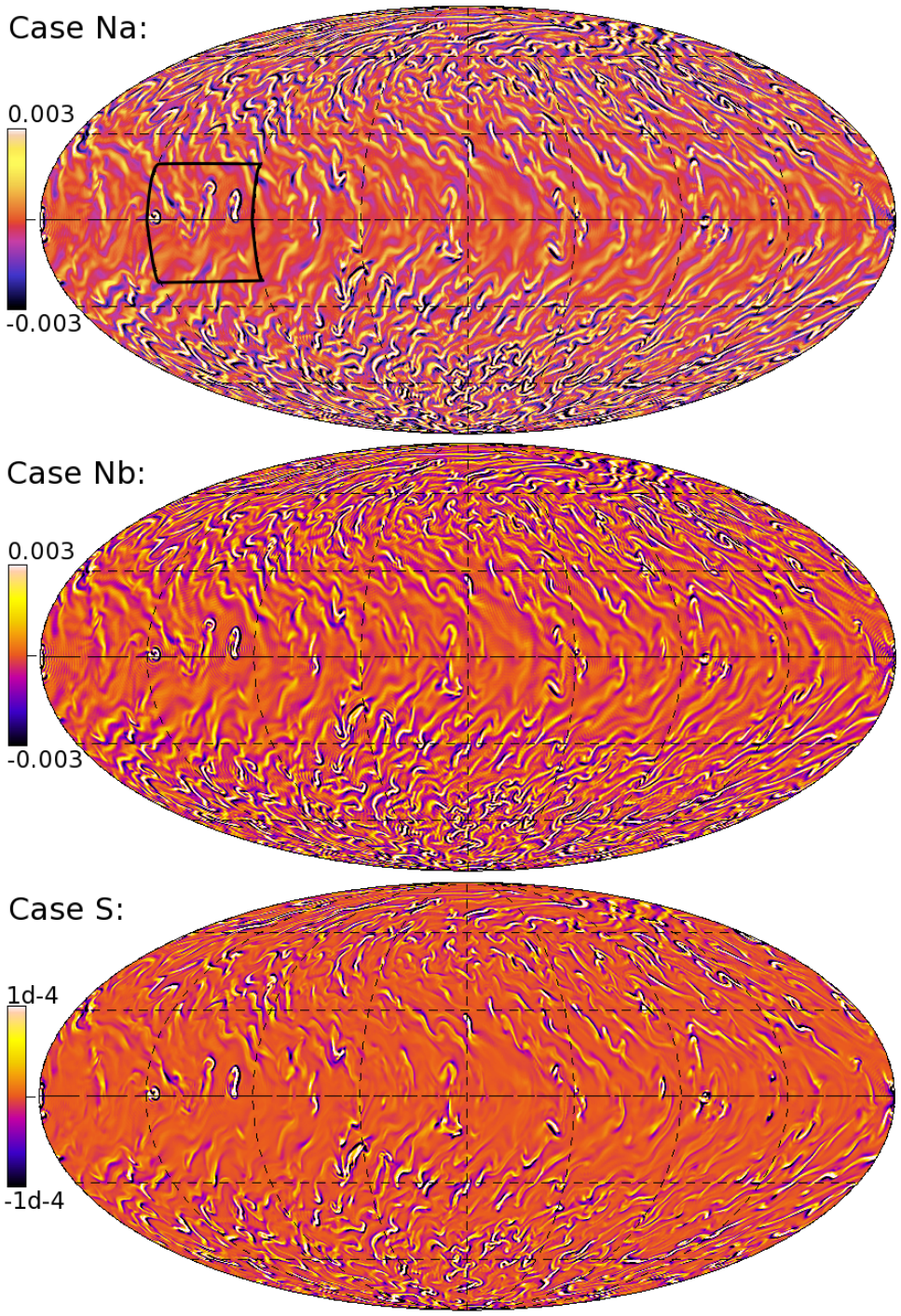

Figure 3.4: Radial viscous force for the EE and DS SGS models with an identical flow field Radial diffusion terms (see Equation 3.17) in units of force per unit volume (dyn cm^{-3}) for cases Na, Nb, and S shown in Mollweide projection at 0.84 $R_\odot$ for an identical flow field. The highlighted region in the top panel corresponds to the regions shown in Figures 3.5(a) - 3.5(d). In all cases the underlying flow field is virtually identical, allowing direct comparisons between these images.

the velocity fields. The velocity and thermodynamic fields were compared to ensure no significant evolution had occurred. The maximum variation at mid-convection zone between any two simulations was less than roughly 1 part in 10^5. By using identical flows, we can then examine the direct effects of the SGS model without considering secondary effects or feedback mechanisms.

3.5.1 Global Properties of Diffusion in SGS Models

Figure 3.4 shows the diffusion term for each of the three cases for the mentioned identical flows over the entire spherical surface at mid-convection zone. One can see clear similarities between the cases and identify common structures in each, however the ranges of values achieved in each case is surprisingly different. Case Na and Nb have, as expected, almost identical morphologies for their viscous force term, since the velocity field $\vec{u}$ is the same in both as is the form of the diffusion operator. The only difference is the magnitude of the viscosity, hence we should expect that the point-by-point ratio of the two fields will be the ratio of their viscosities. In fact if we divide each pixel in case Na by each corresponding pixel in case Nb, after filtering case Nb in order to have equal resolution, we find that the result is almost exactly $3/2 = \nu_{\mathrm{Na}}/\nu_{\mathrm{Nb}}$ over the entire domain. This verifies that the the underlying flows are nearly identical and that our procedure behaves as expected for the EE model.

The diffusion term in Figure 3.4 for case S also looks qualitatively similar to cases Na and Nb, however scaling has changed dramatically. If we take a pixel by pixel ratio of the displayed shell slices for cases Nb (spectrally filtered to the correct resolution) and S, we find that on average the diffusion in case Nb is larger by a factor of 86.5. However, in the 2% of regions in case Nb where the diffusion is strongest that ratio drops to 31.4. As expected, the DS model is focusing the diffusion in areas where it is needed and greatly reducing diffusion over the majority of the domain.

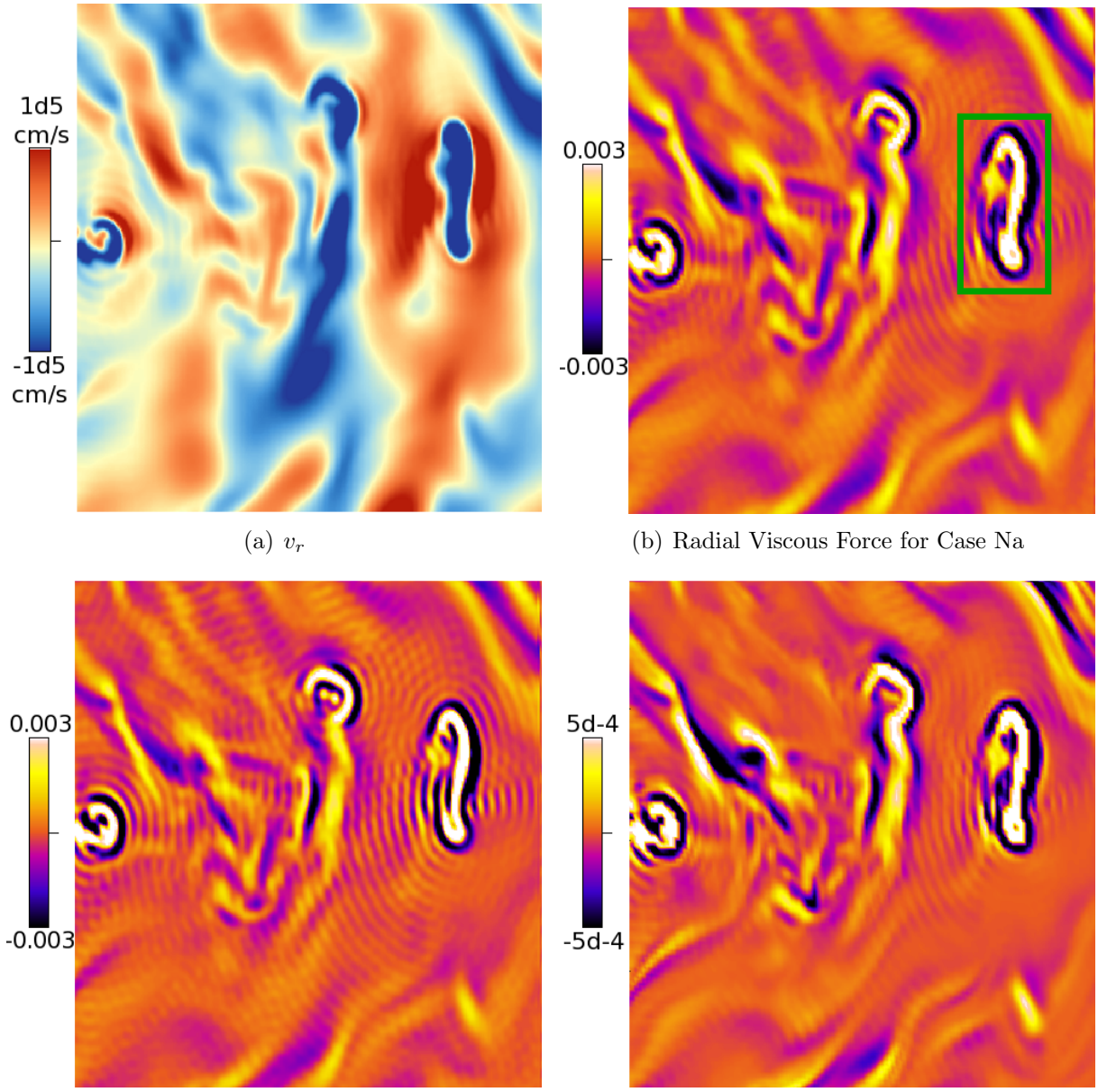

(a) v_r

(b) Radial Viscous Force for Case Na

(c) Radial Viscous Force for Case Nb

(d) Radial Viscous Force for Case S

Figure 3.5: Local radial viscous force for a convective plume in the EE and DS SGS models. (a) Radial velocity field and (b) - (d) radial viscous force terms in units of force per unit volume (dyn cm^{-3}) for the EE viscosities used in cases Na and Nb and the DS viscosity from case S zoomed in on a region spanning 40 degrees in latitude and 45 degrees in longitude. Regions correspond to the highlighted region in the top panel of Figure 3.4. All three viscous force fields are morphologically similar. Downflow plumes are characterized by their strong positive (upward) cores surrounded by negative (downward) entrainment regions. The DS model yields lower amplitudes at all points. Away from the three downflow plumes values can be as much as a hundred-fold smaller in case S than in case Nb.

3.5.2 Local Examples of Diffusion in SGS Models

To gain further physical insight into these SGS models, we have highlighted one small area from the three images in Figure 3.4 for a more detailed examination. This area, which is indicated by the outlined region in the top panel, stretches from 20 degrees below the equator to 20 degrees above the equator and covers 45 degrees in longitude. Figures 3.5(a) - 3.5(d) show the radial velocity field in this region as well as the diffusion term for all three cases. The region contains three strong downflows each interacting with a broader, slower upflow. Two of the downflows have strong latitudinal alignment while the downflow on the left appears to be a more circular event. All three events are also resolved in each of the diffusion fields. In all three plumes, the diffusion is qualitatively similar for cases Na, Nb, and S.

Let us now examine the strong downflow plume on the right of Figures 3.5(a) - 3.5(d), indicated by the green box in Figure 3.5(b). This downflow plume is plunging into a relatively strong upflow and therefore exhibits some of the strongest gradients in the velocity field in the domain. For cases Na, Nb, and S the viscous structure associated with this downflow shows a surprising degree of complexity. The viscous force in the core of each structure is strongly positive, which would lead to an upward acceleration on the core of the downflow, slowing it down. This braking region is surrounded by a region where the viscous term becomes negative, producing a downward acceleration on the fluid. This happens at the interface of the downflow structure with the surrounding upflow as the downflow entrains fluid from the upflow. In Figures 3.5(b) - 3.5(d), there is evidence for even more complex internal structure in the plumes, indicating that there may be important dynamics on scales smaller than the scale of the plumes.

The net effects of diffusion on the downflow plume on the right of Figures 3.5(a) - 3.5(d) vary strongly between the two SGS models considered here. For case Na and Nb the

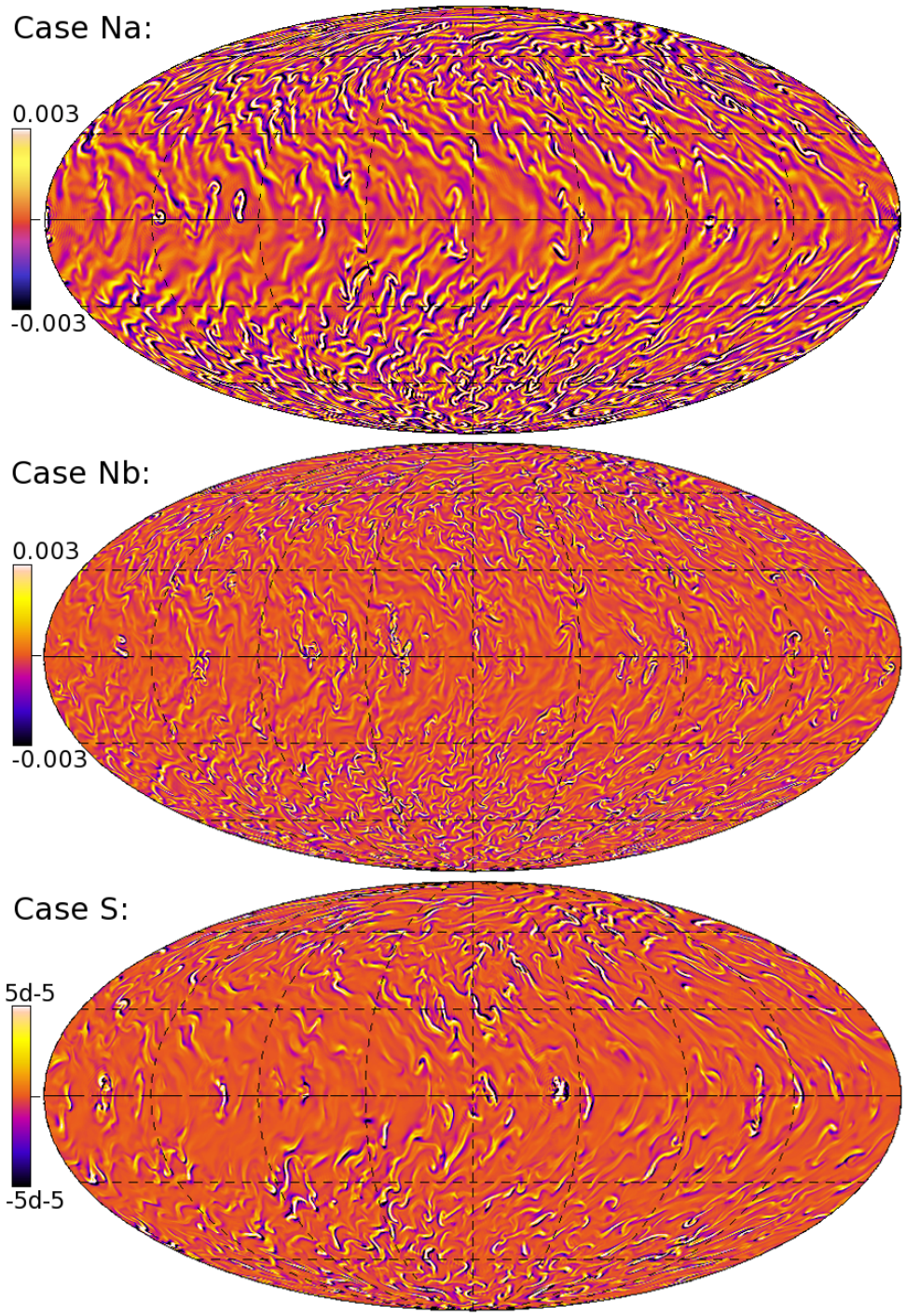

Figure 3.6: Radial diffusion terms in units of force per unit volume (dyn cm^{-3}) for cases Na, Nb, and S after significant time evolution, shown in Mollweide projection at 0.84 $R_\odot$. The top panel is identical to the top panel of Figure 3.4. For each case the flow field is unique and has been taken from each case near the end of their computed evolution (see Table 2.1).

net forces per unit volume of fluid over the highlighted area are -1.85×10^{-2} dyn cm^{-3} and -1.28×10^{-2} dyn cm^{-3} respectively. This net downward acceleration indicates that while the core of the plume is decelerating, the plume structure at this depth is entraining new fluid at a high rate to compensate for the slowing of the core, coming to a rough force balance. For case S, the net force per unit volume on this plume is 7.35×10^{-3} dyn cm^{-3}. Here the plume structure is decelerating on average, as would be expected from a fast plume passing through a viscous medium. The plume is clearly still entraining fluid, but strong upward viscous forces in the core of the downflow dominate the downward forces on the edges of the plume. For comparison the average buoyant force on this structure is-5.76×10^{-3} dyn cm^{-3}. Clearly changing the amplitude of the viscous force by switching to the DS model will have significant impacts on the radial acceleration of this plume. Thus while the morphological similarities of the viscous force fields are encouraging, the change in the detailed balance between the core of the plume and the surrounding entrainment region indicates that we can expect changes to the structure and transport properties of the convection once feedbacks are allowed.

3.5.3 Comparison with Evolved Diffusion Fields

One of the problems with a direct examination of the diffusion fields is that the flow field to which each diffusion operator is applied is not a relaxed solution of the evolution equations. For example, when a DS viscosity is computed using the flow field from a simulation that has been evolved using an EE model, there are natural questions about validity of that test. Since the flow fields are also modified as the SGS model is changed, as will be shown in the following evolved comparison tests, it is useful to compare the diffusion fields computed in the direct comparison to those taken from evolved, relaxed simulations. This will help provide a means to gauge the usefulness of the direct comparison.

Figure 3.6 shows the diffusion fields for each of the three cases after significant time

evolution. A comparison with Figure 3.4 reveals that for each case, the diffusion fields have qualitatively similar properties with cases Nb and S demonstrating more small-scale variability than case Na. The magnitude of the diffusion in each case, however, has changed from the direct comparison test. For case Nb the root-mean-squared (RMS) value of the diffusion field for the direct comparison is 1.76×10^{-3} dyn cm^{-3}, while the RMS value for the evolved state is 1.06×10^{-3} dyn cm^{-3}. This reduction by a factor of two may be explained partially by reduced ringing, but modifications in the flow field have probably also reduced gradients in the flow field. This seems to indicate that for case Nb the decrease in diffusion over case Na is more than the 50% reduction in the enhaced eddy viscosity ν, possibly reducing diffusion by as much as a factor of 4. For case S, the RMS value of the diffusion field for the direct comparison is 4.61×10^{-5} dyn cm^{-3}, while the RMS value for the evolved state is 1.82×10^{-5} dyn cm^{-3}. As in case Nb, this reduction by a factor of roughly 2 can be partially attributed to ringing, though again the values are close to those from the direct comparison. For both cases Nb and S we can therefore be somewhat confident in the trends shown by direct comparisons.

3.6 Evolved Comparisons of SGS Models

The objective of any SGS model is to reproduce observed features of a turbulent system. Here we will compare various aspects of the flows, thermodynamic fields, and transport properties of the three cases. This is often referred to as a posteriori testing of a SGS model (see Meneveau & Katz, 2000). Although all cases trace back to the same initial conditions, the chaotic nature of these solutions make it impossible to compare any two cases at a single point in time after significant time evolution. Instead, we will compare temporal averages of large-scale features and statistical descriptions of small-scale behaviors. In the optimal case, the changes in moving from case Na to case S would be of the same form as the changes seen in comparing cases Na and Nb, although possibly of different amplitude We will show that

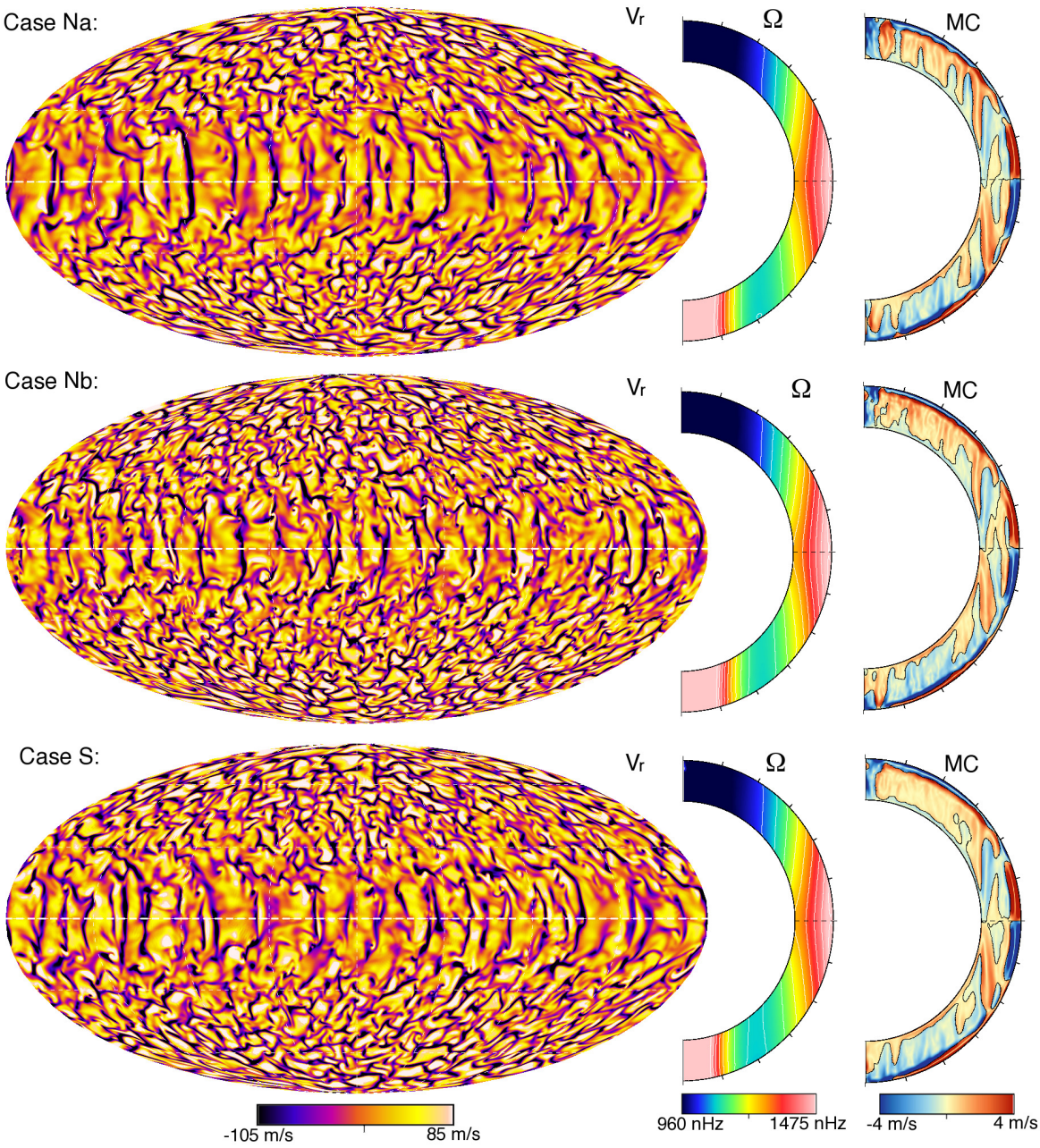

Figure 3.7: Radial velocities, rotation profiles, and meridional circulation streamlines for the three cases. *Left*: Radial velocities at 0.95 $R_\odot$ seen in Mollweide projection with broad, warm upflows in light tones and narrow, cool downflows in dark tones. *Center*: Mean rotation profiles averaged in time and longitude showing some aspects of solar-like differential rotation with fast equators and slow mid-latitudes. All three cases display a fast south pole, which may be a transient phenomena that would decay if significant additional time evolution were undertaken. *Right*: Mean meridional circulations averaged over time and longitude, where red shows counter-clockwise flow, blue shows clockwise flow and darker colors indicate faster flows.

while case S succeeds in this metric for some features of case Nb, it does not reproduce all important aspects of the higher resolution EE case.

3.6.1 Radial Flows

All three of the cases exhibit patterns of turbulent, compressible convection characterized by broad upflows and small, fast downflows. Examining the radial velocity plots in the lefthand column of Figure 3.7, all three cases exhibit large, rotationally-aligned convective structures at the equator, referred to as banana cells, as well as more vortical, smaller-scale convective structures at high latitudes. Similar convective patterns have been previously seen in solar simulations (Miesch et al., 2008) and in case G3 in (Brown et al., 2008). There is a qualitative increase in small-scale motions from case Na to case Nb, as expected, which is evident in both the banana cells at low-latitudes and the smaller-scale cyclonic convection at high latitudes. Case S looks qualitatively more similar to case Nb than to case Na with enhanced small-scales features in both low- and mid-latitudes.

The mean meridional circulation patterns for all three cases are shown in the right-hand column of Figure 3.7. In all three cases the circulations are multi-cellular and highly variable in time. Cases Na and Nb show similar patterns, with a large cell in both hemispheres inside the cylindrical region tangent to the inner boundary (or tangent cylinder) which fill the domain in radius. Case S produces very similar behavior to cases Na and Nb.

We can examine the small-scale flow patterns quantitatively using a time-averaged PDF of the radial velocity field at mid-convection zone. Time averages are taken over about 1000 days for cases Na and S and 500 days for case Nb. Figures 3.8(a) shows that case S produces velocity distributions that generally follow those from cases Na and Nb. If we look at the fractional variation between cases Na and cases Nb and S, we can highlight the differences in the distributions which otherwise look extremely similar. We define the fraction difference

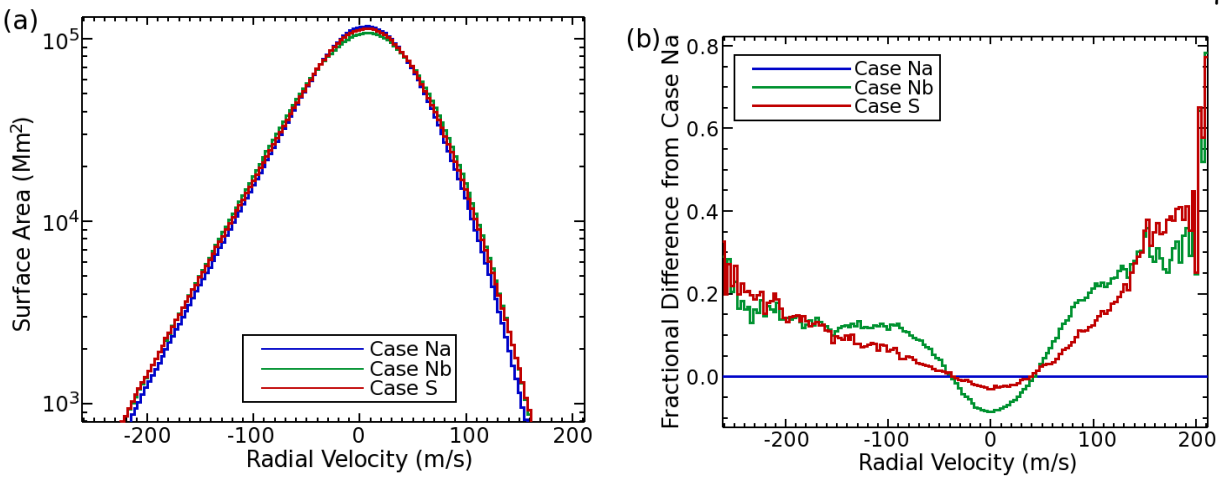

(a) $F(v_r)$ (b) $\Delta F(v_r)$

Figure 3.8: Time-averaged probability distribution functions (PDFs) for radial and latitudinal velocities at mid-convection zone for the three cases. (a) PDFs are extremely similar in amplitude and shape. (b) By examining the fractional change relative to case Na we can see that case Nb has become less peaked (has a larger kurtosis) with a decrease in the core of the PDF and an increase in the wings. Case S follows the trend established by case Nb but to a lesser degree. Averages are carried out over roughly 1000 days for cases Na and S and over roughly 500 days for case Nb. Note that the extreme wings of the PDFs are not shown in order to highlight the core of the distributions.

as

$$\Delta F_C(a) = \frac{F_C(a) - F_{\mathrm{Na}}(a)}{F_{\mathrm{Na}}(a)}. \tag{3.23}$$

Figure 3.8(b) shows the fractional difference for all three cases.

The PDF for case Nb's radial flows becomes less Gaussian compared to that of case Na with a decreased core and increased wings. Statistically this is described by the excess kurtosis of the distribution increasing (becoming more leptokurtic) for the more turbulent case, as expected from turbulence theory (see Pope, 2000). Excess kurtosis is defined as the kurtosis relative to a Gaussian distribution. It is formally defined as

$$\mathrm{kurt}\{a\} = \frac{\int_{-\infty}^{\infty} (a' - \bar{a})^4 f(a')\, da'}{\left[\int_{-\infty}^{\infty} (a' - \bar{a})^2 f(a')\, da'\right]^2} - 3, \tag{3.24}$$

where $f(a)$ is the probability distribution function for quantity a. The time-averaged distribution of radial velocity for case Na shows a standard deviation of 54.1 m s^{-1} and an excess

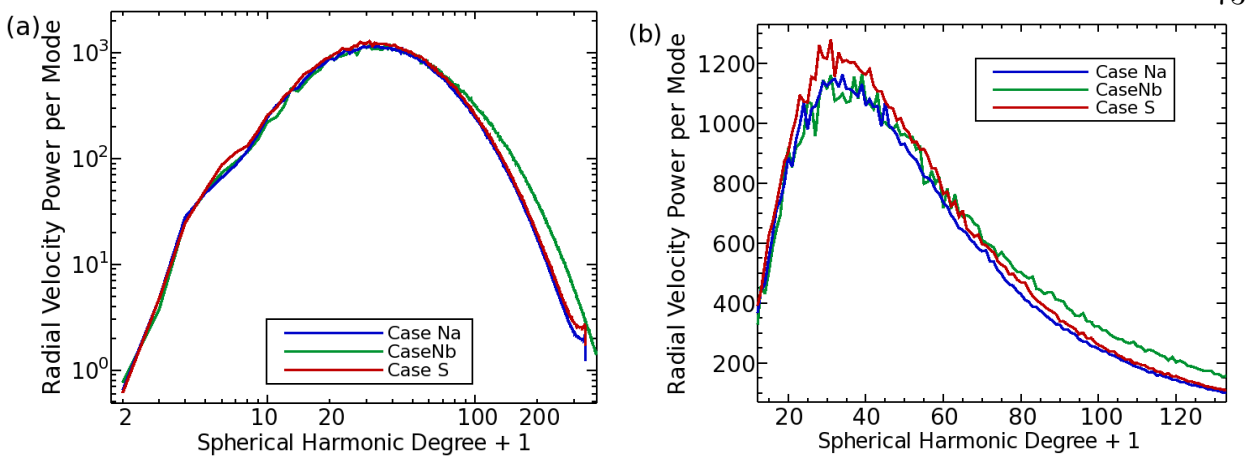

(a) $\breve{v}_r^2$ (b) $\breve{v}_r^2$ for $15 < \ell < 130$

Figure 3.9: Power spectra for radial velocities latitudinal velocities at 0.84 $R_\odot$ shown with (a) logarithmic scales over all spherical harmonic modes, and (b) linear scales over modes dominated by convective driving with $15 < \ell < 130$. Case Nb shows a slight reduction of power at near the peak of the spectra with more power at high-ℓ, as would be expected from an increased level of turbulence. Case S generally follows the other two cases, however it has more power at peak convective scales around $\ell \approx 30$ than either case Na or Nb. At higher values of ℓ case S generally lies between cases Nb and Na, matching onto case Nb for $\ell > 120$. Note that the $\ell = 0$ component of $\breve{v}_r$ is zero to machine precision, since the net mass flux ρv_r into any radius is required by the anelastic approximation to be zero. For convenience and ease of viewing, the $\ell = 0$ component is not shown. For case Nb the spectra continue beyond the plotting range out to $\ell = 682$.

kurtosis of 1.36, while the distribution for case Nb has a standard deviation of 57.0 m s^{-1} and an excess kurtosis of 1.67. This is caused by increased turbulence levels, which drive more high velocity small-scale motions and increase the probability of extreme events on the tails of these distributions. Case S does an excellent job of broadening $F_{\mathrm{S}}(v_r)$ to imitate case Nb, though it does not achieve the same magnitude of fractional difference. For case S the standard deviation in the distribution is 55.8 m s^{-1} and the excess kurtosis is 1.52.

Figures 3.9(a) and 3.9(b) show the time-averaged power spectra for the radial flow field at mid-convection zone. We examine the spherical harmonic spectra at mid-convection zone after summing over m values and averaging the spectra in time. We denote spherical harmonic transforms with a breve and therefore define $\breve{a}\,(r, \ell, m, t)$ as the spherical harmonic

transform of field a at a given radius and over a given time interval. The power spectra of a is given by

$$\breve{a}^2\left(r,\ell\right)=\frac{1}{\Delta t}\int_{t_s}^{t_e}\sum_{m=0}^{\ell}\breve{a}\left(r,\ell,m,t\right)\breve{a}^*\left(r,\ell,m,t\right)dt, \tag{3.25}$$

where * denotes the complex conjugate and $\Delta t = t_e - t_s$. For all spectra in this chapter $\Delta t > 500$ days in order to reduce noise and average over many convective overturning times and rotation periods.

In Figures 3.9(a) and 3.9(b) we can see several features. The spectra of case S shows roughly the same level of agreement with the spectra of both cases Na and Nb. The spectra of case S diverges from the spectra of case Nb for $\ell > 60$, while the spectra from case Na diverges from case Nb for $\ell > 50$. Case S shows peak values in excess of either case Na or Nb and then quickly falls, crossing the power in case Nb at about $\ell = 60$ and finally matching on to case Na for $\ell > 120$. Case S diverges from case Na again at the smallest scales of the simulation. We can compute the RMS variation in the power spectra for cases Na and S, and for cases Nb and S at each ℓ as

$$\Delta\breve{v}_r{}^2(A,B)=\sqrt{\frac{1}{\ell_{\max}}\sum_{i=0}^{\ell_{\max}}\left(\frac{2\left(\breve{v}_{rA}^{\,2}-\breve{v}_{rB}^{\,2}\right)}{\breve{v}_{rA}^{\,2}+\breve{v}_{rB}^{\,2}}\right)^2}, \tag{3.26}$$

where A and B denote the two cases being compared. In doing so we find that $\Delta\breve{v}_r{}^2(Na,S) = 0.137$ and $\Delta\breve{v}_r{}^2(Nb,S) = 0.522$. For comparison $\Delta\breve{v}_r{}^2(Na,Nb) = 0.619$. By this metric case S more closely replicates case Nb than case Na, though the differences are fairly small.

3.6.2 Azimuthal Flows and Differential Rotation

Previous ASH simulations have explored differential rotation in sun-like stars (Brun & Toomre, 2002; Miesch et al., 2008; Brown et al., 2008). There is little reason to expect that a SGS model should directly influence the differential rotation of the simulations, but the non-linear nature of these models means that any change in the system leads to often unexpected

changes elsewhere. Thus it is prudent to establish that a SGS model can achieve solar-like differential rotation under similar conditions to where such a profile may be achieved with the EE SGS model.

All three cases were initiated with a solar-like differential rotation profile. Cases Na began using case G3 of Brown et al. (2008) as initial conditions while both cases Nb and S used case Na as initial conditions. Case G3 has a solar-like differential rotation profile with a fast equator and monotonically decreasing angular velocity with increase latitude, however case Na developed a region of faster rotation at the southern pole before cases Nb and S were created from it. The center column of Figure 3.7 shows the mean differential rotation profiles established by each case with a high-angular velocity region at each south pole. These polar vortices regularly appear in hydrodynamic models of sun-like stars as well as those of F-type stars. We have found that by adding magnetism these fast poles are quickly spun down, resulting in monotonic differential rotation profiles as a function of latitude.

Radial and latitudinal shear are important factors in dynamo calculations, so for simulations related to solar and stellar dynamos, the mean differential rotation profile achieved should mimic the solar differential rotation. All three cases show comparable solar-like differential rotation at the end of their time evolution, with the exception of their south poles. It is possible that case Nb might experience continued evolution in its rotation profile, as we were limited by computational expense to only about 1100 total days of evolution. There is no indication that case Nb was undergoing strong changes at the time these averages were computed, but we have observed significant changes to the differential rotation of other simulations over timescales of thousands of days. Thus while we feel confident in our analysis, we cannot preclude the possibility that case Nb has not reached a fully equilibrated state.

We define the mean latitudinal differential rotation contrast by averaging over both hemispheres to get a measure of latitudinal differential rotation. All cases, irrespective of the symmetry about the equator at their poles are roughly symmetric about the equator for latitudes up to about 60°. We therefore chose to compute the latitudinal differential

rotation between the equator and $\pm 60^\circ$ latitude for a rotation profile averaged over at least 200 days at the end of each simulations' temporal evolution. By this measure cases Na and Nb have latitudinal differential rotation contrasts at the upper boundary of the domain of 28.9% and 28.6% respectively. The radial differential rotation between the top ($0.96 R_\odot$) and bottom ($0.72 R_\odot$) of the domain at the equator for cases Na and Nb are 14.6% and 15.0% respectively. For comparison, in the sun the latitudinal differential rotation contrast at 0.96 $R_\odot$ is roughly 18% and the radial differential rotation contrast at the equator is roughly 7% (Howe, 2009). These values are close to those in a similar ASH model, (case G3) reported by Brown et al. (2008).

For case S the differential rotation profile has remained very similar to cases Na and Nb. The latitudinal differential rotation contrast at the top of the domain in case S is 29.0% and the radial contrast at the equator is 14.7%. Overall the differential rotation is case S appears to have remained largely unchanged by the use of the DS model. One should bear in mind, however, that the diffusion time across the domain has increased by more than an order of magnitude, so it is possible that if diffusive processes are still important in modifying the differential rotation of case S, it may not have been simulated for a long enough time to capture the change. However no trend in the differential rotation of the simulation is seen in either a sequence of 50 day time-averages spanning over 1,500 days or the volume-averaged differential rotation kinetic energy over the same period. This indicates that the DS SGS model does not disrupt the transport of angular momentum needed to sustain solar-like differential rotation, either directly or through feedbacks on the properties which drive convective transport.

3.6.3 Convective Transport

In addition to looking at the flows themselves, we can also examine the balance of energy transport in these models. The average radial flux of energy in the anelastic approx-

imation can be written as

$$\mathcal{L}_r = \mathcal{L}_{\rm KE} + \mathcal{L}_{\rm EN} + \mathcal{L}_{\rm VD} + \mathcal{L}_{\rm TD} + \mathcal{F}_{\rm RD}, \tag{3.27}$$

where the terms represent to luminosity flux due to kinetic energy, enthalpy, viscous diffusion, thermal diffusion, and radiative diffusion, respectively. Each term can be written as

$$\mathcal{L}_{\rm KE} = \frac{\bar{\rho} u_r}{2}\left(u_r^2 + u_\theta^2 + u_\phi^2\right) \tag{3.28}$$

$$\mathcal{L}_{\rm EN} = C_P \bar{\rho} u_r \left(T - \bar{T}\right) \tag{3.29}$$

$$\mathcal{L}_{\rm VD} = \left(\vec{u} \cdot \mathbf{D}\right)_r \tag{3.30}$$

$$\mathcal{L}_{\rm TD} = -\kappa_{00} \bar{\rho} \bar{T} \frac{\partial\left(\bar{S} + S\right)}{\partial r} \tag{3.31}$$

$$\mathcal{L}_{\rm RD} = -\kappa_{\rm rad} \bar{\rho} C_P \frac{\partial \bar{T}}{\partial r}. \tag{3.32}$$

The viscous diffusion flux depends on the SGS model chosen and so is left in a general form here.

Figure 3.10 shows the transport of the solar luminosity through the domain by kinetic energy flux, enthalpy flux, and the total flux as functions of radius. For cases Na, Nb, and S we have chosen to use identical values for κ_{00} and $\kappa_{\rm rad}$. Additionally, $\mathcal{L}_{\rm VD}$ is always less than 3% of the solar luminosity for all three cases. We have chosen to omit the three diffusive fluxes from Figure 3.10 for visual clarity. The primary balance through the bulk of the convection zone is between outward enthalpy and inward kinetic energy transport. All three cases produce similar balances, though case Nb shows a slightly larger inward kinetic energy flux and case S shows a slightly larger enthalpy flux. This illustrates that on a basic level the DS SGS model can achieve an average convective transport which settles into an appropriate balance.

Figures 3.11(a) and 3.11(b) show the time- and shell-averaged root-mean-squared values of the temperature perturbations $\left\langle \sqrt{\langle T^2 \rangle_{\theta,\phi}} \right\rangle_t$ and their fractional difference from those in case Na. Time averages are taken over about 500 days for each case. All three cases

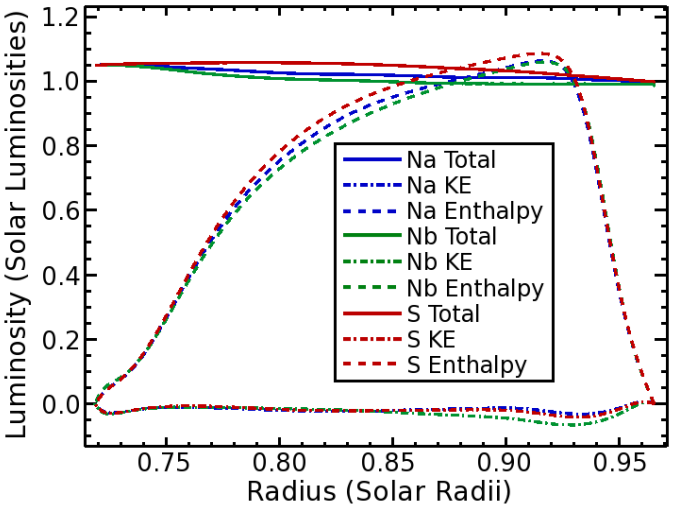

Figure 3.10: Shell- and time-averaged (over at least 500 days) luminosities as a function of radius for each case, showing the total luminosity as well as the luminosity from the outward enthalpy flux and inward kinetic energy flux for each case. All cases achieve an approximate balance. In all cases, a radiative flux carries a solar luminosity into the bottom of the domain and an unresolved flux representing small-scale convective transport from granular scales carries a solar luminosity out of the domain. All cases use identical radiative and unresolved fluxes. Also note that the viscous luminosity flux is not shown, but is small ($< 0.03 L_\odot$) through the bulk of the domain for all cases.

show the same general pattern with roughly the same amplitude of thermal perturbations at each radial level. When we examine the variations from case Na in Figure 3.11(b) we see that case S has not changed in same way as case Nb. Case Nb shows slightly larger perturbations in temperature near the surface and in the lower half of the convective layer as might be expected from increased levels of turbulence, though there is an odd dip around $0.90 R_\odot$. Comparing with Figure 3.10 we notice that this dip corresponds to the peak in the convective enthalpy transport. Case S shows smaller values for the entire convection zone below about $0.93 R_\odot$ with a small rise near the top of the domain. This inability to mimic case Nb is somewhat troubling as it indicates that the DS SGS treatment has altered the thermal structure of the plumes in a way that differs from that of a higher resolution EE SGS treatment. Although there is a clear morphological difference between cases Nb and S, both changes are very small relative to the RMS values in case Na. With variations from

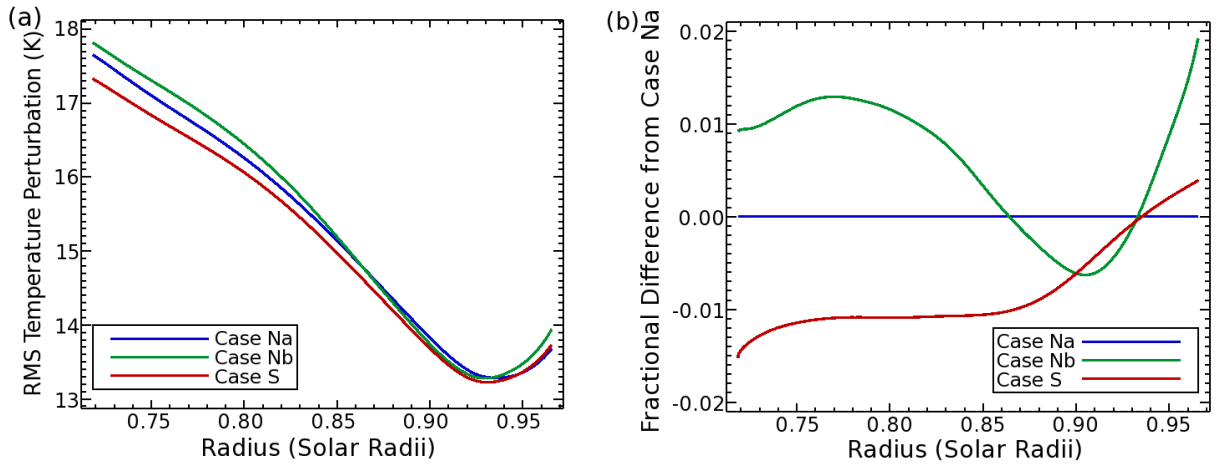

(a) $\left\langle \sqrt{\langle T^2 \rangle_{\theta,\phi}} \right\rangle_t$ (b) $\left\langle \sqrt{\langle T^2 \rangle_{\theta,\phi}} \right\rangle_t$ Relative to Case Na

Figure 3.11: (a)Time-averaged RMS temperature perturbations as a function of radius for cases Na, Nb, and S. All three cases show similar radial variation with thermal perturbations decreasing in amplitude with increasing radial location. (b) Fractional variation of the same temperature perturbations for cases Nb and S relative to case Na, highlighting that case S has changed in a very different way relative to case Na than case Nb has changed relative to case Na.

case Na on the order of 1%, these changes may not produce significant modifications to the overall convective dynamics.

Another spectral measure of convective energy transport can be found by examining the enthalpy flux spectrum. Continuing to use breves to denote spherical harmonic transforms, we can define the enthalpy flux spectra as

$$\breve{\varepsilon}\left(r,\ell\right) = \mathrm{Re}\left[\frac{c_p\bar{\rho}}{\Delta t}\int_{t_s}^{t_e}\sum_{m=0}^{\ell}\breve{T}\left(r,\ell,m,t\right)\breve{v}_r\left(r,\ell,m,t\right)dt\right], \tag{3.33}$$

where $\mathrm{Re}[x+iy] = x$ for real x and y. The enthalpy flux spectra shows the scales on which enthalpy transport from convection is occurring. As the energy flux due to enthalpy $\mathcal{L}_{\mathrm{EN}}$ is the product of only two terms which vary on spherical surfaces, the enthalpy flux spectra can be compute such that it represents the scale-by-scale contribution to the total enthalpy flux through a given spherical surface. It should also be noted that both the entropy variance and the enthalpy flux spectra use the entropy and temperature perturbations about the mean,

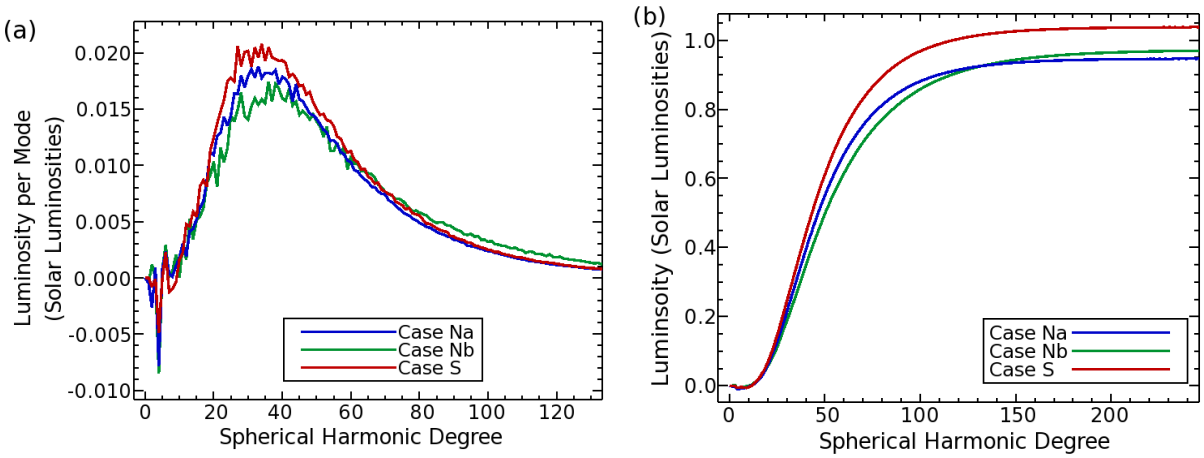

(a) $\breve{\varepsilon}$ (b) $\breve{\varepsilon}_{\mathrm{C}}$

Figure 3.12: (a) Signed enthalpy flux spectra $\breve{\varepsilon}$ at $0.84R_{\odot}$ showing the mode-by-mode contribution of the temperature and radial velocity fields to the total enthalpy flux. Convective scales (roughly $20 < \ell < 100$) dominate the energy transport. Case Nb shows a lower peak and slower decline than case Na, while case S shows a higher peak value and then asymptotically approaches the value case Na at high ℓ. (b) Cumulative enthalpy flux spectra $\breve{\varepsilon}_C$ at the same depth, highlighting that case S does not follow the trend from cases Na to Nb but rather moves in the opposite direction of higher peak values and overall more total enthalpy flux.

and so the $\ell = 0$ component of both are zero to machine precision. We can also construct the cumulative enthalpy flux spectra $\breve{\varepsilon}_{\mathrm{C}}(r, \ell)$ such that

$$\breve{\varepsilon}_{\mathrm{C}}(r, \ell) = \sum_{i=0}^{\ell} \breve{\varepsilon}(r, i)\,. \tag{3.34}$$

This gives the total enthalpy flux at a given radial level for all modes with spherical harmonic degree of ℓ or less.

Figure 3.12(a) shows the enthalpy flux spectra for all three cases. The spectrum for case Nb has a lower peak and slower fall-off at high ℓ compared to case Na. Case S has increased enthalpy flux for $20 < \ell < 60$ compared to both case Na and case Nb. At $\ell \approx 65$ the spectrum for case S crosses the spectrum of case Nb, and by $\ell \approx 100$ matches onto the spectrum of case Na. The increase in the energy carried at the peak of the spectra by case S while case Nb showed a decrease for the same modes indicates that the DS model is not

correctly capturing more turbulent convective transport. On the other hand, the increase in enthalpy transport by case S relative to case Na for the high-ℓ tail of the distribution is mimicking the behavior of case Nb. The DS model is therefore simultaneously failing to behave as a more turbulent simulation for the peak of the spectrum while succeeding to do so for the tail of the distribution.

This picture is reinforced by the cumulative enthalpy flux spectra shown in Figure 3.12(b). In this view case Nb has clearly moved to a flatter cumulative distribution compared to case Na. The increased flux from the moderate ℓ modes in this view has completely overwhelmed the flattening that should occur at higher ℓ. These are small changes and are partially explained by the higher total enthalpy flux in case S, but they do show that the DS model does not provide the same effect as a higher resolution case with the EE SGS treatment, particularly at moderate scales.

3.7 Discussion

In this work we have numerically investigated the application of SGS models in global-scale 3D simulations of the convection zone of a sun-like star rotating at three times the solar rate. We have found that the DS model, while expensive, reproduces the form of the diffusion term at mid-convection zone of higher resolution simulations with much lower RMS values of the diffusion term in the radial momentum equation, even compared to the highest resolution case using the EE SGS model. The DS model also mimics the effects of higher resolution simulations in turbulent flows while maintaining the overall form of the differential rotation and meridional circulations. The DS model, however, mimics only some aspects of the convective transport in our higher resolution simulation using the EE model. While the general properties of the temperature perturbations and enthalpy flux spectra are similar to those using the EE SGS model, using the DS model does not drive changes in these quantities of the same sense as are seen in higher resolution EE viscosity cases. These deviations are

generally small and do not seem to impact large-scale behaviors such the differential rotation or meridional circulation.

Perhaps it should not be surprising that the DS SGS model applied to anelastic convection performs best in metric which consider the viscous force term and the turbulent convective velocities. The DS model was designed to produce a turbulent viscosity which mimics the turbulent diffusion of momentum by unresolved scales. This would produce the most immediate impact on the velocity fields, which seem to yield the best results. We have additionally applied it to the thermal diffusion in our system by means of a fixed eddy Prandtl number. It may be more appropriate to construct a separate thermal SGS model. However if SGS diffusion primarily represents small-scale mixing by turbulent eddies it may be perfectly acceptable to apply a constant Prandtl number of order unity.

Unfortunately, compressible convective turbulence has been far less studied than incompressible turbulence, so this remains an area of active research. Of particular note is the on-going work in the mesoscale meteorology community where thermal effects due to solar heating of the Earth's surface, as well as water condensation and evaporation, play large roles (see Sullivan & Patton, 2011). We have also not considered magnetic fields here. MHD turbulence is far less understood than hydrodynamic turbulence. Suitable SGS models for MHD turbulence are the focus of considerable ongoing study (e.g., Chernyshov et al., 2008, 2010).

The DS SGS model shows potential as an effective method for reducing diffusion in ASH simulations without the computational expense of increased resolution required by the EE model. The DS model does not cause drastic changes to the fundamental properties of the underlying convection. While expensive, the DS model is less expensive than comparable simulations using the EE model. Effective resolution can be defined in many ways, but on a rough level we can gauge that the effective resolution increase in moving from case Na to case S must be less than the increase from case Na to case Nb. Since we know that case Nb has twice the resolution of case Na, we can state that case S must have an effectively

higher resolution than case Na but not by more than a factor of two. Judging from the radial velocity PDFs, we might estimate that the DS SGS model in ASH provides roughly a 50% increase in effective resolution while increasing computational expense by a factor of three. This is considerably less than the factor of roughly twelve cost increase required from simply increasing the resolution of the simulation and using the EE SGS model with smaller coefficients of viscosity and thermal conductivity. Additionally, the DS model allows for levels of effective diffusion which are on average smaller than a comparable simulation by factors of 20 or more. As we will show in Chapters 4, 7, and 8, the ability to achieve extremely low levels of diffusion plays a key role in the creation of buoyant magnetic loops which rise through our simulated domain.

Chapter 4

The Discovery of Buoyant Magnetic Loops

We begin our discussion of convective dynamo action in ASH simulations of sun-like stars by describing our discovery of buoyant magnetic loops which are self-consistently and spontaneously generated by convective dynamo action. This chapter will largely focus on cases D3b and S3, discussed in Tables 2.1, 2.2, and 2.3. The processes in case D3b which build and maintain the magnetic wreaths and which are responsible for the reversals in magnetic polarity will be discussed further in Chapters 5 and 6. The buoyant magnetic loops from case S3 will be explored in further detail in Chapters 7 and 8. This chapter is based on work published in Nelson et al. (2011b)[1] and is largely a restatement of that paper. I was the primary author of that paper and conducted the simulations presented here. I was also chiefly responsible for all of the analysis in this chapter. My co-authors provided invaluable advice and guidance in recommending and developing the parameters of these simulations and the analysis techniques used on them.

4.1 Overview

The current dynamo paradigm for the Sun and sun-like stars places the generation site for strong toroidal magnetic structures deep in the solar interior. Sunspots and star-spots on sun-like stars are believed to arise when sections of these magnetic structures become buoyantly unstable and rise from the deep interior to the photosphere. Here we

[1] Nelson, N. J., Brown, B. P., Brun, A. S., Miesch, M. S., & Toomre, J. 2011b, Buoyant Magnetic Loops in a Global Dynamo Simulation of a Young Sun, ApJ, 739, L38

present the first 3-D global magnetohydrodynamic (MHD) simulation in which turbulent convection, stratification, and rotation combine to yield a dynamo that self-consistently generates buoyant magnetic loops. We simulate stellar convection and dynamo action in a spherical shell with solar stratification, but rotating three times faster than the current solar rate. Strong wreaths of toroidal magnetic field are realized by dynamo action in the convection zone. By turning to a dynamic Smagorinsky model for subgrid-scale turbulence, we here attain considerably reduced diffusion in our simulation. This permits the regions of strongest magnetic field in these wreaths to rise toward the top of the convection zone via a combination of magnetic buoyancy instabilities and advection by convective giant cells. Such a global simulation yielding buoyant loops represents a significant step forward in combining numerical models of dynamo action and flux emergence.

4.2 Convection, Rotation and Magnetism

The clearest signature of the global solar dynamo is the emergence of sunspots at the photosphere. Creating these coherent magnetic structures likely requires several dynamical processes operating at various locations in the solar interior. A single 3-D numerical simulation of solar magnetism that extends from the deep interior through the Sun's upper atmosphere, while resolving all relevant scales, is intractable with current computational resources. This leads to three main classes of simulations that address elements of solar-like dynamo processes (see reviews Fan, 2009; Charbonneau, 2010). One approach to study how loops may emerge is to insert a compact magnetic field structure into a spherical domain and track its buoyant rise (e.g., Caligari et al., 1995; Fan, 2008; Jouve & Brun, 2009; Weber et al., 2011). Another approach uses local planar models with mechanical forcing to generate large-scale shear that drives dynamo action and creates buoyant magnetic loops (e.g., Cline et al., 2003; Vasil & Brummell, 2009; Guerrero & Käpylä, 2011). Planar models have also been used to study 3-D buoyancy instabilities in a magnetized layer that can lead to rising elements (e.g., Kersalé et al., 2007). The third approach uses global convective MHD models.

These incorporate the rotating spherical-shell geometry needed to self-consistently generate differential rotation and meridional circulation through Reynolds stresses (see review Miesch, 2005). Such models have captured the formation of magnetic structures and cycles in solar (Ghizaru et al., 2010; Racine et al., 2011) and rapidly-rotating sun-like stellar models (Brown et al., 2010, 2011), yielding differential rotation, dynamo action, and large-scale magnetic fields, but not buoyant magnetic loops that rise toward the top of the convective layer.

Here we report on a global convective dynamo simulation of a sun-like star rotating at three times the mean solar angular velocity ($3\Omega_\odot$), such as our Sun did when it was younger and as do many solar analogues (Petit et al., 2008). This simulation (i) attains a differential rotation profile created by the interplay of convection, rotation and stratification (e.g., Brun & Toomre, 2002; Miesch & Toomre, 2009), (ii) forms global-scale toroidal magnetic structures that undergo cycles of magnetic activity and reversals of global polarity, and (iii) achieves buoyant magnetic loops from the strongest portions of the toroidal structures which rise from the base of the convection zone. This work extends the work of Brown et al. (2010, 2011) in which simulations of rapidly-rotating suns with moderate levels of diffusion were able to accomplish (i) and (ii). The formation of buoyant loops is facilitated in our current work by adopting a dynamic Smagorinsky subgrid-scale model (Germano et al., 1991), which serves to minimize the diffusion of well-resolved structures.

4.3 Simulation Parameters and Properties

We have conducted 3-D MHD simulations of turbulent convection and dynamo action in a spherical shell spanning the bulk of the convection zone from $0.72R_\odot$ to $0.97R_\odot$ involving a density contrast of 25, and rotating at $3\Omega_\odot$ (1240 nHz, once every 9.3 days). We use the anelastic spherical harmonic (ASH) code (e.g., Brun et al., 2004). The anelastic treatment lets us follow the subsonic flows in the deep convection zone. Within this nearly adiabatically stratified region, we expect that magnetic buoyancy instabilities captured by our anelastic

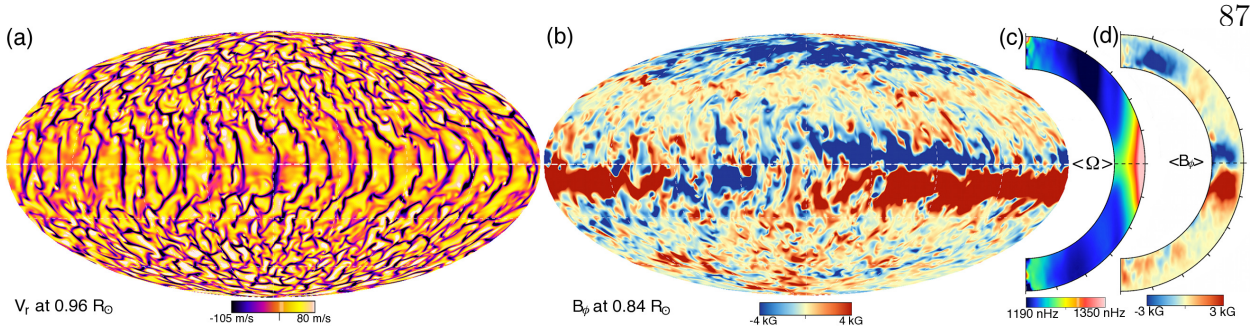

Figure 4.1: Snapshots of flows and fields in case S3 when a buoyant loop begins to rise at time t_b. (a) Radial velocity v_r in global Mollweide projection (equator is dashed) near the top of the computational domain, showing fast, narrow downflows (dark tones) and broad, slower upflows (light tones). (b) Companion view of toroidal magnetic field B_ϕ at mid-convection zone. Effects of turbulent convection contribute to the ragged nature of the wreaths. Several buoyant magnetic loops (see Figure 4.3) are generated in the negative-polarity wreath segment just above the equator and right of image center. (c) Time and zonal average of rotation profile $\langle\Omega\rangle$, possessing an equatorial region with fast rotation and slower rotation at higher latitudes. (d) Longitudinally-averaged toroidal magnetic field $\langle B_\phi\rangle$ revealing a prominent axisymmetric field component.

treatment differ from fully compressible treatments by no more than a few percent in either growth rate or scale (Berkoff et al., 2010). ASH is a large-eddy simulation (LES) code that resolves the largest scales of motion and uses a subgrid-scale (SGS) model to parameterize the effects of unresolved, small-scale turbulence. The dynamo simulations of Brown et al. (2010) and Brown et al. (2011) used a SGS model where the turbulent magnetic diffusivity η_t was constant on spherical shells and in time, and varied only slowly with depth as the inverse square-root of the background density. Brown et al. (2010) examined a simulation (case D3, at $3\Omega_\odot$) which exhibited persistent toroidal magnetic structures, whereas Brown et al. (2011) studied a simulation that achieved cycles of magnetic activity and global polarity reversals (case D5, at $5\Omega_\odot$). These simulations had $\eta_t = 2.64 \times 10^{12}$ and $1.88 \times 10^{12}\,\mathrm{cm^2\,s^{-1}}$ respectively at mid-convection zone.

Here we consider a new ASH simulation, case S3, which achieves much lower levels of diffusion through the use of a dynamic Smagorinksy (DSMAG) SGS model. This assumes self-similar behavior in the resolved portion of the inertial range of scales in a turbulent flow

in order to extrapolate the effects of unresolved small-scale motions on the resolved scales. The resulting viscosity ν_S is determined by the properties of the grid and the flows, and varies by orders of magnitude in all three spatial dimensions and in time. To determine the thermal and magnetic diffusion coefficients we assume constant thermal and magnetic Prandtl numbers. In cases D3, D5 and S3 these are set to 0.25 and 0.5 respectively. We reserve further discussion of the properties of ASH simulations using the DSMAG SGS model for Chapters 7 and 8. In case S3 the DSMAG SGS model allows a simulation (with 1024 longitudinal, 512 latitudinal, and 193 radial grid points) to achieve a mean magnetic diffusion coefficient at mid-convection zone of $\bar{\eta}_t = 4.8 \times 10^{10}\,\mathrm{cm^2\,s^{-1}}$. This reduction in diffusion by a factor of about 40 from case D3 is critical for the formation and coherent rise of buoyant magnetic loops.

Case S3 exhibits turbulent convective patterns shown in Figure 4.1(a) which are largely vortical at high latitudes and aligned with the rotation axis near the equator. The convection builds and maintains a strong differential rotation that is prograde at the equator and retrograde at mid to high latitudes (Figure 4.1(c)). This organized shear drives the creation of toroidal magnetic structures at low latitudes in each hemisphere, as demonstrated in B10. Here the increased level of turbulence enhances the power in smaller-scale components of the toroidal field B_ϕ (Figure 4.1(b)) while still retaining a substantial zonally-averaged toroidal field $\langle B_\phi \rangle$ (Figure 4.1(d)).

In addition to creating strong magnetic structures near the base of the convective region, case S3 also undergoes cycles of magnetic activity and reversals of global magnetic polarity similar to those described in case D5 in B11. This is consistent with results from parameter surveys with ASH simulations, which indicate that decreasing both ν and Ω can yield cyclic behavior seen at $5\Omega_\odot$ at lower rotation rates (Brown et al., 2011). Because of the large computational cost of the DSMAG SGS model, case S3 was started using a less diffusive descendant of case D3 in B10, which we label case D3b, as initial conditions (Nelson et al., 2011a). Figure 4.2(a) shows the temporal evolution of the hemispherical

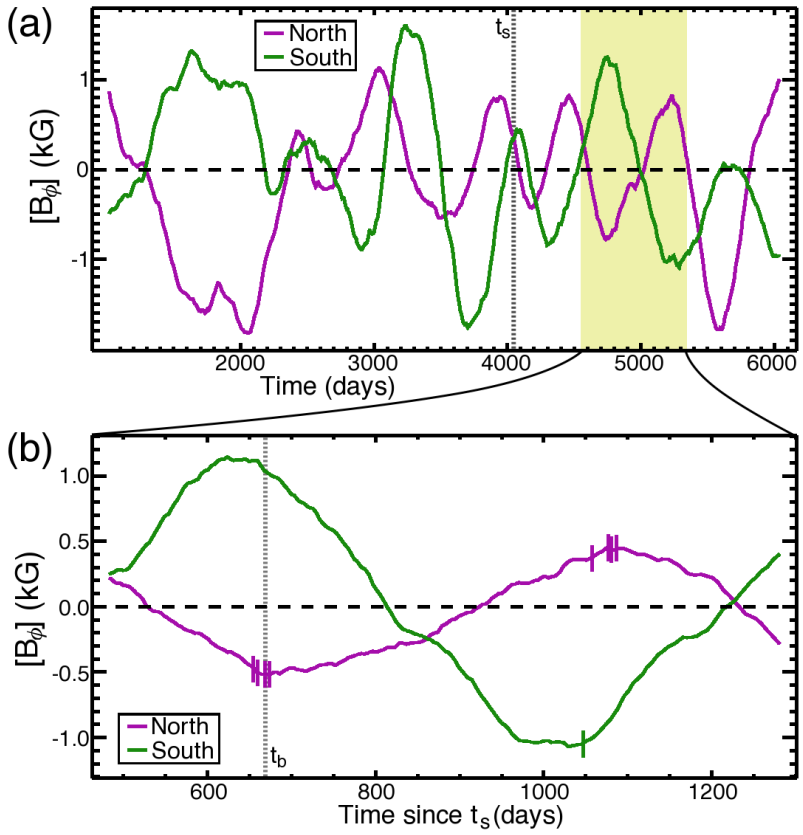

Figure 4.2: Field reversals with time. (a) Hemispherical volume-averaged toroidal magnetic field $[B_\phi]$ of progenitor case D3b over nearly 6000 days, displaying irregular magnetic activity cycles. Case S3 branched from case D3b at time t_s (dotted line). (b) $[B_\phi]$ for case S3 over about 800 days. Case S3 continues the cyclic behavior of D3b, but additionally produces buoyant loops. The creation of loops which pass $0.90R_\odot$ are indicated by tick marks in the lower panel. Detailed information on the buoyant loop at time $t_b = t_s + 683$ days (dotted line) is shown in Figures 4.1 and 4.3.

volume-average of toroidal magnetic field, $[B_\phi]$, in the progenitor case over approximately 5000 days, demonstrating the irregular cycles this model yields. Case S3 continues this behavior over about 1300 simulated days starting from time t_s. The temporal evolution of $[B_\phi]$ in case S3 is shown in Figure 4.2(b), revealing two reversals of global magnetic polarity.

Some caution should be used in interpreting any LES dynamo simulation, given the potential sensitivity of dynamo action to magnetic dissipation and the nonlinear, nonlocal nature of turbulent magnetic induction, which makes reliable SGS modeling difficult. How-

ever, we believe the essential large-scale dynamics exhibited in this simulation are robust and are largely insensitive to the SGS model. Indeed convective dynamo simulations with differing prescriptions for SGS diffusion exhibit similar large-scale magnetic structures (Brown et al., 2010, 2011; Ghizaru et al., 2010; Racine et al., 2011).

Here we will discuss buoyant magnetic structures which coherently rise above $0.90R_\odot$ while remaining connected to the large-scale toroidal wreaths. Using these criteria, we have identified nine buoyant magnetic loops, indicated by hash marks in Figure 4.2(b). Eight loops are seen in the northern hemisphere and one in the southern hemisphere. We expect that the apparent asymmetry is simply the result of having studied only two magnetic cycles.

4.4 Buoyant Magnetic Loops

Buoyant magnetic loops arise from the cores of toroidal magnetic wreaths near the base of the simulated domain. These wreaths have significant $\langle B_\phi \rangle$ components that peak around 5 kG while also having strong non-axisymmetric fields. Figure 4.1(b) shows a typical B_ϕ configuration involving a negative polarity wreath in the northern hemisphere spanning 95° in longitude and a positive polarity wreath in the southern hemisphere extending over 270° in longitude. As demonstrated in cases D3 (B10) and D5 (B11), these magnetic wreaths are highly nonuniform and display significant internal variation as well as a high degree of connectivity with the rest of the domain. In case S3 portions of the wreaths can have coherent cores in which B_ϕ can regularly exceed 25 kG and have peak values as high as 54 kG. In these cores, bundles of magnetic field lines show very little local connectivity with the rest of the domain or even the other portions of the wreath. A single wreath of a given polarity may not form a coherent core at all or may have more than one core, and a single core may produce multiple buoyant loops. Of the nine buoyant loops investigated here to rise past $0.90R_\odot$, one coherent core produces four buoyant loops, another produces three, and two more cores each yield a single buoyant loop.

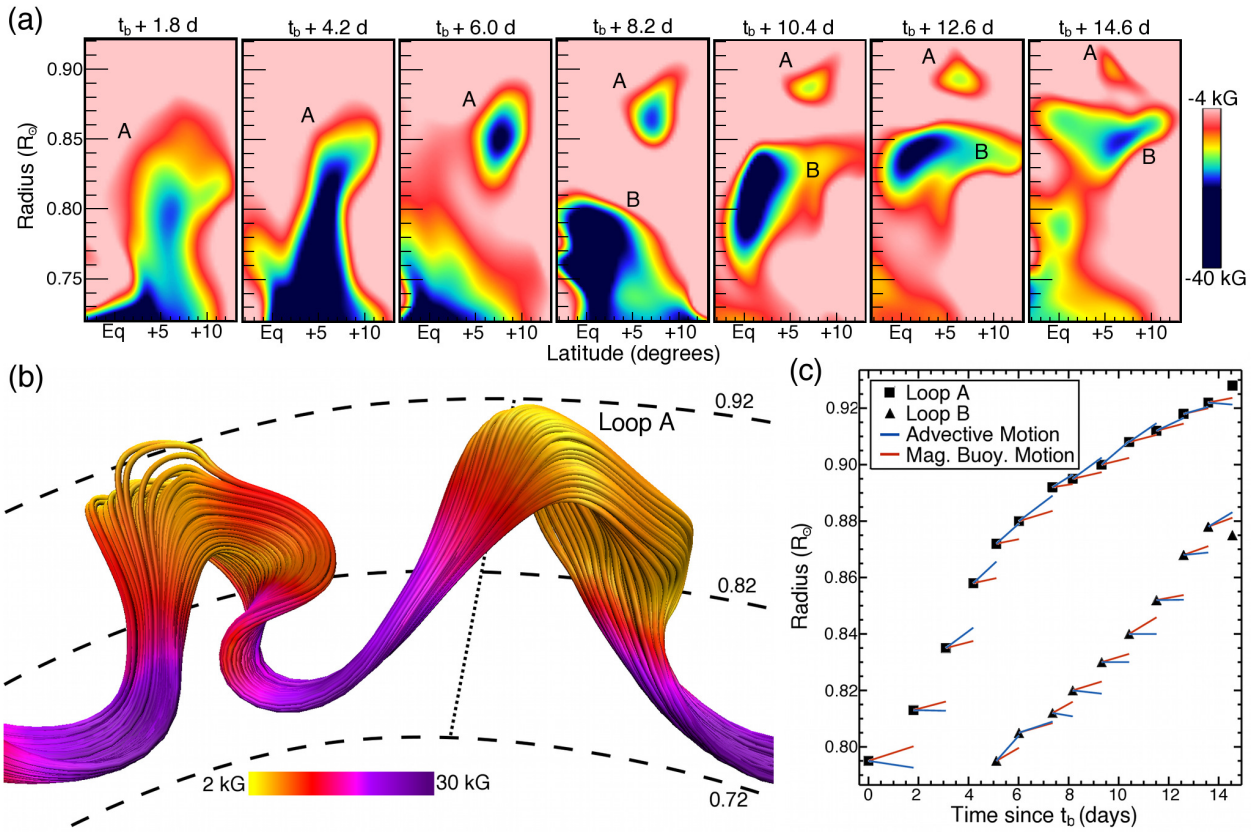

Figure 4.3: Analyzing a rising loop. (a) 2-D cuts in longitude at successive times (tracking in longitude at the local rotation rate of the loop) showing toroidal magnetic field over radius and latitude. The rising magnetic loop A is seen in cross-section starting at $0.81R_\odot$ at $t = t_b$ and rising to $0.91R_\odot$ after roughly 15 days. Proto-loop B is also seen rising starting at 8.6 days, but the top of loop B never rises above $0.88R_\odot$. (b) 3-D visualization of magnetic field lines in the core of a wreath which produces four loops (two shown here, one of which is loop A) at $t_b + 14.6$ days. Perspective is looking down along the rotation axis toward the equatorial plane. Coloring indicates field magnitude. Dashed lines indicate radial position. Dotted line shows the cutting plane used in the left-most panel above. (c) Radial location of the top of a buoyant loop as a function of time since t_b, along with movement attributable to magnetic buoyancy (red lines) or to advection by convective upflows (blue lines).

Some of the coherent wreath cores can become buoyant magnetic loop progenitors or proto-loops. In these proto-loops the strong Lorentz forces result in highly suppressed convective motions. If we examine extended regions in the cores of wreaths with a local ratio of magnetic to kinetic energy above a fiducial value of 100, we identify at least 35 proto-loops at the times where the nine buoyant loops arise. Thus the large majority of proto-loops do not

evolve into mature buoyant loops, generally due to unfavorable interactions with convective flows. When magnetic field strengths exceed 35 kG the proto-loops become significantly underdense as magnetic pressure displaces fluid, causing buoyant acceleration. With some rise a proto-loop can enter a region of less suppressed giant cell convection. These flows will advect portions of the proto-loop downward at cell edges and upward in the core of the giant cells. The rise of the top of a magnetic loop is shown in cross-section by sampling B_ϕ roughly every 2 days in Figure 4.3(a). Not all proto-loops become buoyant loops by our criteria. For example, loop B in Figures 4.3(a,c) begins to rise but is prevented from passing 0.88 $R_\odot$ when the top of the loop encounters a strong downflow.

One way to track these buoyant loops is to use 3-D tracings of magnetic field lines using the VAPOR software package (Clyne et al., 2007). In our simulations with finite resistivity, individual field lines do not maintain their identity in time. However, one can achieve some measure of consistency as the structure moves and evolves by tracking field line ensembles. We track the very strong fields at the bottom of the loops near the base of the domain and we randomly seed large numbers of field lines (here 1000) in those highly magnetized footpoints at each time step. Figure 4.3(b) shows a 3-D rendering of magnetic fields lines for two sample loops near the peak of their rise. Similar field line tracings have been studied at various times during the rise of these loops.

At maximum rise, the sample magnetic loop A extends from $0.73R_\odot$ to $0.93R_\odot$. The magnetic fields exceed 40 kG at the base of the loop but become much weaker near the top of the loop, with field strengths as low as 2 kG. Such loops are embedded in the much larger wreaths which have an average cross-sectional area of 13800 Mm^2. The cross-sectional area of loop A is 120 Mm^2 at $0.795R_\odot$ and 520 Mm^2 at its peak radial position of $0.923R_\odot$. Accounting for the continued expansion that would likely occur if this loop were able to rise further, the cross-sectional area is reasonable compared with the typical area of a large sunspot at the solar surface, which is roughly 2500 Mm^2 Zwaan (1987). If the loop were rising adiabatically over the same interval, the cross-sectional area should change in inverse

proportion to the change in background pressure, which decreases here by a factor of 17.1, rather than the observed expansion by a factor of 4.3. The top of the loop must then have a net outflow of heat or material in order to avoid expanding adiabatically. The loops show a measurable deficit in density and thermodynamic pressure relative to their surroundings, but they do not possess any detectable signature in temperature or entropy. This indicates that they are thermally "leaky" and able to equilibrate quickly compared to the timescale for radial motion. A simple estimate of the thermal diffusion time across one of these structures at mid-convection zone is on the order of 50 days, implying that there is likely also a divergent flow at the top of the loop, moving fluid along field lines. We see some evidence for such flows with roughly $1\,\mathrm{m\,s^{-1}}$ speeds.

Once a loop has begun to rise, its radial motion is dominated by advection and magnetic buoyancy. Figure 4.3(c) illustrates the motion of loop A which begins to rise buoyantly at t_b, while also indicating the components of the motion due to advection and magnetic buoyancy. To compare motion due to magnetic buoyancy, we define a magnetic buoyancy velocity v_{mb} at the times sampled in Figure 4.3(c). Magnetic buoyancy acceleration is here the fractional density deficit in the loop compared to the average density of the surrounding fluid times the local gravitational acceleration. For a magnetic structure in local thermal equilibrium, this reduces to the ratio of magnetic pressure inside the loop to thermodynamic pressure in the surrounding fluid times gravitational acceleration. To compute v_{mb} we integrate the magnetic buoyancy acceleration over the intervals between times plotted in Figure 4.3(c) (roughly 2 days), which likely provides a lower bound on this velocity. The advective velocity v_{ad} is the volume-averaged velocity of the surrounding fluid. The pressure and velocity of the surrounding fluid are calculated by taking averages over the convective updraft while excluding regions with field magnitude greater than 4 kG. Initially the sample proto-loop experiences an upward $v_{\mathrm{mb}} = 46.1\,\mathrm{m\,s^{-1}}$. After 3 days of movement dominated by magnetic buoyancy, the loop gets caught in a convective updraft and v_{ad} becomes greater than v_{mb}. Even though advective motions dominate, magnetic buoyancy continues to drive

an average upward motion at $32.3\,\mathrm{m\,s^{-1}}$ relative to the surrounding fluid. Continued buoyant acceleration of the loop as the magnetic pressure weakens is achieved because its density perturbation decreases at roughly the same rate as does the background density stratification. Once the top of the loop has entered the main convective upflow it experiences advection at an average velocity of $53.1\,\mathrm{m\,s^{-1}}$. The presence of magnetic buoyancy forces allow this loop to rise in 14.6 days while the average upflow traverses the same distance in 21.7 days and magnetic buoyancy alone would require 30.6 days.

Additional accelerations are present but not shown, including thermal buoyancy, which is significant early in the rise of the loop, and magnetic tension, which is of the same order of magnitude as the advective motion near maximum radial extent at 14.6 days and helps tether the loop to that height. Thermal buoyancy is distinguished from magnetic buoyancy by averaging over the convective updraft but excluding regions with magnetic fields above 4 kG. An additional apparent motion at early times is produced as toroidal magnetic field used to track the loop is converted to radial magnetic field in the sides of the loop. Because advection plays a crucial role in the transport of these magnetic loops, their size scale is set by the size of the convective giant cells. The nine loops studied here have an average extent of 15.4° in longitude when measuring across the bottom of the loop, whereas the average distance between convective downflows in the equatorial region is 16.4° in longitude.

4.5 Reflections

In this chapter we have presented a 3-D MHD simulation that combines turbulent convection, rotation, and stratification to produce solar-like differential rotation and wreaths of large-scale toroidal magnetic field at the base of the convection zone. These undergo cycles of magnetic activity and reversals of global magnetic polarity. Most notably the wreaths also exhibit buoyant magnetic loops capable of coherently traversing much of the convective layer. Such loops can only be realized when the field amplitude in a portion of a wreath exceeds

35 kG, the diffusion timescale across the proto-loop (here 50 days) is much longer than the timescale for rise due to magnetic buoyancy, and the interactions between rising loops and convective flows are favorable. These buoyant loops which appear at cycle maximum can have toroidal field strengths of 45 kG at their base and 5 kG at their top. Their size scales are set by the size of the convective giant cells and they have cross-sectional areas at $0.90 R_\odot$ that are reasonable compared to the area of a large sunspot.

We must be cautious in suggesting that these rising magnetic loops can make it through to the surface of the star. Our global simulations here only extend to $0.97 R_\odot$ and currently place an impenetrable boundary there, for we cannot cope with the intense small scales of convection seen as supergranulation and granulation near the surface. The presence of the domain boundary deflects all flows, leading to some uncertainty about the fate of the rising loops that could only be resolved by linking flows and magnetism in the upper reaches of ASH to another high-resolution compressible domain closer to the surface. This is a task we are now pursuing in parallel with global modeling.

It is noteworthy that within this simulation convection generates differential rotation which in turn generates toroidal flux which then buoyantly destabilizes and rises. Each link in this chain is physically well established. Our primary accomplishment here is to capture all these processes self-consistently within a single simulation. This represents an essential step toward unifying numerical models of global-scale convective dynamos and surface flux emergence.

Chapter 5

Magnetic Wreaths

Having discussed the discovery of buoyant magnetic loops in a convective dynamo simulation at $3\Omega_\odot$, we now turn to a more systematic survey of dynamo action at the same rotation rate with varying levels of explicit diffusion. We study the large-scale magnetic fields which can be achieved at various levels of turbulence. In Chapter 6 we will further examine the temporal variability of these large-scale magnetic fields and the possibility of cyclic reversals in global magnetic polarity.

This chapter is the first of two based on the work published in Nelson et al. (2013b) [1] and is largely quoted from that publication. I was the primary author of that paper. I ran most of the simulations presented here and conducted all of the analysis. Notably Benjamin Brown ran cases D3, D3-pm1, and D3-pm2. My co-authors provided essential contributions in formulating the simulations and the analysis, and in providing significant guidance in the writing process.

5.1 Overview

Solar-type stars exhibit a rich variety of magnetic activity. Seeking to explore the convective origins of this activity, we have carried out a series of global 3D magnetohydrodynamic (MHD) simulations with the anelastic spherical harmonic (ASH) code. Here we

[1] Nelson, N. J., Brown, B. P., Brun, A. S., Miesch, M. S., & Toomre, J. 2013a, Magnetic Wreaths and Cycles in Convective Dynamos, ApJ, 762, 73

report on the dynamo mechanisms achieved as the effects of artificial diffusion are systematically decreased. The simulations are carried out at a nominal rotation rate of three times the solar value ($3\Omega_\odot$), but similar dynamics may also apply to the Sun. Our previous simulations demonstrated that convective dynamos can build persistent toroidal flux structures (magnetic wreaths) in the midst of a turbulent convection zone and that high rotation rates promote the cyclic reversal of these wreaths. Here we demonstrate that magnetic cycles can also be achieved by reducing the diffusion, thus increasing the Reynolds and magnetic Reynolds numbers. In these more turbulent models, diffusive processes no longer play a significant role in the key dynamical balances that establish and maintain the differential rotation and magnetic wreaths. Magnetic reversals are attributed to an imbalance in the poloidal magnetic induction by convective motions that is stabilized at higher diffusion levels. Additionally, the enhanced levels of turbulence lead to greater intermittency in the toroidal magnetic wreaths, promoting the generation of buoyant magnetic loops that rise from the deep interior to the upper regions of our simulated domain. The implications of such turbulence-induced magnetic buoyancy for solar and stellar flux emergence are also discussed.

5.2 Dynamos at $3\Omega_\odot$

We study convection and dynamo action in the deep interior of solar-like stars using the anelastic spherical harmonic (ASH) code (Clune et al., 1999; Brun et al., 2004). Our simulation approach is briefly described here, but is more fully explained in Brown et al. (2010). ASH solves the anelastic MHD equations in a rotating spherical shell with a background stratification taken from a 1D model of solar structure. We focus on simulating the bulk of the solar convection zone from $0.72R_\odot$ to $0.97R_\odot$ ($R_\odot$ is solar radius) with a density contrast of about 25. We do not model the near-surface layers of the sun, for we are limited by the anelastic approximation to subsonic flows. Additionally we cannot resolve the small-scales of motion needed to simulate granular and supergranular scales. We also do not include the

stably-stratified radiative zone or the tachocline in these simulations, although simulations including those components are an active area of research (see Brun et al., 2011). We have done some preliminary work in adding a tachocline to these simulations and found that it does not drastically change the dynamo action in the bulk of the convective layer. The effects of a tachocline will will explored further in a future paper. Our results tend to support the recent studies with mean-field dynamo models, which suggests that the differential rotation of the convection zone may play a greater role in the generation of toroidal magnetic field than the tachocline (e.g., Dikpati & Gilman, 2006; Muñoz Jaramillo et al., 2009). We use impenetrable and stress-free boundary conditions on both the top and bottom of the domain. We impose the entropy gradient at the top and bottom of the domain for the thermal boundary conditions. For the magnetic fields we use a perfect conductor condition on the bottom boundary and match to an external potential field on the top boundary. These conditions and our evolution equations are described in detail in Brown et al. (2010).

ASH is a large-eddy simulation which employs a subgrid-scale model to account for the effects of unresolved scales of motion. The standard subgrid-scale (SGS) model in ASH simulations uses enhanced values of viscosity, thermal diffusivity, and magnetic resistivity relative to those expected from atomic values in order to represent additional mixing due to unresolved turbulent motions. In this enhanced eddy SGS model, viscosity ν, thermal diffusivity κ, and magnetic resistivity η all scale as $\bar{\rho}^{-1/2}$, where $\bar{\rho}$ is the spherically-symmetric background density of the simulation. This prescription, along with constant Prandtl and magnetic Prandtl numbers throughout the domain, follows that of Brown et al. (2010, 2011). All cases presented in this paper use $\mathrm{Pr} = \nu/\kappa = 0.25$, but variable Pm (see Table 5.1).

Table 5.1: Dynamo simulations at three times the solar rotation rate. All simulations have inner radius $r_{\rm bot} = 5.0 \times 10^{10}$cm and outer radius of $r_{\rm top} = 6.72 \times 10^{10}$cm, with $L = (r_{\rm top} - r_{\rm bot}) = 1.72 \times 10^{10}$cm the thickness of the spherical shell. Evaluated at mid-depth are the Rayleigh number $\mathrm{Ra} = (-\partial\rho/\partial S)(\mathrm{d}\bar{S}/\mathrm{d}r)gL^4/\rho\nu\kappa$, the Taylor number $\mathrm{Ta} = 4\Omega_0^2 L^4/\nu^2$, the rms Reynolds number $\mathrm{Re} = v_{\rm rms}L/\nu$ and fluctuating Reynolds number $\mathrm{Re}' = v'_{\rm rms}L/\nu$, the magnetic Reynolds number $\mathrm{Rm} = v_{\rm rms}L/\eta$ and fluctuating magnetic Reynolds number $\mathrm{Rm}' = v'_{\rm rms}L/\eta$, the Rossby number $\mathrm{Ro} = \omega/2\Omega_0$, and the convective Rossby number $\mathrm{Roc} = (\mathrm{Ra}/\mathrm{Ta}\,\mathrm{Pr})^{1/2}$. Here the fluctuating velocity v' has the axisymmetric component removed: $v' = v - \langle v \rangle$, with angle brackets denoting an average in longitude. For all simulations, the Prandtl number $\mathrm{Pr} = \nu/\kappa$ is 0.25 and the magnetic Prandtl number $\mathrm{Pm} = \nu/\eta$ ranges between 0.5 and 4. The viscous and magnetic diffusivity, ν and η, are quoted at mid-depth (in units of 10^{11} cm^2 s^{-1}). The total evolution time T_E for each simulation is given in years. The values for case S3 with the dynamic Smagorinsky SGS model utilize the mean viscosity at mid-convection zone averaged on horizontal surfaces as well as in time. For case S3 using the dynamic Smagorinsky SGS model, the values quoted are based on the time-averaged rms viscosity, conductivity, and resistivity at mid-depth, noting that these diffusion coefficients have near hundred-fold spatial variations.

Case	N_r, N_θ, N_ϕ	Ra	Ta	Re	Re′	Rm	Rm′	Ro	Roc	ν	η	Pm	T_E
D3	$97 \times 256 \times 512$	$3.28{\times}10^5$	$1.22{\times}10^7$	173	104	86	52	0.374	0.315	13.2	26.4	0.5	61.6
D3a	$97 \times 256 \times 512$	$5.84{\times}10^5$	$2.41{\times}10^7$	244	154	122	77	0.447	0.295	9.40	18.8	0.5	67.1
D3b	$145 \times 512 \times 1024$	$1.11{\times}10^6$	$6.08{\times}10^7$	343	273	171	136	0.566	0.257	5.92	11.8	0.5	16.9
D3-pm1	$145 \times 256 \times 512$	$2.98{\times}10^5$	$1.22{\times}10^7$	149	102	149	102	0.372	0.300	13.2	13.2	1	18.8
D3-pm2	$145 \times 512 \times 1024$	$3.08{\times}10^5$	$1.22{\times}10^7$	145	101	291	202	0.370	0.306	13.2	6.60	2	13.6
S3	$145 \times 512 \times 1024$	7.68×10^8	4.46×10^{10}	8050	5750	4030	2880	0.581	0.262	0.218	0.435	0.5	4.01

In addition, we have also implemented a more complex SGS treatment, the dynamic Smagorinsky model developed by Germano et al. (1991). By using the dynamic Smagorinsky model in ASH simulations we are able to reduce the mean diffusion at mid-convection zone by a factor of 50 without an increase in resolution. Our implementation of the dynamic Smagorinsky model is summarized in Appendix A. This SGS treatment is only used in case S3, which was first presented in Nelson et al. (2011b).

Table 5.1 presents the computational resolution, relevant non-dimensional parameters, diffusion coefficients, and total evolution time for each of the six cases we will discuss here. We have explored two main branches in parameter space. The first branch includes cases D3, D3a, and D3b, where viscosity ν, thermal diffusivity κ, and magnetic resistivity η have all been dropped together, thus keeping a constant magnetic Prandtl number. The second branch includes cases D3, D3-pm1, and D3-pm2, where ν and κ are held constant and only η is decreased, resulting in increasing magnetic Prandtl numbers. We will refer to the two branches as the constant Pm and increasing Pm branches, respectively. The constant Pm branch was found to be more compelling, as cases D3a and D3b generally produced strong magnetic wreaths that were anti-symmetric about the equator, whereas the high Pm branch produced a wider variety of symmetric and anti-symmetric toroidal field states and was therefore less amenable to study. Such behavior is not unexpected as dynamos with higher magnetic Prandtl number tend to promote small-scale dynamo action. We will generally focus on the constant Pm branch of simulations while referencing the increasing Pm branch to provide additional insight.

Case D3 was initiated from a well developed hydrodynamical simulation that was seeded with a small random magnetic field. Each subsequent case along both branches was started from the preceding case. Thus both cases D3a and D3-pm1 were started using case D3 as initial conditions, case D3b was started using case D3a, and so on. We have re-started case D3a from a random seed field to verify that it settles into a similar region of solution space as the version continued from case D3 and found no strong differences in the

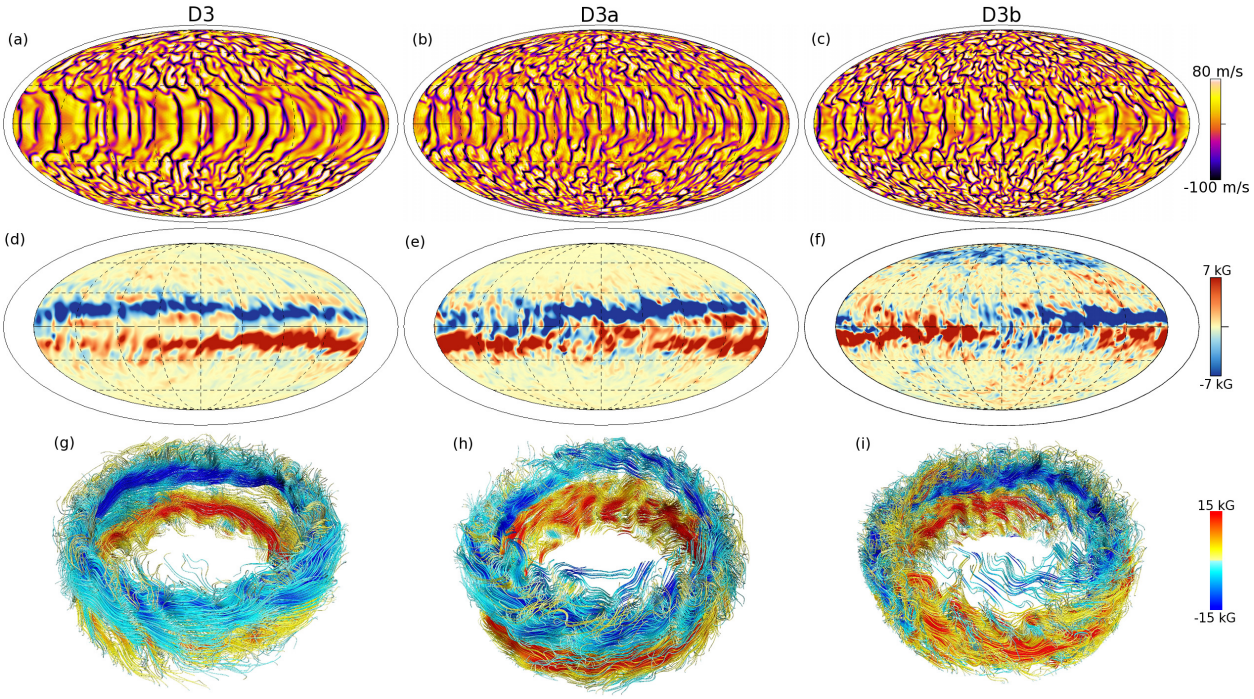

Figure 5.1: Magnetic wreaths. (a)-(c) Shown in global Mollweide view (equator at middle, poles at top and bottom) is the radial velocity of the convection at $0.95R_\odot$ in cases D3, D3a, and D3b, respectively. (d)-(f) Also in Mollweide few, longitudinal magnetic field B_ϕ at mid-convection zone at times t_1 indicated in Figure 6.1. (g)-(i) Shown at the same times for each case is a 3D field line rendering of the magnetic wreaths near the equator. In both types of display for the magnetic field, color gives the polarity and amplitude of the longitudinal field (red positive, blue negative). Times shown correspond to t_1 for each case in Figure 6.1.

time-averaged behavior over several thousand days.

5.3 Magnetic wreaths

The dominant magnetic structures built by each of these simulations are the low latitude bands of predominately toroidal field, which we term wreaths. These wreaths are generally anti-symmetric about the equator, though symmetric states are observed along with states where one hemisphere displays a wreath while the other does not. These irregular states are most common along the increasing Pm branch of our simulations. The wreaths in case D3 are discussed extensively by Brown et al. (2010) and additional wreaths

are analyzed at somewhat faster rotation rate ($5\Omega_\odot$) by Brown et al. (2011).

5.3.1 Magnetic Topology

Figure 5.1 shows snapshots of the turbulent convection and the wreaths for cases D3, D3a, and D3b at mid-convection zone in global Mollweide view as well as at low latitudes in a 3D volume rendering of magnetic field lines colored by B_ϕ. In all three cases strong longitude-averaged fields are present at low latitudes, however the nature of the wreaths change from case D3 where axisymmetric fields dominate to case D3b where a significant axisymmetric field component is present but not dominant. In case D3b the morphology has changed such that the wreaths are confined in longitudinal extent. Figure 5.1 shows a typical field configuration, but the wreaths are observed at various times to extend over as little at 45 degrees and as much as 270 degrees in longitude. All three cases show extensive connectivity between the wreaths and the surrounding domain where magnetic fields are moderate in strength but far less coherent. The wreaths are strongly modulated by the convective flows, producing a ragged appearance that is particularly noticeable in case D3b but present in all three cases. In the more turbulent cases there are also significant small-scale magnetic fields at moderate to high latitudes, and occasional locally-generated wreath-like structures near the poles which persist for less than about 100 days at a time.

Table 5.2: Volume-averaged magnetic and kinetic energies for dynamo simulations at three times the solar rotation rate, as well as the magnitude of the differential rotation contrast in radius at the equator $\Delta\Omega_r$ and the average contrast at the top of the simulated domain between the equator and $\pm 60^\circ$ latitude $\Delta\Omega_\theta$. Shown in units of 10^6 erg cm^{-3} are the total magnetic energy (Total ME), axisymmetric toroidal magnetic energy (TME), axisymmetric poloidal magnetic energy (PME), fluctuating magnetic energy (FME), total kinetic energy (Total KE), differential rotation kinetic energy (DRKE), meridional circulation kinetic energy (MCKE), and fluctuating kinetic energy (FKE). The percentage of the total energy is shown for total magnetic energy (Total ME) and total kinetic energy (Total KE). The percentage of the total magnetic or kinetic energy for each component is shown in parentheses. Values for differential rotation rates are in units of nHz ($3\Omega_\odot = 1240$ nHz). Values are averaged in time over long intervals.

Case	Total ME	TME	PME	FME	Total KE	DRKE	MCKE	FKE	$\Delta\Omega_r$	$\Delta\Omega_\theta$
D3	0.68 (9%)	0.29 (43%)	0.029 (4%)	0.36 (53%)	6.67 (91%)	4.35 (65%)	0.010 (0.1%)	2.31(35%)	112	192
D3a	0.88 (12%)	0.32 (36%)	0.030 (3%)	0.52 (59%)	6.41 (88%)	3.71 (58%)	0.011 (0.2%)	2.68 (42%)	101	163
D3b	0.82 (13%)	0.10 (12%)	0.011 (1%)	0.70 (85%)	5.42 (87%)	2.45 (45%)	0.012 (0.2%)	2.96 (55%)	95	131
D3-pm1	1.04 (18%)	0.26 (25%)	0.033 (3%)	0.75 (72%)	4.87 (82%)	2.63 (54%)	0.010 (0.2%)	2.23 (46%)	87	139
D3-pm2	1.17 (21%)	0.15 (13%)	0.028 (2%)	0.99 (85%)	4.34 (75%)	2.29 (53%)	0.009 (0.2%)	2.04 (47%)	74	121
S3	0.83 (13%)	0.072 (9%)	0.0060 (0.7%)	0.75 (91%)	5.50 (87%)	2.32 (42%)	0.013 (0.2%)	3.17 (58%)	95	133

The shift from structures dominated by axisymmetric fields in case D3 to the patchy wreaths in case D3b is illustrated by the changes in the time- and volume-averaged energy densities shown in Table 5.2. Between cases D3 and D3b there is a roughly 30% increase in the total magnetic energy of the simulation, though the energy in both the axisymmetric toroidal (TME) and poloidal (PME) fields decreases by roughly a factor of three. The doubling of the energy in the non-axisymmetric magnetic fields more than compensates for the decrease in mean fields. When compared with the kinetic energy densities, the changes in the magnetic energies becomes even more striking. Viscous, thermal, and magnetic diffusion in case D3b are all reduced by the same factor relative to case D3. However the total kinetic energy in case D3b dropped by 19%. The non-axisymmetric kinetic energy (FKE) rose only moderately compared to the decrease in differential rotation kinetic energy (DRKE). The high magnetic Prandtl number cases also show a tendency towards larger total and fluctuating magnetic energies, as well as reduced axisymmetric toroidal magnetic energy as the magnetic diffusion is reduced.

It is illustrative to compare cases D3b and D3-pm1, as they have roughly equal levels of magnetic diffusion, with case D3b having comparatively lower levels of viscosity and thermal diffusion. The largest differences are in the axisymmetric magnetic energies which are both about three times greater in case D3-pm1 than in case D3b. This may be due to the more laminar flow in case D3-pm1, which would tend to create fewer sharp gradients in the large-scale magnetic structures and thus lower the effective dissipation in case D3-pm1 compared to case D3b, even though the diffusion coefficients in the induction equation are nearly the same. Case D3-pm1 also show significantly less differential rotation contrast both in radius and latitude compared to case D3b, pointing to the key role of magnetic torques in decreasing differential rotation, which will be discussed further in §5.

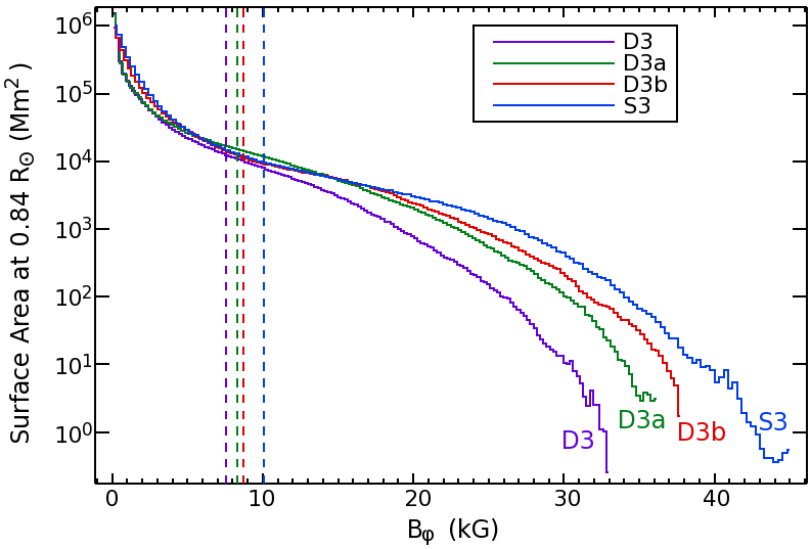

Figure 5.2: Probability distribution functions for unsigned B_ϕ at mid-convection zone for cases D3 (purple), D3a (green), D3b (red), and S3 (blue) showing the surface area covered by fields of a given magnitude. Distributions are averaged over about 300 days when fields are strong and as steady as possible. Dashed vertical lines show the field-strength at which equipartition is achieved with the maximum fluctuating kinetic energy (FKE) at mid-convection zone for each case. Case D3b shows a deficit of field in the 10 kG range, but an excess of surface area covered by extremely strong fields above 25 kG range, as well as higher peak field strengths. Case S3 shows significantly greater regions of fields in excess of 20 kG than all other cases.

5.3.2 Non-axisymmetric Fields

Our discussion of the magnetic wreaths to this point has focused on the axisymmetric fields, which are progressively weaker in moving from case D3 to case D3b. While the axisymmetric fields weaken with increased turbulence, very strong fields become more common when measured by the fraction of the domain they occupy. Figure 5.2 shows the probability distribution function for B_ϕ at mid-convection zone in cases D3, D3a, D3b, and S3. While case D3b has a deficit of fields around 10 kG compared to case D3a, there is a clear excess of fields above 20 kG. Interestingly the distribution for case D3b is greater than that for case D3 for all but the smallest bin, indicating that while case D3 may have stronger axisymmetric fields in the low latitude wreaths, case D3b compensates by having higher amplitude

fluctuating fields throughout the domain. The peak field strength at mid-convection zone is 32 kG in case D3, 36 kG in case D3a, and 38 kG in case D3b. Near the base of the convection zone case D3b exhibits even stronger fields of up to 44 kG. Case S3 posses magnetic fields of up to 45 kG at mid-convection zone and 52 kG near the base of the convective layer. For all four cases fields are seen well in excess of equipartition energies with the maximum fluctuating kinetic energy of the flows. This is a clear indication of turbulent intermittency in the magnetic fields.

A statistical measure of turbulent intermittency is the time-averaged excess kurtosis given by

$$\mathrm{kurt}\{B_\phi\} = \frac{\int_{-\infty}^{\infty} \left(B'_\phi - \bar{B}_\phi\right)^4 f\left(B'_\phi\right) dB'_\phi}{\left[\int_{-\infty}^{\infty} \left(B'_\phi - \bar{B}_\phi\right)^2 f\left(B'_\phi\right) dB'_\phi\right]^2} - 3, \tag{5.1}$$

where $f(B'_\phi)$ is the probability distribution function (see Pope, 2000). For reference a Gaussian distribution would have an excess kurtosis of 0. The level of turbulent intermittency is measured by how leptokurtic the distribution is found to be, with large values corresponding to increased intermittency. For case D3 $\mathrm{kurt}\{B_\phi\} = 9.6$, while for case D3a $\mathrm{kurt}\{B_\phi\} = 10.5$, and for case D3b $\mathrm{kurt}\{B_\phi\} = 12.1$. Leptokurtic distributions are likely to experience strong coherent structures, such as the strong regions of coherent toroidal field in these simulations. At even lower levels of diffusion than can be realized with the enhanced eddy SGS model, the strong-field regions become sufficiently buoyant and coherent so as to form buoyant magnetic loops as realized in case S3 (Nelson et al., 2011b), for which $\mathrm{kurt}\{B_\phi\} = 15.6$. Highly leptokurtic distributions like these indicate that extreme events are enhanced relative to a Gaussian distribution, and the trend towards increasing kurtosis as simulations become more turbulent points to turbulent amplification of magnetic fields. As we will discuss further in §7, this provides an alternate pathway to produce regions within the larger wreaths which can be amplified through turbulent intermittency to produce coherent regions of strong magnetic field, which can then become buoyant. We term this the turbulence-enabled magnetic buoyancy paradigm.

5.4 Maintaining Rotational Shear

A crucial component in the construction of magnetic wreaths is the strong latitudinal and radial shear from the differential rotation. The Ω-effect has previously been shown to be the primary production mechanism for the magnetic wreaths in cases D3 and D5 (Brown et al., 2010, 2011), and it plays a key role in these simulations as well. Thus the angular momentum transport required to maintain the differential rotation is an important physical process in these dynamo models. In the hydrodynamic models explored by Brown et al. (2008), angular momentum transport in simulations at $3\Omega_\odot$ was shown to be a balance between Reynolds stress supporting solar-like differential rotation with the meridional circulation and viscous diffusion tending to dissipate gradients in the rotation profile. With the addition of magnetic fields, Maxwell stress and mean magnetic torques can also transport angular momentum, changing the balance supporting the strong differential rotation achieved in the hydrodynamic cases. Even in cases without magnetic cycles such as case D3, Brown et al. (2010) showed that there are significant feedbacks on the differential rotation profile due to variations in the strength of the magnetic fields over time. It is thus useful to examine not only the steady state balance of angular momentum transport over long time averages covering many magnetic cycles, but also to look at the temporal variability of those balances.

In order to explore the transport of angular momentum, let us examine the physical mechanisms which come into play. The balance of specific angular momentum along the rotation axis is determined by taking the product of the cylindrical radius $\lambda = r\sin\theta$ and the longitudinal component of the longitude-averaged momentum equation, which can be expressed as

$$\frac{\partial \mathcal{L}_z}{\partial t} = \nabla \cdot \vec{\mathcal{F}}. \tag{5.2}$$

We decompose the flux vector of mean angular momentum $\vec{\mathcal{F}}$ into radial and latitudinal components following prior convention (Elliott et al., 2000; Brun et al., 2004; Brown et al.,

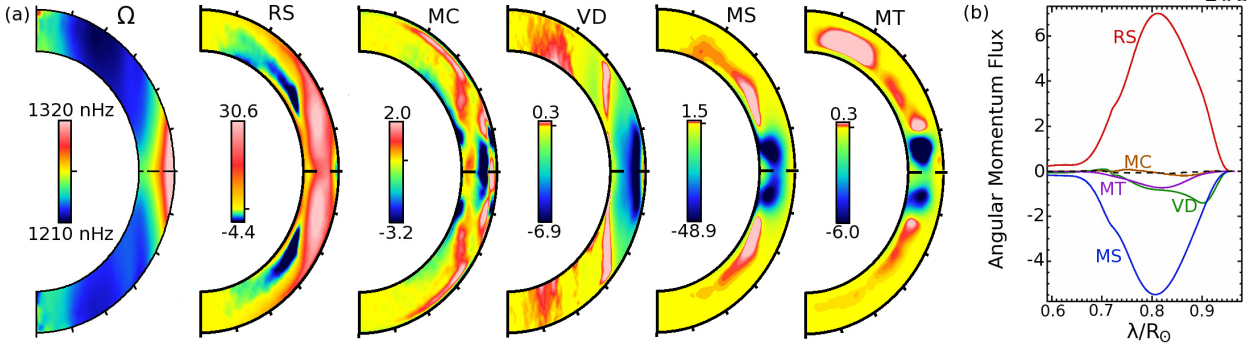

Figure 5.3: Differential rotation and the terms contributing to the accompanying redistribution of angular momentum in case D3b averaged over many magnetic cycles. (a) Angular velocity Ω profile with radius and latitude, accompanied in turn by profiles of specific angular momentum flux in cylindrical radius (λ) by Reynolds stress (RS), meridional circulation (MC), viscous diffusion (VD), Maxwell stress (MS), and mean magnetic torques (MT), respectively. Terms are defined in detail in Equations A.1 and A.2. They are here averaged in time and longitude, and given in units of 10^{15} g s^{-2}. (b) Scalar plot of z-integrated fluxes of angular momentum with cylindrical radius λ in units of 10^{38} g cm^2 s^{-2} . Reynolds stress (RS, red) balance Maxwell stress (MS, blue), with viscous diffusion (VD, green) and magnetic torques (MT, purple) playing less of a role. Contribution from the meridional circulation (MC, brown) are small. The sum of all five terms are also plotted (black dashed line).

2011). We also decompose the flux vector into cylindrical coordinates along cylindrical radius (λ) and along the rotation axis (z), which in many ways is advantageous for displaying these quantities. A detailed description of this decomposition is given in Appendix B. The cylindrical flux of angular momentum is shown for case D3b over a long time average in Figure 5.3. The differential rotation is again clearly maintained by the Reynolds stress (RS), however here the terms opposing the differential rotation have changed compared to similar hydrodynamic cases. In case D3b the Maxwell stress (MS) is the largest term opposing the Reynolds stress with viscous diffusion (VD) and the mean magnetic torques (MT) each playing a small role, while contribution of the meridional circulation (MC) is almost insignificant.

Table 5.3: Total production and dissipation of kinetic energy in the axisymmetric differential rotation profile over the entire simulated volume and averaged in time. Values for energy production rates are in units of 10^{32} erg s^{-1}. Production and dissipation terms are split following Equation (5.3) into contributions from viscous dissipation, Reynolds stress, meridional circulations, Maxwell stress, and mean magnetic torques, respectively. Production terms are defined in Appendix A.

Production and Dissipation of Differential Rotation Kinetic Energy

Case	$L_{\rm RS}$	$L_{\rm MC}$	$L_{\rm VD}$	$L_{\rm MS}$	$L_{\rm MT}$
D3	4.26	-0.020	-2.45	-1.36	-0.68
D3a	3.18	-0.032	-1.11	-1.36	-0.70
D3b	2.59	-0.003	-0.64	-1.94	-0.19
D3-pm1	3.64	-0.014	-1.68	-1.87	-0.35
D3-pm2	3.32	-0.024	-1.61	-1.95	-0.31

We can write the evolution of the total energy of the differential rotation $\mathcal{E}_{\rm DR}$ as

$$\frac{\partial \mathcal{E}_{\rm DR}}{\partial t} = L_{\rm VD} + L_{\rm RS} + L_{\rm MC} + L_{\rm MS} + L_{\rm MT}, \tag{5.3}$$

where the terms on the right-hand side represent the sources and sinks of kinetic energy in the differential rotation due to, respectively, viscous diffusion, Reynolds stress, meridional circulations, Maxwell stress, and mean magnetic torques. Appendix A provides a derivation of Equation (5.3) and an expansion of the sources and sinks.

Using this decomposition, we can examine the balance of production and dissipation of $\mathcal{E}_{\rm DR}$ averaged over long time intervals in each simulation. The balances are represented in Table 5.3 and Figure 5.4. For the increasing Pm branch the Reynolds stress change only slightly while the mean magnetic torques and viscous diffusion are systematically replaced by the Maxwell stress. Similar trends are observed in the constant Pm branch of cases, though here the magnitude of the Reynolds stress and viscous diffusion terms decrease more dramatically. This shift from unresolved dissipation in the form of SGS viscosity to resolved, small-scale torques from the Maxwell stress indicates that the balances which maintain strong

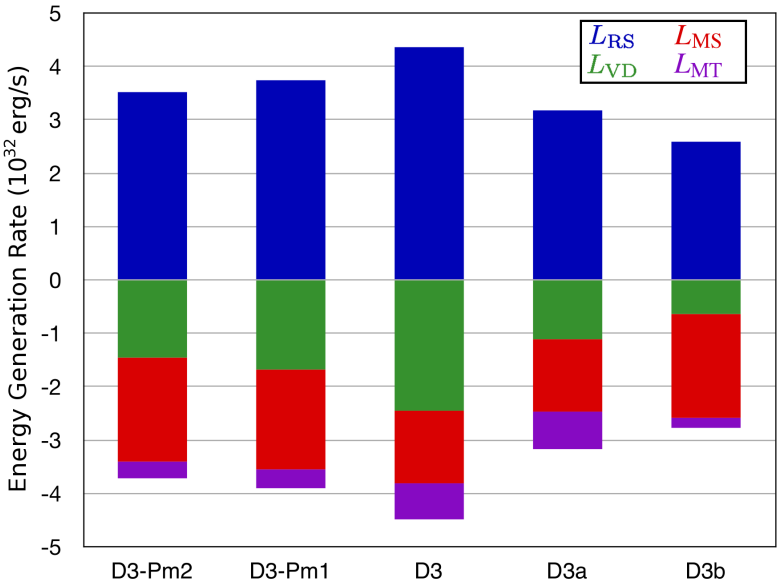

Figure 5.4: Companion to Table 5.3, showing the balance of time-averaged generation terms for the kinetic energy in the differential rotation profiles for each case indicated. In all cases the differential rotation is maintained by a balance between the Reynolds stress and a combination of viscous diffusion and fluctuating and mean magnetic torques. The contribution from meridional circulations are not shown due to their small magnitude.

differential rotation can persist in less diffusive regimes, assuming that magnetic energies remain significantly smaller than kinetic energies.

Turning to the temporal variability in these balances, we find that for case D3b the departures from the values presented in Table 5.3 and Figure 5.4 are about 10% for $L_{\rm MS}$ and $L_{\rm MT}$ when averaged over about 10 days, whereas those in $L_{\rm RS}$, $L_{\rm MC}$ and $L_{\rm VD}$ are about 1%. This leads to decreases in the differential rotation when magnetic fields are strong, such as near the peak of the magnetic activity cycles. Conversely, we observe modest increases in the differential rotation when magnetic fields are weak, such as during reversals of magnetic polarity.

Figure 5.5 shows the differential rotation in case D3b over several magnetic reversals. The differential rotation profile at mid-convection zone in Figure 5.5(a) is persistent, though there are small systematic variations in Ω revealed in Figure 5.5(b) during each magnetic

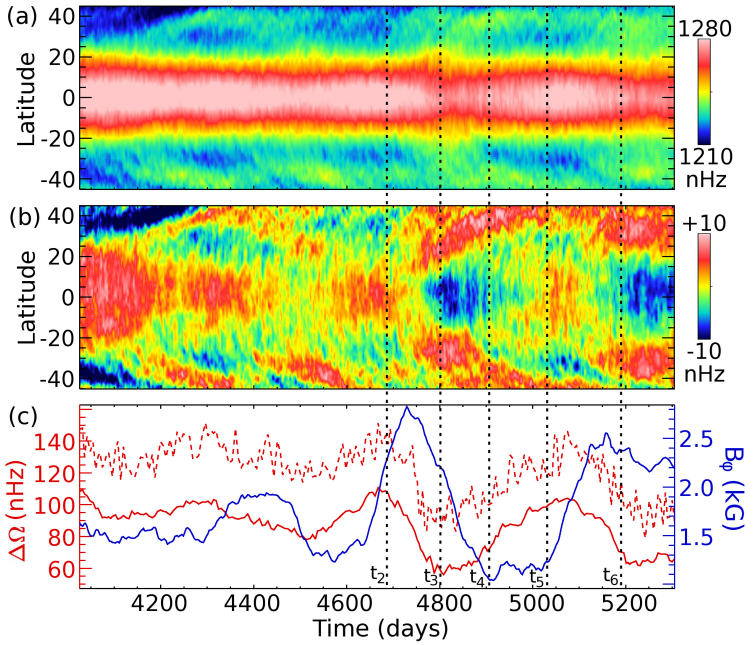

Figure 5.5: Temporal variability of differential rotation in case D3b over the same interval as in Figure 6.9. (a) Longitudinally-averaged rotation rate at mid-convection zone as a function of time and latitude. (b) Temporal variations are accentuated by subtracting the time-averaged Ω at each latitude. Bands of faster rotating fluid move poleward on about the cycle period. (c) Rotation contrasts in radius at the equator Δ_r (red, solid) and in latitude between the equator and $\pm 60^\circ$ in the upper convection zone Δ_θ (red, dashed). The volume-averaged toroidal field strength is also shown (blue, solid), with a phase-lag between peaks in magnetic field strength and decreases in differential rotation. Dotted lines indicate times t_2 through t_6 from Figure 6.2.

cycle. Figure 5.5(c) shows the differential rotation contrast in both radius and latitude over time as well as the volume-averaged toroidal magnetic field strength, indicating that the modest variations in the differential rotation are related to those in the magnetic field.

5.5 Generation of Toroidal Magnetic Energy

The transition from persistent wreaths in case D3 to cyclic wreaths and global polarity reversals in case D3b indicates that by reducing the levels of diffusion in these simulations we have fundamentally altered the balance of terms in the magnetic induction equation. The details of the reversal mechanism are likely to be very subtle in these highly nonlinear

systems. In order to better understand the reversal mechanism, we explore the nature of the balances in the production and dissipation of toroidal and poloidal magnetic fields and provide indications of where and why changes in those balances are occurring, as well as some hints as to the nature of the reversal mechanism.

In Brown et al. (2010) a detailed analysis of the balance of toroidal component of the axisymmetric induction equation was presented. We write the toroidal component of the induction equation as

$$\frac{\partial B_\phi}{\partial t} = \left[\nabla \times \left(\vec{v} \times \vec{B}\right)\right]_\phi - \nabla \times \left(\eta \nabla \times (B_\phi \hat{\phi})\right). \tag{5.4}$$

Using vector identities, the first term on the right-hand side can be written as the sum of shearing terms, advection terms, and a compression term; additionally all of these terms can be decomposed into mean and fluctuating components (for a full derivation, see Appendix A in Brown et al., 2010). That work also showed that the wreaths in case D3 are primarily generated by the Ω-effect and dissipated by a combination of small-scale advection, shear, and diffusion.

Here we perform a similar analysis, but instead of examining the generation of $\langle B_\phi \rangle$, we choose to examine the generation of the volume-integrated energy of the axisymmetric toroidal fields over the entire computational domain $\mathcal{V}$, given by

$$\mathcal{E}_{\rm TME} = \int_{\mathcal{V}} \frac{\langle B_\phi \rangle^2}{8\pi} \, d\mathcal{V}. \tag{5.5}$$

We can construct an evolution equation for $\mathcal{E}_{\rm TME}$ by multiplying Equation (5.4) by $\langle B_\phi \rangle$. The result can be written as

$$\frac{\partial \mathcal{E}_{\rm TME}}{\partial t} = G_{\rm MS} + G_{\rm FS} + G_{\rm MA} + G_{\rm FA} + G_{\rm AC} + G_{\rm RD}, \tag{5.6}$$

where the six terms on the right-hand side represent, from left to right, the shearing of axisymmetric magnetic fields by mean flows associated with the Ω-effect ($G_{\rm MS}$), the average of fluctuating flows shearing fluctuation fields ($G_{\rm FS}$), the advection of mean fields by mean

flows ($G_{\rm MA}$), the average of fluctuating flows advecting fluctuating fields ($G_{\rm FA}$), the anelastic compression of fields ($G_{\rm AC}$), and the resistive diffusion of mean fields ($G_{\rm RD}$). Unlike in previous analyses which looked at the generation of magnetic field vectors, here we are concerned with scalar quantities.

The terms on the right-hand side of Equation (5.6) are computed as

$$G_{\rm MS} = \int_{\mathcal{V}} \langle B_\phi \rangle \left[\left(\langle \vec{B} \rangle \cdot \nabla \right) \langle \vec{v} \rangle \right]_\phi \, d\mathcal{V}, \tag{5.7}$$

$$G_{\rm FS} = \int_{\mathcal{V}} \langle B_\phi \rangle \left[\left\langle \left(\vec{B}' \cdot \nabla \right) \vec{v}' \right\rangle \right]_\phi \, d\mathcal{V}, \tag{5.8}$$

$$G_{\rm MA} = -\int_{\mathcal{V}} \langle B_\phi \rangle \left[\left(\langle \vec{v} \rangle \cdot \nabla \right) \langle \vec{B} \rangle \right]_\phi \, d\mathcal{V}, \tag{5.9}$$

$$G_{\rm FA} = -\int_{\mathcal{V}} \langle B_\phi \rangle \left[\left\langle \left(\vec{v}' \cdot \nabla \right) \vec{B}' \right\rangle \right]_\phi \, d\mathcal{V}, \tag{5.10}$$

$$G_{\rm AC} = \int_{\mathcal{V}} \langle B_\phi \rangle \left\langle v_r B_\phi \frac{\partial \ln \bar{\rho}}{\partial r} \right\rangle \, d\mathcal{V}, \tag{5.11}$$

$$G_{\rm RD} = -\int_{\mathcal{V}} \langle B_\phi \rangle \nabla \times \left(\eta \nabla \times \langle B_\phi \rangle \right) \, d\mathcal{V}. \tag{5.12}$$

For consistency, angle brackets denote longitude averages.

Figure 5.6 shows the temporal evolution of the integrated energy of the axisymmetric toroidal field for cases D3 and D3b and the behavior of the production terms governing the variation of $\mathcal{E}_{\rm TME}$. We have chosen to combine the contributions of the mean shear and advection terms and the fluctuating shear and advection terms for ease of viewing. The mean advection term $G_{\rm MA}$ is generally positive and always much smaller than the mean shear term $G_{\rm MS}$. The fluctuating shear and advection terms are both generally negative, of approximately the same magnitude, and tend to vary in phase with each other.

Let us first look at the average levels of each term plotted in Figure 5.6 to get a sense for the basic balance of terms. The production of $\mathcal{E}_{\rm TME}$ is dominated by the mean shear term which is large and always positive in both case D3 and D3b. The compression term in both cases is roughly an order of magnitude smaller but is again always positive due to the asymmetry in upflows and downflows in compressible convection, which gives

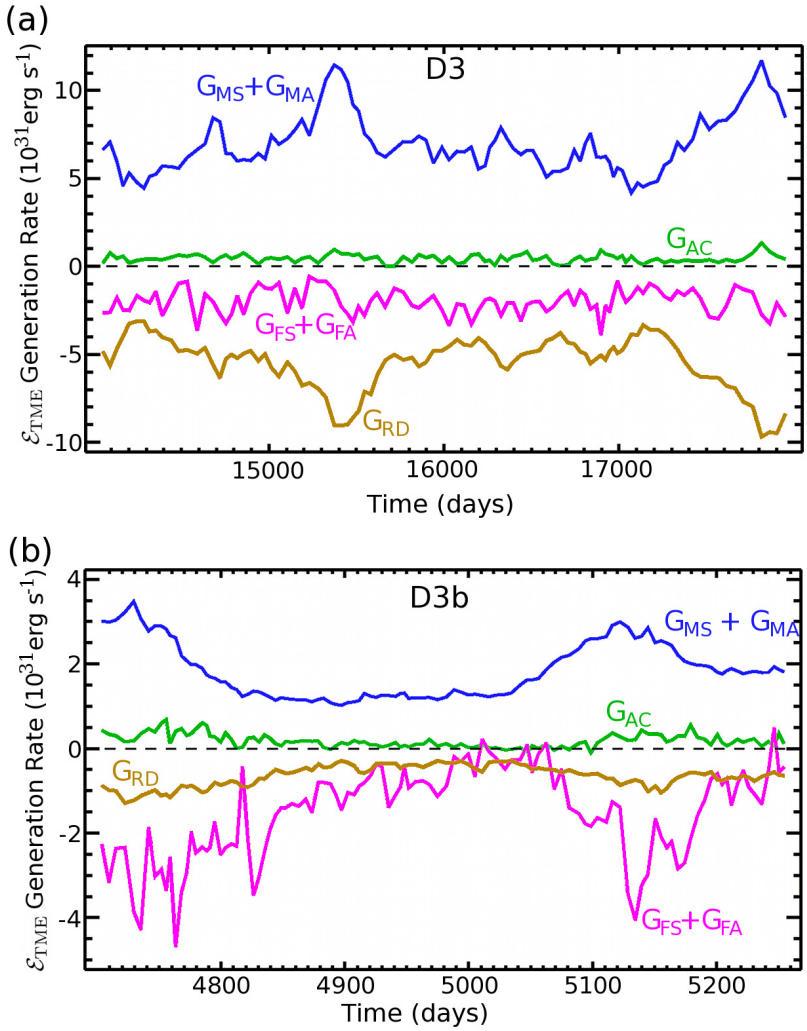

Figure 5.6: Volume-integrated production terms of magnetic energy in the mean toroidal fields from Equation (5.6) for (a) case D3 and (b) case D3b. We have combined the mean shear and mean advection terms (blue line) and the fluctuating shear and fluctuating advection (purple line). In both simulations, energy is produced primarily by the shearing of mean fields by mean flows. Also in both cases compression of fields (green line) plays a very small role. In case D3 diffusion (red line) and the advection and shear of fluctuating flows on fluctuating fields destroy energy, with diffusion generally a factor of 2.5 larger. In case D3b, however, the dissipation of energy by fluctuating advection and shear is 2.2 times greater on average than diffusion. Thus in case D3b resolved turbulence is the primary mechanism for dissipating the magnetic wreaths.

preference to downward pumping of magnetic field causing an increase in magnetic energy due to compression. The production of magnetic energy is opposed by the resistive diffusion,

fluctuating advection, and fluctuating shear terms. In case D3 resistive diffusion is roughly three times larger than the sum of the two fluctuating terms, while in case D3b the roles are reversed and resolved turbulent dissipation does most of the destruction of $\mathcal{E}_{\rm TME}$ while the unresolved turbulent dissipation represented by our explicit resistivity is relegated to a less prominent role. Supporting this transition from unresolved to resolved dissipative processes, in case D3 the sum of the fluctuating terms does not show noticeable changes in behavior when the magnetic energy is high versus when it is low. Instead the response is seen primarily in the resistive dissipation term. In case D3b, however, the fluctuating terms show strong variations in response to changes in the magnetic energy.

This transition from wreath-building dynamos that rely on our SGS diffusion to wreath-building dynamos that are sufficiently turbulent to be dominated by resolved turbulent dissipation answers one important question relative to the extension of this dynamo mechanism to even more turbulent states. It had long been postulated that global-scale magnetic structures could not exist in the convection zone as they would be quickly destroyed by the intense turbulence. While it is clearly possible that our wreaths may not be able to survive if we were able to simulate far more turbulent conditions, case D3b marks an important milestone along the path towards the possibility of magnetic wreaths coexisting with highly turbulent convection.

Returning to Figure 5.6, let us now look at the time-variation in the production terms. Both cases show variability of $\mathcal{E}_{\rm TME}$, but for case D3b we have chosen to show a time period that includes states before, during, and after a reversal in global magnetic polarity. For both cases, careful examination shows that changes in $\mathcal{E}_{\rm TME}$ are initiated primarily by changes in $G_{\rm MS}$, not by changes to the terms dissipating energy. The terms representing both resolved and unresolved diffusion respond to changes in $\mathcal{E}_{\rm TME}$ rather than drive them. In case D3 this is supported by the cross-correlation of $G_{\rm MS}$ and $G_{\rm RD}$ peaking at a 39 day lag, while there is no significant cross-correlation between $G_{\rm MS}$ and either $G_{\rm FS}$ or $G_{\rm FA}$ for any shift in time. In case D3b both the cross-correlation of $G_{\rm MS}$ with $G_{\rm FS}$, and $G_{\rm MS}$ with $G_{\rm FA}$ both peak at a lag

of 11 days. Resistive diffusion responds faster in case D3b with a peak in cross-correlation for a lag of only 5.6 days. This demonstrates that the variability in the toroidal fields is driven by changes in the generation of field by the Ω-effect.

If we more closely examine the structure of $G_{\rm MS}$ from Equation (5.7), we can expand it to

$$G_{\rm MS} = \int_{\mathcal{V}} \left(\langle B_\phi \rangle \langle B_r \rangle \frac{\partial \langle v_\phi \rangle}{\partial r} + \frac{\langle B_\phi \rangle \langle B_\theta \rangle}{r} \frac{\partial \langle v_\phi \rangle}{\partial \theta} + \frac{\langle B_\phi \rangle^2 \langle v_r \rangle}{r} + \frac{\langle B_\phi \rangle^2 \langle v_\theta \rangle}{r \, \tan\theta} \right) d\mathcal{V}. \tag{5.13}$$

The third and fourth terms are geometric terms from the spherical coordinate system which are generally small. In order to produce a change in $G_{\rm MS}$, the dynamo can either change the axisymmetric poloidal field or modify the differential rotation of the domain. We have examined both the amplitude and geometry of the mean shear due to differential rotation and find only very small changes in any of the cases presented here. Additionally, reversals in the polarity of the wreaths such as those seen in cases D3a and D3b require a change in sign for the generation term (obtained by dividing by $\langle B_\phi \rangle$) and there is never a change of sign in the shear profile of the differential rotation observed in any of these cases. Thus we are left with the conclusion that reversals in the polarity of the axisymmetric toroidal fields must be initiated by changes in the axisymmetric poloidal fields.

Chapter 6

Cycles of Magnetic Activity

We now turn to a discussion of the temporal variability of the magnetic wreaths discussed previously. Specifically, we will examine the cycles of magnetic activity and reversals of magnetic polarity which can be achieved by reducing the explicit diffusion in our simulations. This chapter is the second of two based on the work published in Nelson et al. (2013b)[1] and is largely quoted from that publication. I was the primary author of that paper. I ran most of the simulations presented here and conducted all of the analysis. Notably Benjamin Brown ran cases D3, D3-pm1, and D3-pm2. I wrote most of the text, with significant contributions from Mark Miesch in what is now Section 6.2.

6.1 Cyclic Reversals Achieved by Reducing Diffusion

In addition to building strong magnetic wreaths, cases D3a and D3b exhibit cyclic reversals of global magnetic polarity. As is believed to occur in the Sun, the general pattern of the cycles is that the toroidal fields peak at roughly the time when the poloidal field is reversing sign, and the poloidal fields peak in amplitude when the toroidal fields are reversing sign. There are also a number of variations on this pattern, where one hemisphere may develop considerably stronger fields than the other or where both hemispheres have the same sense of toroidal field, pointing to large contributions at these times from quadripolar

[1] Nelson, N. J., Brown, B. P., Brun, A. S., Miesch, M. S., & Toomre, J. 2013a, Magnetic Wreaths and Cycles in Convective Dynamos, ApJ, 762, 73

poloidal fields. Cases D3-pm1 and D3-pm2 also display strong variations in the strength and topology of their axisymmetric fields. However the irregularities are more pronounced for these cases over the time simulated.

6.1.1 Reversals in Global Magnetic Polarity

Figure 6.1 shows the temporal evolution of the longitude-averaged toroidal field $\langle B_\phi \rangle$ at mid-convection zone over the history of cases D3 (Figure 6.1(a)), D3a (Figure 6.1(b)), and D3b (Figure 6.1(c)). In case D3 we see persistent wreaths centered at about 20° above and below the equator. These wreaths persist for about 68 years or as long as we have run the simulation. The polarity of the wreaths is constant in time, though variations on roughly 6 year time scales can be seen in both the amplitude of the low latitude wreaths as well as the propagation of field to higher latitudes. The behavior of this case is discussed in detail in Brown et al. (2010). Figure 6.1(b) shows case D3a over a comparable length of time as in the first panel. Case D3a undergoes reversals in global magnetic polarity as well as three significant irregular states. Additionally there are modulations in the amplitude of the wreaths and poleward movements of field on roughly 3 year time scales. These variations are not always synchronized between the two hemispheres, and neither are the reversals, indicating that the poloidal field can have a complicated structure.

Figure 6.1(c) shows the temporal evolution of $\langle B_\phi \rangle$ at mid-convection zone for case D3b over about 13 years, with indications of cycles of magnetic activity and reversals of global polarity. We have simulated 10 reversals as measured by the time-smoothed antisymmetric component of $\langle B_\phi \rangle$ changing sign. The time between reversals ranges from 0.6 to 1.9 years and, as in case D3a, the two hemispheres are not always synchronized. There are several times when one hemisphere shows significantly stronger fields than the other or when both hemispheres have the same sense of fields. This is partly due to the averaging procedure used to create these figures and the fact that we are only looking at a single depth. Analysis of the

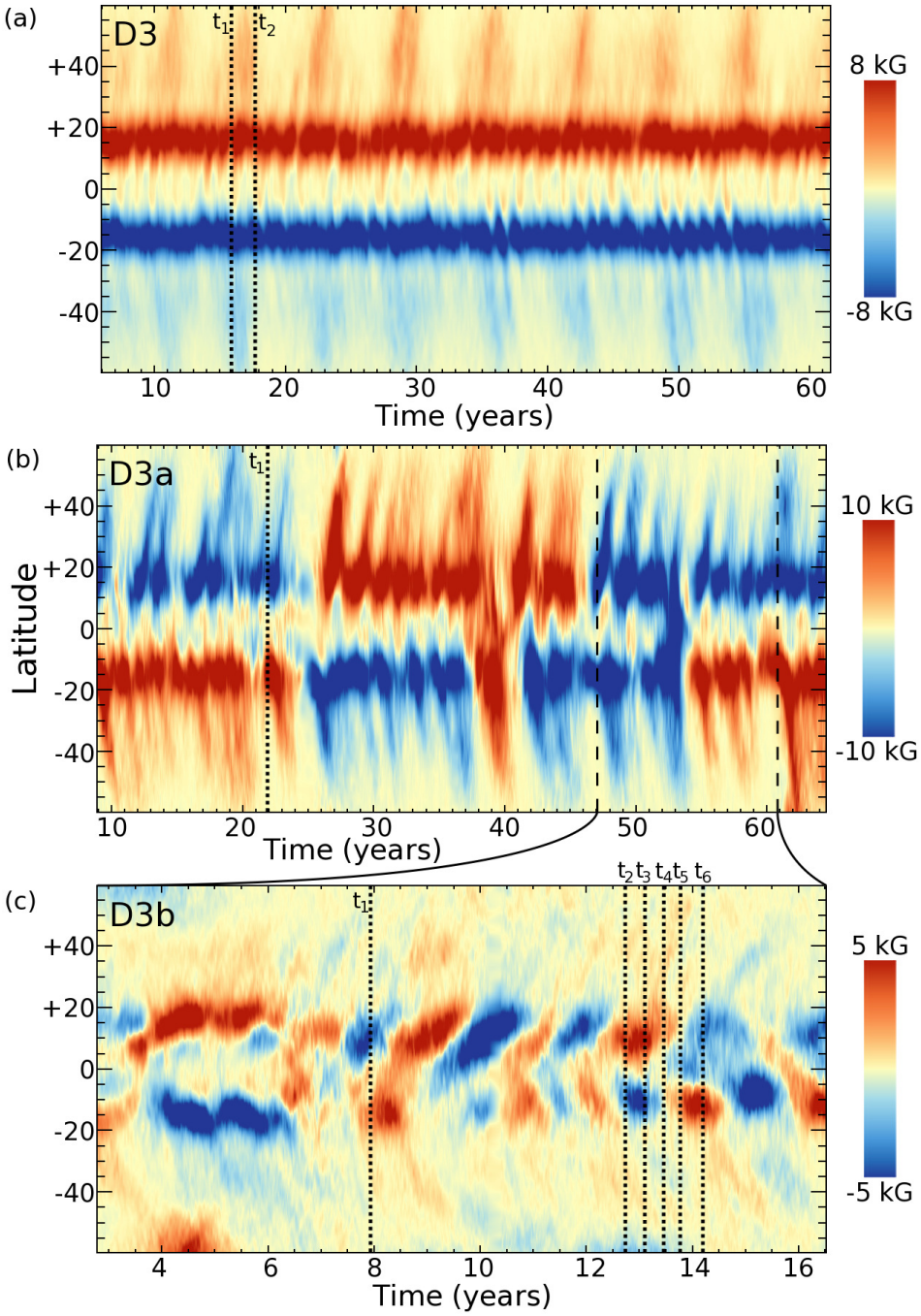

Figure 6.1: Time-latitude plots of longitude averaged toroidal magnetic field $\langle B_\phi \rangle$ at $0.79R_\odot$ for (a) case D3 over about 56 years, (b) case D3a over the same amount of time, and (c) case D3b over about 13 years. Dotted lines show times referenced in Figures 5.1, 6.2, 6.5, 6.6, and 6.9. Dashed lines on (b) indicate the time period covered by (c). Case D3b was started from case D3a at t_2 (dotted line). The evolution of case D3b is limited by the increased computational cost of the higher resolution required for computational stability.

full 3D data shows that there is almost always a wreath-like structure in each hemisphere.

Figure 6.2 shows a sequence of snapshots of B_ϕ at mid-convection zone in case D3b over a full spherical shell and of $\langle B_\phi \rangle$ over the domain before, during, and after a reversal in the polarity of the wreaths. Each snapshot is roughly 120 days after the previous snapshot. The wreaths start appearing as strong mean-field structures in the longitudinal average, but the non-averaged cut at mid-convection zone shows that there is significant longitudinal variation in the wreaths, with the northern wreath covering roughly 120° and the southern wreath covering 180° in longitude. There is also substantial evidence for interactions between the wreaths near the center of the image in Figure 6.2(a). As time progresses, the axisymmetric fields weaken as the non-axisymmetric components begin to dominate. Small patches of strong field persist, but they are largely washed out in the longitudinal averages. After about 480 days (Figure 6.2d) strong patches of opposite polarity field begin to appear and by the final frame (Figure 6.2e) the strong mean fields have been reestablished in the opposite hemispheres from the initial configuration.

6.1.2 Variability at Higher Magnetic Prandtl Number

The simulations on the increasing Pm branch also show increased temporal variability relative to case D3. There is also evidence for a change in the nature of the dynamo action in these simulations. Figure 6.3 shows the evolution of $\langle B_\phi \rangle$ at 0.79 $R_\odot$ over the history of case D3-pm1, along with snapshots of the toroidal magnetic field at mid-convection zone at three representative times. This case has selected a configuration of toroidal field that is largely symmetric about the equator and of essentially the same polarity at most times. Some periods of positive polarity field are seen, though the dominant field in both hemispheres is clearly of negative polarity. Unlike cases D3a and D3b, case D3-pm1 does not undergo a true global reversal of magnetic polarity. It does, however, exhibit strong temporal variability in the wreaths seen in both hemispheres to an extent not seen in cases D3 or D3a.

Figure 6.4 shows a similar view of case D3-pm2 over its temporal evolution. Again it tends to avoid the anti-symmetric states characteristic of cases D3, D3a, and, to a lesser extent, D3b. This case, however, does exhibit clear reversals of global magnetic polarity. Interestingly, these reversals do not appear to occur at regular intervals, and often one hemisphere can reverse without a noticeable change in the other hemisphere. As an example, the southern hemisphere maintains a positive polarity wreath between about $t = 5.5$ years and $t = 10.5$ years while the northern hemisphere exhibits four reversals in that same time interval.

The preference for irregular polarity states in B_ϕ along the increasing Pm branch is clearly related to the decreased level of magnetic diffusion, though it may also be indicative of a shift in behavior due to the transition from small to large magnetic Prandtl number. In cases D3, D3a, and D3b magnetic diffusion occurs on scales larger than those related to the diffusion of momentum. This tends to promote the concentration of magnetic energy at large scales. For high Pm dynamos, the resistive scale is smaller than the viscous scale, which tends to promote the growth of magnetic energy at small scales (e.g., Schekochihin et al., 2004). There is still considerable large-scale organization of magnetic field by the differential rotation, but the increasing Pm branch exhibits less ordered behavior than the constant Pm branch of simulations.

When examining the relative importance of decreased magnetic diffusion and increased levels of turbulence, it is perhaps most instructive to compare cases D3b and D3-pm2. Table 5.2 shows that the division of magnetic energies between the axisymmetric toroidal, axisymmetric poloidal, and fluctuating magnetic fields are roughly equivalent in the two cases, although case D3-pm2 has more magnetic energy overall. The kinetic energies in case D3-pm2 are, however, more similar to case D3 than case D3b with the exception of decreased differential rotation kinetic energy due to enhanced Lorentz force feedbacks. This suggests that the onset of reversals is driven primarily by decreasing magnetic diffusion rather than by some subtle shift in the velocity fields or correlations between magnetic fields and velocities

on small scales.

6.1.3 Collapse of Resistive Balance Leading to Reversals

The key to understanding the reversals seen in cases D3a and D3b lies in the generation of poloidal field. When the poloidal field reverses sign the Ω-effect can then build wreaths of the opposite polarity and reverse the sign of the axisymmetric toroidal field. It is difficult to identify a simple model for the generation of poloidal field in these cases, particularly in case D3b. We can, however, identify the change in the generation mechanism that occurred between cases D3 and D3b.

Following the work of Brown et al. (2010, 2011), we choose to examine the evolution of the ϕ component of the mean vector magnetic potential $\langle \vec{A} \rangle$. This is convenient as $\langle A_\phi \rangle$ completely specifies the components of the axisymmetric poloidal magnetic field by

$$\nabla \times \left(\langle A_\phi \rangle \hat{\phi} \right) = \langle B_r \rangle \hat{r} + \langle B_\theta \rangle \hat{\theta}. \tag{6.1}$$

The temporal variations in the magnetic wreaths are driven by changes in the shear of mean poloidal magnetic fields by mean differential rotation and that only the axisymmetric poloidal fields can change sign, hence changes in the polarity of the wreaths can be traced back to the evolution of $\langle A_\phi \rangle$. Further, the key region of the domain in which we should monitor $\langle A_\phi \rangle$ is near the equator where the gradients in differential rotation are largest and where the wreaths are primarily generated.

The evolution of $\langle A_\phi \rangle$ is governed by

$$\frac{\partial \langle A_\phi \rangle}{\partial t} = \left(\langle \vec{v} \rangle \times \langle \vec{B} \rangle \right)_\phi + \left(\langle v' \times B' \rangle \right)_\phi - \eta \langle J_\phi \rangle. \tag{6.2}$$

We have ignored a gauge term in Equation (6.2) which is permissible for any longitudinally-periodic gauge. We take a time-integral of this equation to look at the changes in $\langle A_\phi \rangle$ over

about 500 days in cases D3 and D3b, and define the time-integral of each term as

$$(\Delta A_\phi)_{\rm ME} = \int_{t_1}^{t_2} \left(\langle \vec{v} \rangle \times \langle \vec{B} \rangle \right)_\phi dt \tag{6.3}$$

$$(\Delta A_\phi)_{\rm FE} = \int_{t_1}^{t_2} \left(\langle v' \times B' \rangle \right)_\phi dt \tag{6.4}$$

$$(\Delta A_\phi)_{\rm RD} = -\int_{t_1}^{t_2} \eta \langle J_\phi \rangle dt. \tag{6.5}$$

Thus the change in $\langle A_\phi \rangle$ can be written as

$$\Delta \langle A_\phi \rangle = (\Delta A_\phi)_{\rm FE} + (\Delta A_\phi)_{\rm ME} + (\Delta A_\phi)_{\rm RD} \,. \tag{6.6}$$

Figures 6.5 and 6.6 show the evolution of $\langle A_\phi \rangle$ in cases D3 and D3b, respectively, as well as the time-integrated production of terms shown above and the net change over the time interval. For case D3b we chose a time period spanning a reversal in global magnetic polarity. In both cases $(\Delta A_\phi)_{\rm ME}$ is small and the evolution is primarily governed by the balance between fluctuating EMF and resistive diffusion. The primary difference between cases D3 and D3b is the collapse of the resistive balance. Both cases show similar patterns in $(\Delta A_\phi)_{\rm FE}$, namely that the fluctuating EMF in both cases is seeking to create a region of opposite polarity poloidal field near the equator while reinforcing the current sense of poloidal field at mid-latitudes. Thus in both cases D3 and D3b the turbulent correlations between the existing field and the convective turbulence tends to build poloidal field near the equator of the opposite sense than the field that built the current wreaths through the Ω-effect. The difference between cases D3 and D3b is that in case D3 the diffusion term is sufficiently large to prevent the reversal by diffusing away the opposite polarity poloidal field at the equator before it can accumulate sufficiently to cause a reversal.

What causes the fluctuating EMF to display this propensity towards reversing the polarity of $\langle A_\phi \rangle$ near the equator? It would seem that there should be some link back to the strong toroidal wreaths, however when we expand the fluctuating EMF, we find that

$$\left(\langle v' \times B' \rangle \right)_\phi = \langle v'_r B'_\theta - v'_\theta B'_r \rangle. \tag{6.7}$$

Clearly, neither the axisymmetric nor fluctuating components of B_ϕ come into play here, indicating that to complete a reversal we need to connect the large-scale toroidal fields to correlations between small-scale poloidal fields and poloidal flows. As shown in Figure 5.1(i), the wreaths are not purely toroidal structures, thus the small-scale fields needed in Equation 6.7 may be supplied by the wreaths themselves. However, we have not been able to definitively link the poloidal components of the wreaths to the reversal process. While the subtle nature of this process remains difficult to pin down, we do have some hints at its origin.

6.1.4 Exploring An α-Like Effect

The final step in the reversal process is what is often described in the parlance of mean-field dynamo theory as the α-effect (see Charbonneau, 2010). Generally, the α-effect is the source of the axisymmetric component of the turbulent EMF, defined as

$$\langle \vec{\epsilon'} \rangle = \langle \vec{v'} \times \vec{B'} \rangle. \tag{6.8}$$

Specifically, we are interested in the zonal component which generates the mean poloidal field and its connection to the axisymmetric toroidal field, which might be expressed as

$$\langle \epsilon'_\phi \rangle = \alpha_{\phi r} \langle B_r \rangle + \alpha_{\phi\theta} \langle B_\theta \rangle + \alpha_{\phi\phi} \langle B_\phi \rangle. \tag{6.9}$$

In its simplest formulation, the components of α_{ij} in Equation (6.9) are constants, however more complex formulations exist.

For case D3b, we have computed the value of the three components of the α tensor in Equation (6.9) using a singular value decomposition following the work of Racine et al. (2011). We compute values for α_{ij} at each radial and latitudinal location, assuming that α_{ij} is constant in time. The results of Figure 6.7 demonstrate that the $\alpha_{\phi\phi}\langle B_\phi \rangle$ is the most important term in the generation of the fluctuating toroidal EMF. Thus, it is particularly intriguing to focus on the connection

$$\langle \epsilon'_\phi \rangle = \alpha_{\phi\phi} \langle B_\phi \rangle. \tag{6.10}$$

Brown et al. (2010) showed that for one formulation of an α-effect in case D3, $\alpha_{\phi\phi}$ was spatially nonlocal, which would not be picked up in our fitting procedure.

The exact mechanism for connecting mean fields and the fluctuating EMF is subtle, but we find that in case D3b an α-like effect emerges, which is nonlocal in time, acting on the same time scale as convective overturning. If we consider correlations between the volume-averaged magnetic field components and similarity the fluctuating toroidal EMF, we find evidence that the α-like effect in case D3b is not instantaneous but rather acts on a time scale (47 days) which is commensurate with the convective overturning time. The volume averages, denoted by curly braces, are computed separately for each hemisphere over all depths and longitudes, and between the equator and $\pm 30^\circ$ in latitude. Combining the data for both hemispheres, the cross-correlation is computed and shown in Figure 6.8 as a function of the temporal interval Δ_τ by which $\{\epsilon'_\phi\}$ is offset relative to $\{B_r\}$, $\{B_\theta\}$, and $\{B_\phi\}$ in turn. The peaks in the cross-correlation which exceed 2σ in significance occur when $\{\epsilon'_\phi\}$ leads $\{B_\phi\}$ by 312 days and when $\{B_\phi\}$ leads $\{\epsilon'_\phi\}$ by 47 days.

Analysis of the autocorrelation of both $\{B_\phi\}$ and$\{\epsilon'_\phi\}$ indicates that the two peaks are not due to periodicities in either of the two time series individually. Further, the widths of these peaks largely originates from the coherence time for $\langle B_\phi \rangle$ of about 100 days. The first peak at 312 days represents the time scale for the Ω-effect and agrees well with the estimate from mean-field theory τ_Ω given by

$$\tau_\Omega = P_{\rm rot} \frac{\Omega_0}{\Delta\Omega} \frac{\langle B_\phi \rangle}{\langle B_{\rm pol} \rangle}, \tag{6.11}$$

where $P_{\rm rot}$ is the rotation period, Ω_0 is the frame rotation rate, $\Delta\Omega$ is the differential rotation rate, and $\langle B_{\rm pol} \rangle$ is the strength of the poloidal field. For case D3b, this yields a value of 324 days. The second peak in the cross-correlation between the two fields occurs when $\tau_\Delta = -47$ days. This peak suggests that the correlations which generate the turbulent zonal EMF are related in some way to the axisymmetric toroidal fields, and that whatever mechanism establishes this correlation, it has a time scale of about 50 days. This temporally and

spatially nonlocal α-effect clearly points to convection as a key player, as other mechanisms like the meridional circulation are at least an order of magnitude slower.

In addition to a timescale for an α-like effect which is commensurate with the convective overturning time, we also find evidence for an upscale transfer of magnetic energy related to magnetic reversals. Figure 6.9 shows the temporal evolution of $\langle B_\phi \rangle$ at mid-convection zone over both latitude and spherical harmonic degree ℓ. Several reversals of global magnetic polarity are evident in Figure 6.9(b), including the reversal shown in detail in Figure 6.2. Figure 6.9(a) shows the coefficients of the spherical harmonic expansion of the axisymmetric toroidal field for the anti-symmetric (odd ℓ) modes with $1 \leq \ell \leq 29$ over roughly three magnetic activity cycles. In both physical space and spectral space, it is clear that each cycle has opposite polarity from the preceding cycle.

There is a preference for antisymmetric modes with odd values of ℓ, as would be expected from the Ω-effect acting on a poloidal field that is preferentially symmetric about the equator (even ℓ). The upscale cascade involving odd modes is expected from both theoretical and observational studies families of dynamo modes (see Nishikawa & Kusano, 2008; DeRosa et al., 2012). As a reversal occurs we see power showing up first at moderate ℓ and then cascading upscale to smaller ℓ values until it peaks at $\ell = 3$ or 1 depending on the cycle. The reversal starts at $25 \lesssim \ell \lesssim 29$ and then each successive mode reverses. There is considerable overlap between cycles, in some cases reversals are seen in the high-ℓ modes in as little as a hundred days after the previous reversal is completed at low-ℓ. We note that convective power peaks at spherical harmonic degrees between about 25 and 40 in these simulations. This suggests that the reversals are caused by turbulent processes interacting with the wreaths, yielding an upscale energy transfer which organizes the large-scale fields. Combined with our cross-correlation analysis, this upscale transfer indicates the key role of convection in connecting mean toroidal magnetic fields with the fluctuating toroidal EMF.

As illustrated schematically in Figure 6.10, the reversal mechanism involves three main processes. First, axisymmetric wreaths of toroidal magnetic field (Figure 6.10(a)) lead to

correlations in the non-axisymmetric poloidal velocity and magnetic fields which drive an axisymmetric turbulent EMF through an α-like effect. The upscale transfer of magnetic energy and the fact that the correlation between the magnetic energy of the wreaths and the turbulent EMF peaks on roughly a convective overturning time would seem to point towards the convective motions as a key player in this α-like process. In the second step, the turbulent EMF reinforces the dominant poloidal field at mid-latitudes but is the opposite sign near the equator (Figure 6.10(b)), creating an octopolar configuration, with strong radial field concentrations at low latitudes (Figure 6.10(c)). As the reversal progresses, the region of new poloidal field shown in red in Figure 6.10(c) will expand and eventually replace the old sense of field shown in blue. The third step involves axisymmetric poloidal magnetic field being sheared by differential rotation. Here the differential rotation is largely cylindrical, thus radial poloidal field is primarily converted into toroidal magnetic field through the Ω-effect, which results in axisymmetric toroidal fields of the opposite polarity (Figure 6.10(d)). The process then repeats with the opposite polarity.

6.2 Turbulence-Regulated Flux Emergence

Photospheric active regions are thought to arise from the buoyant destabilization, rise, and emergence of coherent, subsurface toroidal flux structures. It is often argued that these subsurface flux structures originate below the convection zone, where the strong shear of the tachocline promotes toroidal flux generation and the subadiabatic stratification of the overshoot region promotes flux storage by inhibiting the buoyancy instability (Galloway & Weiss, 1981; van Ballegooijen, 1982). In this section we offer an alternative viewpoint that is inspired and supported by the numerical models presented here. Namely, we argue that buoyant flux structures may be produced in the Sun and stars not only in the tachocline but also in the lower convection zone through the combined action of rotational shear and turbulent intermittency.

In previous papers we have demonstrated that organized systems of toroidal flux can persist within a turbulent convection zone despite the inhibiting influence of turbulent dispersal (Brown et al., 2010, 2011). Here we have demonstrated that this continues to hold as we decrease the diffusion, crossing a threshold beyond which resolved motions replace artificial dissipation in the dynamical balances that sustain mean flows and fields. Furthermore, as the diffusion is decreased, intense, localized wreath cores form where the magnetic energy density exceeds the surrounding kinetic energy density (Figure 5.2). This trend is highlighted most dramatically by case S3, where the much lower diffusion promotes coherent wreath cores strong enough to become buoyant, as first demonstrated by Nelson et al. (2011b).

Here we explore in more general terms the link between magnetic wreaths and flux emergence, addressing in particular on how it might operate in real stars where the dissipation is many orders of magnitude less than in simulations. We begin by noting that the Ω-effect does not just operate on axisymmetric fields; poloidal fields of all longitudinal wavenumbers (m) in the convection zone are converted to toroidal fields (of the same m) and amplified by rotational shear, blurring the distinction between mean and fluctuating fields. Turbulent intermittency in the surrounding convection can further amplify shear-generated flux structures, promoting the generation of fibril magnetic fields and coherent, localized wreath cores (Figure 5.2).

The low Mach number of stellar convection zones ensures that the gas pressure adjusts rapidly to any imbalance of mechanical and magnetic stresses. Thus, the formation of fibril, intermittent flux concentrations (wreath cores) will induce a pressure perturbation $\delta P \sim P_t - P_m$, where P_t is the turbulent (kinetic plus magnetic) pressure of the surrounding medium and P_m is the magnetic pressure associated with the coherent flux that defines the wreath core. We have neglected the turbulent pressure within the wreath core which may be suppressed by magnetic tension, providing a positive feedback mechanism that can further promote the formation of coherent, superequiparition wreath cores and buoyant loops

(Kleeorin et al., 1989; Rogachevskii & Kleeorin, 2007; Käpylä et al., 2012a).

Weak magnetic flux concentrations, $P_m < P_t$, are not susceptible to buoyancy instabilities because their magnetic pressure is insufficient to balance the surrounding turbulent pressure, resulting in $\delta P > 0$. It is only the strongest wreath cores that develop a pressure deficit $\delta P < 0$, in particular only those cores in which the magnetic pressure P_m exceeds the stabilizing influence of the surrounding convective motions. This implies that a necessary but not sufficient condition for the wreath cores to become buoyant is that they must be superequipartition relative to the surrounding convection. The surrounding flows may in turn enhance or retard the tendency for such structures to rise. As demonstrated in Figure 5.2, this is indeed achieved in our simulations and it becomes more pronounced as the artificial diffusion is reduced, eventually inducing buoyant rise.

If these superequipartition wreath cores form adiabatically, this pressure deficit will be accompanied by a density deficit $\epsilon = \delta\rho/\rho \sim \delta P/(\gamma P)$, established by diverging flows along the axis of the wreath core. Radiative heating can further warm and rarify the wreath cores, enhancing the the density deficit to $\epsilon \sim \delta P/P = (P_m - P_t)/P$ on a time scale of

$$\tau_r^{-1} = \frac{\epsilon}{r^2 \rho T C_p} \frac{\partial}{\partial t} \left(r^2 \rho T C_P \kappa_r \frac{\partial T}{\partial r} \right) \tag{6.12}$$

where κ_r is the radiative diffusivity (Fan & Fisher, 1996). Inserting values from Model S (Christensen-Dalsgaard et al., 1996) for $\epsilon \sim 10^{-6}$ yields $\tau_r < 100$ days through most of the solar convection zone. This value of ϵ corresponds to an emergence time $\tau_e \sim (2D/\epsilon g)$, of about 10-15 days, where D is the depth of the convection zone, and a magnetic field strength of $B \sim (8\pi\epsilon P)^{1/2} \sim$ 20-40 kG over and above the equipartition value.

Convection can also promote the buoyant rise of a wreath segment by introducing a finite-amplitude undular displacement, resulting in a draining of fluid from from the apex of the loop (Jouve & Brun, 2009; Nelson et al., 2011b; Weber et al., 2011). This could in principle operate for any field strength but in practice weak fields will by shredded and reprocessed by convection before they emerge (e.g., Fan, 2009).

The dynamics discussed here are indeed exhibited by our most turbulent simulation, case S3. Relative to more diffusive simulations, this case generates more regions of strong, superequipartition fields, as demonstrated in Figure 5.2, and these regions are located in coherent, intermittent wreath cores, as illustrated in Figure 6.11. Figure 6.12 highlights two examples in which such wreath cores become buoyant and rise. As discussed in Nelson et al. (2011b) and Nelson et al. (2013a), the loops rise through the convection zone through the combined influence of magnetic buoyancy and advection, reaching as high as $0.94R$ before they are dissipated by diffusion. The wreath which formed these two loops (and two others not shown) is not axisymmetric; rather, it spans about 180° in longitude, reaching peak field strengths of 45 kG. We expect the process to be even more efficient in stars where the intermittency is presumably much more extreme.

In summary, this paradigm of turbulence-induced flux emergence postulates that the combined action of turbulent intermittency and rotational shear generates a broad distribution of toroidal magnetic structures and it is only the most extreme events, in the high-B tail of the pdf, that become buoyant. It is analogous to the theory of turbulence-regulated star formation, whereby supersonic turbulence in interstellar molecular clouds generates a spectrum of density fluctuations but only the extreme events on the tail of the pdf are dense enough to trigger the Jeans instability and condense to form protostars (Krumholz & McKee, 2005). It is also closely related to the negative magnetic pressure instability described by Kleeorin et al. (1989) (see also Rogachevskii & Kleeorin, 2007; Käpylä et al., 2012a; Kemel et al., 2012), although it does not necessarily rely on the assumptions that underlie that instability analysis, namely scale separation, the invariance of the small-scale turbulent energy, and the proportionality between variations in the mean and turbulent magnetic energy (attributed to kinematic shredding).

The radial location of the flux bundles that ultimately form active regions depends on the kinetic energy density in the convection (FKE) relative to that in the differential rotation (DRKE), as well as the efficiency of magnetic pumping. In the simulations presented here,

DRKE/FKE $\gtrsim 1$, suggesting that the generation of the wreaths is efficient enough that they can persist in the convection zone despite magnetic pumping. If this ratio falls much below unity, as might be expected for lower rotation rates, the wreaths may get pushed toward the base of the convection zone. Likewise, if the simulations are over or under-estimating the efficiency of magnetic pumping, this will influence the location of flux generation and the threshold to trigger the magnetic buoyancy instability. However, the basic paradigm should still be valid.

The scenario outlined here may resolve several current observational and theoretical puzzles. In particular, the non-axisymmetric nature of turbulence-induced flux emergence is consistent with the results of Stenflo & Kosovichev (2012) who find that many large bipolar active regions on the Sun violate Hales's polarity rules, and furthermore, that the anti-Hale regions often occur at the same latitude as bipoles that obey Hale's rules. The fraction of anti-Hale magnetic regions increases from about 4% for the largest active regions (flux $\Phi \gtrsim 10^{23}$ Mx) to more than 25% for smaller bipoles with $\Phi \sim 10^{20}$ Mx. The result that more than 70% of intermediate-sized bipoles ($\Phi \sim 10^{20}$ Mx) obey Hale's laws suggests the presence of organized toroidal flux systems throughout the convection zone since all of these regions are unlikely to be anchored in the tachocline. Meanwhile, the diminishing of magnetic activity patterns with decreasing flux, including an increasing fraction of anti-Hale bipoles as well as an increased scatter in tilt angles and emergence latitudes, is often attributed to the influence of convection on rising flux tubes (Jouve & Brun, 2009; Weber et al., 2011, 2012; Jouve et al., 2013; Weber et al., 2013). We propose that this intimate coupling between flux tubes and convection exists not only in their rise, but also in their very formation. Finally, the non-axisymmetric nature of turbulence-induced flux emergence may also account for the phenomenon of active longitudes (Nelson et al., 2013a).

The observed tilt angles and emergence latitudes of bipolar magnetic regions on the Sun is best reproduced by models of rising flux tubes with initial field strengths of 20-100kG (e.g., Fan, 2009; Jouve & Brun, 2009; Weber et al., 2011; Pinto et al., 2011). However,

generating such super-equipartition fields is not a trivial matter and in fact represents a formidable, unresolved problem in solar dynamo theory (e.g., Rempel & Schüssler, 2001). Laminar amplification of toroidal fields by rotational shear, the Ω-effect, tends to saturate at field strengths well below equipartition due to the back-reaction of the Lorentz force (Vasil & Brummell, 2009; Guerrero & Käpylä, 2011). Turbulent intermittency can help by tapping the energy in the convection that is ultimately provided by the solar luminosity. It is clear from Figure 5.2 that the coupled action of turbulence and shear can generate superequipartition fields of the required amplitude.

The paradigm proposed here may also help address other difficulties with tachocline-based dynamos discussed by Brandenburg (2005). For example, toroidal flux generation does not rely on the radial shear of the tachocline, which is maximum near the poles. Instead, the expected location of flux generation is where $|\nabla\Omega|$ is maximum in the convection zone. This corresponds to the latitudinal shear at mid-latitudes, precisely where active regions first emerge at the beginning of a cycle, as emphasized by Spruit (2011). Note that the potential role flux emergence plays in establishing the solar cycle is a separate question that we do not address here.

6.3 Richness of stellar dynamos

In this chapter we have explored the complex behavior of a class of numerical simulations of convective dynamo action in rapidly rotating solar-like stars. More broadly, however, we have also touched upon the rich landscape of convective dynamo simulations by discussing both persistent wreath-building dynamos such as cases D3 and D3-pm1, and cyclic wreath-building dynamos including cases D3a, D3b, D3-pm2, and S3. Although the simulations considered here are ostensibly rotating three times faster than the Sun ($3\Omega_\odot$), the Sun may actually be in a similar Rossby number regime, as noted in §1. Thus the results presented here may have some bearing on the solar dynamo as well as the dynamos of younger, more

rapidly-rotating solar analogues.

We have focused on two open questions that arose out of our previous work on wreath-building dynamos. The first is "Can magnetic wreaths persist in the highly turbulent conditions of a stellar convection zone" and the second is "What physical mechanisms establish and regulate the magnetic cycles we see in our simulations?" We have also touched upon a third question that all solar and stellar dynamo models must eventually face, and that is "How are sunspots and bipolar active regions produced from dynamo-generated magnetic fields?".

The principal issue with regard to the first question is whether magnetic wreaths can persist in stellar convection zones where the magnetic, viscous, and thermal diffusion coefficients are many orders of magnitude lower than in our simulations. We have investigated this question by systematically decreasing the diffusion in our simulations along two complementary paths, one in which only the magnetic diffusion coefficient, η, was reduced, and one in which the magnetic and viscous diffusivitiy, η and ν, were reduced together, keeping the magnetic Prandtl number constant (at a value of 0.5). In both cases magnetic wreaths with quasi-cyclic polarity reversals were attained, although the constant Pm branch exhibited more regular spatial and temporal behavior and thus became the focus of our analysis (see Figure 6.1).

Although no simulation can approach the extreme parameter regimes of stellar interiors, we have demonstrated a shift in the dynamical balances that bodes well for the possible persistence of magnetic wreaths at much higher Reynolds and magnetic Reynolds numbers. In short, our simulations suggest that the answer to the first question may be "Yes, magnetic wreaths may indeed occur in actual stars". We have investigated in particular the balance of angular momentum transport which maintains the differential rotation in our simulations and the balance of processes responsible for creating and destroying the magnetic energy of the wreaths. In both cases, as we move from case D3 to case D3b we find that resolved turbulent dissipation has taken the place of SGS dissipation (see Figures 5.4 and 5.6). This

is an important milestone towards demonstrating that wreaths can exist in highly turbulent settings and that they are not reliant on the explicit diffusion in previous simulations.

We have found that magnetic wreaths persist in our higher-resolution, lower-dissipation, more turbulent simulations, yet their nature is altered in a fundamental and significant way. Most notably, they are no longer axisymmetric. In our more turbulent simulations such as case D3b, the nearly axisymmetric wreaths of case D3 are replaced by coherent wreath segments, typically spanning between 45° and 270° in longitude. This is associated with a shift in the magnetic power spectrum from longitudinal wavenumber $m = 0$ to moderate m values. It also has important implications for flux emergence, as discussed with regard to question 3 below.

The first clues as to the origin of magnetic cycles in our simulations (question 2) were uncovered by Brown et al. (2010, 2011), showing that one can move from a persistent wreath-building dynamo state to a cyclic one by increasing the rotation rate. Here we have shown that a similar transition from persistent to cyclic wreaths can be achieved by decreasing the effective magnetic diffusion, and thereby increasing the magnetic Reynolds number at a fixed rotation rate. As mentioned above, the constant-Pm branch of solutions exhibited more regular cyclic behavior despite the higher degree of turbulence.

We have not obtained a definitive exposition of the physical mechanisms that give rise to and regulate magnetic reversals. However, we have traced their operation to the zonal component of the turbulent electromotive force (EMF) near the equator. In case D3 diffusion prevented reversals in the polarity of the axisymmetric poloidal field by locally offsetting the creation of mean poloidal field by turbulent fluctuations. In the lower-dissipation case D3b, this balance breaks down, leaving a residual turbulent EMF near the equator that creates poloidal field with a polarity that is opposite to that of the pre-existing field, as shown in Figure 6.6. Once magnetic reversals are thus initiated, the overall reversal process follows the schematic description found in Figure 6.10.

Our simulations cannot directly address the third question regarding how solar and

stellar dynamos produce sunspots and bipolar active regions. The detailed dynamics of flux emergence are too intricate to reliably capture in any current global dynamo simulation. However, the change in the nature of the wreaths as the dynamical balances shift suggests that they may play an important role in generating buoyant magnetic loops in actual stars. As discussed in §7, these simulations suggest that strong, coherent magnetic structures of moderate angular extent can be created in the cores of the magnetic wreaths. If this trend were to continue to the extremely low diffusion regimes of actual stellar convection zones, one would expect these flux bundles to become buoyantly unstable and rise. Indeed, this expectation is confirmed by our simulation Case S3 that employs a less diffusive SGS model and that exhibits the self-consistent generation of buoyant toroidal flux tubes in a global convective dynamo simulation. This picture of flux emergence as a fundamentally turbulent process contrasts strongly with more idealized scenarios where the principal role of convection is simply to produce a differential rotation. One might expect this revised paradigm to have observable consequences in such active region characteristics as distribution, tilt angle, and helicity. Furthermore,it may call into question our traditional reliance on sunspots as a straightforward proxy for the axisymmetric toroidal field at or below the base of the convection zone.

The rich behavior of these systems provides important insight into the dynamo models for the Sun and solar-type stars. The trend towards non-axisymmetric fields with enhanced turbulence, while still maintaining global-scale organization, pushes at the boundaries of our understanding of dynamo theory in solar-like settings. That these mechanisms are accessible with current computational resources clearly invites further intensive study of these topics.

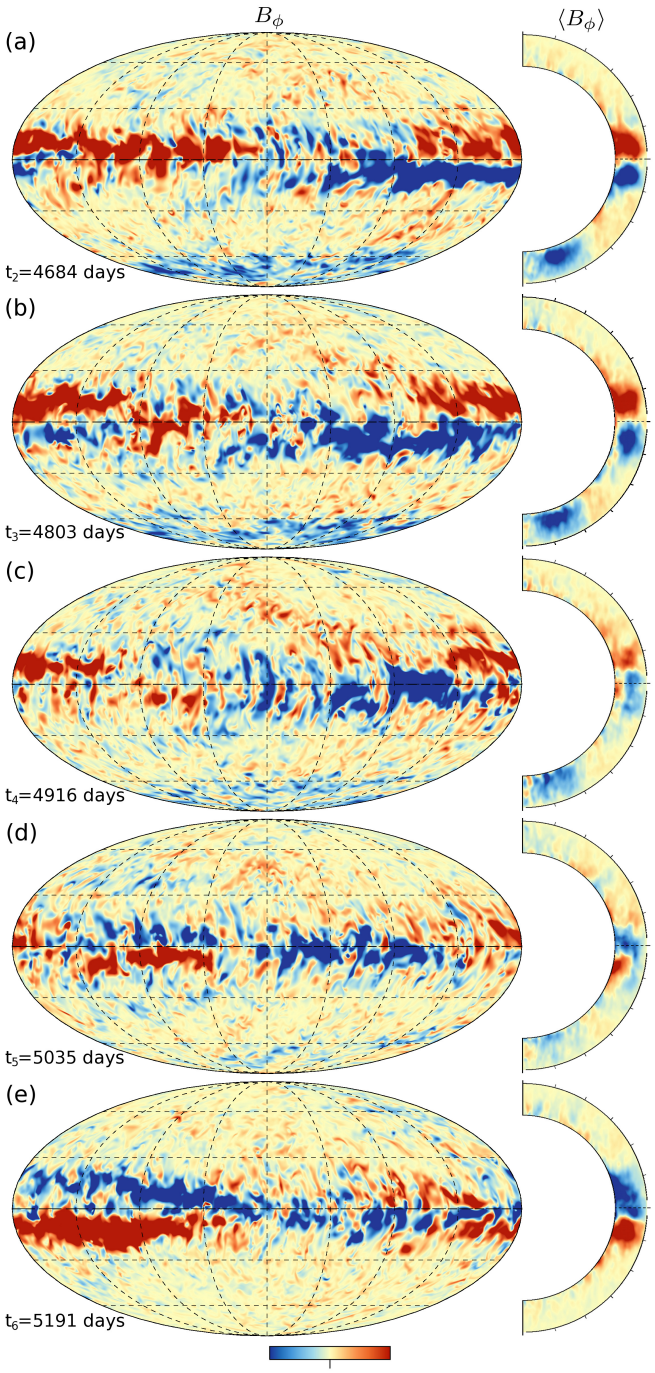

Figure 6.2: Reversal in magnetic polarity of the toroidal wreaths in case D3b shown in B_ϕ in Mollweide projection at mid-convection zone on left, and in $\langle B_\phi \rangle$ in longitudinal average over latitude and radius on right. Color indicates strength of toroidal magnetic field with the color table saturating at ± 7 kG for the Mollweide images and ± 3 kG for the longitudinal averages. Five snapshots corresponding to t_2 through t_6 from Figure 6.1(c) are shown each separated by roughly 120 days.

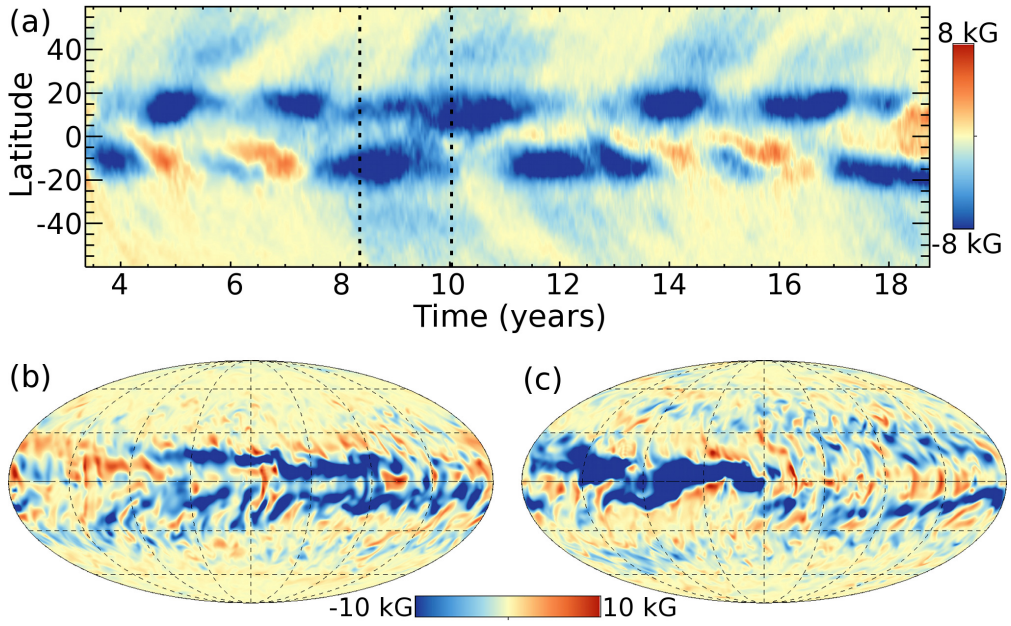

Figure 6.3: (a) Time evolution in case D3-pm1 of the axisymmetric toroidal magnetic field at 0.79 $R_\odot$ over roughly 15 years of simulated time. Strong variability of the mean fields is seen in both hemispheres. (b, c) Companion snapshots of B_ϕ at 0.84 $R_\odot$ showing the spatial variability and non-axisymmetric nature of the wreaths. Successive snapshot times are indicated by dashed lines in (a).

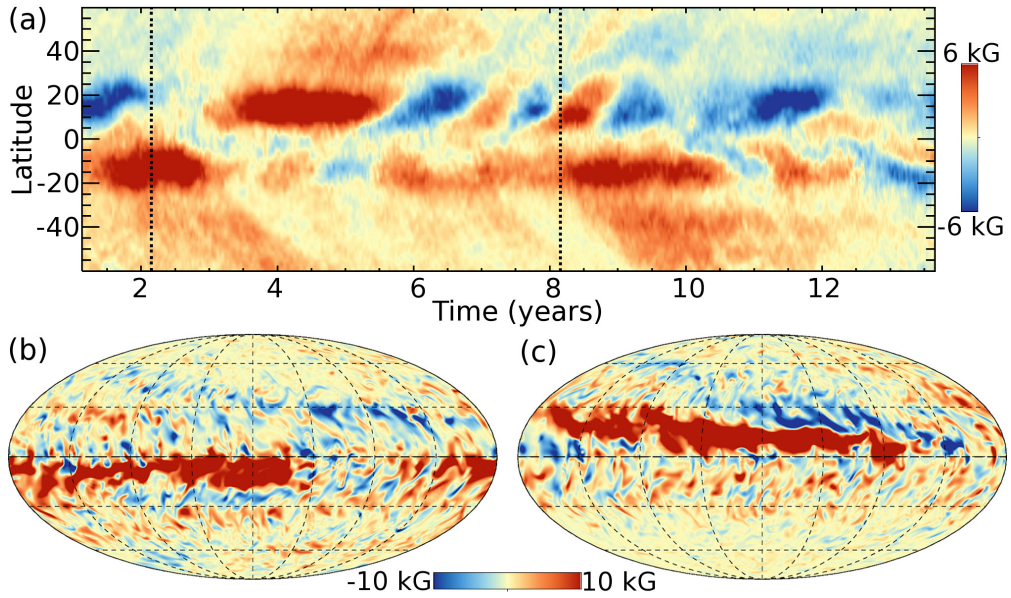

Figure 6.4: (a) Time evolution in case D3-pm2 of the axisymmetric toroidal magnetic field at 0.79 $R_\odot$ over roughly 13 years of simulated time. Strong variability of the mean fields is seen in both hemispheres, along with irregular reversals in polarity, at times in only one hemisphere and at other times globally. (b, c) Companion snapshots of B_ϕ at 0.84 $R_\odot$ showing the spatial variability and non-axisymmetric nature of the wreaths. Successive snapshot times are indicated by dashed lines in (a).

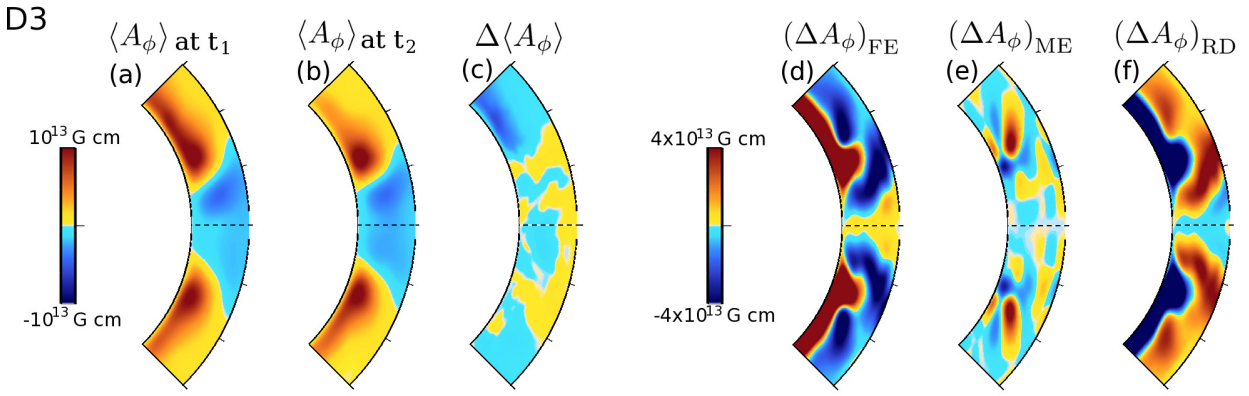

Figure 6.5: Time-evolution of $\langle A_\phi \rangle$ between $\pm 45^\circ$ latitude for case D3 over about 500 days. Times t_1 and t_2 for case D3 correspond to times indicated in Figure 6.1. Shown are $\langle A_\phi \rangle$ at (a) the beginning and (b) end of the time interval, (c) the net change between those times $\Delta\langle A_\phi \rangle$, the changes in $\langle A_\phi \rangle$ due to (d) the fluctuating EMF $(\Delta A_\phi)_{\rm FE}$, (e) the mean EMF $(\Delta A_\phi)_{\rm ME}$, and (f) resistive diffusion $(\Delta A_\phi)_{\rm RD}$. Of particular importance is the region of positive production in $(\Delta A_\phi)_{\rm FE}$, which if left unimpeded by diffusion would lead to a reversal in global magnetic polarity. The color table has been chosen with a sharp transition from light blue to yellow around zero, thus low-amplitude signals, such as seen in (c) and (e), are highlighted.

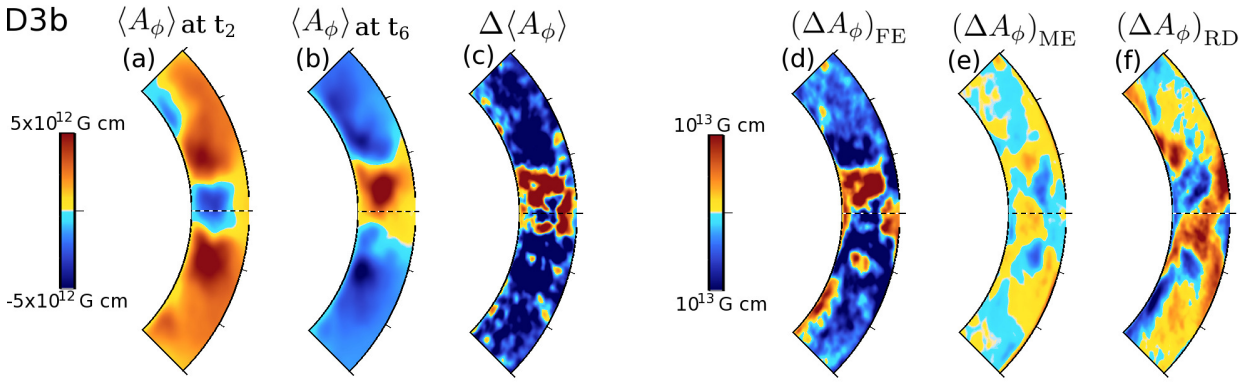

Figure 6.6: Same as Figure 6.5, but for case D3b. Times t_2 and t_6 for case D3b correspond to times indicated in Figures 6.1 and 6.9. The turbulent EMF induces field of the opposite sense to that which was present at t_2 and is opposed by the resistive diffusion. Note that $(\Delta A_\phi)_{\rm FE}$ and $(\Delta A_\phi)_{\rm RD}$ for both cases are topologically similar, but that $(\Delta A_\phi)_{\rm RD}$ is smaller in case D3b, rendering it unable to prevent the reversal of $\langle A_\phi \rangle$ by the fluctuating EMF which begins with the positive region near the equator.

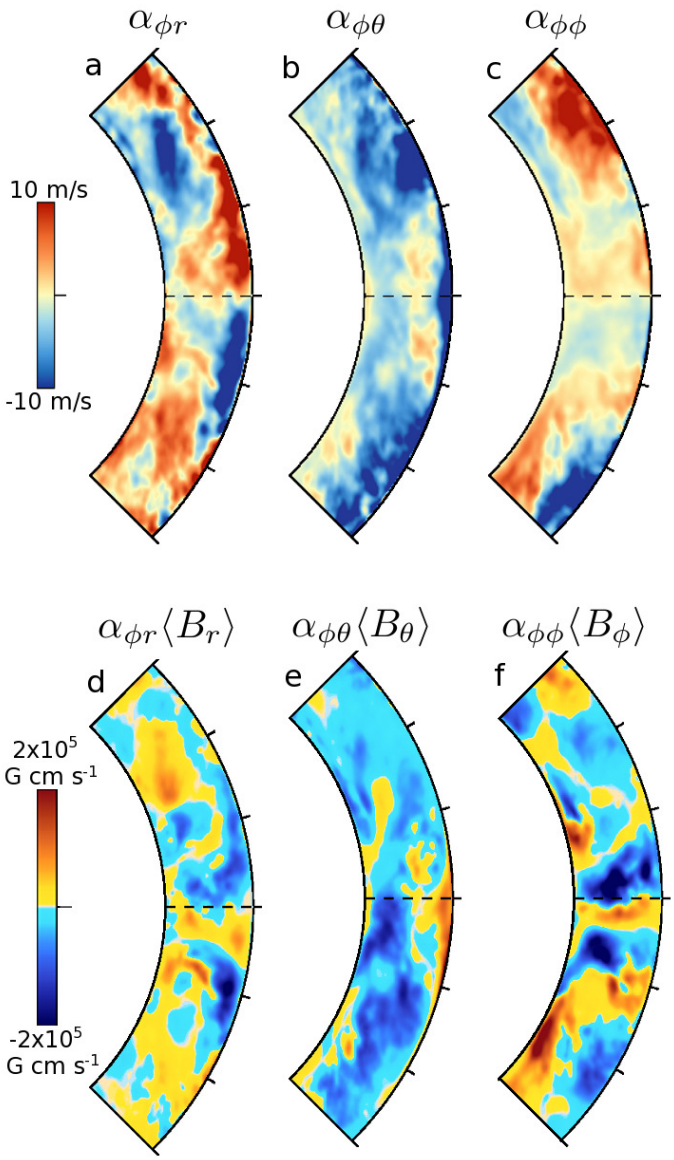

Figure 6.7: (a-c) Values for the three components of α tensor relevant to the generation of $\langle \epsilon'_\phi \rangle$ as a function of radius and latitude. Values are computed using a singular value decomposition over approximately 3000 days of simulation time with the assumption that these components of α are spatially local and do not vary in time. The $\alpha_{\phi r}$ component is very small, whereas the $\alpha_{\phi\theta}$ and $\alpha_{\phi\phi}$ components show significant spatial variability and comparable amplitude. (d-f) Values for components of $\alpha_{\phi j}\langle B_j \rangle$, showing the effect of each component on $\langle \epsilon'_\phi \rangle$. Magnetic fields have been averaged over the same interval as in Figure 6.6 (about 480 days). Here the contribution of $\alpha_{\phi\phi}\langle B_\phi \rangle$ is dominant, with a smaller but still significant contribution by $\alpha_{\phi\theta}\langle B_\theta \rangle$. This figure has been corrected from the version included in Nelson et al. (2013b). A minor error was discovered after publication that changed the details of this figure, but did not substantially alter the conclusions drawn from this figure.

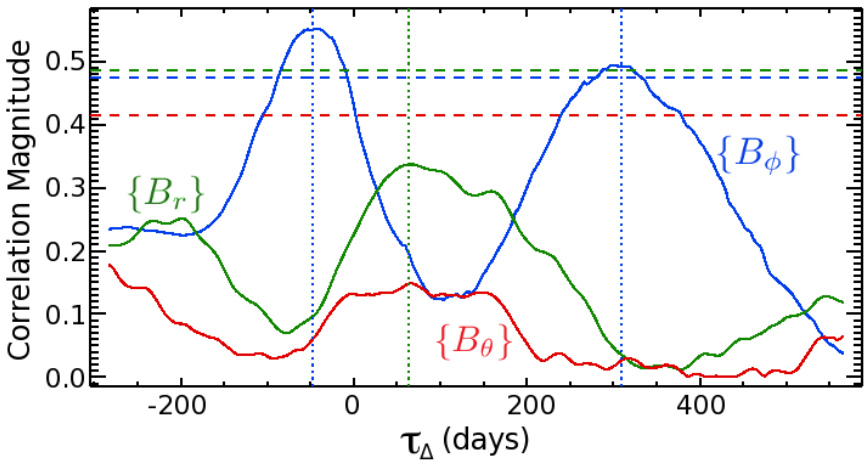

Figure 6.8: Magnitude of cross-correlation in time of $\{\epsilon'_\phi\}$ and $\{B_r\}$ (green), $\{B_\theta\}$ (red), and $\{B_\phi\}$ (blue) for case D3b. Cross-correlation is computed as a function of the temporal offset τ_Δ,/ with negative offsets indicating magnetic fields precede the toroidal EMF. Also shown are the 2σ confidence levels (dashed), computed using a Markov chain Monte Carlo method (Wall & Jenkins, 2003). The only statistically significant peaks are those relating $\{\epsilon'_\phi\}$ and $\{B_\phi\}$.

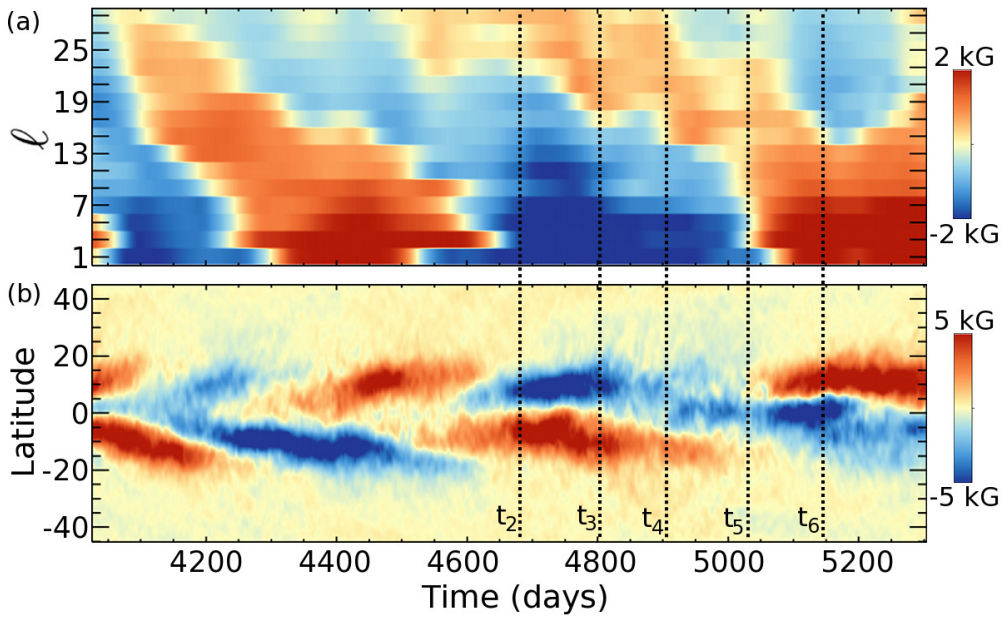

Figure 6.9: Companion plots of the time evolution in case D3b of (a) the spherical harmonic coefficients for antisymmetric modes with $1 \leq \ell \leq 29$ and $m = 0$ for B_ϕ, and (b) $\langle B_\phi \rangle$ in physical space as a function of latitude, both at mid-convection zone. Dashed lines show times referenced in Figures 6.1, 6.2, 6.5, and 6.6. A factor of $(-1)^{(\ell-1)/2}$ is applied to the spherical harmonic coefficients to remove the effect of the wreaths confinement to low latitudes. There is a clear progressive spectral transfer of magnetic energy from high ℓ modes to low ℓ modes as each cycle progresses. Reversals begin at moderate scales (high ℓ) and then progress to large scales (low ℓ).

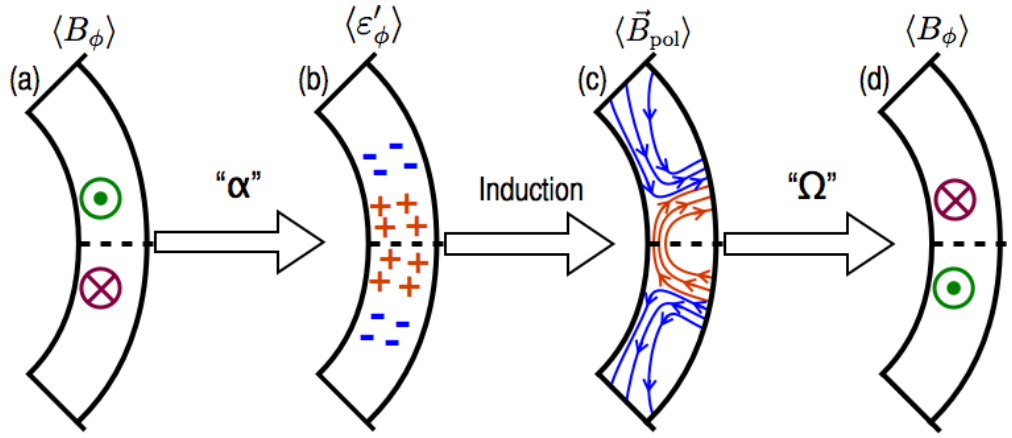

Figure 6.10: Schematic description of the reversal mechanism for cyclic convective dynamos in four steps. (a) Two toroidal wreaths at low latitude which generates a turbulent EMF via a nonlocal "α"-effect, either through nonlinear interactions across the equator or via helical convection. The sign of the EMF changes at roughly the location of the wreaths. (b) Correlations in turbulent poloidal velocities and fluctuating magnetic field drive an induction of mean poloidal field which is roughly octopolar. (c) Mean poloidal field near the equator is sheared by differential rotation to generate mean toroidal field through the Ω-effect. In these simulations, the largest component is the shearing of radial field lines by radial gradients in the differential rotation. (d) Toroidal wreaths of opposite polarity are generated.

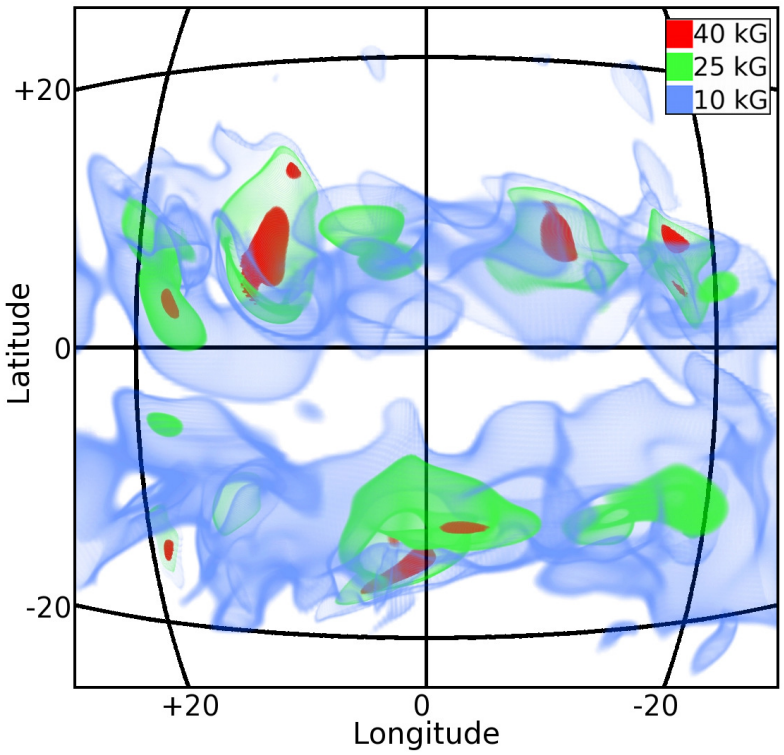

Figure 6.11: Three-dimensional volume renderings of isosurfaces of magnetic field amplitude in case S3. Blue surfaces have amplitudes of 10 kG, green surfaces represent 25 kG, and red surfaces indicate 40 kG fields. Grid lines indicate latitude and longitude at 0.72 $R_\odot$ as they would appear from the vantage point of the viewer. Small portions of the cores of these wreaths have been amplified to field strengths in excess of 40 kG while the majority of the wreaths exhibit fields of about 10 kG or roughly in equipartition with the mean kinetic energy density (see Figure 5.2).

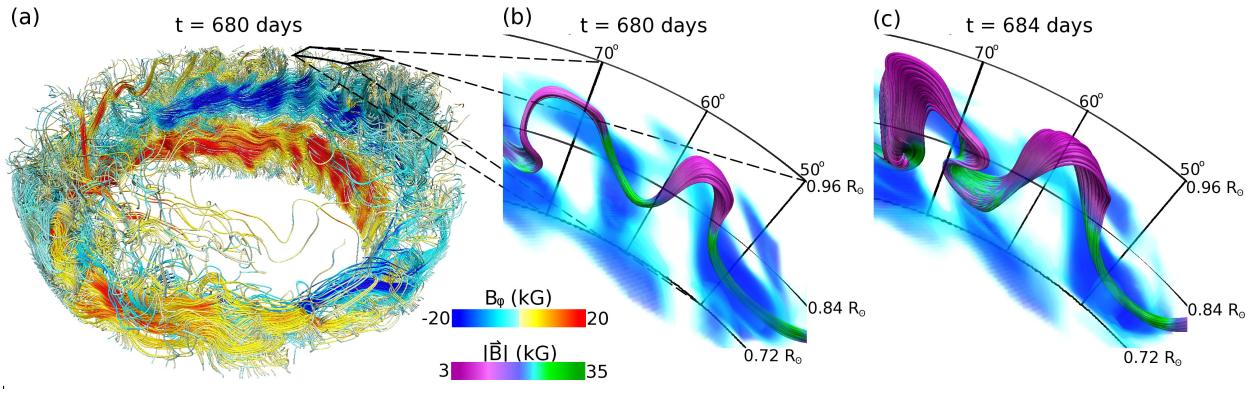

Figure 6.12: Buoyant magnetic loops evolving from small-scale wreath sections amplified by turbulent intermittency. (a) Field line rendering of magnetic wreaths at low latitudes in case S3. Field lines are colored by B_ϕ (negative in blue, positive in red) to highlight the two wreaths present. (b) Zoom-in on region indicated in (a) showing field line tracings of the core of the buoyant magnetic loops at the same instant colored by magnitude of $\vec{B}$ (weak fields in purple, intense fields in yellow). Volume rendering shows B_ϕ using the same color scheme as in (a). (c) The same region 4 days later, showing the continued rise of the loops through the stratified domain and their expansion.

Chapter 7

Buoyant Magnetic Loops Over Magnetic Activity Cycles

The dynamo models discussed in the previous three chapters offer a new paradigm in flux emergence. Previous models had sought laminar generation mechanisms for the strong toroidal field at the base of the convective layer. In contrast we have provided an example of a dynamo simulation where turbulent intermittency can create relatively highly coherent, small-scale magnetic fields with energies well in excess of equipartition with the convective kinetic energy which surrounds them.

Now we turn to a detailed analysis of the data set for case S3, which yields a large number of buoyant magnetic loops. In this chapter we will explore the properties of these wreaths and the variety of buoyant magnetic structures this simulation can achieve. In the following chapter we will examine the statistical properties of these loops over a magnetic activity cycle. This is the first of two chapters which are largely quoted from Nelson et al. (2013a)[1] . I was the primary author of this paper, and as such I carried out all of the simulation and analysis work. I primarily wrote the text of the paper. My co-authors provided essential contributions in formulating the simulations and the analysis, and in providing significant guidance in the writing process.

[1] Nelson, N. J., Brown, B. P., Brun, Sacha A., Miesch, M. S., & Toomre, J. 2013b, Buoyant Magnetic Loops Generated by Global Convective Dynamo Action, Sol. Phys. Online First, DOI:10.1007/s11207-012-0221-4

7.1 Overview

Our global 3D simulations of convection and dynamo action in a Sun-like star reveal that persistent wreaths of strong magnetism can be built within the bulk of the convention zone. Here we examine the characteristics of buoyant magnetic structures that are self-consistently created by dynamo action and turbulent convective motions in a simulation with solar stratification but rotating at three times the current solar rate. These buoyant loops originate within sections of the magnetic wreaths in which turbulent flows amplify the fields to much larger values than is possible through laminar processes. These amplified portions can rise through the convective layer by a combination of magnetic buoyancy and advection by convective giant cells, forming buoyant loops. We measure statistical trends in the polarity, twist, and tilt of these loops. Loops are shown to preferentially arise in longitudinal patches somewhat reminiscent of active longitudes in the Sun, although broader in extent. We show that the strength of the axisymmetric toroidal field is not a good predictor of the production rate for buoyant loops or the amount of magnetic flux in the loops that are produced.

7.2 Flux Emergence and Convective Dynamos

Convective dynamo action in the interior of the Sun is source of the magnetism which creates sunspots and drives space weather. Such magnetism is not limited to the Sun, as magnetic activity is observed to be ubiquitous among sun-like stars. To understand the origin of sunspots and starspots, the processes which generate magnetic structures and then transport them through the convection zone to the surface must be explored. Here we present the results of a global numerical simulation, called case S3, which self-consistently generates wreaths of strong magnetic field by dynamo action within the convective zone. Case S3 models the convection zone of a sun-like start nominally rotating at three times the current solar rate, or $3\Omega_{\odot}$. The wreaths reverse polarity in a cyclic fashion, yielding cycles

of magnetic activity. Portions of these wreaths form buoyant magnetic structures, or loops, which rise through our convective envelope. Initial results on the behavior of a small number of these loops were reported in Nelson et al. (2011b).

Here we discuss the properties of a much larger number of loops in order to get a statistical description of their properties. We find coherent magnetic structures with a variety of topologies, latitudinal tilts, twists, and total fluxes. Additionally, we observe only a weak correlation between the unsigned magnetic flux in a buoyant loop and the axisymmetric toroidal magnetic field at that latitude and time, indicating that the generation mechanism for these loops relies on local, coherent toroidal field structures amplified by turbulent intermittency rather than large-scale instabilities of axisymmetric fields. We also find evidence for longitudinal intervals which preferentially produce buoyant loops, hinting at a possible origin for active longitudes for sunspots (Henney & Harvey, 2002), though out intervals are quite broad.

7.3 Nature of the Simulation

We use the 3-D anelastic spherical harmonic (ASH) code to model large-scale convective dynamo action in the solar convective envelope. ASH solves the anelastic MHD equations in rotating spherical shells (Clune et al., 1999; Brun et al., 2004). ASH is limited to the deep interior due to the anelastic approximation, which limits us to low Mach number flows. Additionally we stay away from the near-surface layers because we cannot resolve the small scales of granulation and super granulation realized near the photosphere. Our simulation extends from 0.72 $R_\odot$ to 0.965 $R_\odot$, covering a density contrast of about 25 from top to bottom. The details of the numerical scheme used in case S3 are described in Brown et al. (2010), and the specific parameters are given in Nelson et al. (2013b). Of special note, in case S3 the Rossby number is 0.581, which is in the same rotationally influenced regime as the giant cell convection realized in the solar interior (Miesch, 2005). Thus the dynamics in case S3 may be broadly applicable to stars like the Sun in which rotational influences on

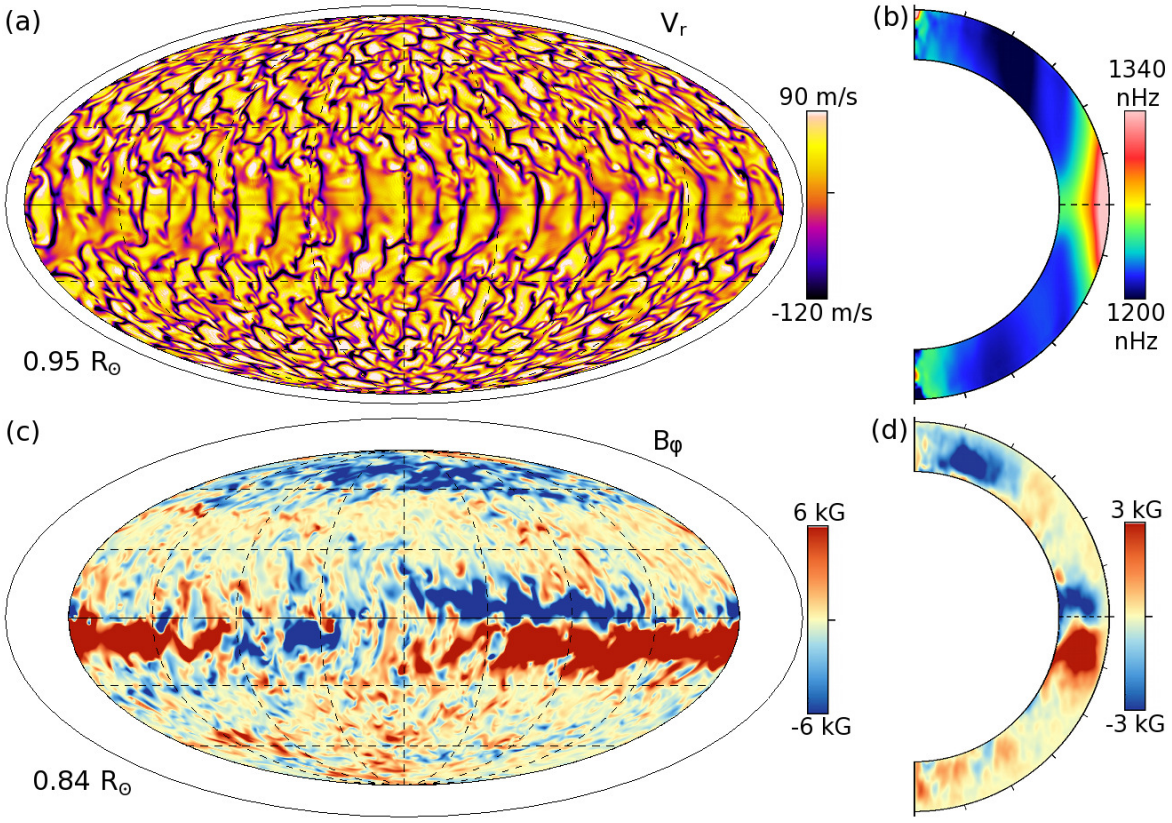

Figure 7.1: (a) Snapshot of radial velocities v_r at time $t_1 = 716$ days in case S3 on a spherical surface at $0.95R_\odot$ shown in Mollweide projection (equator at center, lines of constant latitude parallel) in proportional size (outer ellipse represents photosphere). (b) Rotation rate Ω averaged in longitude and time. Strong differential rotation is achieved in radius and latitude over the simulated domain. (c) Companion snapshot of toroidal magnetic field B_ϕ at $0.84R_\odot$, with a strong coherent magnetic wreath in each hemisphere (blue negative, red positive, ranges labeled), with considerable small-scale fields also present. (d) Azimuthally-averaged toroidal magnetic field $\langle B_\phi \rangle$ at the same instant. Low-latitude wreaths are evident in both hemispheres .

convective motions are significant.

To achieve very low levels of diffusion, we employ a dynamic Smagorinsky subgrid-scale (SGS) model which uses the self-similar behavior in the inertial range of the resolved turbulent cascade to extrapolate the diffusive effects of unresolved scales. In this model the viscosity at each point in the domain is proportional to the magnitude of the strain

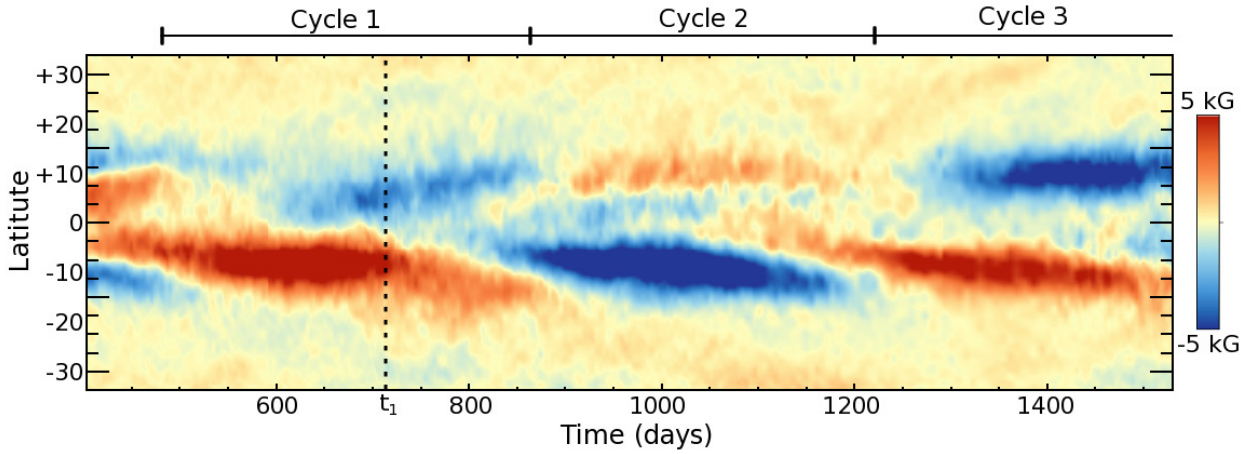

Figure 7.2: Evolution in time of the longitudinally-averaged toroidal magnetic field $\langle B_\phi \rangle$ at mid-convection zone shown in a time-latitude plot. Three magnetic reversals are realized, each with a period of about 280 days (reversals indicated by hash marks, cycles labeled 1-3 for convenience). Considerable asymmetry is seen between hemispheres in both the phase and amplitude of the reversals. The time t_1 at which snapshots in Figures 7.1 and 7.3 are sampled is indicated by the dotted line at 716 days.

rate tensor and the constant of proportionality is determined using the resolved flow and an assumption of self-similiar behavior. A detailed description of the dynamic Smagorinsky SGS model is provided in Chapter 3. Here we employ constant SGS Prandtl and magnetic Prandtl numbers of 0.25 and 0.5, respectively. In practice this permits a reduction in the average diffusion by about a factor of 50 compared to a simulation with identical resolution and a less complex SGS model, such as in Brown et al. (2011). This reduction in diffusion is critical not only in enhancing the turbulent intermittency of the magnetic field, but also in permitting the buoyant loops to rise through the convective layer without diffusive reconnection altering their magnetic topology.

Figure 7.1(a) shows a snapshot of the convective radial velocities v_r in case S3 at a single instant. The convection near the equator is dominated by convective rolls aligned with the rotation axis, while the higher latitudes have more vortical motions. The rotational influence on the convective motions is key to achieving a pronounced differential rotation (Miesch et al.,

2006). Case S3 maintains strong gradients in angular velocity Ω (Figure 7.1(b)), which are key to generating the large-scale magnetic wreaths through the Ω-effect. Figures 7.1(c-d) show snapshots of the wreaths, both on a spherical surface at mid-convection zone and in their axisymmetric component. The wreaths are dominated by non-axisymmetric fields and thus have a limited longitudinal extent, while clearly still retaining global coherence.

Remarkably, the wreaths are generated and maintained in the bulk of the convective layer without a tachocline of shear. It had been reasonably postulated that coherent, large-scale fields in the convection zone would be shredded by the intense turbulence of the convective motions. However, the convective turbulence evidently does not destroy the wreaths. In fact, Nelson et al. (2013b) showed that while the axisymmetric fields show some decrease in amplitude with increased turbulence, regions of extremely strong fields actually become more common due to increased turbulent intermittency. In regions of particularly strong magnetic fields, the convective motions are diminished by the Lorentz force, resulting in even less convective disruption of the wreaths.

The dynamic Smagorinsky procedure requires additional computational expense, limiting the time evolution of our simulations. Case S3 presented here was run for 3.4 million time steps, with an average of 40 seconds of simulated time per step. In total, case S3 covers about 4 years of simulated time, compared to the rotational period of 9.3 days and the convective over-turning time of about 50 days. Figure 7.2 shows the time evolution of the axisymmetric toroidal magnetic field $\langle B_\phi \rangle$ in case S3 over about 1100 days. In this interval there are three reversals of global magnetic polarity. While the true polarity cycle involves two reversals, we term the interval between each reversal an activity cycle in the same way the Sun's 11-year activity cycles are just about half of the true 22-year polarity cycle. These three activity cycles have durations of about 280 days, although the reversals are not generally synchronized between the two hemispheres. This nonuniform behavior hints at the important role of asymmetries in the flows between the two hemispheres (DeRosa et al., 2012).

7.4 Identifying Magnetic Loops

In order to provide a consistent treatment, we define a magnetic loop as a coherent segment of magnetic field which extends from below $0.80R_\odot$ to above $0.90R_\odot$ and back down again (Nelson et al., 2011b). Additionally, we require that the buoyant loops have peak magnetic field strengths greater than 5 kG above $0.90R_\odot$ at selected samples in time. To find magnetic loops fitting that description, we have developed a pattern-recognition algorithm which searches the 3-D volume of our simulation. The most direct method of finding loops is to look for magnetic field lines which pass through a region where $|B_\phi| > 20$ kG below $0.80R_\odot$, then pass through a region above $0.90R_\odot$ with $|B_\phi| > 5$ kG, and then again through a region where $|B_\phi| > 20$ kG below $0.80R_\odot$ over less than 50° in longitude. In practice, this can be done much more efficiently by recognizing that the loops start as primarily toroidal magnetic field structures, but that as they rise into a region of faster rotation the loops are tilted in longitude so that one side of the loop retains a strong component of B_ϕ while the other becomes almost totally radial. Thus we initially identify loop candidates by looking for this pattern of B_ϕ and B_r. The loop candidates are then verified using field line tracings.

Case S3 uses 1024 grid points in longitude, 512 in latitude, and 192 in radius for 8 evolution variables (velocity $\vec{v}$, magnetic field $\vec{B}$, entropy S, and pressure P), thus each snapshot in time requires over 3 GB of data. We are therefore limited in the number of time steps we can analyze. For the 278 days of cycle 1 we have run our loop finding procedure on snapshots of the simulation spaced roughly every 4 days. In doing so we have identified 131 buoyant loops. Additionally we have sampled cycle 2 for 20 days and cycle 3 for 40 days with the same 4 day cadence and found 27 additional loops. We anticipate that we would find many more loops if we carried out a more complete search through cycles 2 and 3.

For a subset of the 158 loops found in case S3, we have carried out detailed analyses of the dynamics of the rise of 22 of the loops (11 from cycle 1 and 11 more from cycle 3). To do this we have used data with a time resolution of about 10 hours, which is sufficient to

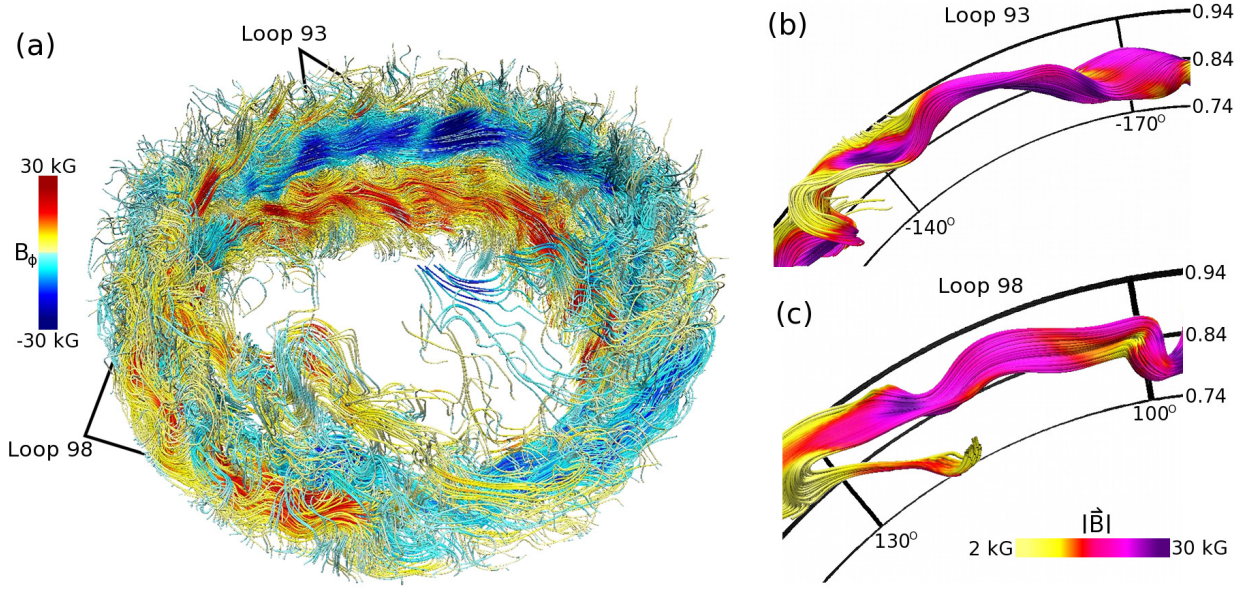

Figure 7.3: (a) Volume-renderings of magnetic field lines at low latitudes colored by toroidal field B_ϕ (red positive, blue negative, amplitudes labeled). Strong magnetic wreaths exist in each hemisphere with considerable modulation in longitude. The location of two sample buoyant loops (labeled loops 93 and 98) are indicated. In this view it is difficult to distinguish the loops from the surrounding magnetic fields. (b-c) Close-up views of loops 93 and 98 at the same instant with only field lines comprising the buoyant loops rendered for visual clarity. Color shows magnitude of magnetic field strength (yellow weak, purple strong). Loop 93 is part of the negative polarity wreath in the northern hemisphere, while loop 98 is part of the positive polarity wreath in the southern hemisphere. Time shown corresponds to the snapshots in Figure 7.1 and t_1 in Figure 7.2.

track loops backward in time from their peak radial position to their origins in the magnetic wreaths. We find that while the specific evolution of each of these 22 loops varies due to the chaotic nature of the turbulent convection, all 22 loops have significant acceleration due to magnetic buoyancy and are embedded in convective upflows which aid their rise. This agrees with the dynamics of the sample loop studied in detail in Nelson et al. (2011b). While we cannot with certainty say that magnetic buoyancy was a significant factor in the rise of all 158 magnetic loops, we find that for all 22 of the loops studied at high time resolution the average ascent speed due to magnetic buoyancy alone is at least 28% of the total average

ascent speed. Thus we assume that magnetic buoyancy is at least an important factor in the rise of these loops.

Figure 7.3 displays the complex nature of the magnetic fields in case S3 with a volume rendering of magnetic field lines in the convection zone at low latitudes, forming two prominent magnetic wreaths of opposite polarity. We also indicate the location of two buoyant magnetic structures, labeled loops 93 and 98. The simulation continuously exhibits magnetic fields throughout the convection zone, including strong, small-scale magnetic fields, coherent buoyant loops, and large-scale wreaths with global scale organization. Prior studies of magnetic buoyancy typically involved specified buoyant magnetic structures whose rise was studied in a largely unmagnetized domain. In contrast, our convection zone has on average 77% of our simulated volume containing magnetic fields in excess of 1.5 kG, and 21% posses field amplitudes in excess of 5 kG. This makes identification of the buoyant loops difficult. Figures 7.3(b-c) show close up renderings of only the field lines comprising buoyant loops 93 and 98. We have omitted rendering other field lines in those regions for visual clarity. Magnetic fields in the loops can be quite strong even near the top of our domain, with portions of loop 93 exceeding 25 kG at $0.92R_{\odot}$.

7.5 Properties of Rising Loops

Unlike many previous models of buoyant magnetic transport in which convective turbulence is presumed to play a purely disruptive role, the buoyant loops in our models fall under the turbulence-enhanced magnetic buoyancy paradigm discussed in Nelson et al. (2013b). In this model turbulent intermittency plays a key role in the formation of strong, coherent structures which are magnetically buoyant and can be advected by convective upflows. As was shown in Nelson et al. (2011b), these loops rise through a combination of magnetic buoyancy and advection by giant cell convection. Thus convection plays a key role both in the dynamo which generates the buoyant magnetic fields, and also in the transport of the magnetic loops. Due to the cooperation between convective motions and magnetic buoy-

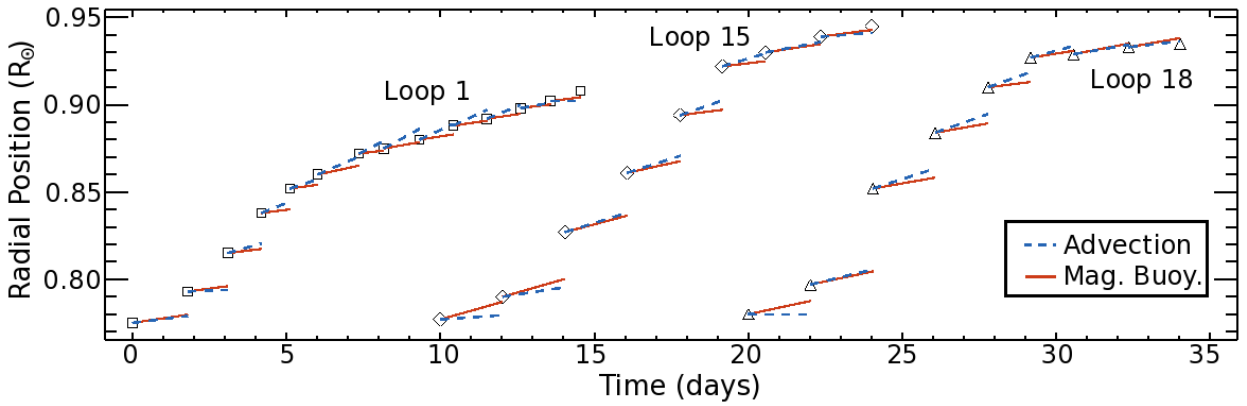

Figure 7.4: Location of three buoyant loops (labeled loops 1, 15, and 18) as a function of time as they rise from the core of the toroidal wreaths in the lower convection zone through the simulated domain to their peak radial positions between 0.91 and 0.95 $R_\odot$. Times are given relative to the launch of the loops with offsets for clarity. Also plotted are the mean motions of the loops at each time interval due to magnetic buoyancy (red lines) and advection by the surrounding convective upflows (blue line). Additional motions due to forces such as thermal buoyancy, viscous drag, and magnetic tension are not plotted, and account for what may appear to be missing in this display.

ancy, the loops are able to rise from below $0.80R_\odot$ to above $0.90R_\odot$ in as little as 12 days, as suggested by Figure 7.4.

7.5.1 Dynamics and Timing of Loop Ascents

Buoyant loops are born from the much larger and less coherent magnetic wreaths shown in Figures 7.1 and 7.3. The wreaths in case S3 are not axisymmetric structures and are typically coherent over spans of between 90° and 270° in longitude. Wreaths exhibit a high degree of magnetic connectivity with the rest of the convection zone, with field lines threading in and out, suggesting rather leaky overall structures. Wreaths in case S3 generally have average field strengths of between 10 and 15 kG and are confined in the lower half of the convection zone by magnetic pumping. In the core of the wreaths convective motions can be limited by Lorentz forces to as little as a 1 m s^{-1}.

Portions of these wreaths can be amplified by intermittency in convective turbulence.

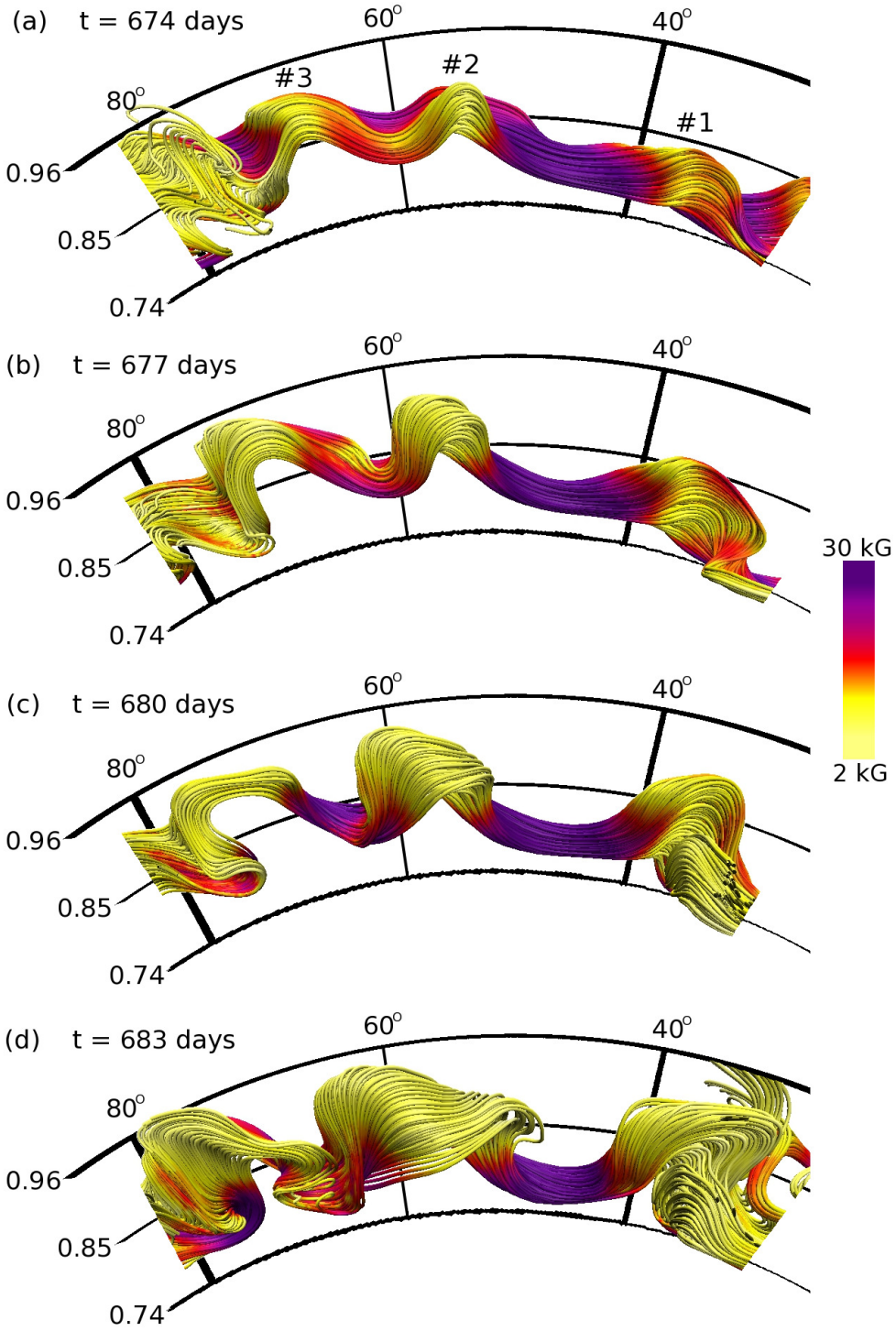

Figure 7.5: Sequence of volume renderings of magnetic field lines which comprise three buoyant loops (labeled loops 1, 2 and 3) as they rise through the convective layer with three days between each frame (times indicated, progressing downward). The expansion of each loop is here evident as they rise. Magnetic buoyancy and advection by convective upflows allow the loops to traverse the radial interval shown here in roughly 10 days. Loop 1 is also shown in Figures 7.4 and 7.7. Loop 3 is also shown in Figure 7.6.

Turbulence has been shown to generate strong, coherent structures in a variety of settings (Pope, 2000). In case S3 localized portions of the wreaths are regularly observed to attain field strengths of 40 kG and be highly coherent over as much as 50° in longitude. These magnetic structures with strong fields are able to rise into regions where vigorous convective motions are present. Many structures are seen to emerge from the core of the wreaths only to be pummeled by a convective downflow, disrupted by a region of unusually strong turbulence, or limited by the development of a particularly unfavorable magnetic configuration. Whether any given magnetic structure becomes a buoyant magnetic loop is therefore not due to the passing of some threshold, but largely a conspiracy of favorable events.

Figure 7.4 shows the radial location of the top of three different loops as they rise from roughly $0.77R_\odot$ to above $0.90R_\odot$. Also plotted are the contributions to the radially outward motion due to magnetic buoyancy and advection by convective upflows. The buoyant acceleration due to magnetism is deduced by comparing the density in the region within the loop and the density of the surrounding convective plume. We do this to separate magnetic and thermal buoyancy effects. Each of these three loops starts in a region where convective motions are largely suppressed by Lorentz forces due to the very strong magnetic fields in the cores of the magnetic wreaths. As they begin to rise, the magnetic energy at the core of the wreath exceeds the kinetic energy of the flows locally by a factor of 10 to 100. As the loops rise, they enter regions of strong upflows and are advected upwards by the convective giant cells. Averaged over their entire ascent, magnetic buoyancy drives an average upward speed of about 50 m s^{-1} for these three loops, in addition to the surrounding upflows which move at an average of about 80 m s^{-1}. At their maximum radial extent, the loops are prevented from rising further by our impenetrable upper boundary condition.

Figure 7.5 shows three sample loops (labeled loops 1, 2, and 3) as they rise over 10 days. The loops remain coherently connected as they rise. Here again all three loops are aided by convective upflows while convective downflows pin the ends of the loops downward. The direction of motion is largely radial with a deflection of as much as 10° in latitude toward

higher latitudes. This deflection is largely due to the roughly cylindrical differential rotation contours realized in this simulation.

Loops expand as they rise through the stratified domain, but less than would be expected for a purely adiabatic rise. Without any diffusion or draining of material along the field lines, the cross-sectional area of the loops should be inversely proportional to the background pressure, leading to expansion by roughly a factor of 20. Instead loops are seen to expand by a factor of 5. This is consistent with previous studies of buoyant magnetic structures in which expansion of magnetic structures is seen to be inversely proportional to the square root of the change in pressure (Fan, 2001; Cheung et al., 2010) .

The expansion of the loops is slowed by draining flows of higher entropy fluid along magnetic field lines, which serves to cool the material at the top of the loop. These divergent flows are too small to be measured in individual loops due to the turbulent background, but when averaged over 158 loops, a mean divergent flow of 47 cm s^{-1} is obtained along the top of the loops. This compares well with estimates from a simple model (neglecting viscosity and thermal diffusion) which assumes that the draining flows are constant in time and uniform perpendicular to the axis of the loop.

Axial flows along loops are also seen as the loops rise through regions of faster rotation. When averaging over many loops, a net axial flow of 5.1 m s^{-1} is detectable in the retrograde direction, consistent with the fluid inside the loop tending to conserve its specific angular momentum as the loop moves radially outward. Loops often become distorted as this retrograde motion interacts with the surround prograde differential rotation as the loop rise across rotational contours (see Figure 7.1(b)).

The geometry of each loops we have examined is uniqued in its details, but Figure 7.6 shows three different perspectives on a single 3D volume-rendering of a typical loop. Loop 3, which is also shown in Figure 7.5, is in the northern hemisphere and its top is roughly centered at 76° N latitude and 12° W longitude. Its parent wreath-segment runs slightly north-west to south-east at this location and time, causing the western foot-point to be

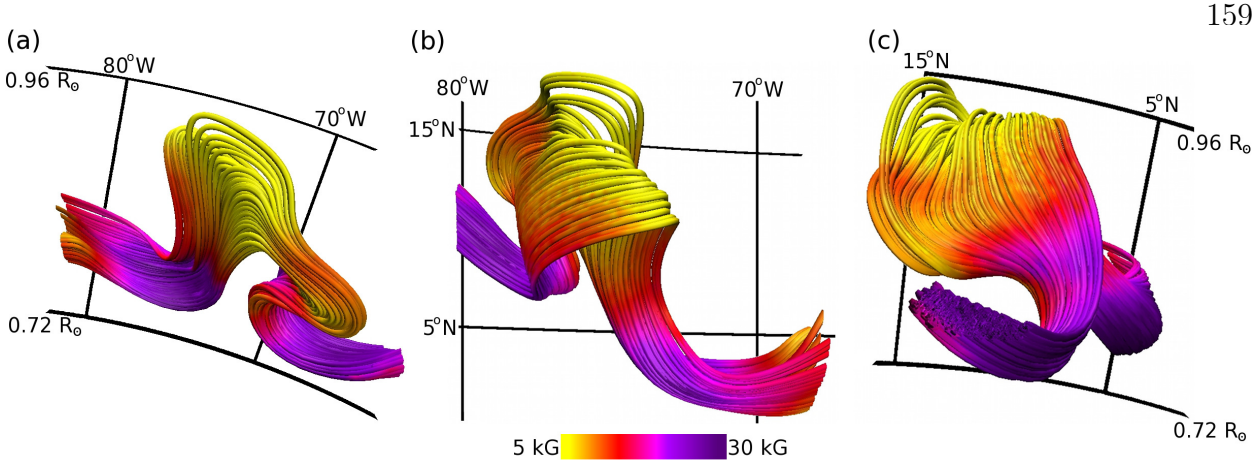

Figure 7.6: Three viewpoints the same volume-rendering of magnetic field lines in Loop 3 at $t = 683$ days (same as in Figure 7.5(d)). Color indicates amplitude of magnetic field (purple strong, yellow weak). Views are looking (a) south along the rotation axis with grid lines in radius (in units of the solar radius) and longitude, (b) radially inward with grid lines in longitude and latitude, (c) westward along the axis of the magnetic wreath.

centered further north than the eastern foot-point. The deflection away from the equator is evident in Figures 7.6(b and c) as the top of the loop is roughly 10° further north than the foot-points. The roughly five-fold expansion of the loop's cross-sectional area can be seen, particularly in Figure 7.6(c). This loop also shows an asymmetric top due to a downflow plume impacting the eastern side of the top of the loop, causing the western wide to extend further in radius.

Loops start with a wide variety of field strengths and sizes and at a variety of initial radial positions. Most loops start between 0.75 and 0.78 $R_\odot$, although loops starting as low as 0.73 $R_\odot$ are evident. When loops are traced backward in time to their starting location in order to identify the flux which will become buoyant and rise, we find that most progenitors of loops begin with about 10^{25} Mx of flux. The structures loose roughly 90% of their flux as they rise to their peak radial positions between 0.90 and $0.96 R_\odot$. Much of the flux is lost as convection in a stratified fluid requires a large fraction of the fluid to overturn prior to reaching the top of the domain. Figure 7.7 shows the magnetic flux as a function of the

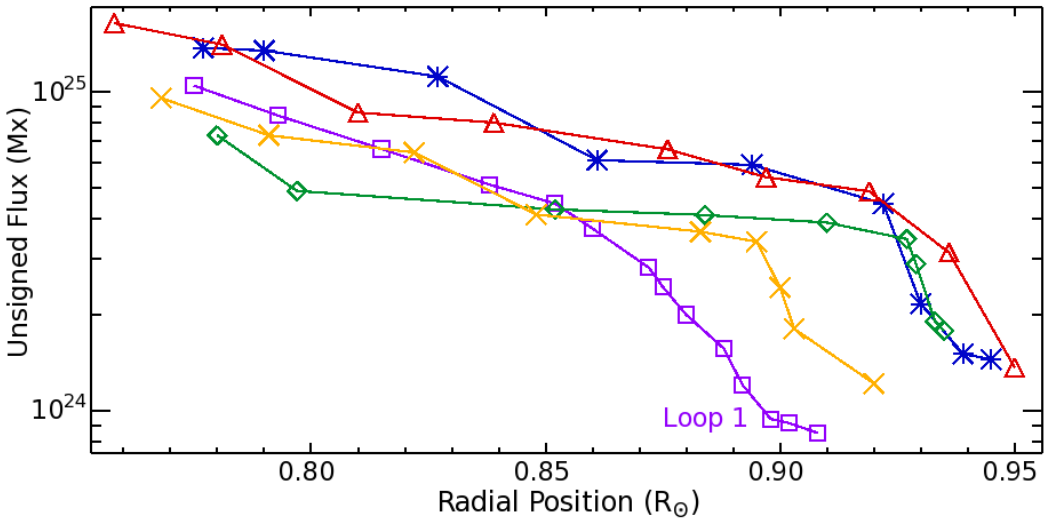

Figure 7.7: Unsigned magnetic flux in five sample loops as they rise through the convective layer, including loop 1 (see Figures 7.4 and 7.5). Loops continuously loose magnetic flux through both diffusion and leakage of fluid. Their ascent is faster than the convective upflows in which they are embedded, leading to the loss of fluid and flux due to drag-like effects. Here and in the 22 loops for which detailed tracking is possible, the initial and final magnetic flux are not correlated.

radial position of the top of the loop for five sample loops. Initial flux and initial radial location do not appear to be good predictors of either final radial location or final magnetic flux.

In the specific case of loop 1, 92% of the magnetic flux it started with is lost over the course of its ascent while 69% of the mass flux at $0.78R_\odot$ turns over below $0.91R_\odot$. The overturning mass flux carries away 61% of the magnetic flux, as regions of lower field strength preferentially are lost. The next largest contributor is resistive diffusion, which dissipates 19% of the initial flux. The remaining 12% of the flux is lost through a combination of small-scale turbulent advection and shear. Eventually diffusive reconnection realigns the fields so that the loops are no longer distinct from the surrounding MHD turbulence.

Chapter 8

Collective Properties of Emergent Magnetic Structures

Having discussed the dynamics of our buoyant magnetic loops, we now turn to a discussion of their collective properties. This is the second of two chapters which are largely quoted from Nelson et al. (2013a) [1] . I developed and applied the analysis presented here. I was also the primary author for the text of that paper.

8.1 Statistical Distribution of Twist and Tilt

Previous MHD simulations of flux emergence have emphasized that magnetic structures must be twisted to remain coherent as they rise (see review Fan, 2009). Twist in this context can be defined by a parameter q_A, which for a uniformly twisted flux tube is defined as

$$B_{\parallel} = a_{\pm}\, q_A \lambda \left| \nabla \times A_{\parallel} \right| , \tag{8.1}$$

where $B_{\parallel}$ and $A_{\parallel}$ are, respectively, the magnetic field and magnetic vector potential along the axis of the flux tube, $a_{\pm}$ is 1 in the northern hemisphere and -1 in the southern hemisphere, and λ is the distance from the axis of the flux tube. For the tube to remain coherent as it rises, previous numerical simulations have suggested that twist must exceed some critical value Q_A (Moreno-Insertis & Emonet, 1996). Fan (2008) used 3-D simulations of buoyant magnetic structures rising through a quiescent, stratified layer and found a critical level of twist $Q_A \approx -3 \times 10^{-10}$ cm^{-1}.

[1] Nelson, N. J., Brown, B. P., Brun, Sacha A., Miesch, M. S., & Toomre, J. 2013b, Buoyant Magnetic Loops Generated by Global Convective Dynamo Action, Sol. Phys. Online First, DOI:10.1007/s11207-012-0221-4

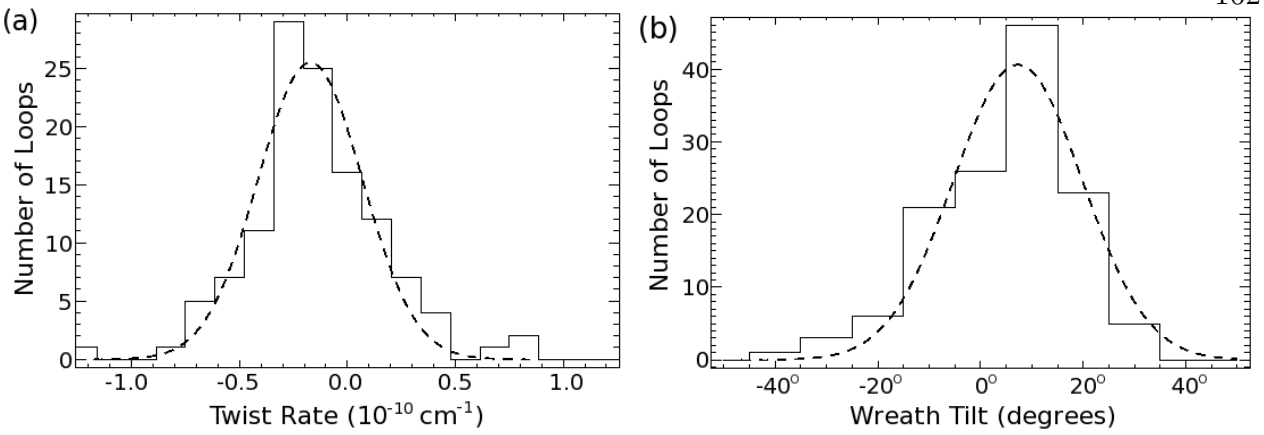

Figure 8.1: (a) Histogram of twist rate parameter q_J values for the 131 loops observed in cycle 1 along with the best-fit Gaussian distribution of those values. The distribution shows a slight preference for negative twist rates, though the mean twist rate is $(-1.8 \pm 2.4) \times 10^{-11}$ cm^{-1}. (b) Histogram of latitudinal tilt Δ_θ values for the same 131 loops. Positive tilts indicate that the leading edge of the loop is closer to the equator than the trailing edge, as used with Joy's law. Tilts have been calculated so that all values fall between $\pm 90°$ for this analysis. Positive tilts are preferred and the mean latitudinal tilt is $7.3° \pm 12.6°$ in latitude.

For our simulation, the loops are clearly not uniformly twisted flux tubes, so we calculate another measure of twist following the procedure used in observational studies (e.g., Pevtsov et al., 1995, 2003; Tiwari et al., 2009). Sunspots often show large variations in the level and even sign of twist, so a weighted average of the twist parameter is employed, which we call q_J. We compute the twist parameter as

$$q_J = a_\pm \left[\frac{J_\phi}{B_\phi} \right], \tag{8.2}$$

where braces denote an average over radius and latitude for a longitudinal cut taken through the loop and $a_\pm$ is 1 in the northern hemisphere and -1 in the southern hemisphere. We restrict our averages to contiguous regions with the correct polarity and where fields are stronger than 2.5 kG. Figure 8.1(a) shows a histogram of values for the twist parameter q_J for the 131 loops identified in cycle 1, as well as the best-fit Gaussian to that distribution which peaks at $\bar{q_J} = -1.8 \times 10^{-11}$ cm^{-1}. For comparison,Tiwari et al. (2009) report an average twist parameter of $\bar{q_J} = -6.12 \times 10^{-11}$ cm^{-1} for a sample of 43 sunspots.

It is difficult to make a direct comparison between the two measures of twist mentioned here. In practice our loops are poorly represented by uniformly twisted tubes. It is possible to compute the value of q_A at each point in the loop and create an average value, but we find that those averages are highly sensitive to the weighting of the points and the region over which the average is taken. Alternatively, we have computed the value of q_J for the formulation employed in Fan (2008) and find that the value varies with the location and size of the magnetic structure in radius and latitude. For most reasonable parameter choices, the q_J/q_A is between 1 and 2. When comparing with photospheric measurements, we must also remember that considerable changes may take place as magnetic flux passes through the upper 5% of the solar convection zone. The dynamics of twisted buoyant loops in that region is beginning to be studied in local domains (Cheung et al., 2010).

Of the 131 loops in cycle 1, only 13 had current-derived twist parameters q_J within an order of magnitude of the critical value Q_A. One explanation may be that convective upflows assisting the rise of these loops reduces the drag that they experience, thus making them less susceptible to disruption as they rise and therefore less dependent on twist for coherence. Whatever the cause, we do not see a critical value of twist beyond which loops are unable to traverse our domain.

Additionally, we can look at the latitudinal tilts of the buoyant loops. We calculate these tilts by computing the center of each loop at all longitudes where the center is within $0.02R_\odot$ of its peak position and then fitting a linear trend to latitudinal locations of the loop center. We define positive tilts to be those with the eastern side of the loop closer to the equator than the western side, as used in Joy's law. Here we do not consider the polarity of the loops, so values are restricted to the interval $[-90°, 90°]$. The distribution of tilts seen in the 131 loops found in cycle 1 is shown in Figure 8.1(b), along with the best-fit Gaussian to that distribution, which peaks at 7.3° but is quite broad. This is similar to observations of tilts in sunspots where the trend towards Joy's law is part of broad distribution in tilt angles (Li & Ulrich, 2012).

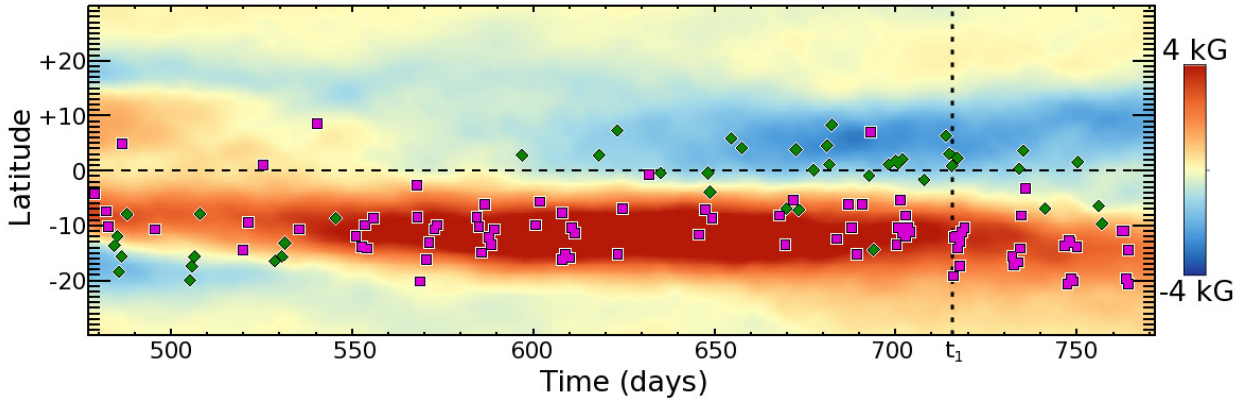

Figure 8.2: Time-latitude display of toroidal magnetic field averaged in longitude and radius during the peak of cycle 1. Over-plotted symbols indicate the time and latitude of 131 buoyant loops in the style of a synoptic map, with positive polarity loops shown as pink squares and negative polarity loops as green diamonds. Some loops may be present from the previous cycle, particularly prior to day 550 in the southern hemisphere. Time t_1 at which the snapshots in Figures 7.1 and 7.3 are taken is indicated by the dotted line.

8.2 Magnetic Cycles with Buoyant Loops

Case S3 achieves three magnetic activity cycles with reversals in global magnetic polarity. If we define the cycle period as the time between changes in the sign of the antisymmetric components of the toroidal field at low latitudes, as in Brown et al. (2011), then cycles 1 and 2 have periods of 278 and 269 days, respectively. Cycle 3 had not ended at the present end of the simulation, but has been simulated for 228 days. The coexistence of cyclic magnetic activity and buoyant loops provides an opportunity to probe the relationship between axisymmetric fields which are commonly used in 2-D dynamo models (see review by Charbonneau, 2010) and the buoyant transport of magnetic flux.

We have chosen to conduct our analysis primarily using cycle 1 since the process of finding and characterizing buoyant loops is too data intensive to be carried out conveniently for all three cycles. Figure 8.2 shows a time-latitude plot of the mean toroidal field (averaged in longitude and in radius over the lower convection zone from 0.72 to 0.84 $R_\odot$), as well as the location in time and latitude of the 131 buoyant loops detected in cycle 1. It is evident

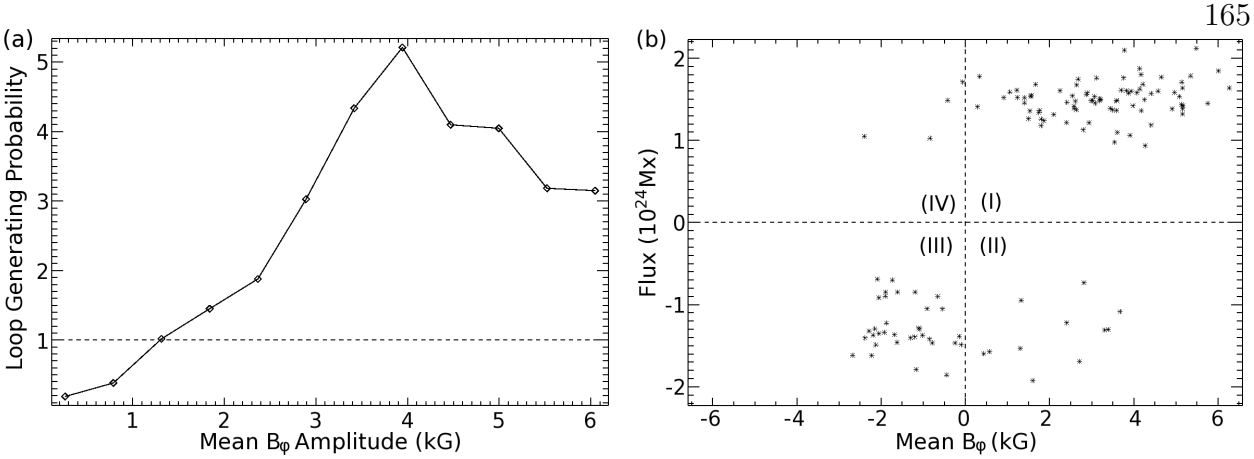

Figure 8.3: (a) Relative probability that a region with given mean B_ϕ will produce a buoyant loop compared to the production rate of buoyant loops in cycle 1 averaged over all events. For cycle 1 the average occurrence rate for loops was 7.6×10^{-3} day^{-1} degree^{-1}. We normalize all probabilities by this rate, thus the dashed line represents the average loop production rate. Note that nearly 60% of the times and latitudes considered have mean field strengths of less than 1.5 kG. (b) Total magnetic flux as a function of axisymmetric toroidal magnetic field averaged in radius at the latitude and time of each of the 131 buoyant loops in Figure 8.2. While most loops are associated with mean magnetic fields of the correct sense, there are 15 loops in quadrants II and IV. These loops arise from wreath segments which are canceled in the longitudinal averaging procedure by large or stronger wreath segments at the same time and latitude of the opposite polarity.

from this representation that the loops do not arise uniformly in time. Although loops tend to appear at times and latitudes when the mean toroidal fields are strong, they can also appear at times and latitudes with relatively weak mean fields. There are even examples in which loops have the opposite polarity to the longitudinally-averaged mean fields at that time and latitude. This is consistent with the non-axisymmetric nature of the wreaths shown in Figures 7.1(c-d) where smaller-scale segments of intense toroidal field can be masked in the longitudinal average by larger segments of the opposite polarity.

8.2.1 Relation of Loop Emergence and Mean Field Strength

In many mean-field models it is assumed that buoyant magnetic flux (which can be used as a proxy for the sunspot number) at a given latitude and time is proportional to the axisymmetric toroidal field strength at that location and time at the generation depth. In

particular, the Babcock-Leighton model postulates that the buoyant transport of magnetic flux occurs whenever the axisymmetric magnetic field exceeds some threshold value (e.g., Durney, 1995; Chatterjee et al., 2004). Here we can test this assumption by looking at the probability that a region with a given axisymmetric field strength will produce a buoyant loop. Figure 8.3 shows the relative probability that a region with a given mean field strength will produce a buoyant loop. Over cycle 1, the average production rate of buoyant loops is roughly one loop every two days within 30° of the equator. Regions with $\langle B_\phi \rangle \leq 1.5$ kG cover about 60% of the time-latitude domain and produce loops at or below the average rate. The generation probability per unit time and latitude rises to five times the mean rate for regions with $\langle B_\phi \rangle \approx 3.9$ kG. Interestingly, the generation probability then falls for the regions of the strongest $\langle B_\phi \rangle$. Indeed, the strongest regions of axisymmetric field are only about three times more likely to produce buoyant loops than the average production rate. The relatively small sample size invites further study on this topic, as only 5% of the domain is covered by fields above 4.2 kG, which fall in the last four bins. However the implication that axisymmetric toroidal fields above some threshold value are less likely to produce buoyant loops may have significant implications for mean-field models of the solar dynamo.

To further explore the correlation between the axisymmetric field strength and the amount of buoyant magnetic flux, we can look for correlations between the amount of flux in a given buoyant loop and the axisymmetric fields at the time and latitude of its launch. Figure 8.3(b) shows the magnetic flux in each of the 131 buoyant loops from cycle 1 as a function of the average value of axisymmetric toroidal field in the lower convection zone at the time of launch. Out of 131 loops, 15 were launched when the axisymmetric B_ϕ was of the opposite sense. Interestingly, Stenflo & Kosovichev (2012) report that roughly 5% of moderate to large active regions violate Hale's polarity law.

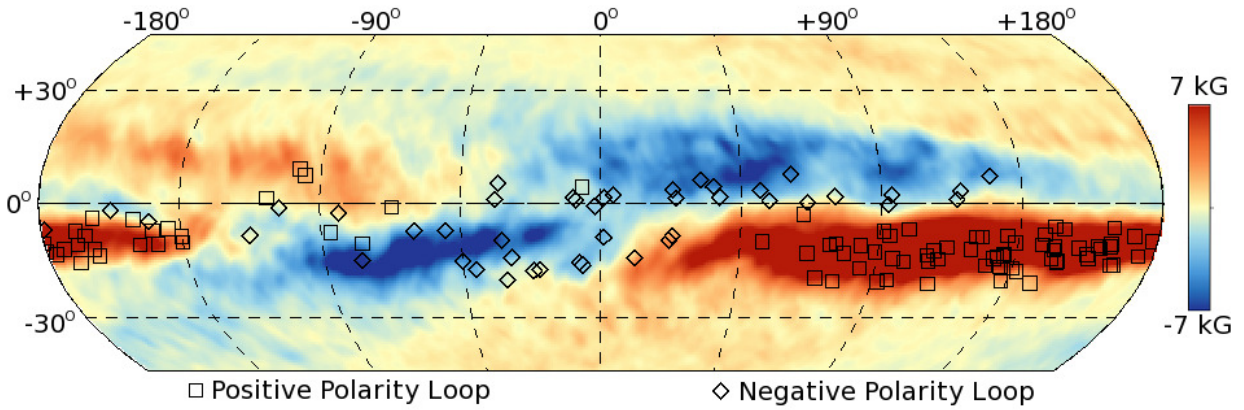

Figure 8.4: Time-averaged toroidal magnetic field on a spherical surface between ±45° of latitude at $0.79R_\odot$ during cycle 1. Symbols indicate the rotational phase in longitude of the 131 buoyant loops from Figure 8.2 at the time they were launched. Squares indicate positive polarity loops while diamonds indicate negative polarity loops. Both the wreaths and loops are confined in longitude. Loops are particularly concentrated in the strong positive wreath segment in the southern hemisphere.

8.2.2 Preferential Longitudes for Loop Creation

The longitudinal concentration of sunspots into so-called active longitudes has been observed for the past several solar cycles (Henney & Harvey, 2002). These active longitudes provide observational evidence that the creation of buoyant magnetic structures is not a purely axisymmetric process. Magnetic wreaths in case S3 tend to be confined in longitude, as was shown in Figure 7.1(c). These wreath segments are generally between 90° and 270° in longitude. Loops tend to be generated in these wreath segments, and thus more likely to appear in those longitudinal patches than other longitudes. Figure 8.4 shows the time-averaged value of B_ϕ at $0.80R_\odot$ over cycle 1 with the longitudinal position of the 131 buoyant loops over-plotted. Loops are much more likely to appear over a roughly 180° patch in longitude in the southern hemisphere. Whereas we have some longitudinal modulation, it is still far from the 10° to 20° confinement seen in active longitudes on the Sun.

The existence of longitudinal patches of both magnetic polarities in case S3 also pro-

vides a potential explanation for the small fraction of active regions of the "wrong" polarity seen in Figure 8.3(b). This provides a possible mechanism for the analogous phenomena in which a small fraction of solar active regions violate Hale's polarity law. While active longitudes in the Sun are more confined than those seen here, the longitudinal confinement of the wreaths in case S3 may provide a possible pathway toward understanding active longitudes.

8.3 Summary and Reflections: Buoyant Loops in Convective Dynamos

Chapters 7 and 8 have explored in detail the first global convective dynamo simulation to achieve buoyant magnetic loops which transport coherent magnetic structures through the convection zone. These buoyant structures arise from large-scale magnetic wreaths, which have been previously described in both persistent (Brown et al., 2010) and cyclic states (Brown et al., 2011; Nelson et al., 2013b). In this work we have focused on case S3, which possesses large-scale magnetic wreaths which undergo cycles of magnetic activity and produce many buoyant magnetic loops. Case S3 was able to achieve buoyant loops due to the use of a dynamic Smagorinsky SGS model which greatly reduced diffusive processes in the simulation.

Although case S3 has a rotation rate greater than the current Sun, the dynamics achieved may be applicable to solar dynamo action. The most salient non-dimensional parameter for the creation of toroidal wreaths is the Rossby number, which considers the local vorticity ω and rotation rate Ω as $\mathrm{Ro} = \omega/2\Omega$. In case S3 the Rossby number at mid-convection zone is 0.581, indicating that the convection is rotationally constrained as is also expected in the bulk of the solar convection zone.

Much of the work on buoyant magnetic flux has generally regarded convection as a purely disruptive process. In our dynamo studies here, convection plays a key role in both the creation of the strong, coherent magnetic fields and the advection of magnetic flux radially outward. Turbulent intermittency provides an effective mechanism for the amplification of magnetic fields to energy densities well above equipartition with the resolved flows (Nel-

son et al., 2013b). Convection also assists in the transport process by the upflows helping to advect the loops. Without convection, buoyant transport of magnetic flux is generally regarded as a low-wavenumber instability on axisymmetric fields. With convection, buoyant loops are formed on convective length scales as the result of non-axisymmetric processes. The loops realized in case S3 are not large-scale instabilities of axisymmetric flux tubes, but rather they result from turbulently amplified coherent structures becoming buoyant and being advected by convective upflows. Similar upward advection of magnetic structures by convection has been seen when considering the impact of convection on flux tubes (Weber et al., 2011, 2012, 2013) or specified magnetic structures (Jouve & Brun, 2009).

When we consider moderate numbers of buoyant loops over an activity cycle, we find a number of trends in their collective behavior. In all of these trends, it is important to note that our statistical sample of 158 loops is significant but still relatively small. First, loops in our simulation clearly show a hemispheric polarity preference analogous to Hale's polarity law for solar active regions, although case S3 shows a slightly higher rate of violations to this trend compared to the Sun. Second, the buoyant loops tend to show latitudinal tilts similar to Joy's law for solar active regions. As in the Sun, a wide variety of tilt angles are observed, though the average tilt angle places the leading edge of the buoyant loop closer to the equator than the trailing edge. Third, the buoyant loops tend to show a degree of twist similar to the twist inferred from photospheric measurements of vector magnetic fields. Again a wide variety of twist parameters are measured centered about a relatively small, negative mean value. Finally there are ranges in longitude which demonstrate repeated emergence of magnetic flux. This longitudinal modulation in the creation of magnetic loops is reminiscent of active longitudes observed in the Sun, but on larger longitudinal ranges than active longitudes in the Sun.

Buoyant transport of magnetic fields is a key ingredient in many models of the solar dynamo. Mean-field models often use parameterizations to represent this buoyant transport. We have considered connections between the axisymmetric toroidal fields in case S3 and the

magnetic flux in the buoyant loops. We find that total flux in a given buoyant loop is only weakly dependent on the strength of the mean field from which that buoyant loop was generated. Additionally, we find that the probability that a buoyant loop will be generated in regions of relatively weak mean fields is significant, and that the strongest mean fields may be less likely to generate buoyant loops than regions of moderate axisymmetric fields.

This simulation is a first step towards connecting convective dynamo models and flux emergence in the Sun and sun-like stars. As we consider the role of turbulent convection, we find clear indications that it plays important roles in the dynamo which generates buoyant magnetic loops and the transport of those loops. This simulation invites continued effort towards linking convective dynamo models and simulations of flux emergence.

Chapter 9

Plume Boundary Conditions in ASH

After discussing convective dynamo models which have achieved very low levels of diffusion both through very high resolution and the use of the Dynamic Smagorinsky SGS model, we now turn to another way in which we can improve our ASH models. In this chapter we will discuss the implementation of and preliminary results from a new boundary condition in ASH which we term a plume boundary condition. This work began in 2011 and is on-going. While I have taken a lead role in this effort, I have benefitted greatly from collaborations with Kyle Augustson, Regner Trampedach, Mark Miesch, Brad Hindman, and Juri Toomre who have provided invaluable assistance. I wrote, debugged, and analyzed this a new module in the ASH code which applies this boundary condition. This work will the subject of a forthcoming journal article.

9.1 Challenges at the Upper Boundary

In the previous chapters we have explored the dynamo processes which yield magnetic wreaths, cycles of magnetic activity, and buoyant magnetic loops in solar-like simulations. With all of these models we have faced two significant challenges. First, all of the models to this point have used an impenetrable upper boundary condition at about $0.97R_{\odot}$. This requires us to use a diffusive process to transport the solar luminosity through the upper boundary of the simulation. This boundary layer has no physical analogue in the real Sun. In the real Sun convection on progressively smaller scales should transport the solar luminosity

all the way to the photosphere. As we outlined in Chapter 2, a global simulation of convective dynamo action that extends to the photosphere is beyond the capabilities of the ASH code for both computational and physical reasons. The scales of motion at the photosphere would require an order of magnitude increase in the maximum spherical harmonic degree of our models. The physical assumptions built into ASH such as low Mach number flows, small variations about the background thermal state, the ideal gas equation of state, and diffusive radiative transfer all become invalid near the photosphere. With these limitations we must place the upper boundary of ASH simulations in the solar interior. If this boundary is impenetrable, we will also induce a significant boundary layer in the solar interior as well. This has serious implications for the behavior of our simulations, particularly in models where buoyant magnetic loops enter this diffusive boundary layer.

The second major challenge in the models of convective dynamo action is maintaining solar-like differential rotation. Differential rotation is crucial to the operation of our dynamo models. As we seek to study solar-like dynamo mechanisms, we require solar-like differential rotation. Fast rotation at the equator requires a sustained transport of angular momentum equatorward by rotationally aligned convective cells in the bulk of the convection zone (Miesch, 2005). Rotational influence relative to inertial forces is measured by the Rossby number. Rotationally-constrained systems such as the Earth's atmosphere or liquid core have low Rossby numbers. Solar surface convection of granulation and supergranulation, which operates on much smaller scales and at higher velocities than the deeper giant cell convection, has a high Rossby number and shows almost no rotational alignment. While there is on-going debate as to the amplitude of the flow speeds in giant cells, by almost all estimates the Sun's giant cell convective flows sit below a Rossby number of unity (Hanasoge et al., 2010; Miesch et al., 2012). ASH simulations at the solar rotation rate yield solar-like differential rotation for moderate levels of turbulence (e.g., Brun & Toomre, 2002; Miesch et al., 2006), but when these models are made less diffusive we see an increase in their convective velocities which pushes them into a higher Rossby number regime with a slowly

rotating equator and fast poles. We term this anti-solar differential rotation. Similar behavior is reported by Gastine et al. (2013) in simulations of giant planet interiors. As much of the convective driving in these simulations occurs near the upper boundary, we believe that the diffusive boundary layer imposed there is leading to excessive convective driving. These over-driven flows are then too fast, allowing their inertial forces to overwhelm their rotational constraints. When we move to slightly faster rotation rates, such as $3\Omega_\odot$, we find that we can maintain solar-like differential rotation, as shown in Chapters 3 and 5.

Both of these challenges are at least partially related to our choice of boundary conditions. By choosing an "open" boundary condition that mimics the convective dynamics occurring in the Sun's near surface layers, we can achieve a simulation without a diffusive boundary layer at its top and with more realistic convective driving. This chapter will focus on the implementation of such a boundary condition. We will also present preliminary results from ASH simulations using a plume boundary condition which has solar-like differential rotation for a moderately turbulent simulation at the solar rotation rate. We will compare this simulation, which we label case P, with three cases using impenetrable upper boundary conditions labeled cases Ia, Ib, and Ic that sample decreasing diffusive processes.

Although we here look at the implication of imposing small-scale plumes entering ASH simulations through the upper boundary, in the longer term these inflows will be largely specified by the properties of smaller-scale solar convection studied with local simulations of the near-surface layers. Advances in local near-surface models have paralleled the progress made in global simulations, reaching high spatial and temporal resolution, and capturing solar-like behaviors which can be compared with observations (e.g., Stein & Nordlund, 2006; Rempel et al., 2009; Augustson et al., 2011). We expect that these models will provide statistical descriptions of the downflowing plume structures and their associated thermal structures which could thence be imposed through our plume boundary condition. These plumes from near-surface convection models would then replace our simplified plume model, described here. We have taken care to define this plume boundary condition to conform

to some of the known properties of surface convection models, though the implementation here relies on somewhat simplified descriptions. Imposing downflows from a near-surface model, even in a statistical sense, is likely to be a challenging undertaking. This chapter will focus on the design and implementation of our plume boundary condition and report on preliminary results from its application to global solar convection models.

9.2 The Consequences of Impenetrable Boundaries

ASH simulations generally use an impenetrable, stress-free condition on their upper boundaries in which

$$v_r = \frac{\partial}{\partial r}\left(\frac{v_\theta}{r}\right) = \frac{\partial}{\partial r}\left(\frac{v_\phi}{r}\right) = 0. \tag{9.1}$$

This formulation ensures that mass and angular momentum are conserved within our domain for hydrodynamic simulations. In addition the domain is heated by a radiative flux at the base of the simulation and energy leaves through the top of the domain via thermal diffusion. All simulations discussed in previous chapters used this formulation. In this manner our hydrodynamic simulations resemble a spherical version of the classic Rayleigh-Benard convection problem which has been studied through theory, simulations, and experiments for close to 90 years (see Chandrasekhar, 1961; Getling, 1998). The major difference, however, is that in Rayleigh-Benard convection the overall heat flux through the horizontal layer is determined by how the convective flows respond to the boundary layers formed at the upper and lower walls, which are typically maintained at fixed temperatures. Thus in Rayleigh-Bernad convection the convection itself determines the heat transport. In ASH simulations we demand that a solar luminosity of energy enter the system at the lower boundary and that one solar luminosity exit the system through the upper boundary. This has important consequences for the resulting flows.

The primary dimensionless parameter that measures convective driving is the Rayleigh

number given by

$$\mathrm{Ra} = -\left(\frac{d\rho}{dS}\right)_P \frac{\partial S}{\partial r}\frac{gL^4}{\rho\nu\kappa}. \tag{9.2}$$

In this formulation Ra is proportional to the entropy gradient $-\partial S/\partial r$ and inversely proportional to each of the diffusion coefficients ν and κ. If we want to drive a more turbulent system by lowering ν and κ, we should get a correspondingly higher value of the Rayleigh number. However by lowering κ we also find there is a nonlinear feedback that yields a narrower upper boundary layer. We demand that thermal diffusion carry a solar luminosity out of the top of our domain. This provides an additional constraint on $\partial S/\partial r$ at the upper boundary such that

$$\frac{\partial S}{\partial r} = -\frac{L_\odot}{4\pi R_o^2 \kappa \bar{\rho}\bar{T}}, \tag{9.3}$$

and thus $\partial S/\partial r \propto 1/\kappa$. A real physical system such as the solar convection zone would not experience this additional increase in Rayleigh number as it does not rely on a diffusive boundary layer to transport energy.

In practice we have found that when we decrease the viscous and thermal dissipation in our models at the solar rotation rate, we see the differential rotation in these models decrease and eventually switch sign to yield a slow equator and fast poles. This state is in many ways conceptually very simple: convection is trying to mix the angular momentum of the layer leading to fast rotation where the lever arm is short and slow rotation where is long. This trend is likely the result of a number of mechanisms which are all interrelated, but the influence of the impenetrable boundary layer is likely to play a significant role.

9.3 Formulation of the Plume Boundary Condition

Conceptually, open boundaries present a number of challenges. On a very basic level an open boundary is an attempt to admit dynamics into a simulation which are not being explicitly treated. Here we make a distinction between truly open, semi-open, and permeable

boundary conditions. Truly open boundary conditions allow the resolved interior dynamics of the simulation to control the behavior of the boundaries. They are particularly challenging because they can permit net fluxes of quantities like mass or momentum, destroying the global conservation properties of a simulation. We are not aware of any solar convective models which use a truly open boundary condition.

Semi-open boundary conditions are those which are designed to be as open as possible while using minimally invasive techniques to preserve global conservation properties. This may be accomplished using an open boundary condition on the velocity fields while imposing pressure gradients at the boundary to regulate the balance between upflows and downflows, or by applying a volumetric forcing near the boundary to counteract the net fluxes through the boundary. Semi-open boundaries have been used in several codes designed for near-surface solar convection, including MuRAM (Rempel et al., 2009; Cheung et al., 2010), Stagger (Trampedach & Stein, 2011), and CSS (Augustson et al., 2011). In these codes the bottom boundary condition is open rather than the upper boundary as we are considering for ASH. As the strongest driving in solar and stellar convection is generally believed to occur at the photosphere, opening the lower boundary may be less problematic than opening the upper boundary. Additionally these are all finite difference codes. Stagger, for example, applies open boundary conditions on outflows but imposes flows and thermodynamic fields on inflows in order to preserve the global conservation of momentum and mass, as well as the solar energy flux.

The final category of open boundary conditions is what we term permeable boundary conditions. These models impose flows through their boundaries in a specified way. They may be constant in time or they may vary. A permeable boundary permits flows to enter or exit the domain, but only in a specified manner. Permeable boundaries can easily control the fluxes of conserved quantities since the fluxes are specified with the boundary condition.

Our plume boundary condition in ASH is composed of three permeable boundary conditions and one semi-open condition. In ASH we impose small-scale plumes of radial

velocity and entropy as a time-dependent boundary condition. We also impose a condition on the opening angle of the plumes in order to mitigate pressure perturbations. Finally we impose a semi-open boundary condition designed to permit the internal dynamics of the simulation to set the differential rotation profile on the boundary and use a volumetric torque on the near-boundary layers to enforce conservation of angular momentum.

Semi-open boundaries are perhaps more challenging in ASH than in some of the other codes mentioned due to ASH's pseudospectral nature. ASH applies boundary conditions through its semi-implicit solve (see Figure 2.2). This is done in spherical harmonic space rather than physical space, thus boundary conditions are applied to spherical harmonic modes rather than physical locations. This makes it essentially impossible to apply different boundary conditions to different structures in our current computational framework. For example, we cannot allow radial outflows to continue unperturbed through a radial gradient boundary condition while at the same time imposing inflows elsewhere.

9.3.1 Plume Boundary Conditions on v_r and S

Perhaps the most straight-forward of our boundary conditions in our plume boundary scheme are those we apply to the radial momentum and entropy equations. Formally, the boundary condition for radial momentum is

$$v_r\left(R_o, \theta, \phi\right) = \mathcal{R}\left(\theta, \phi, t\right) \tag{9.4}$$

and the boundary condition for the entropy equation is likewise

$$S\left(R_o, \theta, \phi\right) = \mathcal{S}\left(\theta, \phi, t\right), \tag{9.5}$$

where R_o is the radius of the outer boundary and $\mathcal{R}\left(\theta, \phi, t\right)$ and $\mathcal{S}\left(\theta, \phi, t\right)$ are arbitrary functions of θ and ϕ and time t. We then choose $\mathcal{R}\left(\theta, \phi, t\right)$ and $\mathcal{S}\left(\theta, \phi, t\right)$ to be composed of N_p small-scale plume structures, each with some velocity amplitude $\mathcal{V}$ and entropy amplitude

$\mathcal{E}$. Thus we can write these fields as

$$\mathcal{R}(\theta,\phi,t) = \sum_{i=1}^{N_p} \mathcal{V}_i \mathcal{P}_i(\theta,\phi) F(t) \tag{9.6}$$

$$\mathcal{S}(\theta,\phi,t) = \sum_{i=1}^{N_p} \mathcal{E}_i \mathcal{P}_i(\theta,\phi) F(t), \tag{9.7}$$

where the time dependence is encoded in $F(t)$. The plume profiles are designed such that they have compact support (locally specified generating functions). This greatly reduces the computational cost of applying the plumes. Additionally, we choose $\mathcal{R}(\theta,\phi,t)$ and $\mathcal{S}(\theta,\phi,t)$ such that

$$\int_S \mathcal{R}(\theta,\phi,t)\sin\theta\, d\theta\, d\phi = \int_S \mathcal{S}(\theta,\phi,t)\sin\theta\, d\theta\, d\phi = 0, \tag{9.8}$$

where the integrals are taken over the spherical surface. Thus our plumes carry no net mass flux and set the mean entropy on the boundary to zero, as was done in previous ASH models (see Table 2.1). We have investigated several possible plume profiles to date. Here we will focus on a zero-flux plume profile $\mathcal{P}$ which is designed so that each plume individually has no net mass-flux or entropy because

$$\int_S \mathcal{P}\sin\theta\, d\theta\, d\phi = 0. \tag{9.9}$$

We have also considered a scheme which imposes plumes that are only downflows, and then shifts the mean of the radial velocity field to zero by adding a constant term to all points. Locally mass-conserving plumes are truly local structures, so we choose to investigate them here.

We choose our locally mass-conserving plumes to follow the profile

$$\mathcal{P}(\psi) = \begin{cases} -1 + 20\psi^2 - 50\psi^3 + 45\psi^4 - 14\psi^5 & \text{if } \phi \le 1 \\ 0 & \text{if } \phi > 1 \end{cases} \tag{9.10}$$

where ψ is the angular distance from the center of the plume $\Delta\sigma$ divided by the width of the plume δ. This polynomial representation is continuous in its value, and first and second

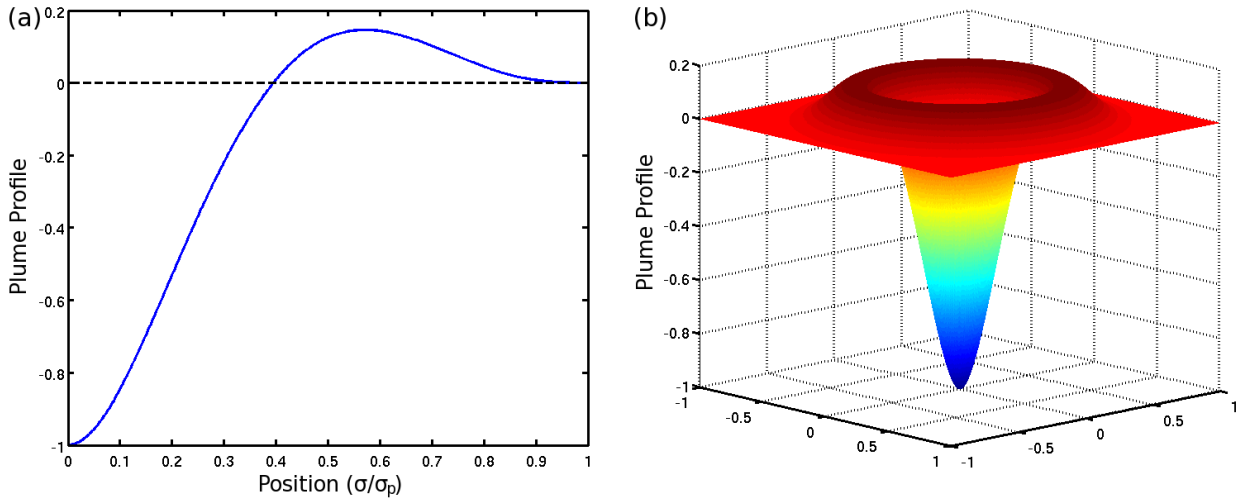

Figure 9.1: (a) Profile of the shape of the imposed plumes as a function of angular distance from the plume center σ divided by the width of the plume δ. (b) 3D surface rendering of the plume shape. The plumes consist of the strong negative core of downflowing low-entropy material surrounded by a weaker positive ring of higher entropy upflows. Surface integrals of this shape are identically zero by design.

derivatives at all points. Figure 9.1(a) shows the polynomial, and Figure 9.1(b) shows a 3D surface rendering of the plume profile. The profile has a large negative core of low-entropy downflow surrounded by a low-amplitude positive ring of higher entropy upflow. This mimics the shape of plume profiles seen in near-surface models (Rast, 2003).

We assign these plumes initially to uniform random locations on the outer boundary, accounting for the spherical geometry. Each plume is assigned an angular width δ. We must then determine the angular distance from each grid point to each plume center in order to apply the piecewise function $\mathcal{P}\left(\Delta\sigma/\delta\right)$. This is a surprisingly difficult task. The distance between two points over the surface of a sphere is given by

$$\Delta\sigma\left(\vec{\gamma},\vec{\gamma}_p\right) = \cos^{-1}\left(\sin\theta\,\sin\theta_p + \cos\theta\,\cos\theta_p\,\Delta\phi\right), \tag{9.11}$$

where $\vec{\gamma} = [\theta,\phi]$, no subscripts are used for coordinate locations, and subscript p represents the position of the plume. Unfortunately, this representation suffers from large round-off error for small angular separations, such as those we seek here for small plumes. A number

of different versions of this formula have been constructed to improve the computational accuracy of this formula. For an extended discussion of this topic at the intersection of ancient geometry and modern numerical methods, see Gade (2010). We here use a numerical implementation designed to be accurate for small angular separations given by

$$\Delta\sigma\left(\vec{\gamma},\vec{\gamma}_p\right)=2\sin^{-1}\left[\sin^2\left(\frac{\Delta\phi}{2}\right)+\cos\phi\,\cos\phi_p\sin^2\left(\frac{\Delta\theta}{2}\right)\right]. \tag{9.12}$$

This implementation suffers errors for separations larger than 90°, but is highly accurate and computationally inexpensive for small angles.

We also choose to have our plume field vary in time. Each plume is assigned a lifetime τ. The plume's amplitude is then modified by $\mathcal{T}\left(t,t_0,\tau\right)$, which is defined as a function of the time since the plume was initiated $t-t_0$ by

$$\mathcal{T}\left(t,t_0,\tau\right)=\begin{cases}\frac{t-t_0}{0.1\tau} & \text{if } 0\leq\frac{t-t_0}{\tau}<0.1\\ 1 & \text{if } 0.0\leq\frac{t-t_0}{\tau}<0.9\\ 1-\frac{t-t_0-0.9\tau}{0.1\tau} & \text{if } 0.9\leq\frac{t-t_0}{\tau}<1.0\end{cases}. \tag{9.13}$$

This provides linear ramp-up and cool-down phases for the plumes, minimizing the spurious pressure perturbations which can plague these simulations. A plume expires when $t-t_0=\tau$. It is then randomly restarted with new parameters. We have applied an additional constraint that new plumes must be at least their width from any existing plumes to avoid extremely fast downflows which limit the size of our time step.

Having decided on the shape of our plumes and their temporal dependence, we are now left to apply plumes to our boundary fields $\mathcal{R}$ and $\mathcal{S}$. Each plume is assigned an angular position $\vec{\gamma}$, an amplitude in both radial velocity $\mathcal{V}_i$ and entropy $\mathcal{E}_i$, an angular width δ_i, and a lifetime τ_i. With all of these parameters, the boundary fields are simply given by

$$\mathcal{R}\left(\theta,\phi,t\right)=\sum_{i=1}^{N_p}\mathcal{V}_i\,\mathcal{P}\left(\frac{\Delta\sigma\left(\gamma,\gamma_i\right)}{\delta_i}\right)\,\mathcal{T}\left(t,t_{0i},\tau_i\right) \tag{9.14}$$

$$\mathcal{S}\left(\theta,\phi,t\right)=\sum_{i=1}^{N_p}\mathcal{E}_i\,\mathcal{P}\left(\frac{\Delta\sigma\left(\gamma,\gamma_i\right)}{\delta_i}\right)\,\mathcal{T}\left(t,t_{0i},\tau_i\right). \tag{9.15}$$

Table 9.1: Parameters for plume boundary condition used in case P

PLUME BOUNDARY PARAMETERS

Parameter	Range	Correlation with $\mathcal{V}$
$\mathcal{V}$	$[240, 360]$ m s^{-1}	–
$\mathcal{E}$	$[8.8, 13.3]$ 10^4 erg K^{-1} g^{-1}	0.5
δ	$[0.056, 0.084]$ rad.	0.5
τ	$[2.0, 4.0]$ days	0.2
θ_p	$[0, \pi/2]$ rad.	0.0
ϕ_p	$[0, \pi/2]$ rad.	0.0

Here we have chosen to use the same widths for both the momentum and entropy profiles. This is done for simplicity, but one might expect that plume structures should have different sizes in entropy and radial velocity. For that matter one might expect that the profiles used for the two fields may be of different shapes. We anticipate addressing these questions in future work.

Clearly there are a large number of free parameters in this model. Each plume requires six parameters, for a total of $6N_p$ parameters to choose. Correlations between these parameters for a given plume could be argued. For example, one might expect faster plumes to be larger in size, or smaller plumes to have shorter lifetimes. We chose to correlate the velocity amplitude, entropy amplitude, plume width, and plume lifetime. The number of plumes has a significant impact on the dynamics as well. We have conducted some preliminary explorations of possible parameter choices guided by preliminary results from near-surface models run with the Compressible Spherical Shell code Augustson et al. (2011), and the constraint that we would like a solar luminosity of enthalpy flux to be transported by the plumes through the boundary on average. None of these sources of guidance are in any way definitive and we plan to conduct extensive additional exploration of these parameters. At this stage we have found that using $N_p = 1000$ with four-fold longitudinal periodicity in ASH (thus 4000 plumes for a full spherical shell), and the parameters shown in Table 9.1,

yields an instructive simulation in the form of case P, along with a series of test simulations that preceded it.

The angular widths of the plumes is chosen to be as small as possible for a given spatial resolution. We find that under-resolved plumes led to significant ringing in our spherical harmonic transforms. For ASH simulations with $\ell_{\max} = 682$ we find that plumes must be at least resolved by placing 12 grid points across their radius. As our grid-spacing is largest at the equator, we have an angular spacing between points there of 0.0031 radians, giving us a minimum plume width of 0.037 radians. We elect to make our minimum plume width 0.056 radians to avoid any potential problems. We have done some tests with plumes widths as small as 0.040 radians which appear stable over time evolutions of roughly 100 days.

Once we have determined the size of the plumes we then choose the number of plumes such that, on average, three-quarters of the boundary is covered by a plume. Simulations with more of the surface covered make it difficult to avoid placing new plumes on top of old plumes, which can produce extremely fast downflows and thus constrain our time step to be smaller than desired. The plumes are placed at uniformly random locations over the sphere. We avoid putting the center of a plume within another plume, thus plumes can initially be no closer to the center of another plume than their width.

Our choice of the peak downflow velocity is motivated partly by near surface models which show radial velocities on the order of a few hundred meters per second. Additionally we require the plumes to carry a solar luminosity of enthalpy flux through the upper boundary. Energy transport due to enthalpy flux is defined as

$$\mathcal{L}_{\text{EN}} = C_P \bar{\rho} u_r \left(T - \bar{T}\right) = \frac{\bar{\rho} u_r}{\bar{T}} \left(S - C_P + \frac{C_P P \left(\gamma - 1\right)}{\bar{P}\gamma}\right), \tag{9.16}$$

where C_P is the specific energy at constant pressure and γ is the adiabatic index. As long as $S/C_P > P/\bar{P}$ in our plumes, our entropy perturbations will drive enthalpy transport across the boundary. This places a constraint on the product of the velocity and entropy perturbations needed to maintain a given enthalpy flux. Thus if we want faster plumes

we must make them less entropy deficient and vice versa. We have experimented with $\mathcal{R}$ ranging from 50 to 1000 m s^{-1}. For high speed plumes we see rapid deceleration and large amounts of viscous heating as the plumes slam into the higher density maternal below them. For very slow plumes we find that they must be so cold that they experience rapid buoyant acceleration away from the boundary. In extreme cases they can coherently penetrate all the way through the domain, reaching speeds of as much as 2 km s^{-1} at mid-convection zone despite starting with speeds of 50 m s^{-1} We find that when the radial velocity plume amplitude $\mathcal{V}$ is $\mathcal{V} \approx 300$ m s^{-1} the plumes are fairly well behaved.

We have also included the ability for horizontal flows to advect the plumes around the outer boundary. This is done by solving a simple advection equation for the plumes as if they were Lagrangian test particles in the horizontal flow. This advection procedure uses a velocity field that is smoothed somewhat over the area of the plume to provide smoother trajectories. Advection using the unsmoothed horizontal velocities has been found to generate some ringing in the pressure field on the boundary. The advection procedure adds measurable computational cost as it forces the processors responsible for the boundary to solve an additional equation that is not solved by the rest of the computational domain. This leads to load imbalance. It is anticipated that ASH could be rebalanced by assigning fewer grid points to processors responsible for the boundary. We have tried test cases both with and without plume advection and find no systematic differences between them over roughly 100 days. Due the additional computational cost, the test cases discussed in this chapter and case P were run without plume advection.

9.3.2 Plume Boundary Conditions on P

As discussed in Chapter 2, the anelastic approximation leads to an elliptic equation for pressure. Rather than directly solving this equation in ASH, we implicitly solve for pressure by solving evolution equations for both the radial momentum and its horizontal divergence.

ASH uses a streamfunction formalism where

$$\bar{\rho}\vec{u} = \nabla \times (Z\hat{r}) + \nabla \times \nabla \times (W\hat{r})\,. \tag{9.17}$$

Solving for each component of the mass flux, this equation yields

$$\bar{\rho}u_r = -\nabla_\perp^2 W \tag{9.18}$$

$$\bar{\rho}u_\theta = \frac{1}{r}\frac{\partial^2 W}{\partial\theta\partial r} + \frac{1}{r\,\sin\theta}\frac{\partial Z}{\partial\phi} \tag{9.19}$$

$$\bar{\rho}u_\phi = \frac{1}{r\sin\,\theta}\frac{\partial^2 W}{\partial\phi\partial r} - \frac{1}{r}\frac{\partial Z}{\partial\theta}, \tag{9.20}$$

where $\nabla_\perp^2$ is the horizontal Laplacian operator. The evolution equations for ASH in spherical harmonic space are equations for the evolution of W, $\partial W/\partial r$, and Z. To specify the radial velocity field we must specify W over the outer boundary. This means that our choice for $\partial W/\partial r$ has two immediate consequences. First, it will implicitly set the boundary condition on the pressure field; second, if $\partial W/\partial r$ is not set to zero our radial velocity boundary condition will partial specify v_θ and v_ϕ.

Initially, we chose to simply set $\partial W/\partial r = 0$ on the boundary. However, if we look at the evolution equation for $\partial W/\partial r$ we find that this choice leads to problems elsewhere. The evolution equation for $\partial W/\partial r$ is given by

$$\begin{aligned}\nabla_\perp^2\frac{\partial}{\partial t}\left(\frac{\partial W}{\partial r}\right) =& -\nabla_\perp^2 P + \nu\nabla_\perp^2\left(\frac{\partial^3 W}{\partial r^3} + \left[\frac{d\ln\bar{\rho}}{dr} - \frac{d\ln\nu}{dr}\right]\frac{\partial^2 W}{\partial r^2}\right.\\ &+\left[\nabla_\perp^2 - \frac{2}{r}\frac{d\ln\bar{\rho}}{dr} - \frac{d^2\ln\nu}{dr^2} - \frac{2}{r}\frac{d\ln\nu}{dr} - \frac{d\ln\bar{\rho}}{dr}\frac{d\ln\nu}{dr}\right]\frac{\partial W}{\partial r}\\ &\left.-\left[\frac{d\ln\bar{\rho}}{dr} + \frac{2}{3}\frac{d\ln\nu}{dr} + \frac{2}{r}\right]\nabla_\perp^2 W\right)\\ &+ Q_{\rm COR} + Q_{\rm ADV},\end{aligned} \tag{9.21}$$

where we have condensed the Coriolis and advective terms into $Q_{\rm COR}$ and $Q_{\rm ADV}$, respectively. If we calculate these terms explicitly, we find that the Coriolis and advective terms are generally much smaller than the viscous term and the pressure term. If we examine the

balance of these terms we find that if we choose a boundary condition such that $\partial W/\partial r = 0$, then we implicitly force the existence of large horizontal variations in the pressure field one grid point in from the boundary. In fact if we run in this manner we find that pressure fluctuations on the order to of $\bar{P}$ build up on timescales of about 500 days. These pressure perturbations soon overwhelm the dynamics of the simulation.

If instead we look at Equation 9.21 in one of these models, we find that the two largest terms of the four viscous terms are those which concern $\partial W/\partial r$ and W. If we simply choose a boundary condition for $\partial W/\partial r$ such that

$$\frac{\partial W}{\partial r} = \left(\frac{d \ln \bar{\rho}}{dr} + \frac{2}{3} \frac{d \ln \nu}{dr} + \frac{2}{r} \right) W = C_G W, \tag{9.22}$$

where we have collected the terms due to geometry, stratification, and viscosity variation into C_G, we find that pressure perturbations due to the plumes are several orders of magnitude smaller. In effect, this boundary condition is setting an opening angle for the plumes as they enter the domain that is constant with the spherical geometry and the variations in density and viscosity. If we substitute Equation 9.22 into Equations 9.18, 9.19, and 9.20 and take the horizontal divergence of the flow, we find that this boundary condition leads to

$$\nabla_\perp \cdot (\bar{\rho} \vec{u}) \propto \frac{\bar{\rho} u_r}{r}, \tag{9.23}$$

indicating that inward plumes with negative u_r should be slightly converging as they enter the domain, as one might expect from the spherical geometry.

9.3.3 Plume Boundary Conditions on Horizontal Velocities

The last remaining boundary condition in our plume boundary formulation concerns the behavior of horizontal flows on the boundary. Ideally we would like these flows to be as unconstrained as possible so that their impact on the differential rotation profile of a simulation is minimal. This could be done, for example, by simply setting radial gradients

of the horizontal components of momentum to zero with

$$\frac{\partial\left(\bar{\rho}u_\theta\right)}{\partial r} = \frac{\partial\left(\bar{\rho}u_\phi\right)}{\partial r} = 0. \tag{9.24}$$

If we examine Equations 9.19 and 9.20 we can immediately see that to do so will require a boundary condition on $\partial W/\partial r$ as well as boundary condition on Z. Unfortunately we have already used the $\partial W/\partial r$ boundary condition to minimize pressure perturbations. Thus the best we can do is to derive a condition on the toroidal streamfunction Z which will make the radial gradient of the contribution from Z to the horizontal mass fluxes vanish at the upper boundary. The can be done by imposing

$$\frac{\partial Z}{\partial r} - \frac{Z}{r} = 0. \tag{9.25}$$

With these boundary conditions, the horizontal velocities are partially constrained such that they must avoid large pressure perturbations and partially free to be determined by the behavior of the interior of the system.

This boundary condition combined with our choice of imposing non-zero radial velocities on the boundaries leads to the possibility of a net flux of angular momentum across the boundary. This would led to a net accumulation or deficit of angular momentum in the system, effectively spinning up or down the domain. Test cases have shown that for most choices of plume parameters there tends to be a net outward flux of angular momentum through the boundary, causing the domain to spin down. For a case at the solar rotation rate, this spin down can be as large as 1% of the mean solar rotation rate roughly every 300 days. Clearly this is not desirable.

To avoid the net change of angular momentum in our simulations caused by these boundary conditions, we have two options. The first employs the angular momentum cleaning discussed in Chapter 2 and the second uses a corrective volumetric torque. Both methods present difficulties. The angular momentum cleaning is achieved via

$$\int_{r_i}^{r_o} \tilde{Z}_1^m r^2 \, dr = 0, \tag{9.26}$$

where Z_1^m are coefficients for the spherical harmonic modes of the toroidal mass-flux stream function Z with $\ell = 1$ and $m = -1$, 0, and 1. This is a non-local condition designed to prevent the accumulation of numerical noise in the net angular momentum of the system. When the net change in the angular momentum of the system is on the order of the accuracy of our numerical scheme this condition works quite well. When we apply it here we find that although it does conserve the total angular momentum of the system, it also introduces infrequent but intense radial pressure perturbations which can drive strong ringing in our system. This ringing is not confined to the near-boundary layers but is seen at all depths in our domain. Simulations using this condition are generally numerically stable, but the accuracy of our numerical algorithm becomes less certain under these conditions. While this is an area that deserves further study, we have chosen not to use this method to enforce global angular momentum conservation in case P.

The second mechanism for enforcing global angular momentum conservation is to measure the net flux of angular momentum across the outer boundary and then use a volumetric torque to add or subtract the correct amount of angular momentum from a thin layer near the top of the domain. The net torque from the boundary is on the order of 10^{-6} of the average angular momentum of the bulk rotation rate. Thus a torque on the same order applied to a thin layer near the boundary can prevent the accumulation of angular momentum in the system. The question then is what latitudinal and radial profile should be used for this corrective torque. We have chosen a radial profile given by a Gaussian generated on the outer boundary with an adjustable width. In all tests discussed here we have used a width or $0.2\Delta R$, where ΔR is the depth of the convective layer.

We have tried four latitudinal profiles for the volumetric torque: a uniform weighting, a uniform plus $\sin\theta$ weighting, a uniform plus $\sin^2\theta$ weighting, and a latitude-by-latitude replacement scheme. The latitude-by-latitude scheme attempted to measure the net flux of angular momentum at each latitude in the simulation and then applied a corrective torque at that latitude. This model was found to exhibit numerical instabilities in that it was possible

for run-away latitudes to emerge where both the boundary flux of angular momentum and the local torque grew to very large values. The other three models are all numerically stable and so we can assess their usefulness. This can best be done by examining the latitudinal profiles of the average total torque on the volume $\hat{Y}_{\rm tot}(\theta)$. We define

$$\hat{Y}_{\rm tot}(\theta) = \hat{Y}_{\rm cor}(\theta) + \frac{\int_V \nabla \cdot \vec{\mathcal{F}}\, dV}{V} = \hat{Y}_{\rm cor}(\theta) - \hat{Y}_{\rm p}(\theta), \tag{9.27}$$

where $\hat{Y}_{\rm cor}$ is the latitudinal profile of the corrective torque, $\vec{\mathcal{F}}$ is the angular momentum flux vector (see Equation A.1 and Appendix A for more details), and hats represent averages in radius and longitude. Using the divergence theorem we can convert the volume integral into a surface integral where we take all but the θ integral to preserve the latitudinal profile, which we label $\hat{Y}_{\rm p}$. By definition if we average $\hat{Y}_{\rm tot}$ in latitude the result will be zero. Our three corrective torque profiles have the functional forms

$$\hat{Y}^{u}_{\rm cor}(\theta) = Y_0 \tag{9.28}$$

$$\hat{Y}^{s}_{\rm cor}(\theta) = Y_0 + Y_1 \sin\theta \tag{9.29}$$

$$\hat{Y}^{s2}_{\rm cor}(\theta) = Y_0 + Y_2 \sin^2\theta. \tag{9.30}$$

Similarly the torques due to angular momentum flux across our upper boundary in these three test cases will be $\hat{Y}^{u}_{\rm p}(\theta)$, $\hat{Y}^{s}_{\rm p}(\theta)$, and $\hat{Y}^{s2}_{\rm p}(\theta)$.

Figure 9.2 shows the torques due to cross-boundary angular momentum flux and corrective procedure for all three latitudinal profiles. Each profile was averaged in time over roughly 100 days. In all three cases there is a large negative torque being applied by the cross-boundary flux at the equator. At high latitudes that is reversed although at much lower amplitudes. The three profiles lead to an effective poleward transport of angular momentum, which promotes anti-solar differential rotation. If we take the average value of $\hat{Y}_{\rm p}(\theta) - \hat{Y}_{\rm cor}(\theta)$ between $\pm 30^\circ$ latitude for each case we find that the uniform case on average transports nearly twice as much angular momentum towards the poles as the sine weighted case, and nearly four times more than the sine-squared weighted case. Interestingly all three

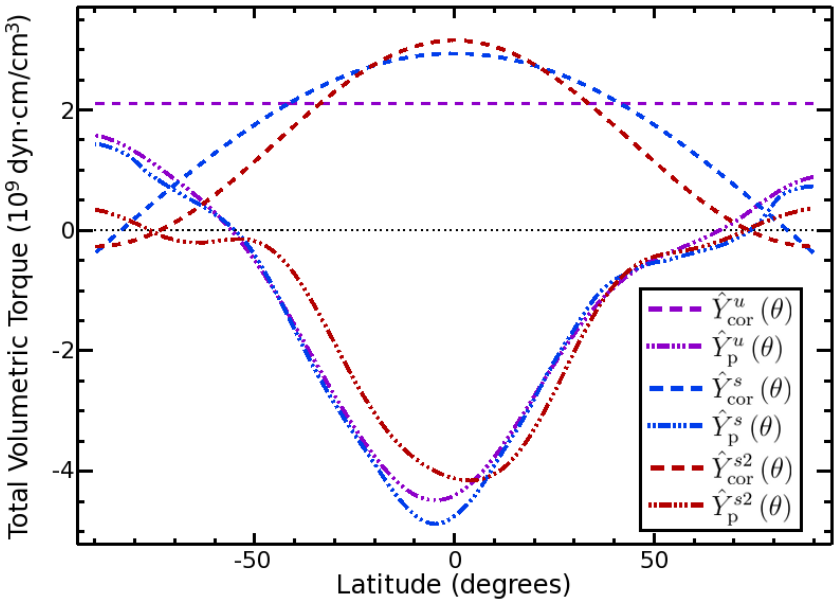

Figure 9.2: Total volumetric torque as a function of latitude in three models using a corrective torque to conserve angular momentum. For three test cases the average volumetric torque due to cross-boundary flows $\hat{Y}_{\rm p}(\theta)$ and the corrective torque applied to conserve global angular momentum $\hat{Y}_{\rm cor}(\theta)$ are plotted. The case using a uniform corrective torque (purple lines) shows a net removal of angular momentum at the equator and a net gain at the poles. The case using a sine weighting in latitude (blue lines) again shows a latitude-by-latitude imbalance but one that is much less severe. The case using a sine-squared weighting (red lines) shows moderately low levels of local imbalance between the corrective torque and the cross-boundary flux torque, although there is still a net transport of angular momentum towards the poles.

profiles shown here under-correct for the angular momentum flux across the boundary at low latitudes and over-correct at high latitudes. In the future we will investigate the use of other latitudinal profiles which may yield even better results. Unfortunately, we find that each torque profile produces feedback on the latitudinal profile of the angular momentum flux through the boundary, so we cannot simply measure the profile of the angular momentum transport for one simulation and then assume that it will remain constant if we change the profile of the volumetric torque. This can be seen, for example, by comparing the high-latitude regions of the three cases in Figure 9.2.

9.3.4 Applying the Plume Boundary Model

Even with a complete set of boundary conditions specified, the plume boundary model is sufficiently complex that a wide range of morphologies and amplitudes in our velocity and thermal fields can be imposed, either explicitly or implicitly, on the boundary. The conditions for v_r and S include time-dependent plumes whose parameters are selected randomly. The condition on P is applied implicitly via a condition on the opening angle of the plumes. The conditions on the horizontal velocities are perhaps most opaque as they are only partially specified. Figure 9.3 shows, for case P, the radial velocity and entropy fields applied as boundary conditions, as well as the pressure fields which is implicitly applied, and the horizontal velocity fields which are both partially imposed and partially determined by the behavior of the interior of the simulation. With large numbers of plumes, it is common for plumes to at least partially overlap, creating larger plume complexes. This becomes even more likely for the largest plumes. Due to the imposed correlations between plume size and amplitude, these plumes tend to create strong downflow regions.

The implicit pressure boundary condition produces well-behaved pressure signatures for the plumes. These are generally low pressure regions, signaling the horizontal convergence of the plumes as well as their low temperatures. With low entropy and low pressure signatures in the downflows, their enthalpy transport is radially outward, producing the desired energy transport properties. The horizontal flows show evidence of the converging flows indicated by the pressure field, but also contain significant flows which are unrelated to single plumes. Interestingly, complexes of plumes can be seen producing coherent horizontal flows on scales larger than individual plumes.

Table 9.2: Shown are the number of radial, latitudinal, and longitudinal grid points. The total evolution time T_E for each simulation is given in days. The viscosity ν in units of $\mathrm{cm}^2\ \mathrm{s}^{-1}$ is quoted at mid-convection zone. The fluctuating Reynolds number $\mathrm{Re}' = v'_{\mathrm{rms}} L/\nu$ gives some indication of the relative level of turbulence in each model. The convective Rossby number $\mathrm{Roc} = (\mathrm{Ra}/\mathrm{Ta}\,\mathrm{Pr})^{1/2}$ demonstrates the level of rotational constraint. See Tables 2.1, 2.2, and 2.3 for additional parameters.

Selected Parameters for Cases Ia, Ib, Ic, and P

Case	N_r, N_θ, N_ϕ	T_E (days)	ν (cm s^{-2})	Re'	Roc
Ia	300, 512, 256	7510	2.41×10^{12}	48	0.462
Ib	500, 1024, 512	6800	1.20×10^{12}	177	0.515
Ic	500, 1024, 512	1960	6.02×10^{11}	418	0.568
P	500, 1024, 512	830	1.20×10^{12}	253	0.503

9.4 Simulation Parameters

As we now have defined our plume boundary conditions, we can begin a preliminary investigation into the behavior of a simulation using this choice of boundary condition. To do this we have selected our most promising test case and evolved in for roughly 800 days to date. We label this simulation case P. For comparison we have also run three cases using the standard impenetrable boundary condition, which we term cases Ia, Ib, and Ic. Table 9.2 gives selected parameters for these models. Further details can be found in Tables 2.1, 2.2, and 2.3. Case Ia is designed to be analogous to case AB2 from Brun & Toomre (2002), which showed a strong solar-like differential rotation profile at the solar rotation rate. Case Ib is like case Ia, but with a decrease in ν and κ by a factor of two. Case Ic reduces ν and κ again by a factor of two. Case P has the diffusivities of case Ib. In order to reduce the computational expense of these models, we have run them in domains which cover only 90° in longitude and are thus four-fold periodic. This allows us to have high spatial resolution at moderate expense, which is especially important for resolving the plumes in case P. This four-fold periodicity precludes flows from crossing over the poles, which can cause the generation of polar vortex structures of very fast rotation. These simulations all rotate at the solar rate.

They extend from the base of the convection zone at $0.72R_\odot$ to $0.983R_\odot$. The additional radial extent compared to simulations in previous chapters provides more density contrast, thus requiring the plumes to mix and entrain fluid more rapidly as they encounter steeper density gradients.

Case Ia was initiated from a solar structure model and run for nearly 7000 days before case Ib was created from it, thus using case Ia as its initial conditions though interpolating to a higher spatial resolution. Case Ia was then run for roughly an additional 500 days. Case Ib was run for about 3000 days, at which stage case Ic was created from it, using it as initial conditions. Case Ib was then run for almost another 4000 days. Case Ic was only run for about 1900 days due to limited computational resources. It appears from examinations of the time variation in the volume-averaged differential rotation kinetic energy that case Ic is still experiencing significant evolution in its differential rotation. From past experience, we anticipate that this will eventually led to strong anti-solar differential rotation.

Case P was initiated from case Ib at the end of its time evolution. Initially all plumes we given the same t_0 and allowed to turn on gradually according to the time dependence shown in Equation 9.13. Each time a plume expires, it is given new randomly generated parameters and reinitiated. Thus initially there was some synchronization in the plumes turning on and off, however we would expect each plume to move away from that collective behavior as a random walk with a step size of about 1 day compared to a mean plume lifetime of 3 days. Thus we would expect almost no correlation after about 9 plume lifetimes or roughly 30 days. Indeed when we examine the start times of plumes after about a hundred days, we find that they form a uniform random distribution.

When evolving case P, we find that there is a very slow timescale for the equilibrations of flux transport in the model. Cases with impenetrable boundary conditions must store considerable energy in their mean entropy stratification in order to build the necessary boundary layer to achieve a sufficient diffusive flux at the top of the simulation. Case Ib has 1.2×10^{41} ergs stored in this entropy gradient, or roughly enough energy to power the solar

luminosity for a year. Initially both thermal diffusion and enthalpy flux from the plume boundary condition transport a solar luminosity of flux out of the domain which begins to remove the excess energy stored in the entropy gradient, but this quickly reduces the gradient in the upper layers of the domain. Within 100 days of the start of case P the total luminosity through the outer boundary was down to $1.11L_{\odot}$. By 400 days the luminosity was still at $1.07L_{\odot}$. This process asymptotically approaches a state of flux balance, but the rate of convergence is slow. At this stage case P still shows a total luminosity through the bulk of the convective layer and out the upper boundary that is $1.04L_{\odot}$.

9.5 Understanding the Effects of the Plume Boundary Condition in ASH

We have conducted a preliminary investigation of the impact of this plume boundary condition compared to similar cases with our standard impenetrable boundary. In doing so, we have tried to answer three major questions:

(1) How does a plume boundary condition change the portion of ASH models which were previously dominated by the thermal and viscous boundary layers?

(2) How does the plume boundary condition modify the flows seen at mid-convection zone?

(3) Can a plume boundary condition promote solar-like differential rotation for moderately turbulent simulations?

While our investigations into these topics are on-going, we can offer some insights into these questions for one possible realization of the plume boundary condition.

Figure 9.3 shows a 3D visualization of a snapshot of radial velocity patterns in case Ia, Ib, Ic, and P. These snapshots are most useful as qualitative tools to give us an impression of the flows in each case. We can see that case P clearly shows higher velocities near the

outer boundary than any of the other cases. It also appears to have convective patterns most similar to those of case Ic even though the diffusion parameters in case P are equal to those in case Ib. Also apparent is case P are the plume trajectories that begin as small downflows on the boundary and then rapidly coalesce into progressively larger downflows as they descend. In contrast, case Ic shows velocity structures which form lanes of downflows. These lanes remain coherent over most of the convective layer, though they must decelerate as they approach the upper boundary.

9.5.1 Replacing Diffusive Boundary Layers with a Boundary Interface

The plume boundary condition was designed to remove the diffusive boundary layers imposed in ASH simulation by our impenetrable boundary condition. The plume boundary condition achieves this goal, however it replaces the diffusive boundary layers with what we term an interface layer where the flows and thermal fields imposed on the boundary interact with the flows in the bulk of the domain. As we have not solved a physical equation to generate our plumes on the boundary there is little reason to expect that they will match solutions to the hydrodynamic equations solved in the interior of the domain. Our plumes have a small range in scales and are all of the same shape, whereas the convection in the bulk of the domain exhibits a range of scales and shapes. Convection tends to form cellular patterns whereas our plume field is simply a uniform random distribution. For this reason we can expect that there will be some layer over which we observe a collision between the giant cells in the interior of our domain and the convective plumes applied on our outer boundary.

Figure 9.5 presents the radial profile of energy transport in case Ib and case P which have identical coefficients of thermal and viscous diffusion. Both cases show very similar fluxes due to entropy diffusion $L_{\mathrm{TD}} \approx 0.2 L_{\odot}$ through the bulk of the convective layer, indicating that the efficiency of convection is roughly equal in both cases through the bulk of

the domain. The profiles of $L_{\rm TD}$ diverge at about $0.93R_\odot$, climbing for case Ib and flattening out at around $0.5L_\odot$ for case P. We may expect that this will decrease somewhat with further thermal equilibration. The fluxes of enthalpy and kinetic energy are morphologically similar for the two simulations up until near the upper boundary, though case P shows higher magnitudes in both components.

Near the upper boundary, case P shows a sharp dip in the enthalpy flux before recovering to carry the solar luminosity specified by the boundary condition. This dip is a result of the Prandtl number of our simulation interacting with our choice of relative shapes for the velocity and entropy components of our plumes. Our Prandtl number is 0.25, and the plumes imposed on the boundary have identical shapes in both v_r and S. The thermal structure of the plumes diffuses faster than the momentum signature, causing the plumes to decelerate as they lose their initial thermal driving. The effective Prandtl number of the plumes could be thought of as the size scale of the velocity structures divided by the scale of the entropy structure. The location of this peak tells us that the bulk of the enthalpy transport is coming from convective structures consistent with the Prandtl number in the bulk of the domain within about the first $0.01R_\odot$ from the upper boundary. As we will see this does not mean that the plumes penetrate only that far, but rather that significant modification to the plumes occurs very quickly as they enter the domain. This is further demonstrated by strong viscous heating within $0.01R_\odot$ of the upper boundary, which points to rapid reorganization of the plume structures as they enter the domain. Thus in some sense we have replaced a spherically-symmetric viscous boundary layer with one that acts on much smaller scales but where diffusive processes still play a key role.

We can get a feel for the changes the plumes experience in case P by looking at Figure 9.6 which shows radial velocity snapshots over a 60° by 60° region at nine successive depths. Plumes rapidly merge into downflow structures on larger scales and with different morphologies. While patterns can be seen imprinting downward from one level to the next there is little correlation with the surface at or below $0.884R_\odot$. As the plumes applied on the

boundaries coalesce they appear to seed the strong downflow lanes seen at mid-convection zone. Very little impact if any is seen on the upflows. This seems to support our choice of plume parameters, for they have not created a pattern which simply imprints through the domain, but rather seems to be influencing the upper portion of the domain without dominating it. It is possible that a better choice of parameters may be able to create even less of a mismatch between the plumes applied on the boundary and those in interior of the simulation, creating a gentler interface layer.

9.5.2 Changes in the Bulk of the Domain

Having examined the near-boundary layers for case P, let us now turn to the bulk of the convective layer. It has long been known that the dynamics of convective flows can be largely determined by their boundary layers. By removing the diffusive thermal and viscous boundary layers and replacing them with an interface layer, we can then expect that changes will not just be limited to regions near the boundary. Figure 9.7 shows snapshots of radial velocity patterns for all four cases at 0.95, 0.85, and 0.79 $R_\odot$. While there is a clear difference between the impenetrable and plume boundary condition cases near the top of the domain, there is surprisingly little morphological difference between cases Ib or Ic and P at mid-convection zone or deeper. The largest difference may be in the amplitude of the flows, which are somewhat larger in case P. This is at least partially due to case P not being fully thermally relaxed, but there is likely also some additional effect from the increase in both enthalpy and kinetic energy transport shown in Figure 9.5. It does appear that case P may achieve smaller-scale convective structures than case Ib, perhaps more like those of case Ic.

Additional tests are needed to assess the differences in the flows in the bulk of the domain, but a preliminary analysis seems to support the conclusion that the plume boundary condition does not dramatically alter the convective patterns achieved in the bulk of the domain either in morphology or amplitude.

9.5.3 Strengthening Solar-like Differential Rotation

Figure 9.8 shows the time- and longitudinally-averaged differential rotation as a function of latitude and radius for all four cases (the helioseismically measured profile is shown in Figure 1.3). Case Ia shows strong solar-like differential rotation similar to case AB2 of Brun & Toomre (2002). Moving to higher levels of turbulence, case Ib shows weak solar-like differential rotation while case Ic shows very little differential rotation. From previous experience we believe that case Ic will produce anti-solar differential rotation if allowed to evolve further in time. In contrast case P shows strong solar-like differential rotation similar to case Ia.

The processes which control solar differential rotation are complex and closely connected with other topics such as the thermal structure of the convection zone (see reviews Miesch, 2005; Miesch & Toomre, 2009). As we have shown, our plume boundary condition includes a volumetric torque designed to correct the non-zero flux of angular momentum allowed by our plume boundary condition. This adds another layer of complexity to analyses of angular momentum transport carried out for previous ASH simulations (e.g., Brun & Toomre, 2002; Miesch et al., 2006; Brown et al., 2008; Nelson et al., 2013b). The solar-like differential rotation in case P is fascinating since it possesses somewhat higher radial velocities at mid-convection zone than even case Ic, though smaller values of both the Rossby and convective Rossby numbers. A full analysis of this case will require the development of additional analysis tools, which are beyond the scope of this thesis at this stage.

Closer examination of the differential rotation profile reveals some additional interesting features. The polar vortices present in the cases with impenetrable boundary conditions are stronger in case P, though there is a thin layer of slower rotation fluid within $0.02R_\odot$ of the upper boundary. Case P's differential rotation profile as a function of latitude at $0.96R_\odot$ is essentially flat between 75° and 45°, then there is a shaper increase between 45° and 30°

followed by a much more gradual increase in Ω from 30° to the equator. In contrast both case Ia and the solar profile show a much more steady increase in rotation rate at a fixed depth when moving toward the poles. Contours of constant rotation in case P are less cylindrical at mid-latitudes that in case Ia, though not as conical as the solar profile. Finally near mid-latitudes the radial gradient of Ω becomes slightly negative above $0.96R_\odot$, perhaps providing a hint of the near-surface shear layer seen above $0.95R_\odot$ in the Sun. Studies of supergranular scale convection have postulated that an interface between rotationally-constrained giant cell convection and more isotropic convective motions on supergranular scales may be required to achieve the near-surface shear layer (Augustson et al., 2011). This type of model may permit investigations of that idea. It bears repeating that all of these findings are preliminary and that we have yet to understand the mechanisms driving these behaviors, but the potential is tantalizing.

9.6 Discussion of the Preliminary Analysis

In this chapter we have formulated a boundary condition that applies a specified set to small-scale plumes to the upper boundary in ASH in an attempt to explore an alternative to our standard boundary conditions which impose an unphysical diffusive boundary layer in a region where convective transport should dominate. We then presented some initial analysis of a simulation, labeled case P, which utilizes this plume boundary condition. Case P was compared with cases at a variety of turbulence levels with impenetrable boundary conditions. This has been conducted essentially as a proof-of-concept study rather than a definitive exploration of this novel boundary condition. We reserve that worthy undertaking for future efforts.

Case P demonstrates that a plume boundary condition in ASH can be implemented and applied in such a way that it greatly reduces the diffusive boundary layers near the upper boundary of an ASH simulation without producing dramatic changes in the morphology or

amplitude of the convective flows through the bulk of the layer. This condition can also drive flows that yield a solar-like differential rotation profile at the solar rotation rate. This differential rotation gives hints of some aspects of the solar differential rotation profile such as conical surfaces of isorotation and the near-surface shear layer.

In addition to the extensive analyses which will be conducted on case P moving forward, this also lays the groundwork for more complex plume models based on statistical descriptions of convective patterns from near surface models. The plumes used in case P follow a simple analytical perception. Real convective downflows at this layer of the solar interior would be expected to be far more complex. By developing improved plume models which can incorporate additional information from near-surface models, we hope to achieve better models of giant-cell convection in the bulk of the convective layer. This would also provide a first step towards coupling ASH with a near-surface code, enabling further development of a coupled simulation capable of treating dynamics over perhaps the entire convective interior of sun-like stars.

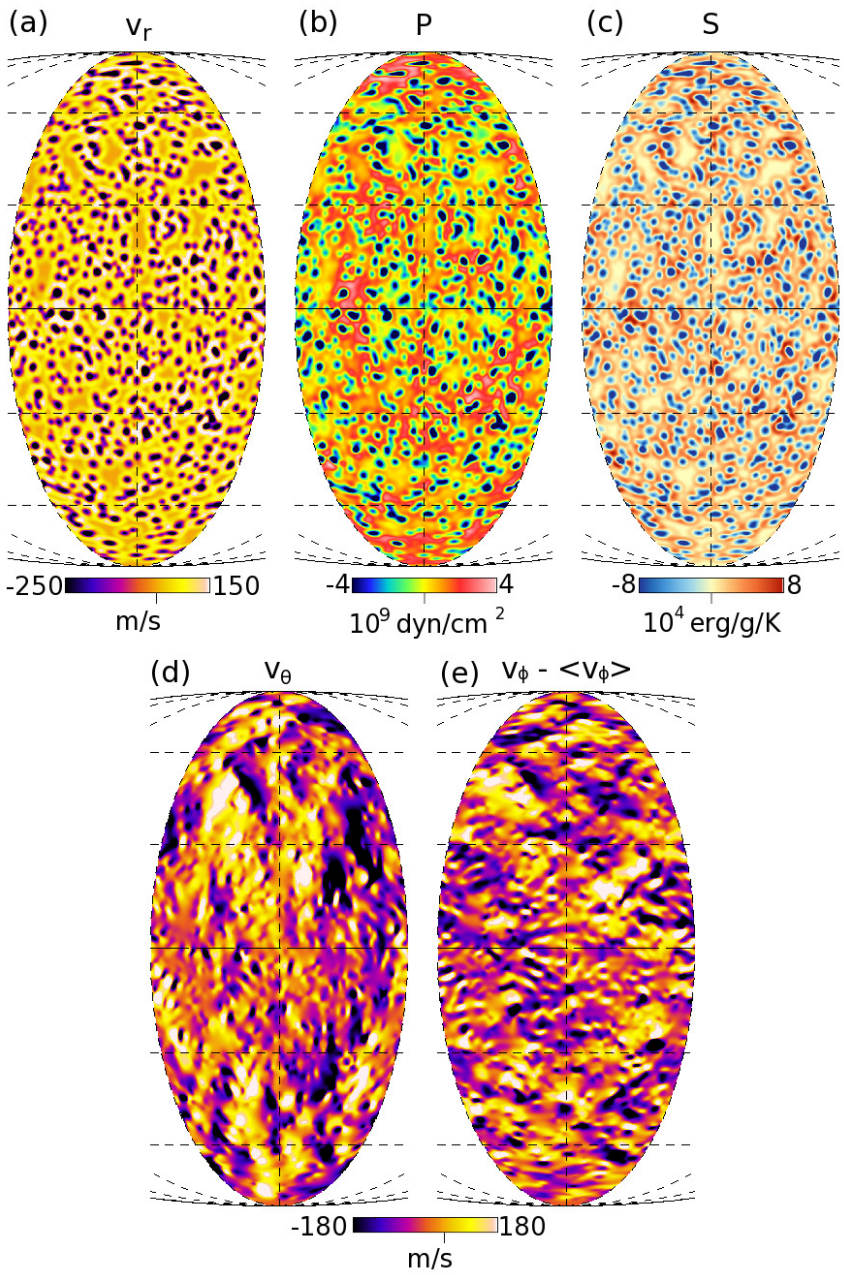

Figure 9.3: Sample snapshot of the upper boundary condition for case P in Mollweide projection. (a) Radial velocity field applied at the outer boundary. (b) Pressure field implicitly applied by a boundary condition on the plume opening angles. The pressure is generally negative in the cold downflows. (c) Entropy field for the same plumes with low entropy in the downflows and high entropy in the upflows. (d) Latitudinal velocity field which is both applied by the implicit boundary condition on pressure and determined by the interior of the domain by a zero radial gradient condition on the toroidal mass flux streamfunction Z. (e) Similarly for longitudinal velocity. We have removed the longitudinally symmetric component to highlight the converging flows around strong plume systems.

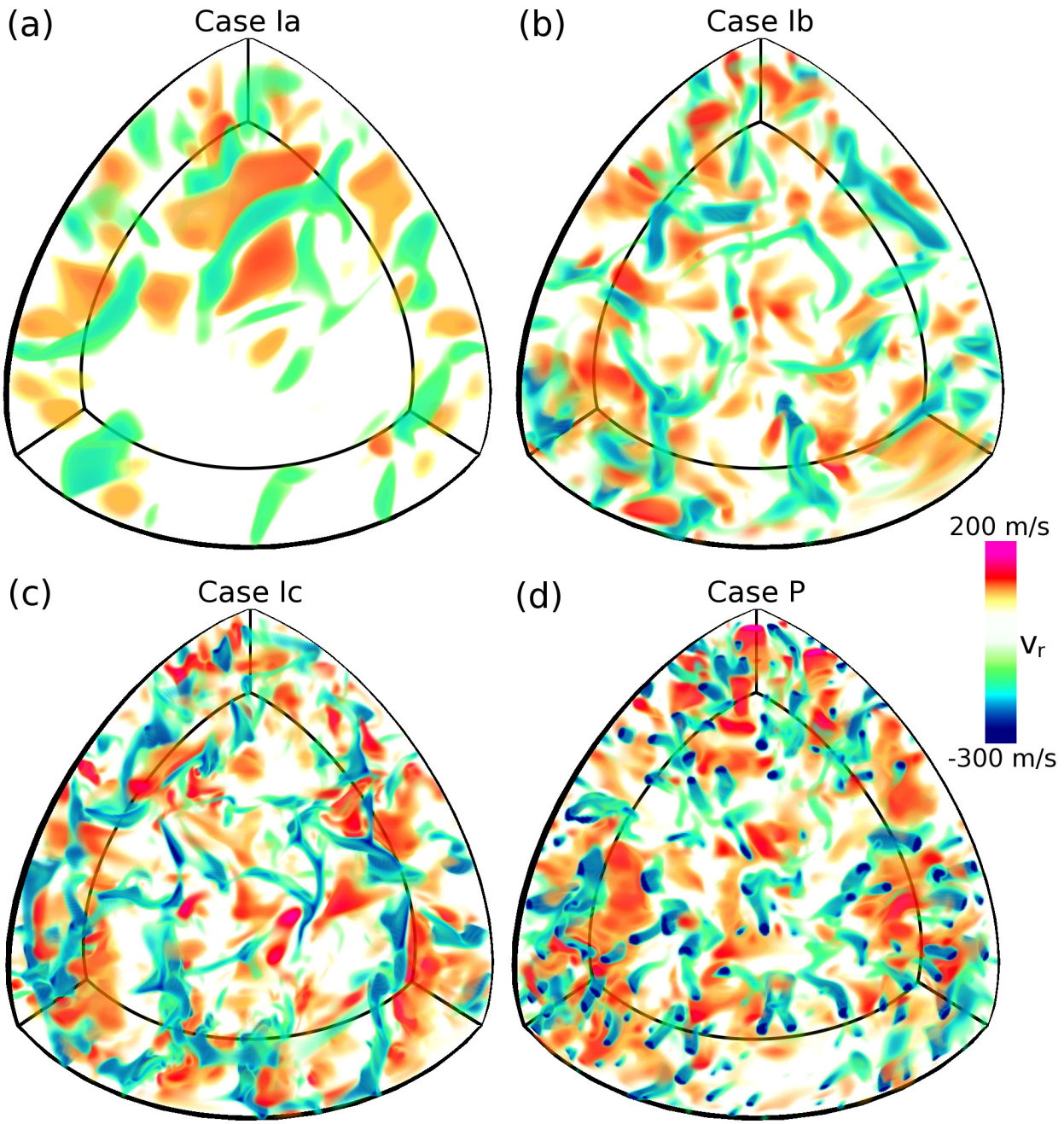

Figure 9.4: 3D volume rendering of v_r at all depths in the northern hemisphere in cases Ia, Ib, Ic, and P. The three impenetrable boundary cases show a wide variety in their convective patterns. Generally more turbulent cases show smaller scale features and posses larger ranges in values. Case P seems qualitatively most similar to case Ic although its diffusion parameters are identical to case Ib. Case P also clearly shows plumes with strong negative radial velocities on the boundary, while cases Ia, Ib, and Ic are required to have small radial velocities near the upper boundary.

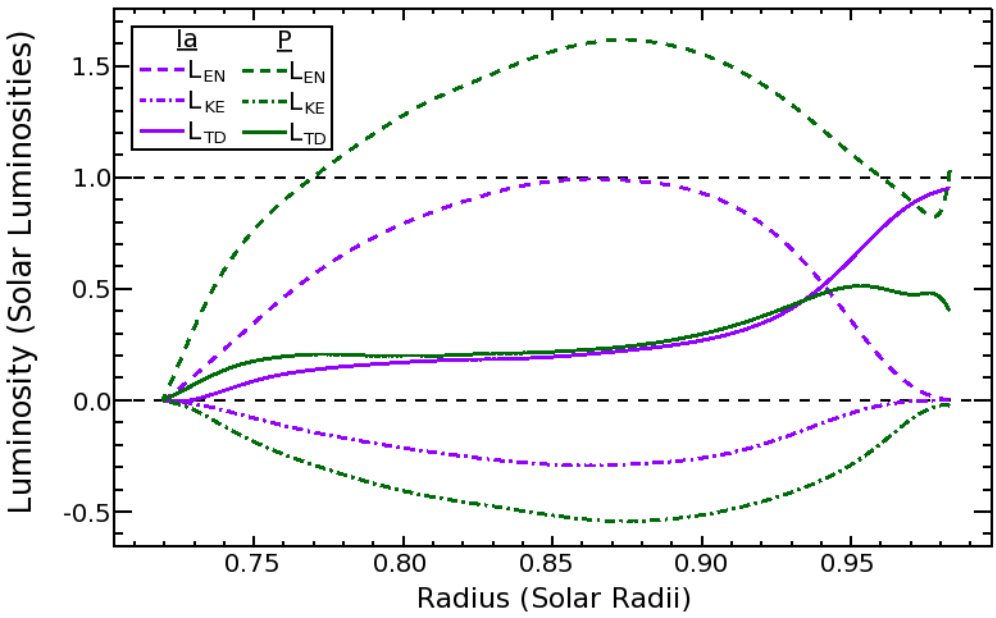

Figure 9.5: Mean radial energy transport by advection of enthalpy ($L_{\rm EN}$, dashed lines), advection of kinetic energy ($L_{\rm KE}$, dash-dot lines), and thermal diffusion ($L_{\rm TD}$, solid lines) for case Ib (purple) and case P (green). Not shown are the radiative diffusion fluxes which carry the solar luminosity through the bottom of the domain and is identical for both models, and the viscous heating flux, which is never greater than $0.02L_\odot$ for case Ib. For case P the viscous heating flux is only significant near the upper boundary, reaching $-0.09L_\odot$ there. In case P the plume boundary condition imposes an outward enthalpy flux of $1.0L_\odot$ and an inward kinetic energy flux of $0.03L_\odot$; these quantities are required to vanish at the upper boundary in case Ib.

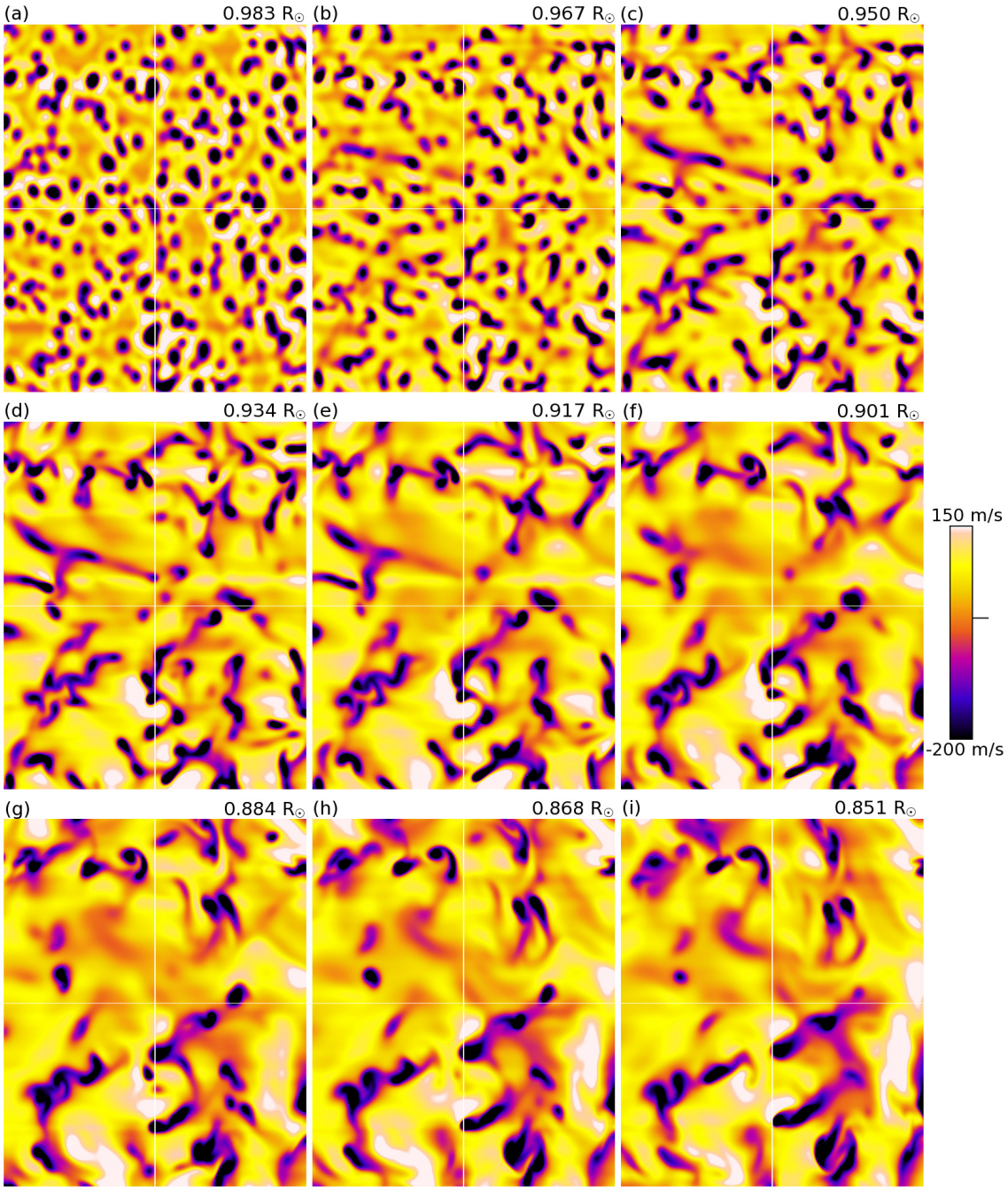

Figure 9.6: Simultaneous snapshots in case P of v_r over a 60° by 60° patch centered on the equator at nine depths between the upper boundary at $0.983R_\odot$ and mid-convection zone at $0.851R_\odot$. Individual plumes rapidly merge into larger structures as they enter the domain. Upflow structures disappear almost immediately. By $0.934R_\odot$ downflow patterns are larger and clearly non-circular, although the influence of groups of plumes are still seen. By $0.884R_\odot$ it is difficult to identify any unambiguous correlation between structures at that level and those at the surface.

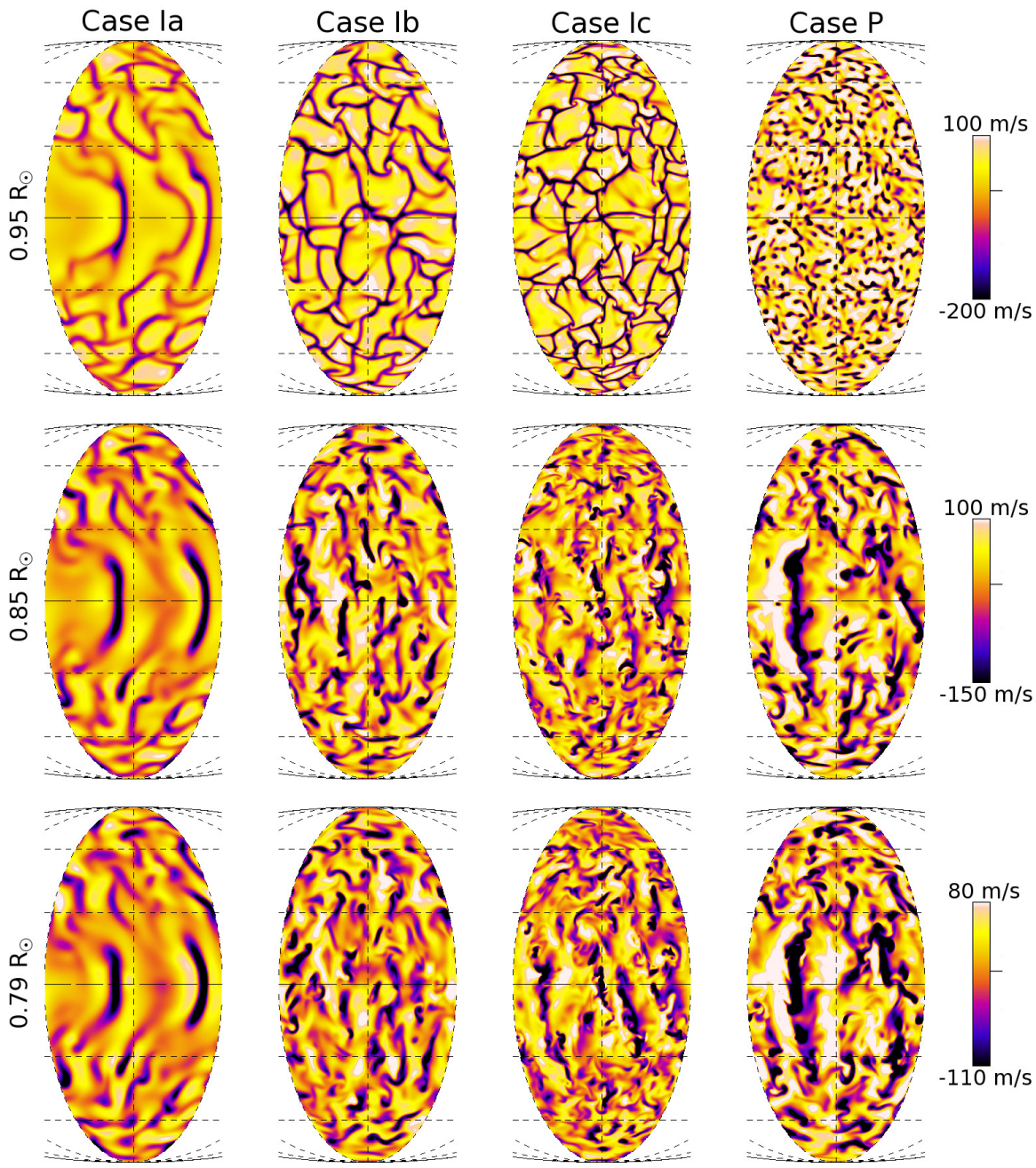

Figure 9.7: Snapshots of v_r at three depths in cases Ia, Ib, Ic, and P. Cases Ia, Ib, and Ic show clearly cellular patterns near their upper boundary, while case P shows much less coherent structures as plumes coalesce into larger structures. At mid-convection zone ($0.85R_\odot$) cellular patterns are less evident, particularly for cases Ib and Ic, while the fairly laminar convection of case Ia retains its cellular pattern. All four cases show some rotational alignment near the equator. Case P shows a particularly strong upflow/downflow pair which do not appear to be caused by the plume boundary condition.

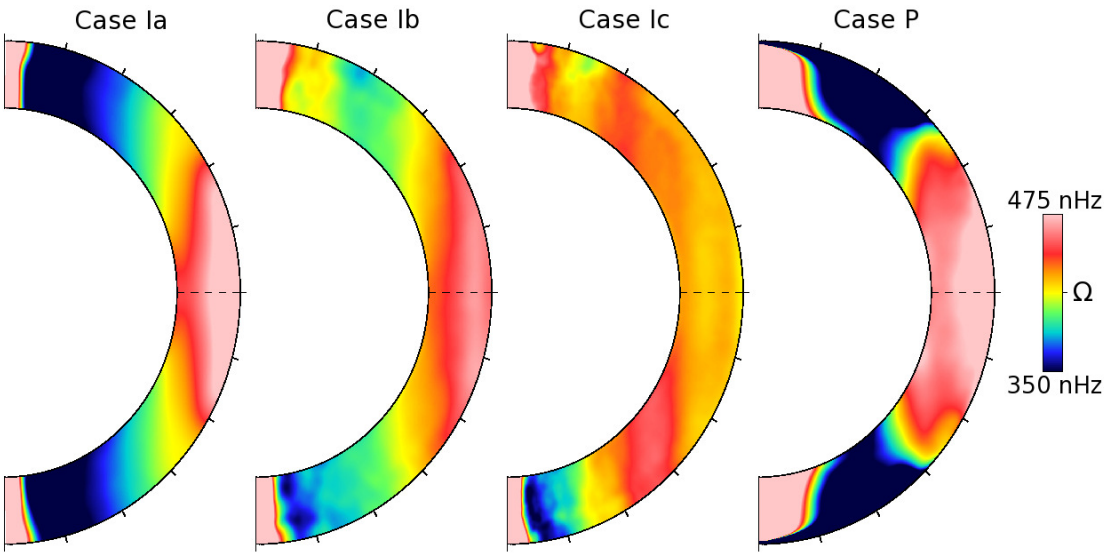

Figure 9.8: Differential rotation profiles in angular velocity $\Omega(r, \theta)$ for case Ia, Ib, Ic, and P averaged over about 100 days each. All cases display polar vortices which may be a result of the four-fold longitudinal periodicity of these models. Cases Ia and P shows strong solar-like differential rotation. Case Ib shows weaker but still solar-like differential rotation. Case Ic possess very little differential rotation. We believe case Ic will produce an anti-solar profile if allowed to continue evolving.

Chapter 10

Ongoing Puzzles and Future Challenges

In the preceding chapters we have sought to explore the fundamental physical processes that enable stars like our Sun to generate magnetic fields which undergo cycles of magnetic activity and emerge from the deep interior toward the surface. The models presented here have made progress on some of the important current questions in convective dynamos. Specifically, we have shown that:

(1) The dynamic Smagorinsky sub-grid scale model can be reliably used to significantly reduce diffusion in ASH simulations while preserving essential elements of the convective flows.

(2) Magnetic wreaths can exist in simulations where explicit diffusion has been reduced and replaced in fundamental balances by resolved turbulent dissipation.

(3) Turbulence plays a key role in the initiation of global reversals in magnetic polarity.

(4) Buoyant magnetic loops can be spontaneously generated in ASH models using the dynamics Smagorinsky SGS model. These loops can rise through the convection zone via a combination of magnetic buoyancy and advection by convective giant cells. Their typical size is set by the size of the giant cells.

(5) The buoyant magnetic loops in our ASH models mimic the statistical distribution of solar active regions in properties such as their tilt and twist. Further these loops

preferentially appear in confined longitudinal patches reminiscent of active longitudes in the Sun.

(6) The standard impenetrable upper boundary condition in ASH can be replaced with a plume boundary condition which imposes large numbers of small-scale plumes on the upper boundary. This plume boundary condition has yielded promising preliminary results for a proof-of-concept model.

As is often the case, these discoveries have led to a series of new questions and directions for future research, as well as reminded us of the existence of continuing puzzles. We will not attempt to outline all of these here, but instead discuss three which we find particularly noteworthy. First, our work with reversals in convective dynamo models has reminded us that we still fundamentally do not understand the mechanism whereby toroidal magnetic field regenerates the poloidal magnetic field. The dynamo community has long sought to identify the physical mechanism which provides the α-effect, namely the connection between the large-scale toroidal magnetic fields and the induction of correlations between small-scale magnetic fields and flows. We have come tantalizingly close in identifying aspects of this connection with case D3b, going so far as to identify a timescale for this process and that it results in an upscale progression of polarity reversals. It is likely that with additional models showing cycles of magnetic activity we will be able to further identify trends in this elusive mechanism. With current advances in the availability of computational resources and the scalability of ASH, all that remains is for an intrepid soul to carry out the simulations, perform the analyses, and discover the final clues that we have overlooked.

Second, the plume boundary condition work has provided a tool for further study of the nature of convective driving in the bulk of the convection zone, possibly providing a way to explore how the Sun's differential rotation is maintained, as well as a means to further explore the possible modes of giant cell convection in that may exist in the Sun. Giant cells are essential components of any realistic model of convective energy transport in the deep

solar interior and are required to provide the angular momentum transport which maintains the solar differential rotation. The giant cells are on solid theoretical footing, but they have not been reliably detected despite considerable observational effort. Advances in helioseismic techniques may be able to finally achieve detection of these structures if they have good models of what they should be looking for. Convection in many settings has a multitude of preferred scales, as can be seen in our models with impenetrable boundaries, however the convection resulting from our plume boundary condition did not show clear cellular patterns with a preferred scale. It may be that giant cells remain undetected because they exist as coalescing smaller-scale plumes forming tree-like structures of downflows rather than cellular patterns. The plume boundary condition in ASH may provide a means to test these ideas which simply was not possible with impenetrable boundaries.

Finally, the plume boundary condition in ASH is designed to remove the diffusive boundary layer at the top of the domain. This boundary layer effectively limits the rise of the buoyant magnetic loops generated in case S3. A number of loops rose coherently all the way to the impenetrable boundary where they were diffused away by the boundary layer. Creating a simulation which combines case S3 with our plume boundary condition may provide a way to allow further rise of the buoyant magnetic loops through and possibly out the top of our simulations. This would be an exceptionality demanding simulation as the number of parameters would be immense. Additionally, feedbacks between the dynamic Smagorinsky model and the plume boundary condition may be very challenging to manage. The current implementation may not be sufficiently open to permit the buoyant loops to emerge through our upper boundary. However the possibility for a model which can self-consistently generate buoyant magnetic loops and monitor their rise from the base of the convection zone to within a few percent of the Sun's radius below the photosphere is enticing.

These three projects have provided only a small sampling of possible future direction this work could inspire. On a basic level they all attempt to provide better models of components of dynamo action in stars like our Sun. With the accelerating rate of advance in this

field, we are enthusiastic about the prospects for answering long standing questions about the origin and variability of solar and stellar magnetism.

Bibliography

Aerts, C., Christensen-Dalsgaard, J., & Kurtz, D. 2010, Asteroseismology, Astronomy and Astrophysics Library (Berlin: Springer), 866

Augustson, K., Rast, M., Trampedach, R., & Toomre, J. 2011, Modeling the Near-Surface Shear Layer: Diffusion Schemes Studied With CSS, J. Phys. Conf. Ser., 271, 012070

Babcock, H. W. 1961, The Topology of the Sun's Magnetic Field and the 22-Year Cycle, ApJ, 133, 572

Babcock, H. W. & Babcock, H. D. 1955, The Sun's Magnetic Field, 1952-1954, ApJ, 121, 349

Baliunas, S. L., Donahue, R. A., Soon, W. H., Horne, J. H., Frazer, J., Woodard-Eklund, L., Bradford, M., Rao, L. M., Wilson, O. C., Zhang, Q., Bennett, W., Briggs, J., Carroll, S. M., Duncan, D. K., Figueroa, D., Lanning, H. H., Misch, T., Mueller, J., Noyes, R. W., Poppe, D., Porter, A. C., Robinson, C. R., Russell, J., Shelton, J. C., Soyumer, T., Vaughan, A. H., & Whitney, J. H. 1995, Chromospheric Variations in Main-Sequence Stars, ApJ, 438, 269

Bardina, J., Ferziger, J. H., & Reynolds, W. C. 1980, Improved Subgrid-Scale Models for Large-Eddy Simulation, American Institute of Aeronautics and Astronautics, Fluid and Plasma Dynamics Conference, 13th, Snowmass, Colo., July 14-16, 1980, 10 p.

Beeck, B., Collet, R., Steffen, M., Asplund, M., Cameron, R. H., Freytag, B., Hayek, W., Ludwig, H.-G., & Schüssler, M. 2012, Simulations of the Solar Near-Surface Layers with the CO5BOLD, MURaM, and Stagger Codes, Astron. Astrophys., 539, A121

Berkoff, N. A., Kersalé, E., & Tobias, S. M. 2010, Comparison of the Anelastic Approximation with Fully Compressible Equations for Linear Magnetoconvection and Magnetic Buoyancy, Geophys. Astro. Fluid, 104, 545

Birch, A. C., Braun, D. C., Leka, K. D., Barnes, G., & Javornik, B. 2013, Helioseismology of Pre-Emerging Active Regions. II. Averge Emergence Properties, ApJ, 762, 131

Borrero, J. & Ichimoto, K. 2011, Magnetic Structure of Sunspots, Liv. Rev. Sol. Phys., 8, 4

Braginskii, S. I. 1965, Transport Processes in a Plasma, Reviews of Plasma Physics, 1, 1

Brandenburg, A. 2003, Computational Aspects of Astrophysical MHD and Turbulence, ed. A. Ferriz-Mas & M. Nunez (London: Taylor and Francis), 269

—. 2005, The Case for a Distributed Solar Dynamo Shaped by Near-Surface Shear, ApJ, 625, 539

Brown, B. P. 2009, Convection and Dynamo Action in Rapidly Rotating Suns, Ph.D. Thesis, University of Colorado at Boulder, Boulder, Colorado, USA

Brown, B. P., Browning, M. K., Brun, A. S., Miesch, M. S., & Toomre, J. 2008, Rapidly Rotating Suns and Active Nests of Convection, ApJ, 689, 1354

—. 2010, Persistent Magnetic Wreaths in a Rapidly Rotating Sun, ApJ, 711, 424

Brown, B. P., Miesch, M. S., Browning, M. K., Brun, A. S., & Toomre, J. 2011, Magnetic Cycles in a Convective Dynamo Simulation of a Young Solar-Type Star, ApJ, 731, 69

Brown, B. P., Vasil, G. M., & Zweibel, E. G. 2012, Energy Conservation and Gravity Waves in Sound-Proof Treatments of Stellar Interiors. Part I. Anelastic Approximations, ApJ, 756, 109

Browning, M. K., Miesch, M. S., Brun, A. S., & Toomre, J. 2006, Dynamo Action in the Solar Convection Zone and Tachocline: Pumping and Organization of Toroidal Fields, ApJL, 648, L157

Brun, A. S., Miesch, M. S., & Toomre, J. 2004, Global-Scale Turbulent Convection and Magnetic Dynamo Action in the Solar Envelope, ApJ, 614, 1073

—. 2011, Modeling the Dynamical Coupling of the Solar Convection Zone with the Radiative Interior, ApJ, 742, 79

Brun, A. S. & Toomre, J. 2002, Turbulent Convection under the Influence of Rotation: Sustaining a Strong Differential Rotation, ApJ, 570, 865

Buffett, B. 2003, A Comparison of Subgrid-Scale Models for Large-Eddy Simulations of Convection in the Earth's Core, Geophys. J. Int., 753

Buscher, D., Creech-Eakman, M., Farris, A., Haniff, C. A., & Young, J. S. 2013, The Conceptual Design of the Magdalena Ridge Observatory Interferometer, eprint arXiv:1307.0391

Caligari, P., Moreno-Insertis, F., & Schüssler, M. 1995, Emerging Flux Tubes in the Solar Convection Zone. I. Asymmetry, Tilt, and the Emergence Latitude, ApJ, 441, 886

Chandrasekhar, S. 1961, Hydrodynamic and Hydromagnetic Stability (New York: Dover), 654

Charbonneau, P. 2010, Dynamo Models of the Solar Cycle, Liv. Rev. Sol. Phys., 7, 3

Chatterjee, P., Nandy, D., & Choudhuri, A. R. 2004, Full-Sphere Simulations of a Circulation-Dominated Solar Dynamo: Exploring the Parity Issue, Astron. Astrophys., 427, 1019

Chernyshov, A. A., Karelsky, K. V., & Petrosyan, A. S. 2008, Three-Dimensional Modeling of Compressible Magnetohydrodynamic Turbulence in the Local Interstellar Medium, ApJ, 686, 1137

—. 2010, Novel Developments in Subgrid-Scale Modeling of Space Plasma: Weakly Compressible Turbulence in the Local Interstellar Medium, Phys. Scrip., T142, 014029

Cheung, M. C. M., Rempel, M., Title, A. M., & Schüssler, M. 2010, Simulation of the Formation of a Solar Active Region, ApJ, 720, 233

Choudhuri, A., Chatterjee, P., & Jiang, J. 2007, Predicting Solar Cycle 24 With a Solar Dynamo Model, Phys. Rev. Let., 98, 131103

Christensen-Dalsgaard, J. 2002, Helioseismology, Rev. Mod. Phys., 74, 1073

Christensen-Dalsgaard, J., Dappen, W., Ajukov, S., Anderson, E., Antia, H., Basu, S., Baturin, V., Berthomieu, G., Chaboyer, B., Chitre, S., Cox, A., Demarque, P., Donatowicz, J., Dziembowski, W., Gabriel, M., Gough, D., Guenther, D., Guzik, J., Harvey, J., Hill, F., Houdek, G., Iglesias, C., Kosovichev, A., Leibacher, J., Morel, P., Proffitt, C., Provost, J., Reiter, J., Rhodes, E., Rogers, F., Roxburgh, I., Thompson, M. J., & Ulrich, R. 1996, The Current State of Solar Modeling, Science, 272, 1286

Cline, K. S., Brummell, N. H., & Cattaneo, F. 2003, On the Formation of Magnetic Structures by the Combined Action of Velocity Shear and Magnetic Buoyancy, ApJ, 588, 630

Clune, T., Elliott, J., Miesch, M. S., Toomre, J., & Glatzmaier, G. A. 1999, Computational Aspects of a Code to Study Rotating Turbulent Convection in Spherical Shells, Parallel Comput., 25, 361

Clyne, J., Mininni, P., Norton, A., & Rast, M. 2007, Interactive Desktop Analysis of High Resolution Simulations: Application to Turbulent Plume Dynamics and Current Sheet Formation, New J. Phys., 9, 301

Cowling, T. G. 1933, The Magnetic Field of Sunspots, MNRAS, 94, 39

Danilovic, S., Beeck, B., Pietarila, A., Schüssler, M., Solanki, S. K., Martínez Pillet, V., Bonet, J. A., del Toro Iniesta, J. C., Domingo, V., Barthol, P., Berkefeld, T., Gandorfer, A., Knölker, M., Schmidt, W., & Title, A. M. 2010, Transverse Component of the Magnetic Field in the Solar Photosphere Observed by SUNRISE, ApJL, 723, L149

Dennery, P. & Krzywicki, A. 1996, Mathematics for Physicists (New York: Dover), 384

DeRosa, M. L., Brun, A. S., & Hoeksema, J. T. 2012, Solar Magnetic Field Reversals and the Role of Dynamo Families, ApJ, 757, 96

Dikpati, M. 2011, Polar Field Puzzle: Solutions from Flux–Transport Dynamo and Surface Transport Models, ApJ, 733, 90

Dikpati, M. & Gilman, P. A. 2006, Simulating and Predicting Solar Cycles Using a Flux Transport Dynamo, ApJ, 649, 498

Donati, J.-F. & Landstreet, J. 2009, Magnetic Fields of Non–Degenerate Stars, Annu. Rev. Astron. Astrophys., 47, 333

Drake, S. 1957, Discoveries and Opinions of Galileo: Translated with an Introduction and Notes (Garden City, N.Y.: Doubleday), 302

Durney, B. 1995, On a Babcock-Leighton Dynamo Model with a Deep-Seated Generating Layer for the Toroidal Magnetic Field, Sol. Phys., 160, 213

Elliott, J. R., Miesch, M. S., & Toomre, J. 2000, Turbulent Solar Convection and Its Coupling with Rotation: The Effect of Prandtl Number and Thermal Boundary Conditions on the Resulting Differential Rotation, ApJ, 533, 546

Fan, Y. 2001, Nonlinear Growth of the Threedimensional Undular Instability of a Horizontal Magnetic Layer and the Formation of Arching Flux Tubes, ApJ, 546, 509

—. 2008, The Three-Dimensional Evolution of Buoyant Magnetic Flux Tubes in a Model Solar Convective Envelope, ApJ, 676, 680

—. 2009, Magnetic Fields in the Solar Convection Zone, Liv. Rev. Sol. Phys., 6, 4

Fan, Y. & Abbett, W. P. 2003, The Dynamic Evolution of Twisted Magnetic Flux Tubes in a Three-Dimensional Convecting Flow. I. Uniformly Buoyant Horizontal Tubes, ApJ, 582, 1206

Fan, Y., Featherstone, N., & Fang, F. 2013, Three-Dimensional MHD Simulations of Emerging Active Region Flux in a Turbulent Rotating Solar Convective Envelope: The Numerical Model and Initial Results, eprint arXiv:1305.6370, 50

Fan, Y. & Fisher, G. 1996, Radiative Heating and the Buoyant Rise of Magnetic Flux Tubes in the Solar Interior, Sol. Phys., 166, 17

Gade, K. 2010, A Non-singular Horizontal Position Representation, J. Navigation, 63, 395

Galloway, D. J. & Weiss, N. O. 1981, Convection and Magnetic Fields in Stars, ApJ, 243, 945

Gastine, T., Duarte, L., & Wicht, J. 2012, Dipolar Versus Multipolar Dynamos: The Influence of the Background Density Stratification, Astron. Astrophys., 546, A19

Gastine, T., Wicht, J., & Aurnou, J. 2013, Zonal flow regimes in rotating anelastic spherical shells: An application to giant planets, Icarus, 225, 156

Gaulme, P., Deheuvels, S., Weiss, W. W., Mosser, B., Moutou, C., Bruntt, H., Donati, J.-F., Vannier, M., Guillot, T., Appourchaux, T., Michel, E., Auvergne, M., Samadi, R., Baudin, F., Catala, C., & Baglin, A. 2010, HD 46375: Seismic and Spectropolarimetric Analysis of a Young Sun Hosting a Saturn-like Planet, Astron. Astrophys., 524, A47

Germano, M., Piomelli, U., Moin, P., & Cabot, W. 1991, A Dynamic Subgrid-Scale Eddy Viscosity Model, Phys. Fluids A-Fluids, 3, 1760

Getling, A. 1998, Rayleigh-Bénard Convection: Structures and Dynamics (River Edge, N.J.: World Scientific), 245

Ghizaru, M., Charbonneau, P., & Smolarkiewicz, P. K. 2010, Magnetic Cycles in Global Large-Eddy Simulations of Solar Convection, ApJ, 715, L133

Gilman, P. 1983, Dynamically Consistent Nonlinear Dynamos Driven by Convection in a Rotating Spherical Shell. II-Dynamos with Cycles and Strong Feedbacks, ApJS, 53, 243

Gizon, L. & Birch, A. C. 2005, Local Helioseismology, Liv. Rev. Sol. Phys., 2, 6

Glatzmaier, G. A. 1985, Numerical Simulations of Stellar Convective Dynamos. II. Field Propagation in the Convection Zone, ApJ, 291, 300

Gough, D. O. 1969, The Anelastic Approximation for Thermal Convection, J. Atmos. Sci., 26, 448

Gough, D. O. & McIntyre, M. 1998, Inevitability of a Magnetic Field in the Sun's Radiative Interior, Nature, 394, 755

Guerrero, G. & Käpylä, P. J. 2011, Dynamo Action and Magnetic Buoyancy in Convection Simulations with Vertical Shear, Astron. Astrophys., 533, A40

Guglielmino, S. L., Martínez Pillet, V., Bonet, J. a., del Toro Iniesta, J. C., Bellot Rubio, L. R., Solanki, S. K., Schmidt, W., Gandorfer, a., Barthol, P., & Knölker, M. 2012, The Frontier Between Small-Scale Bipoles and Ephemeral Regions in the Solar Photosphere: Emergence and Decay of and Intermediate-Scale Bipole Observed with SUNRISE/IMaX, The Astrophysical Journal, 745, 160

Haber, D. A., Hindman, B. W., Toomre, J., Bogart, R. S., Larsen, R. M., & Hill, F. 2002, Evolving Submerged Meridional Circulation Cells within the Upper Convection Zone Revealed by Ring-Diagram Analysis, ApJ, 570, 855

Hale, G. E. 1908, On the Probable Existence of a Magnetic Field in Sun-Spots, ApJ, 28, 315

Hale, G. E., Ellerman, F., Nicholson, S. B., & Joy, A. H. 1919, The Magnetic Polarity of Sun-Spots, ApJ, 49, 153

Hall, J. C. 2008, Stellar Chromospheric Activity, Liv. Rev. Sol. Phys., 5, 2

Hanasoge, S. M., Duvall, T. L., & DeRosa, M. L. 2010, Seismic Constraints on Interior Solar Convection, ApJ, 712, L98

Hathaway, D. H. 1996, Doppler Measurements of the Sun's Meridional Flow, ApJ, 460, 1027

—. 2009, Solar Cycle Forecasting, Space Sci. Rev., 144, 401

—. 2010, The Solar Cycle, Liv. Rev. Sol. Phys., 7, 1

—. 2012, Supergranules As Probes of the Sun's Meridional Circulation, ApJ, 760, 84

Hecht, M. W., Holm, D. D., Petersen, M. R., & Wingate, B. A. 2008, Implementation of the LANS-α Turbulence Model in a Primitive Equation Ocean Model, J. Comp. Phys., 227, 5691

Hellemans, A. 2013, Nanowire Transistors Could Keep Moore's Law Alive, IEEE Spectrum, April 2013, 45

Hempelmann, A., Schmitt, J. H. M. M., & Stępień, K. 1996, Coronal X-ray Emission of Cool Stars in Relation to Chromospheric Activity and Magnetic Cycles., Astron. Astrophys., 305, 284

Henney, C. & Harvey, J. 2002, Phase Coherence Analysis of Solar Magnetic Activity, Sol. Phys., 207, 199

Hindman, B. W., Haber, D. A., & Toomre, J. 2009, Subsurface Circulations within Active Regions, ApJ, 698, 1749

Howe, R. 2009, Solar Interior Rotation and its Variation, Liv. Rev. Sol. Phys., 6, 1

Huber, D., Ireland, M. J., Bedding, T. R., Brandão, I. M., Piau, L., Maestro, V., White, T. R., Bruntt, H., Casagrande, L., Molenda-Żakowicz, J., Aguirre, V. S., Sousa, S. G., Barclay, T., Burke, C. J., Chaplin, W. J., Christensen-Dalsgaard, J., Cunha, M. S., De Ridder, J., Farrington, C. D., Frasca, a., García, R. a., Gilliland, R. L., Goldfinger, P. J., Hekker, S., Kawaler, S. D., Kjeldsen, H., McAlister, H. a., Metcalfe, T. S., Miglio, a., Monteiro, M. J. P. F. G., Pinsonneault, M. H., Schaefer, G. H., Stello, D., Stumpe, M. C., Sturmann, J., Sturmann, L., ten Brummelaar, T. a., Thompson, M. J., Turner, N., & Uytterhoeven, K. 2012, Fundimental Properties of Stars Using Asteroseismology from Kepler and CoRoT and Interferometry from the CHARA Array, ApJ, 760, 32

Ilonidis, S., Zhao, J., & Kosovichev, A. 2011, Detection of Emerging Sunspot Regions in the Solar Interior., Science, 333, 993

Jacoutot, L., Kosovichev, A. G., Wray, A., & Mansour, N. N. 2008, Realistic Numerical Simulations of Solar Convection and Oscillations in Magnetic Regions, ApJ, 684, L51

Jones, C. A., Boronski, P., Brun, A. S., Glatzmaier, G., Gastine, T., Miesch, M. S., & Wicht, J. 2011, Anelastic Convection-Driven Dynamo Benchmarks, Icarus, 216, 120

Jouve, L. & Brun, A. S. 2009, Three-Dimensional Nonlinear Evolution of a Magnetic Flux Tube in a Spherical Shell: Influence of Turbulent Convection and Associated Mean Flows, ApJ, 701, 1300

Jouve, L., Brun, A. S., & Aulanier, G. 2013, Global Dynamics of Subsurface Solar Active Regions, ApJ, 762, 4

Käpylä, P. J., Brandenburg, A., Kleeorin, N., Mantere, M. J., & Rogachevskii, I. 2012a, Negative Effective Magnetic Pressure in Turbulent Convection, MNRAS, 422, 2465

Käpylä, P. J., Mantere, M. J., & Brandenburg, A. 2012b, Cyclic Magnetic Activity Due To Turbulent Convection in Spherical Wedge Geometry, ApJ, 755, L22

Käpylä, P. J., Mantere, M. J., Cole, E., Warnecke, J., & Brandenburg, A. 2013, Effects of Strong Stratification on Equatorward Dynamo Wave Propagation, eprint arXiv:1301.2595

Käpylä, P. J., Mantere, M. J., Guerrero, G., Brandenburg, A., & Chatterjee, P. 2011, Reynolds Stress and Heat Flux in Spherical Shell Convection, Astron. Astrophys., 531, A162

Kemel, K., Brandenburg, A., Kleeorin, N., Mitra, D., & Rogachevskii, I. 2012, Active Region Formation through the Negative Effective Magnetic Pressure Instability, Sol. Phys. Online First, DOI: 10.1007/s11207-012-0031-8

Kersalé, E., Hughes, D., & Tobias, S. M. 2007, The Nonlinear Evolution of Instabilities Driven by Magnetic Buoyancy: A New Mechanism for the Formation of Coherent Magnetic Structures, ApJ, 663, 113

Kleeorin, N. I., Rogachevskii, I. V., & Ruzmaikin, A. A. 1989, The Effect of Negative Magnetic Pressure and the Large-Scale Magnetic Field Instability in the Solar Convective Zone, Pis'ma v Astronomicheskii Zhurnal, 15, 639

Krause, F. & Raedler, K.-H. 1980, Mean-field Magnetohydrodynamics and Dynamo Theory (Oxford, UK: Pergamon), 271

Krumholz, M. R. & McKee, C. F. 2005, A General Theory of Turbulence-Regulated Star Formation, from Spirals to Ultraluminous Infrared Galaxies, ApJ, 630, 250

Kundu, P. & Cohen, I. 2004, Fluid Mechanics, 3rd edn. (San Diego: Elsevier), 759

Latour, J., Spiegel, E. A., Toomre, J., & Zahn, J.-P. 1976, Stellar Convection Theory. I - The Anelastic Modal Equations, ApJ, 207, 233

Leighton, R. B. 1964, Transport of Magnetic Fields on the Sun., ApJ, 140, 1547

Leka, K. D., Barnes, G., Birch, A. C., Gonzalez-Hernandez, I., Dunn, T., Javornik, B., & Braun, D. C. 2013, Helioseismology of Pre-Emerging Active Regions. I. Overview, Data, and Target Selection Criteria, ApJ, 762, 130

Li, J. & Ulrich, R. K. 2012, Long-Term Measurements of Sunspot Magnetic Tilt Angles, ApJ, 758, 29

Llama, J., Jardine, M., Mackay, D. H., & Fares, R. 2012, Using Kepler Transit Observations to Measure Stellar Spot Belt Migration Rates, MNRAS Let., 422, L72

Mackay, D. H. & Yeates, A. 2012, The Sun's Global Photospheric and Coronal Magnetic Fields: Observations and Models, Liv. Rev. Sol. Phys., 9, 6

Meibom, S. r., Barnes, S. A., Latham, D. W., Batalha, N., Borucki, W. J., Koch, D. G., Basri, G., Walkowicz, L. M., Janes, K. A., Jenkins, J., Van Cleve, J., Haas, M. R., Bryson, S. T., Dupree, A. K., Furesz, G., Szentgyorgyi, A. H., Buchhave, L. A., Clarke, B. D., Twicken, J. D., & Quintana, E. V. 2011, The Kepler Cluster Study: Stellar Rotation in Ngc 6811, ApJ, 733, L9

Meneveau, C. & Katz, J. 2000, Scales-Invariance and Turbulence Models for Large-Eddy Simulation, Annu. Rev. Fluid Mech., 32, 1

Metcalfe, T. S., Buccino, A. P., Brown, B. P., Mathur, S., Soderblom, D. R., Henry, T. J., Mauas, P. J. D., Petrucci, R., Hall, J. C., & Basu, S. 2013, Magnetic Activity Cycles in the Exoplanet Host Star Eridani, ApJ, 763, L26

Miesch, M. S. 2005, Large-Scale Dynamics of the Convection Zone and Tachocline, Liv. Rev. Sol. Phys., 2, 1

Miesch, M. S. & Brown, B. P. 2012, Convective Babcock-Leighton Dynamo Models, ApJ, 746, L26

Miesch, M. S., Brun, A. S., DeRosa, M. L., & Toomre, J. 2008, Structure and Evolution of Giant Cells in Global Models of Solar Convection, ApJ, 673, 557

Miesch, M. S., Brun, A. S., & Toomre, J. 2006, Solar Differential Rotation Influenced by Latitudinal Entropy Variations in the Tachocline, ApJ, 641, 618

Miesch, M. S., Featherstone, N. A., Rempel, M., & Trampedach, R. 2012, On the Amplitude of Convective Velocities in the Deep Solar Interior, ApJ, 757, 128

Miesch, M. S. & Toomre, J. 2009, Turbulence, Magnetism, and Shear in Stellar Interiors, Annu. Rev. Fluid Mech., 41, 317

Moffatt, H. K. 1978, Magnetic Field Generation in Electrically Conducting Fluids, Cambridge, England, Cambridge University Press, 1978. 353 p.

Moreno-Insertis, F. & Emonet, T. 1996, The Rise of Twisted Magnetic Tubes in a Stratified Medium, ApJ, 472, L53

Morgenthaler, A., Petit, P., Saar, S. H., Solanki, S. K., Morin, J., Marsden, S. C., Aurière, M., Dintrans, B., Fares, R., Gastine, T., Lanoux, J., Lignières, F., Paletou, F., Ramírez Vélez, J. C., Théado, S., & Van Grootel, V. 2012, Long-term Magnetic Field Monitoring of the Sun-like Star ξ Bootis A, Astron. Astrophys., 540, A138

Muñoz Jaramillo, A., Nandy, D., & Martens, P. C. H. 2009, Helioseismic Data Inclusion in Solar Dynamo Models, ApJ, 698, 461

Nelson, N. J., Brown, B. P., Browning, M. K., Brun, A. S., Miesch, M. S., & Toomre, J. 2011a, Global Magnetic Cycles in Rapidly Rotating Younger Suns, Proc. IAU, 6, 272

Nelson, N. J., Brown, B. P., Brun, A. S., Miesch, M. S., & Toomre, J. 2011b, Buoyant Magnetic Loops in a Global Dynamo Simulation of a Young Sun, ApJ, 739, L38

—. 2013a, Buoyant Magnetic Loops Generated by Global Convective Dynamo Action, Sol. Phys. Online First, DOI:10.1007/s11207-012-0221-4

—. 2013b, Magnetic Wreaths and Cycles in Convective Dynamos, ApJ, 762, 73

Nishikawa, N. & Kusano, K. 2008, Simulation Study of the Symmetry-breaking Instability and the Dipole Field Reversal in a Rotating Spherical Shell Dynamo, Phys. Plasma, 15, 082903

Nordlund, A., Stein, R. F., & Asplund, M. 2009, Solar Surface Convection, Liv. Rev. Sol. Phys., 6, 2

Oláh, K., Kolláth, Z., Granzer, T., Strassmeier, K. G., Lanza, a. F., Järvinen, S., Korhonen, H., Baliunas, S. L., Soon, W., Messina, S., & Cutispoto, G. 2009, Multiple and Changing Cycles of Active Stars, Astron. Astrophys., 501, 703

Parker, E. N. 1955, Hydromagnetic Dynamo Models., ApJ, 122, 293

Patnaik, G., Boris, J. P., Grinstein, F. F., Iselin, J. P., & Hertwig, D. 2012, Flux-Corrected Transport, ed. D. Kuzmin, R. Löhner, & S. Turek, Scientific Computation (Dordrecht: Springer Netherlands), 91

Petit, P., Dintrans, B., Solanki, S. K., Donati, J.-F., Aurière, M., Lignires, F., Morin, J., Paletou, F., Ramirez, J., Catala, C., & Fares, R. 2008, Toroidal Versus Poloidal Magnetic Fields in Sun-like Stars: A Rotation Threshold, MNRAS, 388, 80

Petrovay, K. 2010, Solar Cycle Prediction, Liv. Rev. Sol. Phys., 7, 6

Pevtsov, A. A., Canfield, R. C., & Metcalf, T. R. 1995, Latitudinal Variation of Helicity of Photospheric Magnetic Fields, ApJ, 440, L109

Pevtsov, A. A., Canfield, R. C., Sakurai, T., & Hagino, M. 2008, On the Solar Cycle Variation of the Hemispheric Helicity Rule, ApJ, 677, 719

Pevtsov, A. A., Maleev, V. M., & Longcope, D. W. 2003, Helicity Evolution in Emerging Active Regions, ApJ, 593, 1217

Pinto, R. F., Brun, A. S., Jouve, L., & Grappin, R. 2011, Coupling the Solar Dynamo and the Corona: Wind Properties, Mass, and Momentum Losses During an Activity Cycle, ApJ, 737, 72

Pizzolato, N., Maggio, A., Micela, G., Sciortino, S., & Ventura, P. 2003, The Stellar Activity-Rotation Relationship Revisited: Dependence of Saturated and Non-Saturated X-ray Emission Regimes on Stellar Mass for Late-Type Dwarfs, Astron. Astrophys., 157, 147

Pope, S. B. 2000, Turbulent Flows (Cambridge, UK: Cambridge University Press), 806

Potgieter, M. 2013, Solar Modulation of Cosmic Rays, Liv. Rev. Sol. Phys., 10, 3

Prusa, J., Smolarkiewicz, P. K., & Wyszogrodzki, A. A. 2008, EULAG, a Computational Model for Multiscale Flows, Comput. Fluids, 37, 1193

Racine, E., Charbonneau, P., Ghizaru, M., Bouchat, A., & Smolarkiewicz, P. K. 2011, On the Mode of Dynamo Action in a Global Large-Eddy Simulation of Solar Convection, ApJ, 735, 46

Rast, M. 2003, The Scales of Granulation, Mesogranulation, and Supergranulation, ApJ, 597, 1200

Reiners, A. 2012, Observations of Cool-Star Magnetic Fields, Liv. Rev. Sol. Phys., 8, 1

Rempel, M. & Schlichenmaier, R. 2011, Sunspot Modeling: From Simplified Models to Radiative MHD Simulations, Liv. Rev. Sol. Phys., 8, 3

Rempel, M. & Schüssler, M. 2001, Intensification of Magnetic Fields by Conversion of Potential Energy, ApJ, 552, L171

Rempel, M., Schüssler, M., & Knölker, M. 2009, Radiative Magnetohydrodynamic Simulation of Sunspot Structure, ApJ, 691, 640

Rieutord, M. & Rincon, F. 2010, The Sun's Supergranulation, Liv. Rev. Sol. Phys., 7, 2

Rogachevskii, I. & Kleeorin, N. 2007, Magnetic Fluctuations and Formation of Large-scale Inhomogeneous Magnetic Structures in a Turbulent Convection, Phys. Rev. E, 76, 16

Rudiger, G. & Kitchatinov, L. 1997, The Slender Solar Tachocline: A Magnetic Model, Astron. Nachr., 318, 273

Saar, S. H. & Brandenburg, A. 1999, Time Evolution of the Magnetic Activity Cycle Period. II. Results for an Expanded Stellar Sample, ApJ, 524, 295

Sakurai, K. 1980, The Solar Activity in the Time of Galileo, J. Hist. Astron., 11, 164

Sanz-Forcada, J., Stelzer, B., & Metcalfe, T. S. 2013, ι Horologi, the First Coronal Activity Cycle in a Young Solar-like Star, Astron. Astrophys., 553, L6

Schekochihin, A. A., Cowley, S. C., Taylor, S. F., Maron, J. L., & McWilliams, J. C. 2004, Simulations of the Small–Scale Turbulent Dynamo, ApJ, 612, 276

Simard, C., Charbonneau, P., & Bouchat, A. 2013, Magnetohydrodynamic Simulation-Driven Kinematic Mean Field Model of the Solar Cycle, ApJ, 768, 16

Sivaraman, K. R., Sivaraman, H., Gupta, S. S., & Howard, R. F. 2010, Return Meridional Flow in the Convection Zone from Latitudinal Motions of Umbrae of Sunspot Groups, Sol. Phys., 266, 247

Smagorinsky, J. 1963, General Circulation Experiments with the Primitive Equations, Mon. Weather Rev., 91, 99

Spiegel, E. A. & Zahn, J.-P. 1992, The Solar Tachocline, Astron. Astrophys., 265, 106

Spruit, H. C. 2011, in The Sun, the Solar Wind, and the Heliosphere. Proceedings of the conference held 23-30 August, 2009 in Sopron, Hungary., ed. M. Miralles & J. S. Almeida (Berlin: Springer), 389

Stein, R. F. & Nordlund, A. K. 2006, Solar Small-scale Magnetoconvection, ApJ, 642, 1246

Stenflo, J. O. & Kosovichev, A. G. 2012, Bipolar Magnetic Regions on the Sun: Global Analysis of the Soho/MDI Data Set, ApJ, 745, 129

Strugarek, A., Brun, A. S., & Zahn, J.-P. 2011, Magnetic Confinement of the Solar Tachocline: II. Coupling to a Convection Zone, Astron. Astrophys., 532, A34

Sullivan, P. P. & Patton, E. 2011, The Effect of Mesh Resolution on Convective Boundary Layer Statistics and Structures Generated by Large-Eddy Simulation, J. Atmos. Sci., 68, 2395

Thompson, M. J. & Weiss, N. O. 2009, The Solar Dynamo, Space Sci. Rev., 4, 666

Tiwari, S. K., Venkatakrishnan, P., & Sankarasubramanian, K. 2009, Global Twist of Sunspot Magnetic Fields Obtained From High-Resolution Vector Magnetograms, ApJ, 702, L133

Trampedach, R. & Stein, R. F. 2011, The Mass Mixing Length in Convective Stellar Envelopes, ApJ, 731, 78

Ulrich, R. K. 2010, Solar Meridional Circulation from the Doppler Shifts of the Fe I Line at 5250 Å as Measured by the 150-Foot Solar Tower Telescope at the Mt. Wilson Observatory, ApJ, 725, 658

Usoskin, I. G. 2008, A History of Solar Activity over Millennia, Liv. Rev. Sol. Phys., 5, 3

Usoskin, I. G., Solanki, S. K., & Kovaltsov, G. A. 2007, Grand Minima and Maxima of Solar Activity: New Observational Constraints, Astron. Astrophys., 471, 301

van Ballegooijen, A. A. 1982, The Overshoot Layer at the Base of the Solar Convective Zone and the Problem of Magnetic Flux Storage, Astron. Astrophys., 113, 99

Vasil, G. M. & Brummell, N. H. 2009, Constraints on the Magnetic Buoyancy Instabilities of a Shear-Generated Magnetic Layer, ApJ, 690, 783

Vasil, G. M., Lecoanet, D., Brown, B. P., Wood, T. S., & Zweibel, E. G. 2013, Energy Conservation and Gravity Waves in Sound-Proof Treatments of Stellar Interiors: Part II Lagrangian Constrained Analysis, eprint arXiv:1303.0005, 23

Wachtor, A. J., Grinstein, F. F., DeVore, C. R., Ristorcelli, J. R., & Margolin, L. G. 2013, Implicit Large-Eddy Simulation of Passive Scalar Mixing in Statistically Stationary Isotropic Turbulence, Physics of Fluids, 25, 025101

Wall, J. V. & Jenkins, C. R. 2003, Practical Statistics for Astronomers (Cambridge, UK: Cambridge University Press), 277

Wang, Y. M. & Sheeley, N. R. 1989, Average Properties of Bipolar Magnetic Regions During Sunspot Cycle 21, Sol. Phys., 124, 81

Warnecke, J., Käpylä, P. J., Mantere, M. J., & Brandenburg, A. 2012, Ejections of Magnetic Structures Above a Spherical Wedge Driven by a Convective Dynamo with Differential Rotation, Sol. Phys., 280, 299

Weber, M. A., Fan, Y., & Miesch, M. S. 2011, The Rise of Active Region Flux Tubes in the Turbulent Solar Convective Envelope, ApJ, 741, 11

—. 2012, Comparing Simulations of Rising Flux Tubes Through the Solar Convection Zone with Observations of Solar Active Regions: Constraining the Dynamo Field Strength, Sol. Phys. Online First, DOI: 10.1007/s11207-012-0093-7

—. 2013, A Theory on the Convective Origins of Active Longitudes on Solar-like Stars, ApJ, 770, 149

White, T. R., Huber, D., Maestro, V., Bedding, T. R., Ireland, M. J., Baron, F., Boyajian, T. S., Che, X., Monnier, J. D., Pope, B. J. S., Roettenbacher, R. M., Stello, D., Tuthill, P. G., Farrington, C. D., Goldfinger, P. J., McAlister, H. A., Schaefer, G. H., Sturmann, J., Sturmann, L., ten Brummelaar, T. a., & Turner, N. H. 2013, Interferometric Radii of Bright Kepler Stars with the CHARA Array: theta Cygni and 16 Cygni A and B, MNRAS, 433, 1262

Whittmann, A. & Xu, Z. 1987, A Catalogue of Sunspot Observations from 165 BC to AD 1684, Astron. Astrophys. Supp. Ser., 70, 83

Wright, N. J., Drake, J. J., Mamajek, E. E., & Henry, G. W. 2011, The Stellar-Activity-Rotation Relationship and the Evolution of Stellar Dynamos, ApJ, 743, 48

Zwaan, C. 1987, Elements and Patterns in the Solar Magnetic Field, Annu. Rev. Astron. Astrophys., 25, 83

Appendix A

Generation of Differential Rotation Kinetic Energy

As shown in Equation (5.2), the time evolution of angular momentum in our domain can be written in conservative form as the divergence of a flux vector $\vec{\mathcal{F}}$. The radial component is given by

$$\mathcal{F}_r = \bar{\rho}\lambda \left[-\nu r \frac{\partial}{\partial r}\left(\frac{v_\phi}{r}\right) + \widehat{v'_\phi v'_r} + \hat{v}_r \hat{v}_\phi + \hat{v}_r \Omega_0 \lambda \right. \\ \left. - \frac{1}{4\pi\bar{\rho}} \widehat{B'_\phi B'_r} - \frac{1}{4\pi\bar{\rho}} \hat{B}_\phi \hat{B}_r \right], \tag{A.1}$$

where the terms are from left to right due to viscous diffusion, fluctuating Reynolds stress, mean Reynolds stress from the meridional circulation, the Coriolis force with Ω_0 representing the frame rotation rate, the Maxwell stress, and mean magnetic torques. The latitudinal component is given by

$$\mathcal{F}_\theta = \bar{\rho}\lambda \left[-\frac{\nu \sin\theta}{r} \frac{\partial}{\partial \theta}\left(\frac{v_\phi}{\sin\theta}\right) + \widehat{v'_\phi v'_\theta} + \hat{v}_\theta \hat{v}_\phi + \hat{v}_\theta \Omega_0 \lambda \right. \\ \left. - \frac{1}{4\pi\bar{\rho}} \widehat{B'_\phi B'_\theta} - \frac{1}{4\pi\bar{\rho}} \hat{B}_\phi \hat{B}_\theta \right] \tag{A.2}$$

where the terms have the same ordering and identities as in the radial component. We ignore the flux due to the Coriolis force because while it can be large locally, it cannot do any net work on the system when averaged over the full domain. We can also write the fluxes in cylindrical coordinates in terms of the cylindrical radius λ and the distance from the equatorial plane z. The flux in cylindrical radius is given by

$$\mathcal{F}_\lambda \hat{\lambda} = F_r \sin\theta \hat{r} + F_\theta \cos\theta \hat{\theta}, \tag{A.3}$$

while the flux in z is given by

$$\mathcal{F}_z\hat{z} = F_r\cos\theta\hat{r} - F_\theta\sin\theta\hat{\theta}, \tag{A.4}$$

If we multiply equation (5.2) by the longitude-averaged rotation profile $\hat{\Omega}$, we are left with an equation for the time evolution of the kinetic energy density in the mean differential rotation profile $\langle E_{\rm DR}\rangle$,

$$\frac{\partial\langle E_{\rm DR}\rangle}{\partial t} = \hat{\Omega}\left(\nabla\cdot\vec{\mathcal{F}}\right). \tag{A.5}$$

We take a volume integral over the entire domain in order to calculate the total rate of change in the kinetic energy of differential rotation and rewrite the right-hand side as

$$\int_{\mathcal{V}}\frac{\partial\langle E_{\rm DR}\rangle}{\partial t}dV = \int_{\mathcal{V}}\left[\vec{\mathcal{F}}\cdot\nabla\hat{\Omega} - \nabla\cdot\left(\hat{\Omega}\vec{\mathcal{F}}\right)\right]dV. \tag{A.6}$$

The second term in the integral can be rewritten using the divergence theorem as a surface integral, leaving us with

$$\int_{\mathcal{V}}\frac{\partial\langle E_{\rm DR}\rangle}{\partial t}dV = \int_{\mathcal{V}}\vec{\mathcal{F}}\cdot\nabla\hat{\Omega}dV - \int_{\mathcal{S}}\hat{\Omega}\mathcal{F}_r dS. \tag{A.7}$$

Our choice of impenetrable and stress-free boundaries causes all of the hydrodynamic terms terms in the surface integral to vanish on both the inner and outer boundaries. Likewise our choice of a perfect conductor boundary condition on the lower surface causes both the fluctuating and mean magnetic torques to vanish there. The choice of a potential field boundary condition on the upper surface forces the mean magnetic torques to be exactly zero, however it does in principle allow the Maxwell stress to be non-zero. This reduces the surface integral to

$$-\int_{\mathcal{S}}\hat{\Omega}\mathcal{F}_r dS = \int_0^\pi\int_0^{2\pi}\frac{\hat{\Omega}}{4\pi}\widehat{B'_\phi B'_\theta}R_o^3\sin^2\theta\,d\theta\,d\phi. \tag{A.8}$$

We have calculated this term to be about five orders of magnitude smaller than the volume integral term in Equation (A.7) when averaged over long periods in cases D3, D3a, and D3b. We chose to ignore this surface term in our analysis of time-averaged quantities.

The generation and dissipation of differential rotation kinetic energy can be written as the sum of five terms, as was done in Equation (5.3). Those terms, which represent viscous diffusion, Reynolds stress, meridional circulations, Maxwell stress, and mean magnetic torques, are given in turn by

$$L_{\rm VD} = -\int_{\mathcal{V}} \bar{\rho}\nu r\sin\theta \left[r\frac{\partial}{\partial r}\left(\frac{v_\phi}{r}\right)\frac{\partial\hat{\Omega}}{\partial r} + \frac{\sin\theta}{r^2}\frac{\partial}{\partial\theta}\left(\frac{v_\phi}{\sin\theta}\right)\frac{\partial\hat{\Omega}}{\partial\theta}\right] dV, \tag{A.9}$$

$$L_{\rm RS} = \int_{\mathcal{V}} \bar{\rho} r\sin\theta \left[\widehat{v'_\phi v'_r}\frac{\partial\hat{\Omega}}{\partial r} + \frac{1}{r}\widehat{v'_\phi v'_\theta}\frac{\partial\hat{\Omega}}{\partial\theta}\right] dV, \tag{A.10}$$

$$L_{\rm MC} = \int_{\mathcal{V}} \bar{\rho} r\sin\theta\hat{v}_\phi \left[\hat{v}_r\frac{\partial\hat{\Omega}}{\partial r} + \frac{\hat{v}_\theta}{r}\frac{\partial\hat{\Omega}}{\partial\theta}\right] dV, \tag{A.11}$$

$$L_{\rm MS} = -\int_{\mathcal{V}} \frac{r\sin\theta}{4\pi} \left[\widehat{B'_\phi B'_r}\frac{\partial\hat{\Omega}}{\partial r} + \frac{\widehat{B'_\phi B'_\theta}}{r}\frac{\partial\hat{\Omega}}{\partial\theta}\right] dV, \tag{A.12}$$

$$L_{\rm MT} = -\int_{\mathcal{V}} \frac{r\sin\theta\hat{B}_\phi}{4\pi} \left[\hat{B}_r\frac{\partial\hat{\Omega}}{\partial r} + \frac{\hat{B}_\theta}{r}\frac{\partial\hat{\Omega}}{\partial\theta}\right] dV. \tag{A.13}$$

The time-averaged values of these terms are reported in Table 5.3 and Figure 5.4.